UNIVERSITY OF SOUTHAMPTON

FACULTY OF ENGINEERING AND THE ENVIRONMENT

FINAL THESIS

INSTITUTE OF SOUND AND VIBRATION RESEARCH

Active Strategies for the Control of Acoustic Scattering

Charlie House

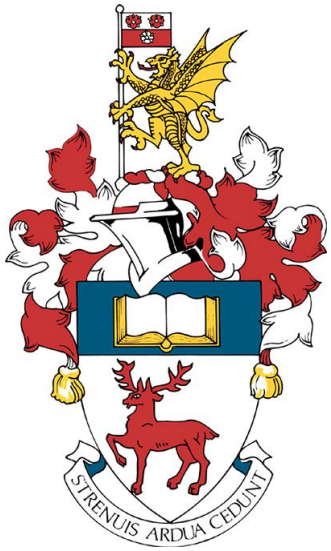

November 6, 2021

Declaration of Authorship

I, Charles House, declare that this thesis titled, 'Active Strategies for the Control of Acoustic Scattering' and the work presented in it are my own.

I confirm that:

- This work was done wholly or mainly while in candidature for a research degree at this University.
- Where any part of this thesis has previously been submitted for a degree or any other qualification at this University or any other institution, this has been clearly stated.
- Where I have consulted the published work of others, this is always clearly attributed.
- Where I have quoted from the work of others, the source is always given. With the exception of such quotations, this thesis is entirely my own work.
- I have acknowledged all main sources of help.
- Where the thesis is based on work done by myself jointly with others, I have made clear exactly what was done by others and what I have contributed myself.
- Parts of this work have been published as:
  - House, C., Cheer, J., & Daley, S. (2018). The Effect of Active Vibration Control on the Sound Field Scattered from a Flexible Structure. In ISMA - International Conference on Noise and Vibration Engineering. Leuven.
  - House, C., Cheer, J., & Daley, S. (2019). On the use of Virtual Sensing for the Real-Time Detection and Active Control of a Scattered Acoustic Field. In ICSV - International Congress on Sound and Vibration. Montreal.
  - House, C., Cheer, J., & Daley, S. (2019). An Investigation into the Performance Limitations of Active Acoustic Cloaking Using an Acoustic Quiet-Zone. In 178th Meeting of the Acoustical Society of America, San Diego, United States.
  - House, C., Cheer, J., & Daley, S. (2020). A Practical Investigation into Active Structural Acoustic Cloaking of a Flexible Cylinder. Applied Acoustics
  - House, C., Cheer, J., & Daley, S. (2020). An Investigation into the Effect of Uncertainty on Active Acoustic Cloaking. In Inter-Noise 2020, Seoul, South Korea.

Signed: _____

Date: 6 Nov 2021

Abstract

University of Southampton
Faculty of Engineering and Physical Sciences
Institute of Sound and Vibration Research
Doctor of Philosophy

Active Strategies for the Control of Acoustic Scattering

by Charlie House

The ability to acoustically cloak an object, such that the soundfield with the presence of the object is identical to that without the presence of the object, has potential applications across a variety of industries and, for this reason, is an active area of research. An object can potentially be acoustically cloaked using either passive or active methods, and this thesis addresses the challenges related to practically implementing active strategies. Active acoustic cloaking has the potential to significantly reduce the acoustic scattering from an object over a broad frequency range, however, examples of practical active acoustic cloaking systems in the literature currently rely on a-priori information that is not practical to obtain in most scenarios, and mostly consider tonal disturbances. The robustness of active acoustic cloaking systems to practical uncertainties has also not yet been considered, which is a key requirement for many practical implementations. The work presented in this thesis will address some of these challenges, using experimental and numerical studies, and provides a number of key insights into the active cloaking problem.

The work presented in this thesis initially considers the acoustic scattering from a rigid sphere, upon which an active acoustic cloaking system is implemented using both tonal and broadband control strategies. The robustness of these systems to realistic perturbations is assessed, and various methods of increasing the robustness are presented. A method of estimating the scattered acoustic pressure in real-time is proposed, which aims to address the requirement for acoustic sensors in the far-field of the scattering object, as well as the challenges associated with directly measuring scattered acoustic pressure, and the performance of this system is quantified.

The acoustic cloaking of flexible bodies is more challenging than that of rigid bodies, due to the presence of resonant scattering components and, therefore, the latter part of this thesis considers the acoustic scattering from a flexible cylinder. The relationship between the structural response of the scattering body and the scattered acoustic field is analysed, and the acoustic effect of implementing Active Vibration Control on the scattering body is investigated. An active structural acoustic cloaking system is also implemented experimentally, and a significant reduction in the scattered acoustic pressure is realised.

Acknowledgements

I would like to thank the following for their support and assistance throughout the PhD process. Without them, I would not have been able to complete this work.

- **Dr Jordan Cheer** - for all of the help and support throughout the past 4 years. This work, and the associated skills which accompany it, would not exist without all of the time and effort you put in. Thank you.
- **Prof. Steve Daley** - for the supervision and guidance throughout the PhD, for the regular discussions around the higher-level context of the work, and for including me in the various additional projects alongside the PhD.
- **CRAC Team**: Joe Milton, Kris Hook, Joe Tan & Lawrence Singleton - for the discussions and coffee room chats, and the various pub trips along the way!
- **ISVR Technical Staff**: Phil Oxborrow, Jon Fithyan, Glen Barber - for talking through the various experimental setups with me, advising on better ways of doing things, and helping to get everything setup and working.
- **EDMC Technical Staff**: Chris Malcolm, Jim Rabbetts, Kevin Smith, and all of the EDMC team - for assisting me with constructing the various components for my experimental setups.
- **BAE Systems Submarines**: Andy Monks, Alastair Sherriff, Paul Douglas - for the industrial support and guidance, and for involving me in various additional projects alongside the PhD.

The author acknowledges the use of the IRIDIS High Performance Computing Facility, and associated support services at the University of Southampton, in the completion of this work.

Contents

List of Figures

List of Tables

List of Abbreviations

ANC	Active Noise Control
AVC	Active Vibration Control
ASACL	Active Structural Acoustic Cloaking
ASAC	Active Structural Acoustic Control
AUV	Autonomous Underwater Vehicle
ADC	Analogue to Digital Conversion
BEM	Boundary Element Method
DAC	Digital to Analogue Conversion
DSP	Digital Signal Processing
DOA	Direction of Arrival
FEM	Finite Element Method
FXLMS	Filtered-X Least Mean Square
FIR	Finite Impulse Response
FFT	Fast Fourier Transform
IFFT	Inverse Fast Fourier Transform
IMC	Internal Model Control
LMS	Least Mean Square
MIMO	Multiple Input Multiple Output
PML	Perfectly Matched Layer
PSD	Power Spectral Density
RMT	Remote Microphone Technique
SPL	Sound Pressure Level
SDOF	Single Degree of Freedom
SONAR	Sound Navigation & Ranging
TMD	Tuned Mass Damper

List of Symbols

Symbol	Description	Units
p	Acoustic Pressure	Pa
p_{tot}	Total Acoustic Pressure	Pa
p_{inc}	Incident Acoustic Pressure	Pa
p_{scat}	Scattered Acoustic Pressure	Pa
ω	Angular Frequency	rads^{-1}
f	Frequency	Hz
λ	Wavelength	m
θ	Azimuthal Angle of Incidence	Degrees
ϕ	Elevational Angle of Incidence	Degrees
W	Acoustic Power	W
W_{scat}	Scattered Acoustic Power	W
W_{tot}	Total Acoustic Power	W
W_{inc}	Incident Acoustic Power	W
ρ_0	Material Density	kgm^{-3}
c_0	Speed of Sound	ms^{-1}
u	Control Signal	
G	Plant Response	
H_s	Transfer Function between primary source and scattered acoustic pressure	
H_t	Transfer Function between primary source and total acoustic pressure	
I	Identity Matrix	
β	Control Regularisation Parameter	
β_{est}	Virtual Sensing Regularisation Parameter	
ϵ	Virtual Sensing Estimation Error	
a	Acceleration	ms^{-2}
e	Control Error	ms^{-2}
κ	Condition Number	
$[]^H$	Hermitian Transpose	
Σ_n	Summation over n Values	
d_s	Scattered Disturbance Signal	
d_t	Total Disturbance Signal	
d_m	Measured Disturbance Signal	
d_v	Virtual Disturbance Signal	
O	Observation Filter	
J	Cost Function	
v	Source Strength	
S_{vv}	Power Spectral Density of Source Strengths	

Chapter 1

Introduction

Acoustic scattering describes the interaction between an object and an incident acoustic wave. When an acoustic wave impinges on a body, if there is a significant difference in the acoustic impedance between the exterior fluid and the object, the acoustic wave will scatter. A portion of the energy will reflect off of the object, whilst the rest will refract around, or be transmitted through, the scattering body. As a result, an acoustic sensor within this scattered sound field will detect the summation of both the incident and scattered acoustic pressures, as shown in Figure 1.1. This is the concept behind active Sound Navigation & Ranging (SONAR), where a pulse of high frequency acoustic energy is emitted through a fluid medium (usually sea water), and a hydrophone is used to detect the acoustic reflections from any objects in the vicinity. The time delay between the sound being emitted and the reflection being received can be related to the distance to the scatterer, whilst a frequency shift describes the relative velocity of the scatterer [1] .

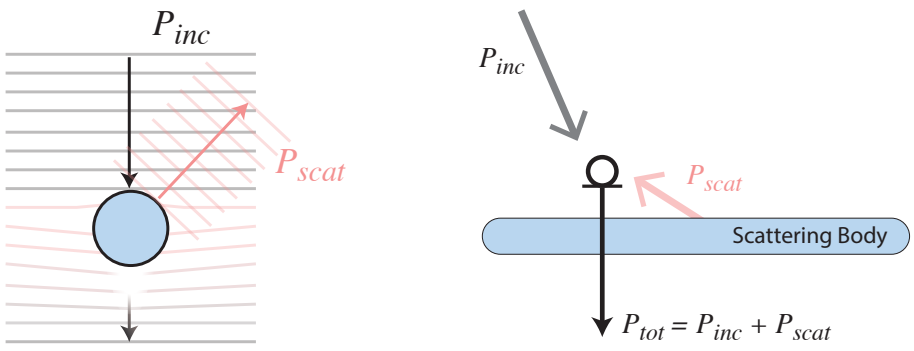

Figure 1.1: Schematic diagrams showing an acoustic scattering body (left), and an acoustic sensor detecting both incident and scattered fields (right).

Knowledge of the acoustic scattering from an object can be leveraged as a scientific research tool, for example using SONAR to map the sea-floor [2], or to understand the way the acoustic scattering from a human's head can be used to localise the direction of a sound source [3]. However, there are applications where there is an interest in reducing the acoustic scattering from an object; for example, when performing acoustic measurements in a non-anechoic space [4–6], or when implementing sound-field control for multiple listeners whose presence in the soundfield causes acoustic scattering [7] and, therefore, a degraded acoustic perfor-

mance. There is also a clear interest from the naval defence community in acoustic stealth, by reducing the acoustic scattering from a vessel and, therefore, reducing the chance of detection by third-party SONAR. The concept of reducing the acoustic scattering from an object, effectively making the sound-field with and without the presence of the object identical, is known as acoustic cloaking. The following sections will provide a review of previous research that has been conducted into the realisation of acoustic cloaks. A review of the literature on acoustic scattering will first be presented, followed by a review of the various active and passive cloaking strategies that have been discussed in the literature.

1.1 Acoustic Scattering

Investigation into the acoustic scattering properties of basic rigid and non-rigid scatterers has been ongoing for many years, dating back to Lord Rayleigh's research in 1871 [8]. In general terms, the acoustic scattering from a rigid scattering object can be described in terms of the forward-scattered component, ie the scattered wave propagating in the same direction as the incident wave, downstream of the scattering object, and the back-scattered component, ie the scattered wave propagating in the opposite direction to the incident wave, upstream of the scattering object. When considering the case of the acoustic scattering from a rigid sphere, it has been widely shown that at low frequencies, approximately $ka < 2$, the backscattering dominates over the forward scatter [9, 10], whilst at high frequencies, approximately $ka > 2$, the forward scatter is dominant due to the acoustic shadowing effect [11]. This can be seen in the soundfield plots shown in Figure 1.2, which have been generated from numerical simulations and present the total, incident, and scattered soundfields when an incident acoustic plane wave, propagating upwards, impinges on a rigid spherical scattering object at $ka = 1$ and $ka = 10$. The directivity of the scattered fields shown in Figure 1.2 is consistent with analytical studies presented in the literature [8, 11–13].

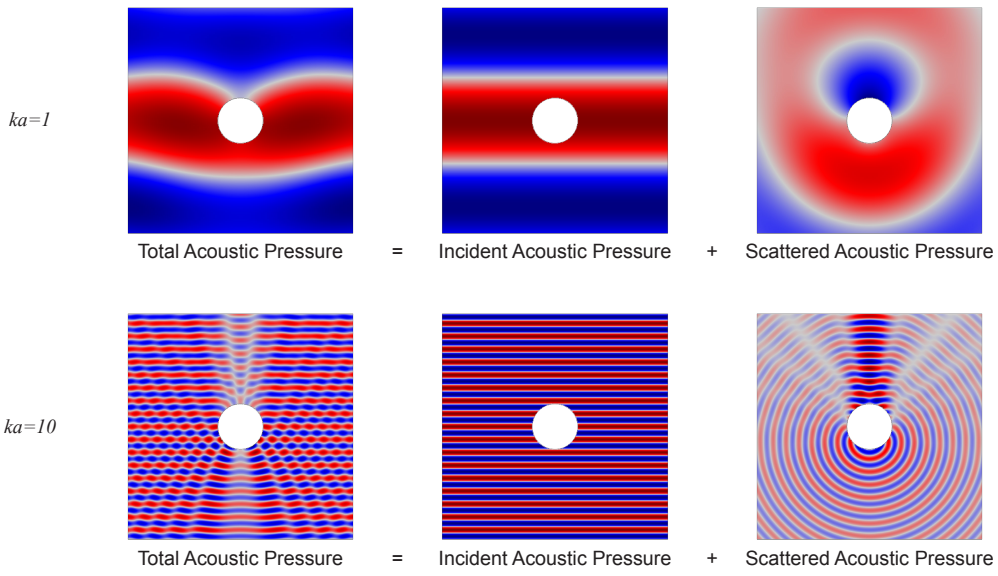

Figure 1.2: A graphic showing the total, incident, and scattered soundfields when a rigid sphere is excited by an incident plane wave propagating upwards at $ka = 1$ (top) and $ka = 10$ (bottom).

Most of the literature discussed above considers a rigid scattering object, however, it is also

insightful to consider the acoustic scattering from flexible scatterers. Faran [14] and Doolittle et al [15] worked on the modelling of rigid and elastic cylinders in 1951 and 1966 respectively, using Hankel functions and spherical harmonics to express the scattered field analytically. Flax et al [16] and Diarmuid Murphy et al [17] continued this work in 1978, comparing the scattering behaviour of rigid and elastic cylinders, and started to investigate the fluid loading effects of the external medium. Diarmuid Murphy et al [18] investigated the resonant scattering from a flexible fluid-loaded elastic shell using normal-mode analysis to isolate the resonant scattering component from the off-resonance component. They concluded that the off-resonance scattering can be approximated by that of a rigid body, leading to the commonly used assumption that the acoustic scattering from an object is composed of rigid and flexible components. In 2006, Bobrovnitskii developed an analytical model to describe the acoustic scattering from an infinite cylinder, based on the impedance difference between the scatterer and the external fluid (water in this instance) [19, 20]. Figure 1.3 shows the results of this model, plotting non-dimensional scattered power against non-dimensional frequency. This was done for three different boundary conditions: Rigid, flexible (assuming steel), and soft. The flexible steel cylinder shows clear resonances in the scattered sound power when compared to the rigid cylinder, confirming the theory that a flexible structure will have increased scattering when it is excited at resonance.

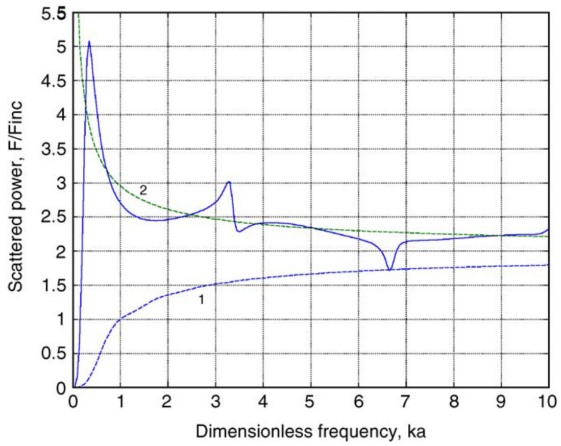

Figure 1.3: Non-dimensional scattered sound power for a steel shell in water (solid line), a rigid cylinder (dashed line 1) and a soft cylinder (dashed line 2) presetned in [20]

Having described the basic principles of scattering from both rigid and flexible structures, the next stage is to consider how this scattering can be controlled. A review of previous work in the active and passive acoustic cloaking fields is presented in the following two sections, with a focus on the practical implementation of such systems.

1.2 Passive Acoustic Cloaking

Passive acoustic cloaking is a means of reducing the acoustic scattering from an object using passive control methods. This usually involves the application of a material to the scattering object, and this may be either a conventional material or an acoustic metamaterial. The former, which utilises the acoustic absorption properties of a material to reduce the amplitude of an incident wave prior to it reaching the scattering body, has the effect of reducing the back-scattered wave, however, has minimal effect on the shadow zone downstream of the object [21]. The low-frequency limit of passive acoustic cloaking using conventional materials is

proportional to the thickness of the material and, therefore, it is often impractical to cloak an object to low frequency incident sound. Acoustic metamaterials, however, consist of arrays of unit-cells containing sub-wavelength structures [22] which, over a narrow frequency band, can provide advanced material properties that result in effective masses and stiffnesses that can be tuned to be significantly larger or smaller than can be achieved using conventional materials [23]. Careful design of the sub-wavelength structure allows for the optimisation of these material properties to achieve a beam-steering effect, which allows an incident acoustic wave to be steered around an object rather than impinging upon it [24].

In terms of metamaterial based acoustic cloaks, Pendry et al [25] presented a method to optimise the effective density and bulk modulus of a metamaterial, and discuss how this could be used to realise an acoustic cloak. Zigoneanu et al [26] have published experimental results of a practical ground cloaking device, using a lattice structure of layers of perforated acrylic, as shown in Figure 1.4. The effective density and bulk modulus of the ground cloak (when excited at 3 kHz) are similar to the material properties of air, minimising the characteristic impedance mismatch and, therefore, causing negligible scattering. The performance of this device, when cloaking a scattering object placed on a ground plane, is shown in Figure 1.5. The presented plots show the scattered acoustic pressure field, measured with a scanning microphone, caused by the ground plane (top), the ground and the object (middle) and the ground and the cloaked object (bottom). Although the ground cloak is not perfect (possibly due to manufacturing tolerances), it is clear from these results that the device significantly reduces the acoustic scattering from the object. Similar ground cloaking devices have been designed by Bi et al [27] and Kerrian et al [28] to cloak objects underwater, with both publications achieving comparable levels of performance to those presented in Figure 1.5. Although passive acoustic cloaks using metamaterials are effective, as shown in Figure 1.5, their performance is limited to a relatively narrow frequency range.

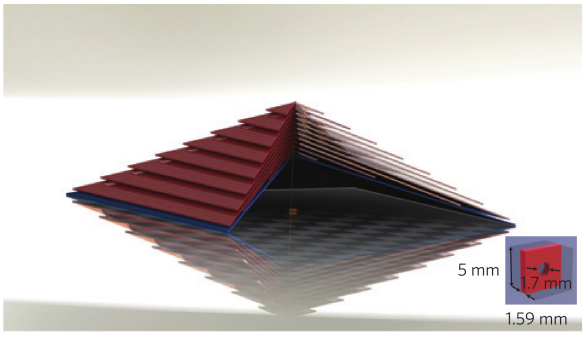

Figure 1.4: Acoustic Cloaking Pyramid presented in [26], consisting of many layers of perforated acrylic

In order to extend the bandwidth over which a metamaterial is effective, additional unit-cells tuned to multiple frequencies can be introduced [29], however, doing so can result in similar size limitations to those experienced when using conventional material for passive control. For these reasons, the use of active control to reduce the acoustic scattering from an object has been investigated, and the following section will present a review of the literature on active acoustic cloaking.

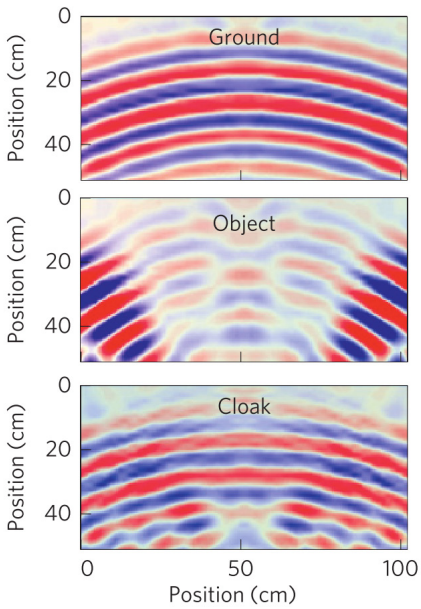

Figure 1.5: Measured scattered fields of the ground, the ground with the object, and the ground with the cloaked object at 3 kHz from [26]

1.3 Active Acoustic Cloaking

Active control is a technique that can be used to attenuate a disturbance signal using secondary control sources [30]. Due to the principle of linear superposition, if a suitable control signal can be generated, the disturbance signal at a given point can be entirely cancelled out through destructive interference [31], as shown in Figure 1.6. Implementing active control to minimise a disturbance at a single location (local active control) can achieve significant levels of attenuation [32], whilst implementing control to minimise the disturbance over a larger area (global active control) can be more challenging due to the need for a large number of control sources and error sensors [33]. Active control systems can be designed to minimise either a broadband disturbance signal [34], or can focus on tonal control; the latter is common when the disturbance signal is dominated by a strong tonal component such as with engines or rotating machinery [35, 36]. Both feedforward and feedback control architectures have been demonstrated practically and in the literature, depending on the availability of a suitable reference signal, and adaptive algorithms are often included to allow for small variations in environmental conditions [37].

The use of active control to minimise the acoustic scattered pressure from an object is often referred to as Active Acoustic Cloaking. This thesis will primarily focus on addressing the challenges of practically implementing an Active Acoustic Cloaking system and, therefore, a review of the literature on Active Acoustic Cloaking will now be presented.

The performance of any active control system is governed by a number of factors, one of which is the suitability of the measured error signal. This is the signal that the active control algorithm attempts to minimise and, therefore, it must accurately represent the undesired physical disturbance. In most active noise control systems, for example, the undesired physical disturbance is the total acoustic pressure, which can be directly measured and, therefore,

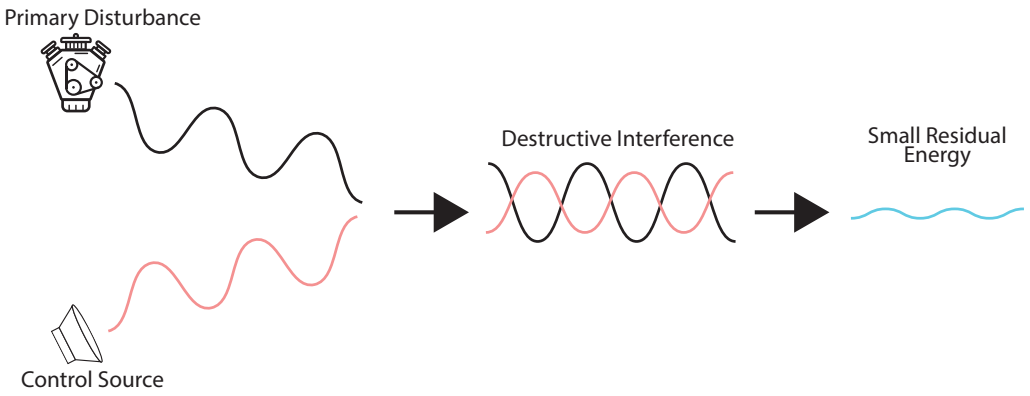

Figure 1.6: A graphic showing how an active control system can use destructive interference to reduce a primary acoustic disturbance.

minimised. In the context of an active acoustic cloaking system, the undesired physical disturbance is the scattered acoustic pressure, as this contains all of the components of the scattered field (rigid scattering, resonant scattering, back scattering, shadowing etc). If the scattered acoustic pressure is identified and directly minimised, using either structural or acoustic control sources, significant attenuation in the scattered sound field can be achieved as has been demonstrated using numerical modelling by Cheer [38] and Eggler [39]. In these studies, acoustic cloaking was demonstrated over a fairly wide frequency range using secondary acoustic sources [38], and secondary structural sources [39], to directly minimise the scattered acoustic field. However, it was assumed in both cases that the scattered disturbance field was perfectly known.

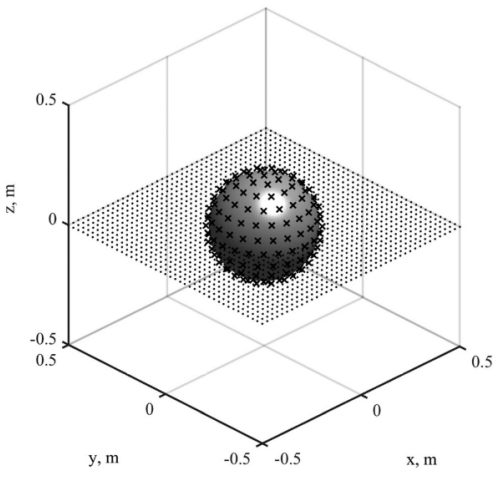

(a) The arrangement for the cloaking system presented in [38], showing the control sources for the exterior control geometry (crosses), and a single plane of the full three- dimensional grid of error sensors (dots), as well as the scattering sphere.

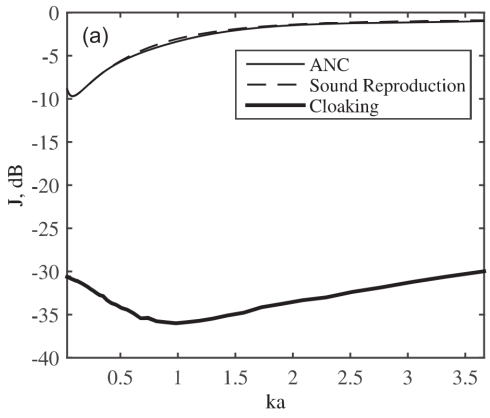

(b) Reductions in the scattered acoustic field achieved by the system presented in [38] when using acoustic control sources. This is plotted against ka, where a is the radius of the sphere, and k is the acoustic wave number.

Figure 1.7: Modelling setup and simulated results from the cloaking system proposed in [38]

Figure 1.7 shows the system considered in [38], as well as the achieved attenuation in the scattered field when the system is used to acoustically cloak a rigid sphere, over a fine fre-

quency sweep. Figure 1.7b shows the cost functions for Active Noise Control, Sound Field Reproduction, and Active Acoustic Cloaking since the performance of these three active strategies are compared in [38], however the Active Noise Control and Sound Field Reproduction systems are not discussed further in this thesis. In addition to investigating the frequency dependence of the cloaking performance, [38] also presents a study into the effect of the position of the acoustic control source array, and shows that as the spacing between the control sources and the scattering object is reduced, the acoustic cloaking performance is increased. This leads to the work by Eggler [39] et al, which investigates the use of structural control actuation in place of the acoustic control sources utilised in [38]. Figure 1.8 presents one of the simulation results published in [39]; Figure 1.8a shows the scattered acoustic field due to an elastic cylinder excited by an incident plane wave at 167 Hz, and Figures 1.8b and 1.8c show the same sound field when the scattered component is controlled using either acoustic or structural control sources respectively. Significant attenuation in the scattered field is shown, especially when using structural control sources. Similar results are also shown in [39] for a range of frequencies between 167 Hz and 350 Hz.

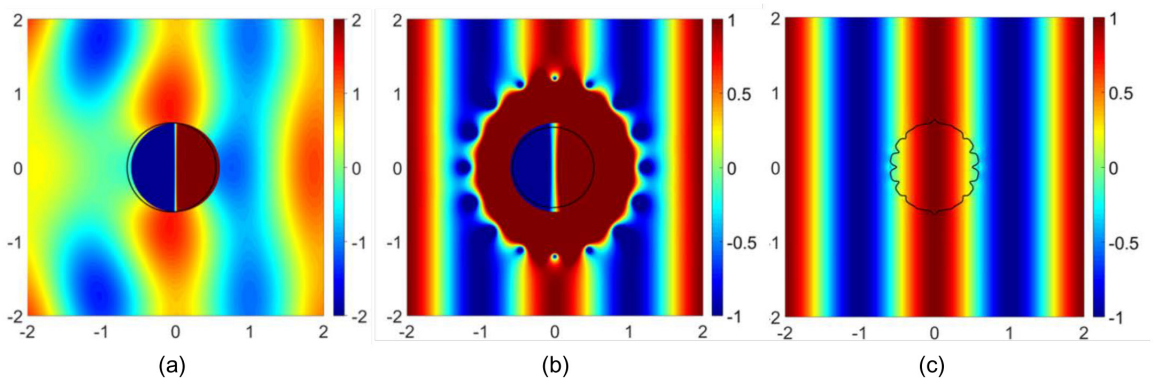

Figure 1.8: Active acoustic cloaking system presented by Eggler [39]. (a) Acoustic pressure field and shell deformation under plane wave excitation at 167 Hz, (b) Acoustic pressure field using acoustic control sources, (c) Acoustic pressure field using structural control sources

Although both [38] and [39] show significant reductions in the scattered acoustic field and, therefore, effective cloaking of the scattering objects, the presented results are all based on computational modelling. They also both assume that perfect knowledge of the scattered acoustic field is available, however, as shown in Figure 1.1, it is impossible to directly measure the incident and scattered sound fields separately in practice and any acoustic sensor will detect both components. Extraction of the scattered field from the total pressure would require an additional processing step or a more advanced sensing strategy. Therefore, although this previous work clearly shows physical insight into the acoustic cloaking problem, the utilised systems are not practically implementable without the development of more advanced sensing methods.

Friot et al [40] developed a potential solution to the scattered field detection problem, with the development of an active acoustic cloaking system using two concentric rings of microphones surrounding the scattering object, as shown in Figure 1.9a. Wave decomposition allows the inward and outward travelling waves to be extracted which, for the given physical setup, correspond to the incident and scattered components. The performance of this system was simulated using numerical modelling, predicting reductions in the scattered field of

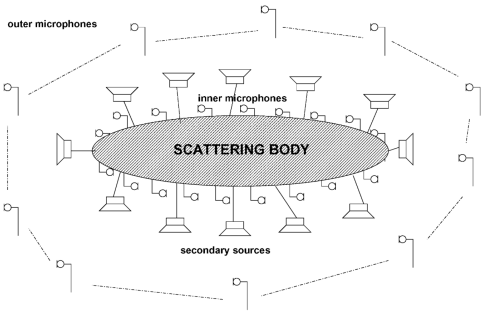

(a) The transducer arrangement for the 2D cloaking system presented in [40], showing the two concentric rings of microphones as well as the ring of control sources.

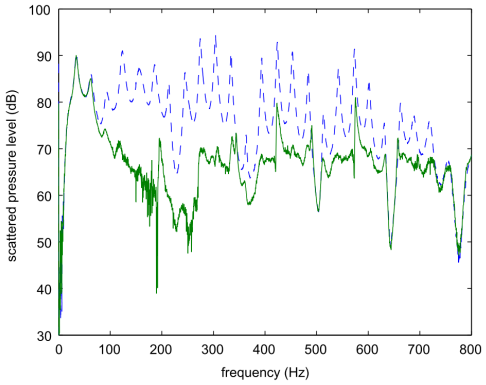

(b) Attenuation in scattered sound pressure achieved by the 1D experimental implementation of the system presented in [40]. The dashed line is the scattered sound pressure level before active control, and the solid line is the scattered sound pressure level after active control.

Figure 1.9: Source/sensor configuration for the 2D computational modelling, and measured results of a 1D implementation, from [40]

an order of magnitude at low frequencies. The high frequency performance of the system was limited by the sensor spacing and, therefore, adjusting the distance between the two rings of sensors, and increasing the number of sensors per ring, is expected to increase the performance bandwidth. The proposed method was initially validated experimentally with a simple 1D experiment in a duct, and over 20 dB of attenuation was achieved in the scattered pressure between 100 Hz and 700 Hz, as shown in Figure 1.9b. However, Friot et al subsequently demonstrated a 2D cloaking capability [41], where a parallelepiped scattering object was placed in an anechoic chamber, along with rings of microphones and loudspeakers as discussed previously. In this experimental study, the incident sound field was a 280 Hz tone generated by a single primary loudspeaker. The experimental setup is shown in Figure 1.10a, with the far-field measured performance (in the $z = 0$ plane) shown in Figure 1.10b. From these results, it can be seen that, by using the proposed strategy of sensing and controlling the scattered field, the proposed method is able to achieve reductions in the scattered field of over 30 dB at the single frequency considered.

Although the acoustic cloaking system described in [40, 41] was able to demonstrate reasonable active cloaking performance, the 2D experimental setup required a large number of microphones to accurately separate the incident and scattered pressure waves, which may not always be practical to implement. Han et al [42] proposed a method to avoid the need for the second ring of error sensors by modelling the transfer function between scattered pressure and total pressure, rather than measuring it. The simulated transfer functions are used to estimate the scattered component of the pressure signals, which are then used as the disturbance signals for an active control system. This system was implemented in a laboratory experiment using a spherical scatterer, and reductions in the scattered field of up to 8 dB were achieved. The robustness of this sensing strategy was not considered in [42] and, given that the accuracy of the sensing strategy is dependent on the quality of the computational model used to generate the transfer functions, it would be insightful to consider the robustness of the system.

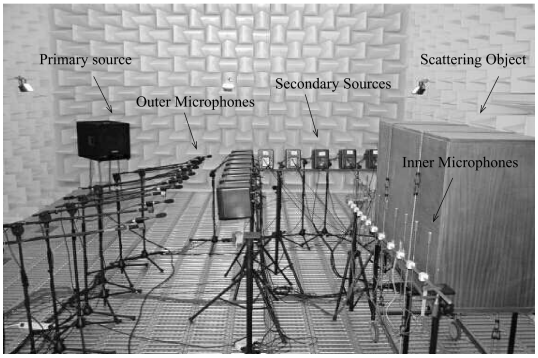

(a) The experimental transducer arrangement for the 2D cloaking system presented in [41], showing the two concentric rings of microphones as well as the ring of control sources.

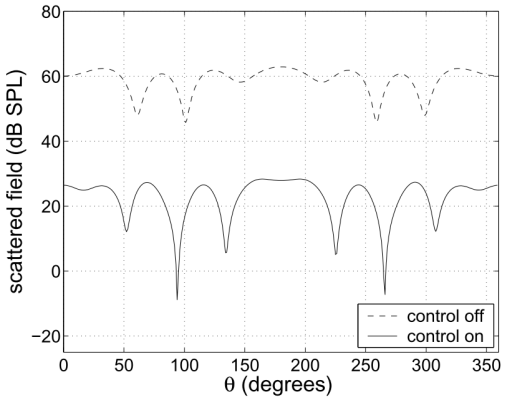

(b) Attenuation in scattered sound pressure achieved by the 1D system presented in [41]. The dashed line is the scattered sound pressure level before active control, and the solid line is the scattered sound pressure level after active control.

Figure 1.10: Experimental setup and measured results for the 2D cloaking system proposed in [41]

It should be noted that the results presented in [40–42] only considered back scattering. The systems did not attempt to reduce refractive scattering (scattering 'downstream' of the scattering object), neither were they able to control scattering in all 3 dimensions. Although the experimental results presented in [41] cloak a 3D object, they only attempt to control the scattered field over a 2D plane. Furthermore, the results consider a tonal disturbance, incident from a single direction, and do not comment on the robustness of the system to physical uncertainties.

An alternative cloaking strategy is proposed in [43] where, instead of attempting to control the scattered pressure directly, the system aims to minimise the total sound pressure level within a region surrounding the scattering object. By minimising the acoustic energy incident on the scattering object, the scattered field will also be reduced without the requirement of a real-time measurement of the scattered acoustic pressure. To do this, the scattering object was surrounded by three arrays of multi-pole point sources. These devices are optimised such that the incident pressure around the scattering object is zero, whilst having a high-order directivity such that their influence in the far-field is negligible. The performance of this cloaking method is investigated using numerical simulations, and an example of some of the results is presented in Figure 1.11. This figure shows the control and total acoustic pressure fields when the control sources are optimised using either a Green's function formulation, or a Singular Value Decomposition formulation, both of which create an effective quiet zone around the scattering object and, therefore, the scattered acoustic pressure-field outside of the control region is negligible.

The concept proposed in [43] has since been analytically applied to a thin plate by Futhazar et al [44], where four 50th order multipole sources were simulated surrounding a scattering object. An extract of the results from this simulation study is presented in Figure 1.12, and shows the quiet zone surrounded by the four sources, which have negligible effect on the exterior field. Whilst demonstrating cloaking capabilities in simulation, the use of high-order multipole acoustic sources in both [43] and [44] significantly limits the practicability of experi-

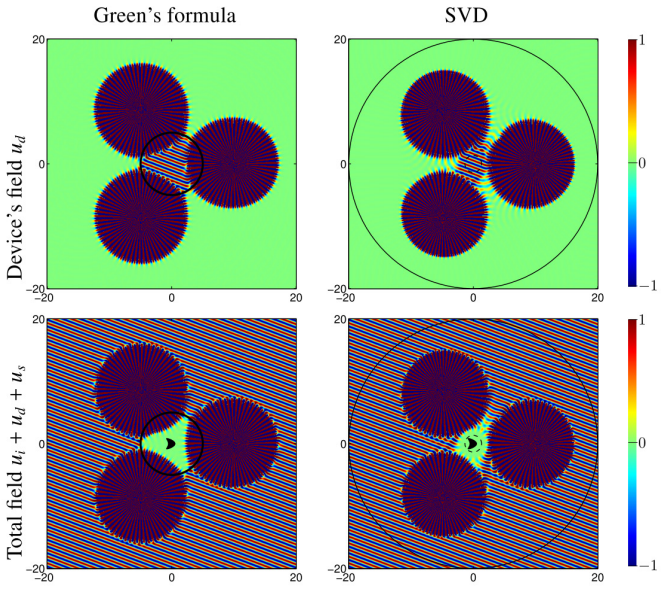

Figure 1.11: The control field (top) and total acoustic field (bottom) of the simulations presented in [43], with two alternative control formulations.

mental implementation. This limitation has been investigated in [45], which presented simulation results comparing the conventional direct-minimisation active acoustic cloaking methods with the quiet-zone cloaking method discussed above, using a realisable array of monopole control sources. This showed that, although the quiet-zone acoustic cloaking method was less effective and less efficient than the direct-minimisation approach, it was still able to achieve up to 10 dB of attenuation in the acoustic scattering from a rigid sphere. The work presented in [45] was conducted by the author of this thesis during the course of the PhD research, but has not been presented in this thesis which, instead, focusses on practical implementations of acoustic cloaking systems.

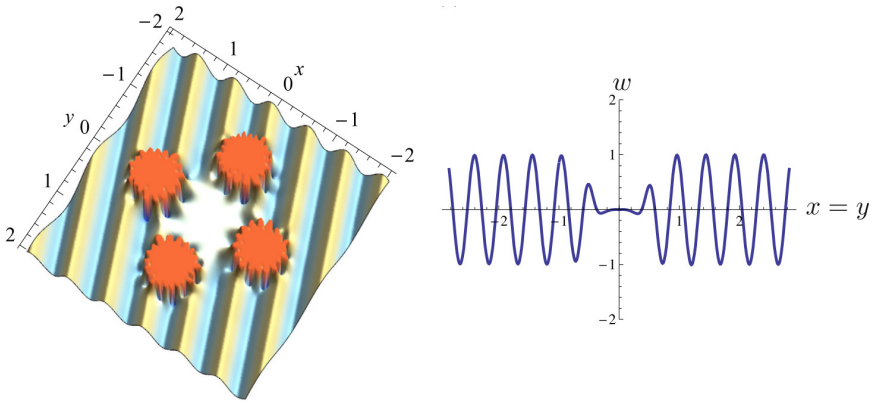

Figure 1.12: Disturbance field (left) and cross-sectional plot of structural excitation (right) from [44], showing the cloaked quiet-zone region around the (0,0) position.

1.4 Thesis Structure and Objectives

This thesis focusses on the development of a practical active acoustic cloaking system. From the preceding literature review, it is evident that, although tonal active acoustic cloaking systems have been well researched, there has been little work on achieving broadband control. Some methods have been presented to overcome the challenges associated with real-time sensing of the scattered acoustic pressure, however, these have also only considered a tonal disturbance and, therefore, this thesis will investigate methods to achieve broadband sensing and control of the scattered field caused by a non-tonal disturbance signal. In a practical active acoustic cloaking system, it is likely that environmental conditions will change over time and, therefore, the system responses may vary. The use of an adaptive algorithm may make the system robust to perturbations in the disturbance field, however, it will offer limited robustness to perturbations in the plant responses and, therefore, the robustness of the various active acoustic cloaking strategies investigated in this thesis will also be considered.

The structure of the thesis is as follows:

Chapter 2
Chapter 2 builds upon the work presented in the literature review by presenting an experimental study into the performance of an active acoustic cloaking system when applied to a rigid spherical scatterer. An experimental setup to measure the acoustic scattering from the sphere, when excited by a tonal disturbance, is presented, including a dual-layer array of loudspeakers, enabling a tonal active acoustic cloaking strategy to be implemented that directly minimises the scattered acoustic pressure signals measured at the microphones. Whilst the ultimate aim of the work presented in this thesis is to achieve broadband control without needing a real-time measure of the scattered acoustic pressure, this straightforward case provides insight into the physical problem and sets a solid foundation upon which the subsequent chapters will build.

Chapter 3
In a practical cloaking realisation, it is likely that the physical system will vary over time, introducing uncertainty to both the plant responses and the disturbance fields. To investigate the effect of uncertainty on the active acoustic cloaking performance, Chapter 3 presents a study into the robustness of the active acoustic cloaking system presented in Chapter 2. The effect of changing the size and position of the scattering object is investigated, as is the effect of adding unstructured noise to all of the sensor channels. Both frequency dependent, and frequency independent regularisation methods are discussed and investigated, and the effect that these have on the robustness of the control system and the performance in the nominal case are presented.

Chapter 4
The tonal control strategy discussed in Chapters 2 and 3 provides insight into some of the limits on active acoustic cloaking, however, in many practical scenarios it is likely that the incident acoustic field will be non-tonal in nature. Therefore, a broadband active acoustic cloaking method is proposed in Chapter 4. This Chapter presents an investigation into the suitability of various reference signals, and the effect of varying the length of the FIR filters used in the control algorithm. Finally, a brief investigation into the robustness of the broad-

band control algorithm is presented.

Chapter 5
Chapter 5 builds upon the previous chapters by presenting a virtual sensing method that is able to estimate the real-time scattered acoustic pressure at a number of far-field sensor locations, based on near-field measurements of the total acoustic pressure. This strategy is based on the remote microphone technique and attempts to address the main limitation in the control approaches discussed in the previous chapters, as the active acoustic cloaking system using the proposed virtual sensing technique does not require a real-time direct measurement of the scattered acoustic pressure in the far-field which, as has been discussed previously, is not practicable. The accuracy of the sensing method is quantified, and the performance of the active control system utilising this sensing strategy is assessed. As in the previous chapters, the robustness of both the virtual sensing strategy and the integrated active acoustic cloaking system is commented on.

Chapter 6
The work presented in Chapters 2-5 is based on measured data corresponding to the acoustic scattering from a rigid sphere, however, the acoustic cloaking of a flexible structure is perhaps more realistic to a number of applications and presents additional challenges due to the presence of resonant scattering and, therefore, Chapter 6 considers the acoustic scattering from a flexible cylindrical shell. To investigate this, an experimental setup is presented and various acoustic and structural transfer responses are measured. The cylindrical shell is instrumented with sensors and actuators, allowing AVC to be implemented on the structure. The effect that AVC has on the scattered acoustic field is then discussed.

Chapter 7
Chapter 7 combines the work from previous chapters and investigates the performance of an active acoustic cloaking system when implemented on the flexible cylindrical shell discussed in Chapter 6, using the broadband control algorithm presented in Chapter 4. The causality of the controller is discussed, and the effect of the control sources on the structural response is also investigated.

Chapter 8
The final chapter presents a summary of the conclusions drawn from the work presented in the preceding chapters, and provides suggestions for future work in this area.

1.5 Contributions

The main original contributions of this thesis are:

1. The experimental investigation into the performance limitations of a broadband acoustic cloaking strategy, on both rigid and flexible scattering structures, using either acoustic or structural control sources respectively.
2. The formulation and validation of a virtual sensing approach for the real-time estimation of far-field scattered acoustic pressure based on measurements of the near-field total acoustic pressure.

3. An investigation into the robustness of active acoustic cloaking, considering both structured and unstructured uncertainties.
4. A study into the effect of implementing Active Vibration Control on the soundfield scattered from a flexible structure.

A number of publications and conference proceedings have arisen from the work presented in this thesis, and these references are given in the declaration of authorship.

Chapter 2

Active Acoustic Cloaking of a Rigid Sphere

The concept of acoustic cloaking, the ability to acoustically conceal an object such that the sound-field with the object present is identical to that without the object present, has been thoroughly discussed in the literature and reviewed in Chapter 1. The use of an active acoustic cloaking method can potentially widen the bandwidth of control when compared to a passive method, and enable adaptation to changes to the system that might occur in practice. However, an active approach has the added complexities of requiring external power, actuators and sensors, and Digital Signal Processing (DSP). This chapter will explore the performance limitations of an active acoustic cloaking system in an experimental environment, and will identify a number of challenges that would need to be solved for a practical active acoustic cloaking system. This chapter will, therefore, form the basis for the rest of the thesis, and these implementation challenges will be explored in detail in subsequent chapters.

This chapter builds on the work by Friot et al [41], who present an experimental investigation into the use of active acoustic cloaking to reduce the acoustic scattering from a hollow parallelepipedic wooden box. Due to experimental limitations, Friot et al only consider the back-scattering from the object at a single frequency. The present study will extend the insight provided by Friot et al, and will investigate the acoustic scattering from a rigid sphere in both the backwards and forwards directions, across a range of frequencies. Friot et al also suggest a method of calculating the acoustic scattered pressure in real-time, which will be further discussed in Chapter 5.

This chapter will present an experimental investigation into the performance of an active acoustic cloaking system, implemented on a rigid spherical scatterer. A tonal control strategy will be used to minimise the acoustic scattering from a rigid sphere using an array of control loudspeakers, arranged as shown in Figure 2.1, and the effect of regularisation on the performance of the control system will be considered. The experimental setup will be described in Section 2.1, and Section 2.2 will detail the control strategy and formulate the optimal source strengths to minimise the acoustic scattered power from the object. Section 2.3 will present results of offline simulations used to investigate the performance of the active control system. Conclusions will be drawn in Section 2.4, and this will help to motivate the research presented in the remaining chapters of this thesis.

Parts of this work have been published in [46].

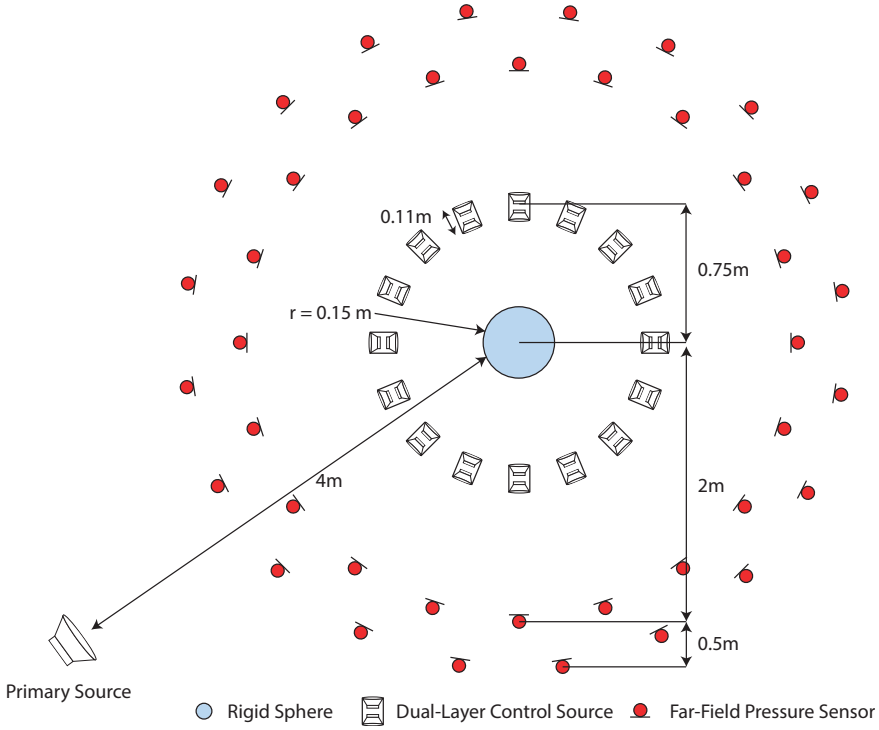

Figure 2.1: Schematic diagram showing the source/sensor arrangement, and the scattering sphere.

2.1 Experimental Setup

In order to investigate the performance of active acoustic cloaking, a series of acoustic measurements have been carried out in the Large Anechoic Chamber at the Institute of Sound & Vibration Research, which will generate a dataset containing the acoustic scattering from a rigid sphere. This data will later be used to investigate the performance of the active acoustic cloaking system described in Section 2.2. The experimental setup and methodology will be described in this Section.

A rigid spherical scatterer was constructed out of Gypsum Plaster, as shown in Figure 2.2. A mould was used to create two hemispheres, which were subsequently attached together and sanded to ensure a smooth, consistent surface finish. A metal plate was cast into the lower sphere, attached to a threaded rod to act as a hanging point from which to suspend the sphere. Hessian fibres were included within the plaster mixture to increase the strength of the sphere, and to ensure that it did not disintegrate under its own weight when suspended. Three spheres were constructed using this method, with radii $r = 110$ mm, $r = 150$ mm and $r = 250$ mm, with the largest sphere weighing 96kg once it had finished drying. The following study will only consider the middle sphere, of radius $r = 150$ mm, however the larger and smaller spheres will be introduced in Chapter 3.

The scattering sphere discussed above was suspended inside the anechoic chamber as

Figure 2.2: Images showing the construction of the scattering spheres.

Figure 2.3: Images of the experimental setup, showing the rigid sphere, the loudspeaker array, and the far-field microphone array.

shown in Figure 2.3. To measure the acoustic scattering, and to provide the error signals for the control algorithm, a far-field microphone array consisting of 2 concentric rings of 20 PCB 130F20 microphones was arranged around the sphere, as shown in Figures 2.1 and the right-hand image of 2.3. Two off-set rings were utilised, rather than a single ring, as preliminary simulations (not presented here) indicated that using a single ring to implement active control would result in local minima being created around each microphone position within the bandwidth of interest, rather than the global effect that is achieved with multiple offset rings of sensors. The effect of reducing the number of sensors in the far-field array will be investigated in Section 2.3.2. The array of control sources consisted of a dual-layer array of 32 Visaton B80 loudspeakers mounted in custom built cylindrical enclosures. A dual-layer array was chosen as this is the most straightforward practical approximation of the continuous layer of monopole and dipole sources required by the Helmholtz integral [33]. Using offset pairs of control sources also allows the control sources to form first-order directional sources [47], and enables more advanced acoustic cloaking methods to be investigated [44, 48]. The incident acoustic pressure field was generated with a dual-concentric high-powered loudspeaker (Tannoy CPA12), placed outside of the far-field microphone array, oriented towards the midpoint of the sphere. It should be noted that as well as the far-field microphone array discussed above, Figure 2.3 also shows a second microphone array in the near-field of the scattering object. The near-field microphone array will not be used in this chapter, however, and will be introduced in Chapter 5. The manufacturer's specification documents for all of the loudspeakers and microphones used throughout this thesis are included in Appendix D for reference.

A schematic diagram showing the measurement equipment and the signal flow is presented in Figure 2.4. The Dante digital audio protocol was used for data-acquisition, which allows for a large number of input and output devices to be efficiently connected together and ensures that the digital clocks in each device remain synchronised. Anti-aliasing and reconstruction filters were also included within the Analogue to Digital Conversion (ADC)s and Digital to Analogue Conversion (DAC)s. As Dante is designed for professional audio applications it only supports a limited number of sampling frequencies and, therefore, the experimental setup was used to acquire data at $f_s = 48\mathrm{kHz}$. To ensure that various acoustic cloaking methods could be investigated without requiring significant computational power, the data was subsequently down-sampled to $f_s = 2.4\mathrm{kHz}$ for some of the following analysis.

The spatial aliasing limit for a circular array of either acoustic sources or acoustic sensors is given as [49, 50]

$$f_{\max} = \frac{cL}{4\pi r}, \tag{2.1}$$

where c is the speed of sound in the fluid, L is the number of elements in the array, and r is the radius of the array. Based on the dimensions shown in Figure 2.1, this gives an upper frequency limit for the loudspeaker array as 582 Hz, and an upper limit for the microphone array as 545 Hz. The low frequency limit of these measurement is set by the low-frequency cut-off of the loudspeakers, which is displayed by the on-axis acoustic response measurement shown in Appendix C. Based on these bandwidth limitations, the data from these measurements will be analysed between 100 Hz and 500 Hz. In addition to the on-axis acoustic response measurements of the control loudspeakers, shown in Appendix C, the technical drawings for the control loudspeaker enclosures are included in Appendix B, the data-sheets for the microphones and loudspeakers are included in Appendix D, and the serial numbers

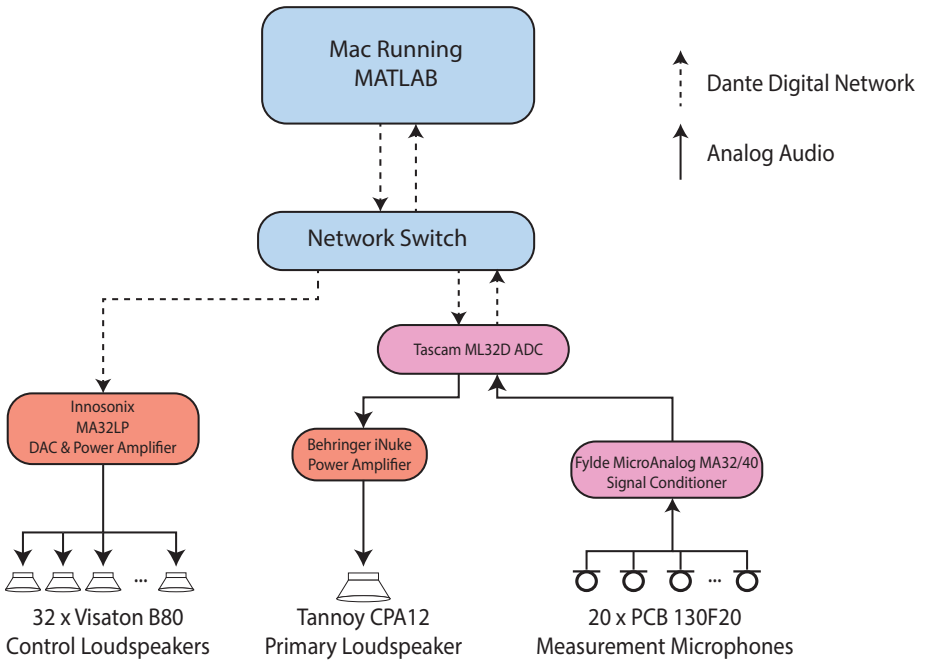

Figure 2.4: Schematic diagram showing the measurement equipment and the signal flow.

of the experimental equipment are included in Appendix A.

The experimental equipment documented above has been used to obtain the 40×32 matrix of acoustic plant responses between the 32 loudspeakers and the 40 far-field measurement microphones, and a 40×1 vector of disturbance responses which will subsequently be used to investigate the performance of the active acoustic cloaking system. Acoustic responses between each source (1 primary acoustic source and 32 secondary control sources) and each acoustic sensor have been measured with the sphere present in the anechoic chamber. Under this condition, the responses measured at the microphone array when the primary source is driven give the vector of total acoustic pressures, $\mathbf{d}_t$, which can be expressed in terms of the linear summation of the vectors of incident, $\mathbf{d}_i$, and scattered, $\mathbf{d}_s$, pressures as shown in Equation 2.2. To extract the scattered pressures from these measurements, it is necessary to remove the sphere and re-measure the transfer responses between the primary source and all of the microphones, which provides a direct measure of the vector of incident pressures, $\mathbf{d}_i$. According to Equation 2.2, by subtracting the transfer responses from the primary source to each microphone with and without the scattering object present, the scattered acoustic pressure can be calculated at each microphone location. Due to the requirement of obtaining acoustic measurements with and without the object present, this method of calculating the scattered acoustic pressure is clearly not viable for a real-time adaptive control system. A potential solution to this will be presented in Chapter 5, however the current study will assume that the soundfield is stationary and that the scattered pressure can be measured in advance using the method outlined above.

For each transfer response measurement, each source was driven in turn with an 11 s broadband measurement signal, which was then de-convolved with the inverse sweep to calculate

the transfer response [51]. The 11 s measurement signal consisted of a 10 s logarithmic sine sweep, providing a frequency resolution of 0.1 Hz [52], followed by 1 s of silence to ensure that the reverberation tail was sufficiently captured. Each microphone was individually calibrated, and background noise measurements were taken to ensure that the scattered component of the pressure field was above the noise floor. Figure 2.5a shows a spectrogram of the raw time-series data from one of the acoustic transfer response measurements, showing the logarithmic sweep and displaying a small amount of low-level harmonic distortion being generated by the loudspeaker. Figure 2.5b shows the acoustic and electrical noise floors of the experimental setup, and also includes one of the acoustic transfer response measurements for comparison. The scale is normalised to display the full 144 dB of dynamic range that can be achieved by a 24-bit data acquisition system. Figure 2.5b clearly shows that the dynamic range of the measurement equipment has been maximised, and that the acoustic measurements are significantly above the measurement noise floors. Each measurement was performed three times with the resulting transfer responses being averaged, to minimise any variations caused by small fluctuations in the measurement conditions. To ensure repeatability of the measurement process, a repeatability study was carried out. The scattered sound power was measured three times using the adopted measurement process. In-between each repeat, the sphere was completely removed from the anechoic chamber, the vector of incident acoustic pressures was measured, before the sphere was re-hung in the chamber and the vector of total acoustic pressures was measured. The scattered acoustic power was calculated three times using these measurements, and the repeatability study confirmed that, with the adopted measurement process, the scattered field could be measured with less than 0.6 dB variability between repeats, as shown in Figure 2.6.

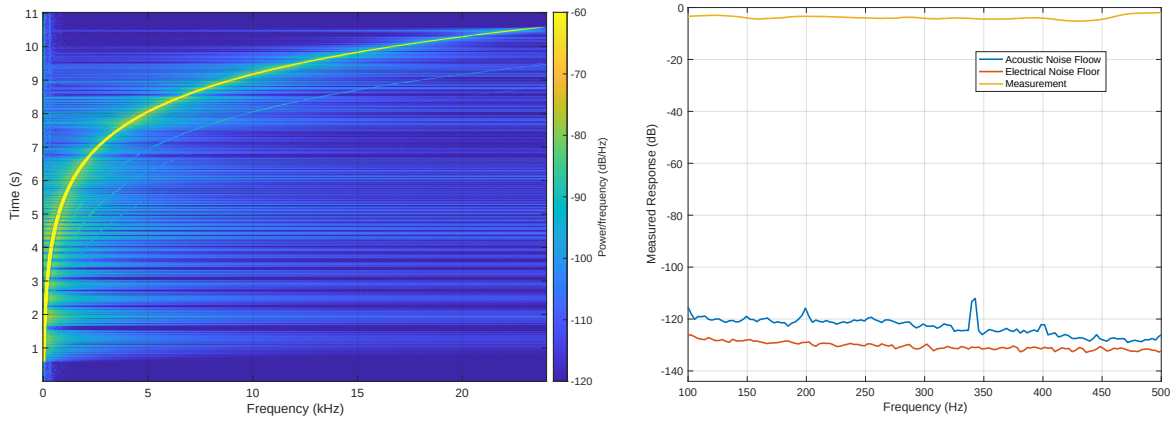

(a) A spectrogram showing the time-series data measured at one of the acoustic sensors when excited by one of the acoustic control sources.

(b) A plot showing the acoustic and electrical noise floors of the experimental setup, in comparison to the level of the measurements. The scale has been normalised to show the full dynamic range of the 24-bit data acquisition system.

Figure 2.5: Plots showing the noise floor and harmonic distortion of the raw measurements.

2.2 Control Formulation

In order to investigate the performance of the active acoustic cloaking system, an optimal harmonic control strategy will be used. The following section will formulate the optimal solution for the tonal control problem, as described in [37]. The tonal controller has been selected as

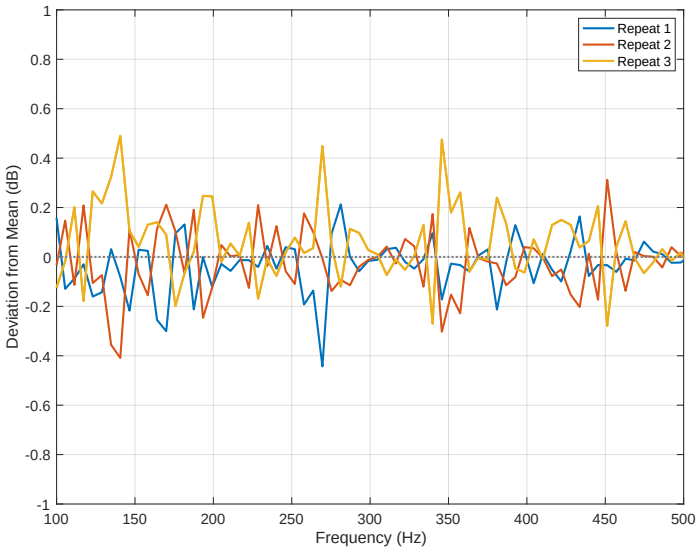

Figure 2.6: Plot showing the variability in the scattered sound power across three iterations of the repeatability study.

it represents the best-case scenario, allowing the performance limitations imposed by the geometry and transducer arrangement of the system, as presented in Figure 2.1 and discussed in Section 2.1, to be investigated without considering causality constraints, the selection of a suitable reference signal, or the ability to directly measure the acoustic scattered pressure. These practical considerations are discussed in Chapters 4, 5 and 7 respectively.

An object can be acoustically cloaked by directly minimising the acoustic scattered pressure measured at a number of sensor locations in the far-field of the scattering object, $\mathbf{d}_s$, using an array of control sources located in the near-field of the scattering object. Assuming that the total acoustic pressure at these sensor locations, $\mathbf{d}_t$, can be expressed as the linear summation of the far-field incident acoustic pressures, $\mathbf{d}_i$, and the far-field scattered pressures, then the vector of scattered acoustic pressures can be expressed, at a single frequency, as

$$\mathbf{d}_s\left(e^{j\omega t}\right) = \mathbf{d}_t\left(e^{j\omega t}\right) - \mathbf{d}_i\left(e^{j\omega t}\right). \tag{2.2}$$

For notational convenience, the frequency dependence $\left(e^{j\omega t}\right)$ will be dropped in subsequent equations. The vector of scattered acoustic pressures at each sensor location after control, $\mathbf{e}_s$, can be expressed as

$$\mathbf{e}_s = \mathbf{d}_s + \mathbf{G}\mathbf{u}, \tag{2.3}$$

where $\mathbf{G}$ is the matrix of complex plant responses between the control sources and the far-field sensor array and $\mathbf{u}$ is the vector of control source strengths. In the context of active acoustic cloaking, the controller aims to minimise the cost function defined by the sum of the squared scattered acoustic pressures after control [38], which is given as

$$J = \mathbf{e}_s^{\mathrm{H}}\mathbf{e}_s. \tag{2.4}$$

By combining Equations 2.3 and 2.4, and imposing a constraint on the control effort, the cost

function can be written as

$$J = (\mathbf{d}_s + \mathbf{G}\mathbf{u})^{\mathrm{H}} (\mathbf{d}_s + \mathbf{G}\mathbf{u}) + \beta \mathbf{u}^{\mathrm{H}}\mathbf{u}, \tag{2.5}$$

where the term β acts as a Tikhonov regularisation term [53], included to constrain the magnitude of the source strengths and reduce the effects of ill-conditioning on the matrix inversion. By expanding and differentiating Equation 2.5 with respect to the real and imaginary parts of the vector of control filter coefficients, and setting the real and imaginary parts to 0 as outlined in [37], the optimal set of control source strengths, $\mathbf{u}_{\mathrm{opt}}$, is given as

$$\mathbf{u}_{\mathrm{opt}} = -\left[\mathbf{G}^{\mathrm{H}}\mathbf{G} + \beta\mathbf{I}\right]^{-1} \mathbf{G}^{\mathrm{H}}\mathbf{d}_s. \tag{2.6}$$

2.3 Acoustic Cloaking Performance

This section will present the performance of the control strategy described in Section 2.2 using the responses measured according to the method outlined in Section 2.1. The performance of the control system can be evaluated in terms of the cost function defined in Equation 2.5 and, provided that the error microphones are positioned in the far-field, this can give an approximation of the scattered acoustic power, W_s, as [54]

$$W_s = \frac{\mathbf{e}_s^{\mathrm{H}}\mathbf{e}_s}{2\rho_0 c_0} \tag{2.7}$$

where ρ_0 is the fluid density and c_0 is the speed of sound in the fluid. It should be noted that to achieve a true measure of the sound power, the scattering object should be surrounded by a 3D sphere of microphones. Due to experimental limitations, this requirement has been relaxed and only a 2D ring of microphones has been utilised which, therefore, will give an approximation of the sound power. The effect of this is discussed in more detail in Appendix I.2. This metric has been calculated before and after the implementation of active control, allowing the attenuation in the scattered acoustic power caused by the controller to be quantified. Figure 2.7 shows the attenuation in the scattered acoustic power achieved by the active control system using all 32 loudspeakers over a range of frequencies and with increasing values of the regularisation parameter, β. The optimal source strengths have been calculated using Equation 2.6, assuming perfect knowledge of both the plant response matrix and the disturbance signal vector, and the scattered acoustic pressure after control has been calculated using Equation 2.3. Figure 2.7 shows that the performance of the controller is not significantly affected by the level of regularisation until it reaches approximately $\beta = 10^{-4}$. As the regularisation is increased above this point, the performance rapidly deteriorates and the system can be said to be over-regularised.

Whilst Figure 2.7 shows negligible change in the acoustic cloaking performance when the value of regularisation is below $\beta = 10^{-4}$, the conditioning of the matrix of plant responses, with respect to matrix inversion, will deteriorate and, therefore, the robustness of the system to practical uncertainties in the plant responses will be reduced. An in-depth study into the robustness of the active acoustic cloaking system is presented in Chapter 3, however a brief investigation into the the conditioning of the matrix of plant responses, $\mathbf{G}$, is presented below.

As shown in Equation 2.6, the matrix $\mathbf{G}^{\mathrm{H}}\mathbf{G} + \beta\mathbf{I}$ has to be inverted to calculate the optimal

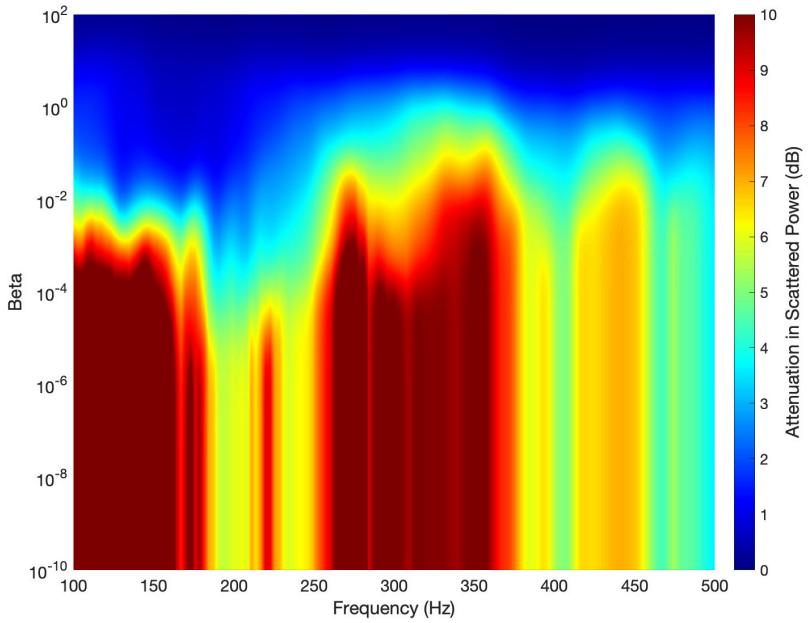

Figure 2.7: Contour plots showing the attenuation that the control system is able to achieve in the scattered sound power over frequency and a range of values of β.

source strengths. If this matrix is poorly conditioned then the resulting performance will be less robust and uncertainties in the system will have a significant effect on the performance. The condition number of the matrix $\mathbf{G}^{\mathrm{H}}\mathbf{G} + \beta\mathbf{I}$ has been calculated over a range of frequencies and values of β, and is presented in Figure 2.8. Figure 2.8 shows that increasing the value of regularisation in Equation 2.6 reduces the condition number, as is expected. Figure 2.8 also shows that the conditioning of the system is significantly poorer at frequencies below approximately 230 Hz, corresponding to the frequency at which an acoustic wavelength is equal to the diameter of the loudspeaker array: $1.5\mathrm{m}$. This is perhaps unsurprising, as it is known from the literature that the low frequency limit of a circular loudspeaker array is defined by the array diameter, whilst the high frequency limit is defined by the array source spacing [49, 50, 55].

According to the results presented in Figures 2.7 and 2.8, a regularisation value of $\beta = 10^{-5}$ results in minimal degradation in the attenuation performance, whilst reducing the low-frequency condition number significantly. Under nominal conditions, without uncertainties, a value of $\beta = 10^{-5}$ provides a practically achieveable level of control and, therefore, this value of regularisation has been selected for the current study. It should be noted that this will not necessarily give the most robust solution to variations in the physical system, which will depend on the form of the uncertainties in practice, however the selection of regularisation for robust performance will be investigated in more detail in Chapter 3. Optimal control source strengths were calculated according to Equation 2.6, with the regularisation parameter set to $\beta = 10^{-5}$, and the resulting acoustic cloaking performance was calculated according to Equation 2.3. The results are presented over frequency in Figure 2.9, and show that the proposed active acoustic cloaking system can achieve between 4 dB and 19 dB attenuation in the scattered sound power across the investigated frequency range. The acoustic cloaking performance exhibits local minima at approximately 200 Hz and 380 Hz, corresponding to the frequencies at which the the surface of the scattering sphere is approximately half a wave-

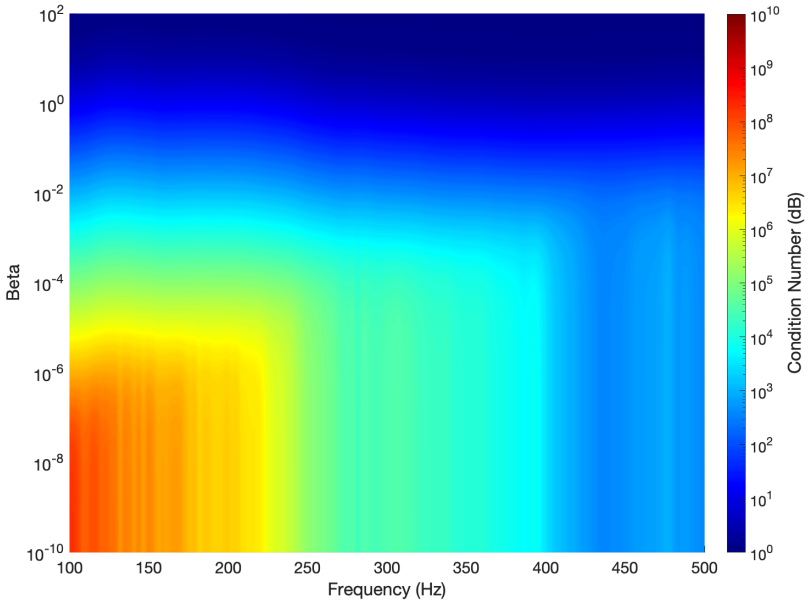

Figure 2.8: Contour plot showing the condition number of the matrix $\mathbf{G}^{\mathrm{H}}\mathbf{G} + \beta\mathbf{I}$ over frequency and a range of values of β.

length away from the far-field microphone array, and the control-source array, respectively. These are smeared in frequency due to the fact that the control sources and microphones are not point sources/sensors, and that the measurement setup will not be perfect, which explains the fairly broad dips in performance around these frequencies.

To provide further insight into the acoustic cloaking performance of the proposed system, the directivity of the acoustic scattered pressure has been plotted before and after the implementation of active control, and can be seen presented at five separate frequencies in Figure 2.10 with the grey arrow indicating the direction of the incident acoustic wave. It can be seen from Figure 2.10 that the scattered field before control appears to have a null in the direction of the incident acoustic wave, which is inconsistent with previous analytical studies investigating the acoustic scattering from rigid spheres [11, 56, 57]. The experimental results presented in Figure 2.10 utilise a relatively large loudspeaker to generate the incident acoustic field, whilst previous analytical studies have considered point-sources. The finite-size of the primary loudspeaker in the current study results in standing waves forming between the loudspeaker and the scattering body and, therefore, the microphone directly in-line with these objects will measure a lower level of acoustic scattering than the rest of the array.

2.3.1 Effect of Control Source Arrangement

As discussed previously, the control source arrangement shown in Figures 2.1 and 2.3 consists of a dual-layer array, with a ring of inward pointing loudspeakers and a ring of outward pointing loudspeakers; this allows the control source pairs to approximate any first-order directivity pattern, as required. It is insightful to consider whether the optimal source strengths, calculated according to Equation 2.6, drive the sources with a uniform directivity, or whether the directivity of each control source pair is predictable in some other way. To investigate this, the directivity of the far-field pressures radiated by each pair of control sources is plotted in Figure 2.11 at the five frequencies considered previously. In each case, the maximum magnitude of the two source strengths has been normalised to 0 dB to allow for easy comparison of

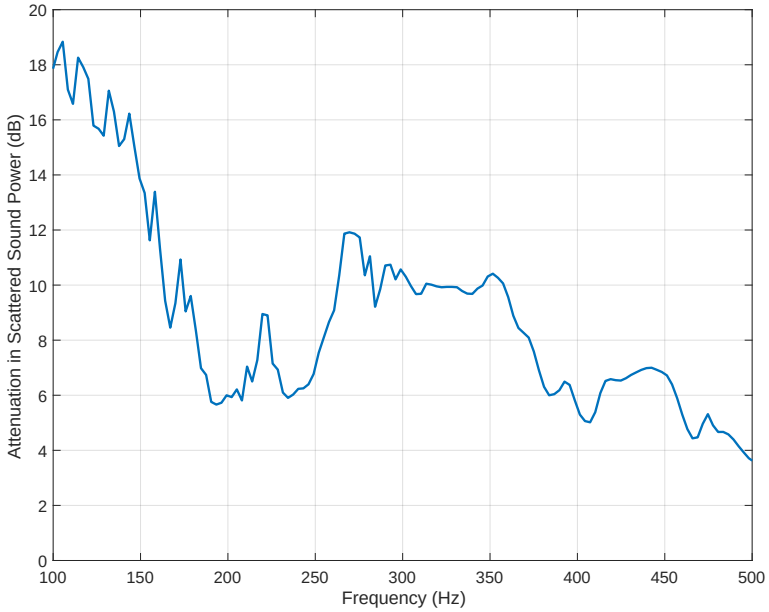

Figure 2.9: A plot showing the level of attenuation in the scattered sound power that the control system is able to achieve when regularised with a value of $\beta = 1 \times 10^{-6}$.

the directivity patterns. The directivity plots shown in Figure 2.11 are relatively coarse (18 ° increments), due to the limited resolution of the far-field microphone array, however, they they still provide insight into the directivity of the control sources. Figure 2.11 shows that, at 100 Hz, the control source pairs are largely driven in-phase with one another to achieve an omnidirectional pattern, with the exception of *Pair 6* that shows more of a cardioid directivity. As the frequency increases, in general, the sources become more directional, with a number of pairs showing a super-cardioid directivity at 500 Hz. Whilst, due to the limited resolution, the interpretation of these results is not straightforward, Figure 2.11 clearly shows that, in many cases, the active acoustic cloaking system is driving the control source pairs to achieve directionality and, therefore, the use of a dual-layer array of control loudspeakers is perhaps justified, however it is also worth observing the control achieved by different combinations of the available sources.

In practical engineering systems it is often advantageous to reduce weight, cost, and system complexity and, therefore, there is an interest in reducing the numbers of loudspeakers and microphones required for active acoustic cloaking. For this reason, it is insightful to observe the performance of the presented active acoustic cloaking system when the numbers of loudspeakers and microphones are reduced. To investigate this, the performance of the active acoustic cloaking system has been calculated when using only a subset of the full loudspeaker array. The performance of various subsets has been investigated, as detailed below and shown in Figure 2.12.

- Using both rings: 32 loudspeakers (as already considered above)
- Using the outer ring: 16 loudspeakers
- Using the inner ring: 16 loudspeakers
- Alternating between the outer and inner rings: 16 loudspeakers
- Alternating between loudspeaker pairs: 16 loudspeakers

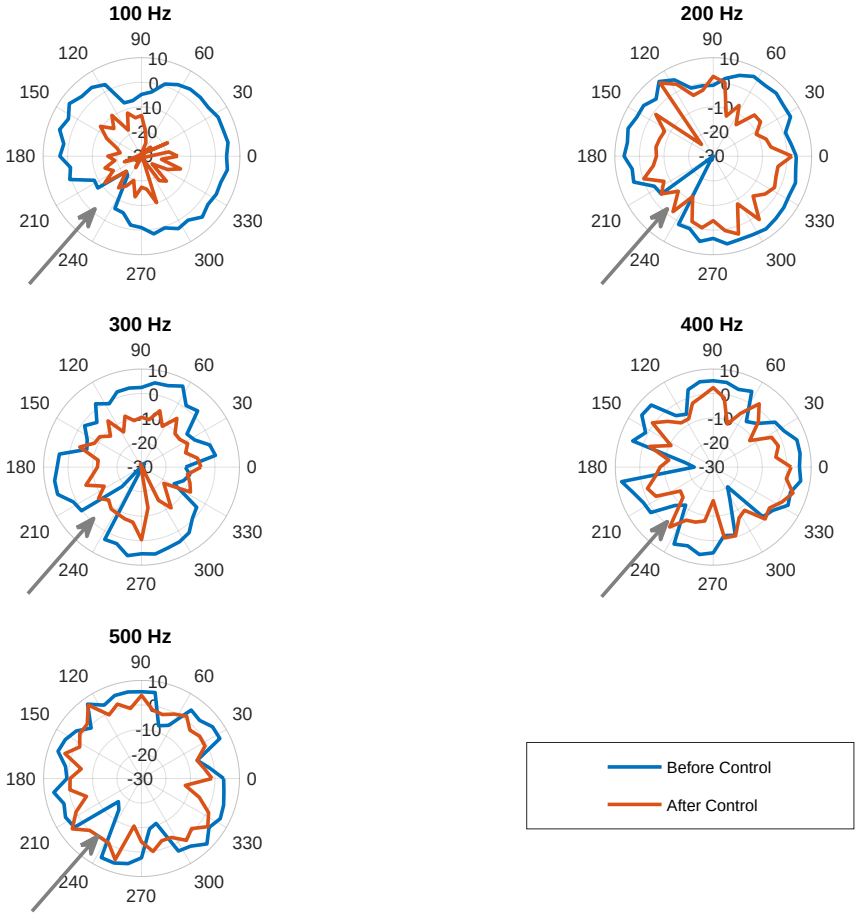

Figure 2.10: A set of polar plots showing the directivity of the acoustic scattered field before and after the implementation of active control, at five separate frequencies. The grey line indicates the direction of the incident acoustic wave.

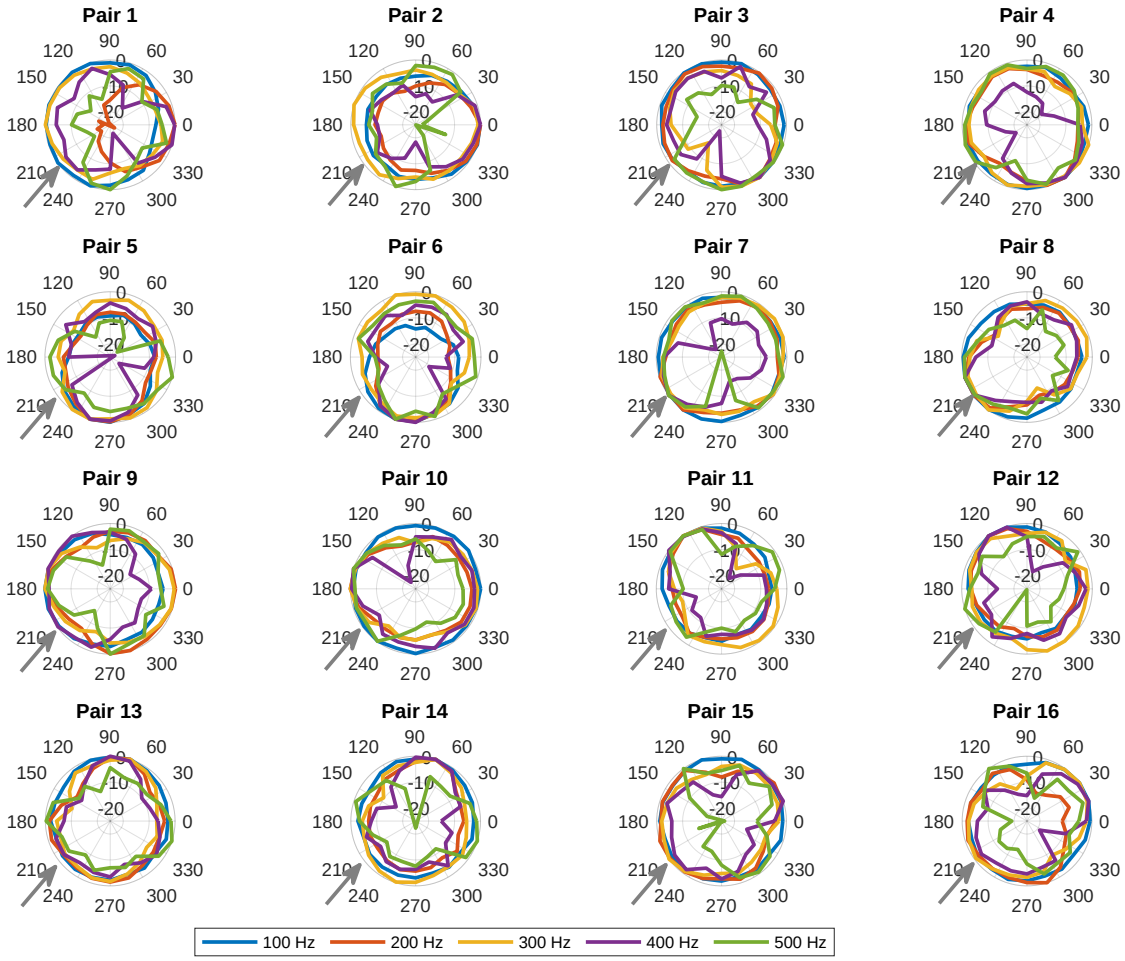

Figure 2.11: A set of polar plots showing the directivity of each control source pair at five separate frequencies. The magnitude of the directivities are normalised to 0 dB and a grey arrow indicates the direction of the incident wave.

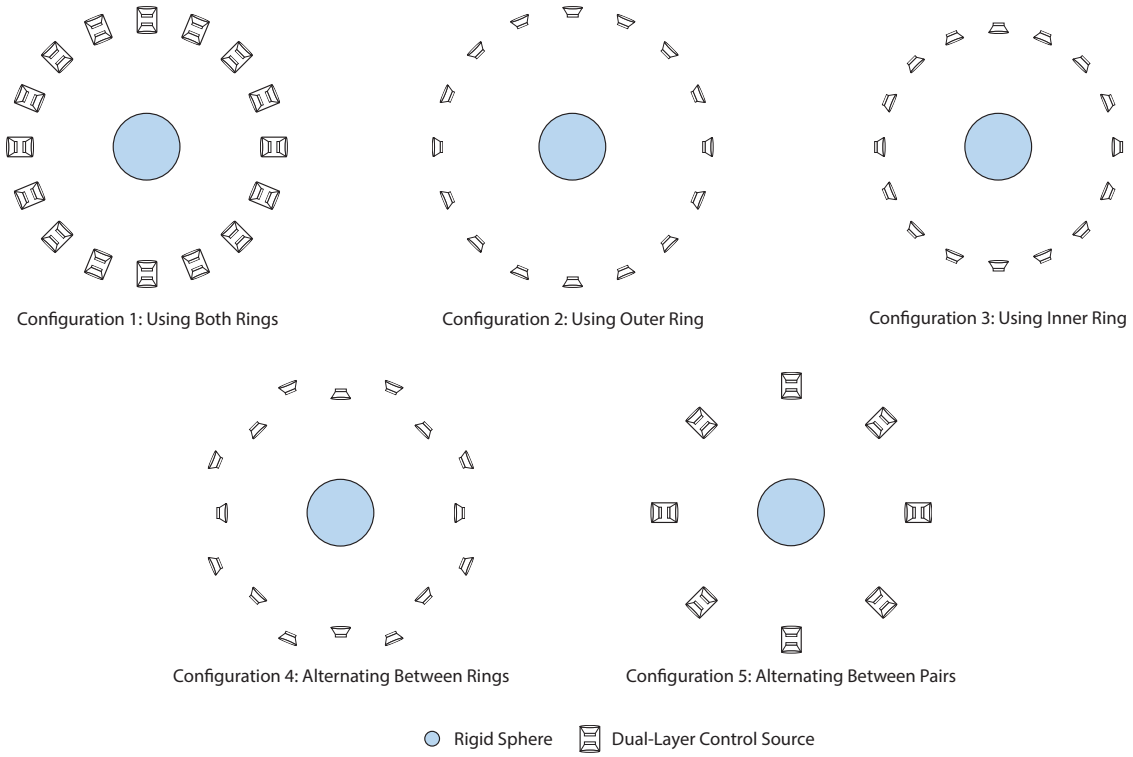

Figure 2.12: A diagram showing each of the control source arrangements.

In each case, the control parameter β was set to ensure that the condition number of the matrix inversion shown in Equation 2.6 was comparable across all of the subset configurations. The performance of the acoustic cloaking system with each subset of loudspeakers is presented in Figure 2.13. It can be seen from Figure 2.13 that the performance of the proposed active acoustic cloaking system varies significantly as the number of loudspeakers is reduced, with the system achieving less than 6 dB of control across the investigated frequency range when only one ring of control sources is selected, and achieving less than 10 dB of control when the loudspeaker selection alternates between the two rings. It is interesting to note that the performance of the acoustic cloaking system is superior, especially below 200 Hz, when the array consists of a subset containing loudspeakers from both the inner and outer rings. In this case, the controller is still able to enforce some level of directivity to the control source array which, as shown in Figure 2.11, is required to achieve optimal control. This is somewhat surprising, as the directivity plots presented in Figure 2.11 show that most of the pairs of control sources are largely omnidirectional at 100 Hz, therefore it is surprising that the controller still requires both the inner and outer arrays to achieve high levels of control.

2.3.2 Effect of Error Sensor Arrangement

As discussed above, there is often an interest in practical active control implementations to reduce the weight, cost, and complexity of the control system. This can be achieved by reducing the number of control sources, as investigated in the previous section, or reducing the number of error sensors. The performance limitations imposed by decreasing the number of error sensors used in the system will be investigated in this section. The results presented in Figure 2.9 utilise two concentric rings of microphones as the error sensors, as shown in Figure 2.1 and the performance limitations introduced by reducing the number of

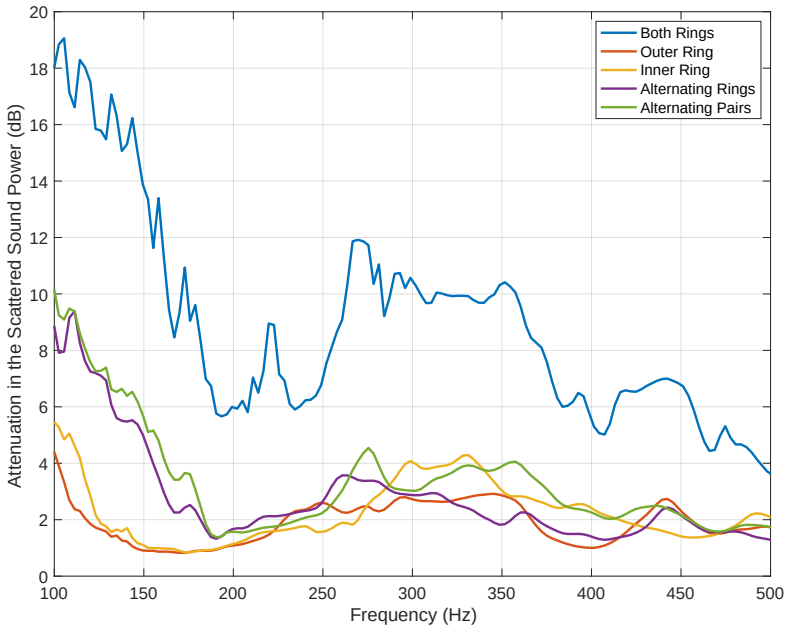

Figure 2.13: A plot showing the attenuation in the scattered sound power for various control source arrangements.

error sensors will now be investigated. Equation 2.6 will be used to calculate the optimal control source strengths using a subset of the far-field microphone array, however the full array of sensors will be used to evaluate the performance of the acoustic cloaking system. In each case, the control parameter β was set to ensure that the condition number of the matrix inversion shown in Equation 2.6 was comparable across all of the subset configurations. As the number of sensors used in the calculation of optimal source strengths is reduced from 40 to 20, the cost function shown in Equation 2.4 becomes underdetermined. Therefore, the matrix inversion shown in Equation 2.6 must be replaced with a pseudo-inverse [58] to overcome this issue. Figure 2.14 presents the attenuation achieved by the active acoustic cloaking system using various subsets of the far-field microphone array. It can be seen that any reduction in the numbers of microphones results in a heavily degraded acoustic cloaking performance, which causes significant enhancement of the acoustic scattered field at some frequencies.

With the reduced number of far-field sensors, the controller creates local minima in the acoustic scattered pressure at each microphone location rather than globally attenuating the scattered acoustic power. At the lower frequencies of this study, the acoustic wavelength is significantly greater than the angular spacing of the microphone array and, therefore, it may not be immediately apparent that local minima would occur. However, the microphone array shown in Figure 2.1 has very little resolution in the radial direction as the array only consists of two concentric rings of sensors. Therefore, when the number of sensors is reduced, the acoustic cloaking system creates a ring at which control is achieved, but outside of this ring the acoustic scattering is not controlled, and may even be enhanced. It should be noted that this may still be occuring when the controller uses the full microphone array shown in Figure 2.1, and the acoustic cloaking system may just create a wide ring of control around the scattering sphere, however practical limits to the experimental setup prevent a full far-field grid of sensors being used to investigate whether or not this is the case.

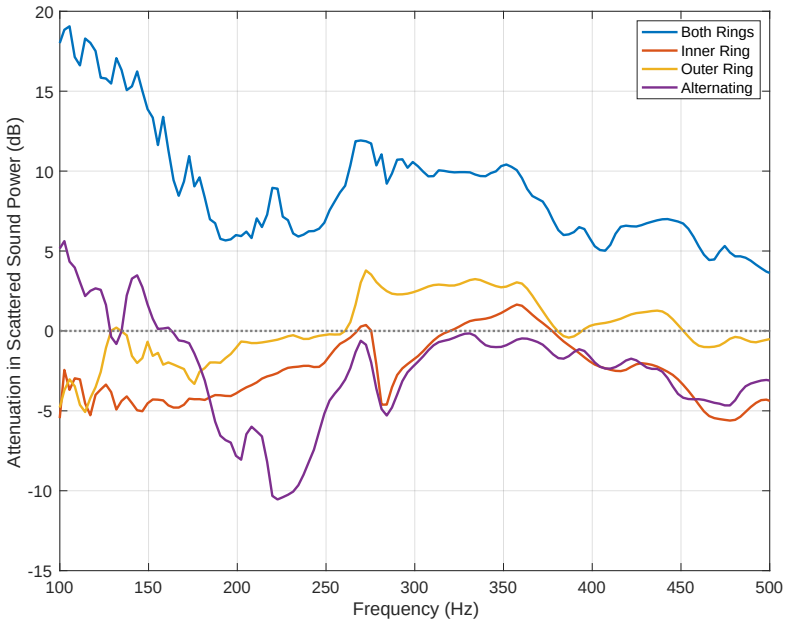

Figure 2.14: A plot showing the attenuation in the scattered sound power as the numbers of error sensors are reduced.

From the above two studies, it can be concluded that the active acoustic cloaking system shown in Figure 2.1 cannot be condensed to utilise less control sources or error sensors without resulting in a significant deterioration in the acoustic cloaking performance. This should be considered when designing a practical active acoustic cloaking system, and the required level of acoustic cloaking performance should be traded-off against the weight, cost, and complexity impact of implementing such a system. In some practical active acoustic cloaking systems, whilst there is a requirement to reduce the number of sources/sensors in the exterior field of the scattering object, there may be less concern about sources/sensors that are attached to, or in the very near-field of, the scattering body. This will be discussed further in Chapters 6 and 7.

2.4 Conclusions

This Chapter has presented an experimental investigation into the performance of an active acoustic cloaking system with a rigid spherical scattering body. An array of acoustic control sources was used to minimise the scattered acoustic pressure at a far-field microphone array using an optimal harmonic control formulation. Using this configuration, it has been shown that between 4 dB and 19 dB of attenuation in the far-field scattered acoustic power can be achieved across the bandwidth investigated, and the frequency variation in the acoustic cloaking performance can be linked to the system geometry. The effect of regularisation on both the control performance and the matrix conditioning was investigated, and the condition number of the plant responses was linked to the on-axis response of the control loudspeakers. The directivity of the optimal source strengths for each pair of control sources was plotted, and it was shown that, whilst the active control system is driving some of the control source pairs with a first-order directivity pattern, this was not consistent across either frequency or control source position. The effect of reducing the numbers of control sources

or error sensors was also investigated, and it was shown that any reduction in either array for the considered scattering control configuration will result in significant performance degradation.

This study represents an initial investigation into the potential best-case performance of an active acoustic cloaking system. A number of simplifications and assumptions have been made in this study which will be discussed in detail in subsequent chapters and, therefore, this chapter forms a motivator for the rest of the thesis. An optimal harmonic control strategy was used, which neglects the real-world implementation challenges of causality and obtaining a suitable reference signal, both of which are discussed in Chapters 4 and 7. A rigid spherical scattering object was used for this study, however it is known from the literature that the acoustic scattering caused by a resonant body is more complex and probably of greater practical significance; therefore this will also be discussed in detail in Chapters 6 and 7. It was assumed in Equation 2.6 that the scattered acoustic pressure can be directly measured at the far-field microphone array, however, in practice this is not possible and therefore additional signal-processing steps will be required to obtain real-time measurements of the scattered acoustic disturbance. A potential method to achieve this is presented in Chapter 5. A brief investigation into the conditioning of the plant responses has been presented, however, a more thorough investigation into the conditioning and the effect of uncertainties on the acoustic cloaking performance, will be discussed in the following chapter.

Chapter 3

An Investigation into the Robustness of an Active Acoustic Cloaking System, Applied to a Rigid Sphere

Active acoustic cloaking has been thoroughly discussed in the literature, and reviewed in Chapter 1. The ability to acoustically conceal an object, such that the sound-field with the object present is identical to that without the object present, would have significant benefits across a variety of industries, but has generally been investigated from a theoretical or simulation-based perspective [38, 59, 60], without considering all of the implications of practical realisations. For example, practical systems require real-time knowledge of the scattered acoustic field, which cannot be directly measured and, as in the previous chapter, the literature on the topic has often assumed that the scattered pressure field is known in advance. Various methods of estimating the scattered acoustic pressure from a directly measurable quantity have been discussed in Chapter 1 [39, 40, 61, 62], however, the majority of these systems rely on prior-knowledge of the scattering object, measured in an initial setup stage. These measurements are then used in the real-time estimation of the acoustic scattered pressure, however, the robustness of these systems to variations in the plant responses or uncertainties in the disturbance field remains an open area of research.

This chapter will present an investigation into the effect of uncertainty on the active acoustic cloaking system presented in Chapter 2, which used a tonal control strategy to minimise the acoustic scattering from a rigid sphere using an array of control loudspeakers, arranged as shown in Figure 2.1. Optimal control source strengths to minimise the acoustic scattering from the perturbed system will be formulated, and compared to the solution for the nominal case. The effect of unstructured uncertainty will be considered, as will the effects of varying the size and position of the scattering sphere, on the acoustic cloaking performance using experimental data, and the effect of regularisation on the robustness of the control system will be considered. A further study will also be presented, which investigates how the effect of uncertainty on the acoustic cloaking performance can be reduced if the controller has knowledge of either the change in the plant response, or the change in the disturbance field.The effect of frequency dependent regularisation will be investigated, and the performance benefits that this gives over frequency independent regularisation will be quantified.

Whilst previous studies have used experimental data to investigate the performance of active acoustic cloaking, very few consider the robustness of the control system to practical uncertainties. Therefore, the study presented in this chapter will form one of the major contributions of the thesis, as detailed in Section 1.5. Parts of this work have been published in [46].

3.1 Formulation with Uncertainty

To investigate the robustness of active acoustic cloaking, the control strategy and experimental setup described in detail in Chapter 2 will be used. An optimal harmonic controller has been used to directly minimise the scattered acoustic pressure, measured at a number of sensor locations in the far field. As described in Chapter 2, the transfer responses between a far-field source and an array of pressure microphones was measured with and without the scattering sphere present, and the difference between these responses gives the vector of acoustic scattered pressure, $\mathbf{d}_s$, calculated at each sensor location, as given by Equation 2.2. The transfer responses between an array of acoustic control sources and the array of far-field pressure sensors was also measured to form the complex matrix of acoustic plant responses, $\mathbf{G}$. The optimal set of control source strengths that minimises the far-field acoustic scattered pressure, $\mathbf{u}_{\mathrm{opt}}$, was formulated without considering uncertainty in Chapter 2. A robust solution will now be presented, by considering the case where the vector of scattered acoustic pressures and the matrix of complex plant responses contain uncertainties, which are assumed here to be additive in nature and so can be expressed as [37, 63–65]

$$\mathbf{d}_s = \mathbf{d}_{s_0} + \Delta\mathbf{d}_s, \tag{3.1}$$

$$\mathbf{G} = \mathbf{G}_0 + \Delta\mathbf{G}, \tag{3.2}$$

where $\mathbf{d}_{s_0}$ and $\mathbf{G}_0$ represent the nominal responses, and $\Delta\mathbf{d}_s$ and $\Delta\mathbf{G}$ represent perturbations from the nominal. The error after control, $\mathbf{e}_s$, can be expressed in the perturbed case as

$$\mathbf{e}_s = \mathbf{e}_{s0} + \Delta\mathbf{e}_s, \tag{3.3}$$

which can be written in terms of the summation of the components due to the disturbance and the control sources as

$$\mathbf{e}_s = \mathbf{d}_s + \mathbf{G}\mathbf{u}, \tag{3.4}$$

and by substituting Equation 3.1 and 3.2 can be expressed as

$$\mathbf{e}_s = \mathbf{d}_{s0} + \Delta\mathbf{d}_s + (\mathbf{G}_0 + \Delta\mathbf{G})\,\mathbf{u} \tag{3.5}$$

As in Chapter 2, the cost function in the context of acoustic cloaking is defined as the sum of the squared scattered acoustic pressures after control [38], which is given as

$$J = \mathbf{e}_s^{\mathrm{H}}\mathbf{e}_s. \tag{3.6}$$

By combining Equations 3.4 and 3.6, the cost function can be expressed as

$$J = (\mathbf{d}_s + \mathbf{G}\mathbf{u})^{\mathrm{H}}(\mathbf{d}_s + \mathbf{G}\mathbf{u}). \tag{3.7}$$

By expanding and differentiating Equation 3.7 with respect to the real and imaginary parts of the vector of control filter coefficients, and setting the real and imaginary parts to 0 as outlined in [37], the robust optimal set of control source strengths, $\mathbf{u}_{\mathrm{opt}}$, can be calculated

as

$$\mathbf{u}_{\text{opt}} = -\left[\mathbf{G}^{\text{H}}\mathbf{G}\right]^{-1}\mathbf{G}^{\text{H}}\mathbf{d}_s \tag{3.8}$$

which, by substituting in Equations 3.1 and 3.2, can be expressed as

$$\mathbf{u}_{\text{opt}} = -\left[\mathbf{G}_0^{\text{H}}\mathbf{G}_0 + \Delta\mathbf{G}^{\text{H}}\Delta\mathbf{G} + \mathbf{G}_0^{\text{H}}\Delta\mathbf{G} + \Delta\mathbf{G}^{\text{H}}\mathbf{G}_0\right]^{-1}\mathbf{G}_0^{\text{H}}\mathbf{d}_{s0}+\Delta\mathbf{G}^{\text{H}}\mathbf{d}_{s0}+\mathbf{G}_0^{\text{H}}\Delta\mathbf{d}_s+\Delta\mathbf{G}^{\text{H}}\Delta\mathbf{d}_s. \tag{3.9}$$

In the special case where $\Delta\mathbf{G}$ and $\Delta\mathbf{d}_s$ are random and uncorrelated with one another, it can be shown that [64]

$$\text{E}\left[\mathbf{G}_0^{\text{H}}\Delta\mathbf{G}\right] = 0, \tag{3.10}$$

$$\text{E}\left[\Delta\mathbf{G}^{\text{H}}\mathbf{G}_0\right] = 0, \tag{3.11}$$

$$\text{E}\left[\Delta\mathbf{G}^{\text{H}}\mathbf{d}_{s0}\right] = 0, \tag{3.12}$$

$$\text{E}\left[\mathbf{G}_0^{\text{H}}\Delta\mathbf{d}_s\right] = 0, \tag{3.13}$$

$$\text{E}\left[\Delta\mathbf{G}^{\text{H}}\Delta\mathbf{d}_s\right] = 0, \tag{3.14}$$

$$\text{E}\left[\Delta\mathbf{G}^{\text{H}}\Delta\mathbf{G}\right] \approx \beta\mathbf{I}, \tag{3.15}$$

and therefore Equation 3.9 reduces to the regularised solution for the nominal system without uncertainty

$$\mathbf{u}_{\text{opt}} = -\left[\mathbf{G}_0^{\text{H}}\mathbf{G}_0 + \beta\mathbf{I}\right]^{-1}\mathbf{G}_0^{\text{H}}\mathbf{d}_{s0}. \tag{3.16}$$

Therefore, if it can be shown that the statements in Equations 3.10 to 3.15 are valid for practical uncertainties, then simply including Tikhonov regularisation in the matrix inversion is sufficient to ensure a solution that is robust to uncertainty. If it is shown that the statements in Equations 3.10 to 3.15 are not valid, then the optimal solution is given by Equation 3.9 which requires knowledge of the uncertainties. This will be considered in Section 3.4.1.

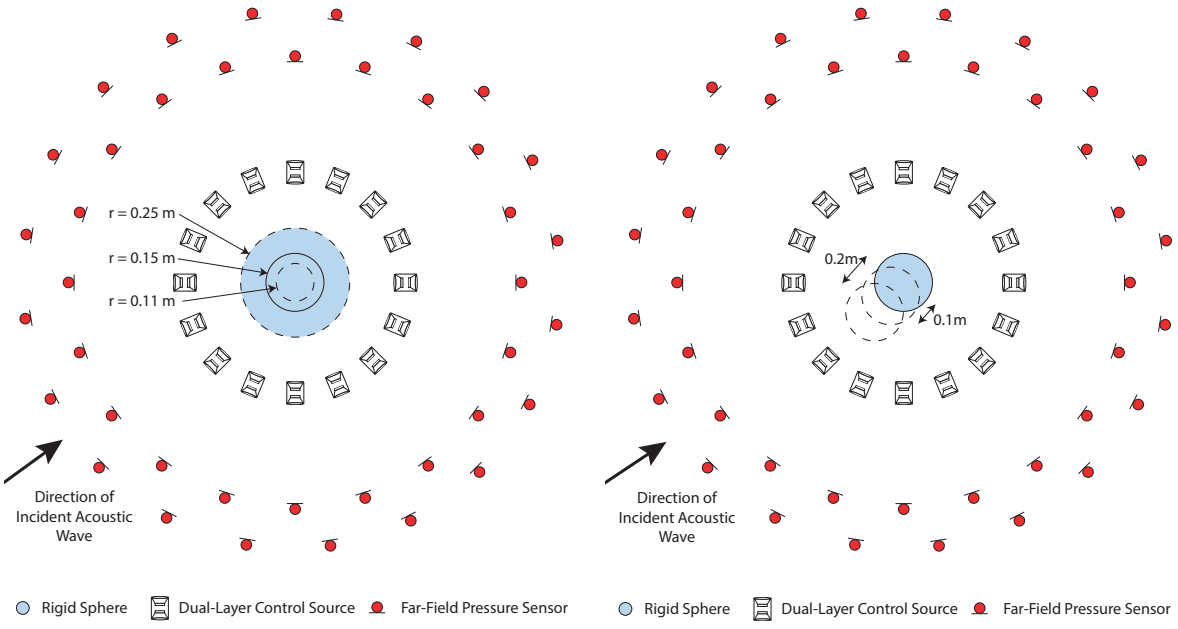

(a) Perturbation in size of scattering body. *(b) Perturbation in location of scattering body.*

Figure 3.1: Schematic diagram showing the source/sensor arrangement, and the nominal and perturbed scattering bodies.

As described in Chapter 2, a rigid spherical scatterer of radius $r_0 = 150$ mm, made of plaster, has been suspended inside an anechoic chamber, and will henceforth be referred to as the nominal scattering body. To allow an investigation into the effect of uncertainty in the size of the scattering object on the control performance, two further spherical scatterers have also been constructed, of radii $r_+ = 250$ mm and $r_- = 110$ mm, as shown in Figure 3.1a. The experimental procedure outlined in Chapter 2 has been used to measure the matrix of acoustic transfer responses, $\mathbf{G}$, and the vector of acoustic scattered pressures, $\mathbf{d}_s$, for all three sphere sizes. In addition, acoustic measurements were also taken with the r_0 sphere displaced by 10 cm and 20 cm in the direction of the primary loudspeaker, as shown in Figure 3.1b, to allow for an investigation into the effect of uncertainty in the position of the scattering object.

The above measurements will allow for an investigation into the robustness of the control system to structured perturbations, however it is also insightful to investigate the robustness of the active acoustic cloaking system to random, unstructured, uncertainty, as would be the case with incoherent measurement noise. Unstructured uncertainty can be added to each transfer response as

$$\mathbf{G} = \Delta_n \mathbf{G}_0 e^{j\phi_n}, \tag{3.17}$$

where $\mathbf{G}_0$ is the nominal transfer response, and Δ_n and ϕ_n are normally distributed random numbers, used to introduce unstructured uncertainty into the magnitude and phase of the response respectively. This was repeated 1000 times to allow a statistical analysis into how unstructured uncertainty influences the acoustic cloaking performance. It should be noted that an alternative method of simulating unstructured uncertainty is to apply the normally distributed random numbers to the real and imaginary parts of the nominal value, rather than the magnitude and phase, as in [66]. Whilst it would be insightful to consider what difference this has on the subsequent robustness analysis, this study falls outside the scope of the thesis and has been left for future work.

From the measured data of the perturbed system, and the statistical analysis described above, the variation in the plant response, $\Delta\mathbf{G}$, and the variation in the disturbance field, $\Delta\mathbf{d}_s$ have been calculated, and are presented in Figure 3.2. In the case of the structured perturbations, $\Delta\mathbf{G}$ has been averaged across each microphone and loudspeaker combination and $\Delta\mathbf{d}_s$ has been averaged across each microphone, with the magnitude plotted in decibels relative to the nominal case. In the case of the unstructured uncertainty, Δ_n and ϕ_n have been set to give comparable levels of perturbation to the measured results, and the range of perturbations has been plotted as a cloud plot.

It can be seen from Figure 3.2 that varying the radius of the scattering object to r_+ results in the largest change in the response, especially in the disturbance field where the perturbation from the nominal due to the large sphere is over 10 dB greater than the the other perturbations. This can be directly attributed to the relative differences between r_0 and r_-, and between r_0 and r_+, as the smallest sphere has a reduction in radius of 26% whilst the largest sphere has an increase in radius of 66% from the nominal. Across all of the perturbations investigated, $\Delta\mathbf{G}$ is fairly constant over frequency, whereas $\Delta\mathbf{d}_s$ increases by approximately 30 dB across the bandwidth presented in Figure 3.2. It is clear from Figure 3.2 that $\Delta\mathbf{G}$ is significantly larger than $\Delta\mathbf{d}_s$ across all of the perturbation conditions investigated, especially at low frequencies. At its peak, in the case of the large sphere, $\Delta\mathbf{G}$ is only 2.4 dB smaller than $\mathbf{G}_0$, and the effect of this high level of uncertainty on the acoustic cloaking performance

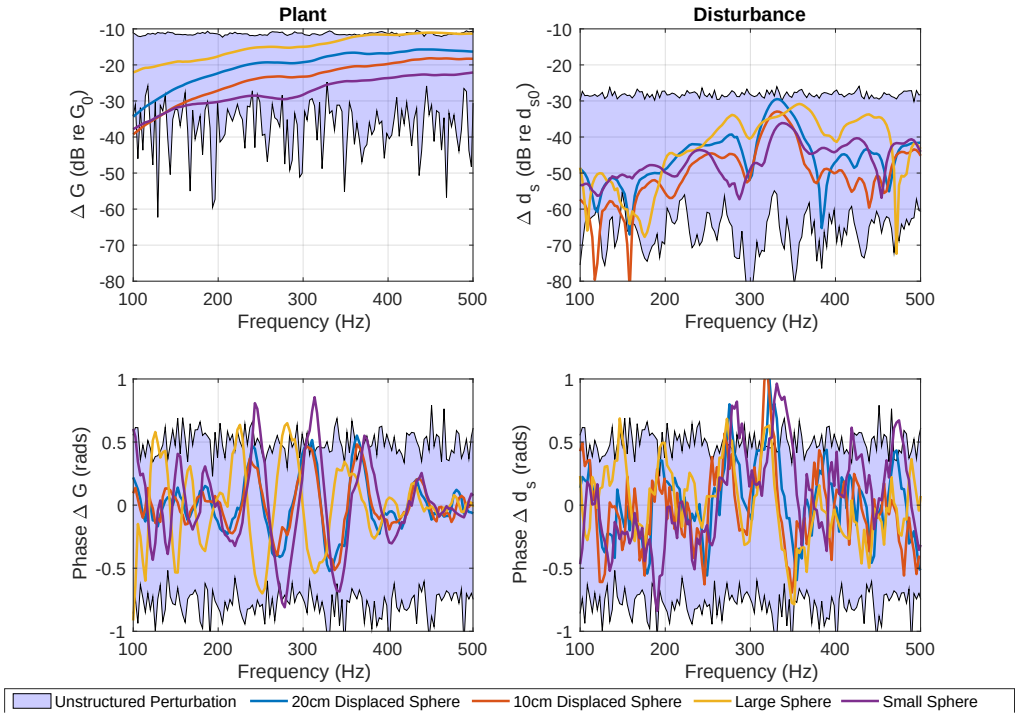

Figure 3.2: Plots showing the magnitude and phase of $\Delta\mathbf{G}$, averaged across each microphone and loudspeaker combination, and the magnitude and phase of $\Delta\mathbf{d}_s$, averaged across each microphone. The range of the unstructured uncertainty is also included as a cloud plot.

will be discussed in the following sections.

3.2 An Investigation into the Characteristics of the Perturbations

It has been shown by Equations 3.9 to 3.16 that the full solution for the optimal source strengths, when the plant and disturbance fields are perturbed, can be simplified to a regularised form of the nominal solution if $\Delta\mathbf{G}$ and $\Delta\mathbf{d}_s$ are random and uncorrelated with one another. This would clearly be advantageous for a practical setup, as the optimal source strengths can be calculated without requiring exact knowledge of $\Delta\mathbf{G}$ and $\Delta\mathbf{d}_s$. The following section will present an investigation into the assumption that the perturbations are random and uncorrelated with one another, and will discuss the validity of each of the statements shown in Equations 3.10 to 3.15.

3.2.1 Magnitude of the Cross Terms

As explained above, Equation 3.9 can be simplified to Equation 3.16 if the statements given by Equations 3.10 to 3.15 are valid. This section will investigate the first five of these statements by quantifying the magnitude of these cross-terms. In the case of the specific structured perturbations considered in this study, these terms correspond to real-world measured data and, therefore, measurement noise means their magnitudes will not reach 0. Instead, the assumptions can be considered valid if the magnitude of each term is significantly smaller than the magnitude of the relevant nominal term. In this way, it has been assumed that the

conditions shown in Equations 3.10 to 3.14 can be relaxed to

$$\mathbf{G}_0^{\mathrm{H}}\Delta\mathbf{G} \ll \mathbf{G}_0^{\mathrm{H}}\mathbf{G}_0, \tag{3.18}$$

$$\Delta\mathbf{G}^{\mathrm{H}}\mathbf{G}_0 \ll \mathbf{G}_0^{\mathrm{H}}\mathbf{G}_0, \tag{3.19}$$

$$\Delta\mathbf{G}^{\mathrm{H}}\mathbf{d}_{s0} \ll \mathbf{G}_0^{\mathrm{H}}\mathbf{d}_{s0}, \tag{3.20}$$

$$\mathbf{G}_0^{\mathrm{H}}\Delta\mathbf{d}_s \ll \mathbf{G}_0^{\mathrm{H}}\mathbf{d}_{s0}, \tag{3.21}$$

$$\Delta\mathbf{G}^{\mathrm{H}}\Delta\mathbf{d}_s \ll \mathbf{G}_0^{\mathrm{H}}\mathbf{d}_{s0}. \tag{3.22}$$

To investigate the validity of these statements, the 2-norm of each of the cross-terms shown in Equations 3.18 to 3.22 has been calculated for each structured perturbation condition, over a range of frequencies. The expectation of these cross-terms has also been calculated over 1000 iterations of random unstructured perturbation, as discussed previously, for comparison. The resulting values are presented in Figure 3.3, plotted in decibels relative to the 2-norm of the respective nominal term. As $\mathbf{G}_0^{\mathrm{H}}\Delta\mathbf{G} = \Delta\mathbf{G}^{\mathrm{H}}\mathbf{G}_0$, this term has only been plotted once. From Figure 3.3 it can be seen that, across all of the structured perturbation conditions, the terms associated with perturbations in the plant response, $\mathbf{G}_0^{\mathrm{H}}\Delta\mathbf{G}$ and $\Delta\mathbf{G}^{\mathrm{H}}\mathbf{d}_{s0}$, are of comparable magnitude to one another and, at some frequencies, are not significantly smaller than their respective nominal terms. In contrast, the terms associated with structured perturbations in the disturbance signals, $\mathbf{G}_0^{\mathrm{H}}\Delta\mathbf{d}_s$ and $\Delta\mathbf{G}^{\mathrm{H}}\Delta\mathbf{d}_s$, are always more than 10 dB smaller than their respective nominal terms, and at low frequencies can reach 40 dB less than the nominal case. In the case of the unstructured perturbations, all of the cross-terms are at least 20 dB smaller than the nominal terms and the $\Delta\mathbf{G}^{\mathrm{H}}\Delta\mathbf{d}$ term is over 40 dB smaller.

In the case of the unstructured perturbations, both the cross-terms related to perturbations in the disturbance signals, $\Delta\mathbf{d}_s$, and the cross-terms related to perturbations in the plant response, $\Delta\mathbf{G}$, are likely to be small enough that they can be neglected. In the case of structured perturbation, the cross-terms related to perturbations in the disturbance signals, $\Delta\mathbf{d}_s$, are small enough that they can be neglected, whereas the cross-terms related to perturbations in the plant response, $\Delta\mathbf{G}$, are significantly larger and may not be neglectable. This observation is consistent with the results presented in Figure 3.2, which showed that the magnitude of $\Delta\mathbf{G}$ is significantly greater than the magnitude of $\Delta\mathbf{d}_s$. The effect of these differences on the performance of the controller will be investigated in more detail in Section 3.4.1, where the optimal source strengths will be calculated assuming that the controller has prior knowledge of either $\Delta\mathbf{G}$ or $\Delta\mathbf{d}_s$.

3.2.2 Diagonal Dominance of $\Delta\mathbf{G}^{\mathrm{H}}\Delta\mathbf{G}$

In addition to the magnitude of the cross-terms, discussed above, the diagonality of $\Delta\mathbf{G}^{\mathrm{H}}\Delta\mathbf{G}$ must be considered before simplifying Equation 3.9 to Equation 3.16. As shown in Equation 3.15, it is assumed that the matrix $\Delta\mathbf{G}^{\mathrm{H}}\Delta\mathbf{G}$ can be approximated by a scaling parameter β multiplied by an identity matrix. This assumption can only be considered valid if $\Delta\mathbf{G}^{\mathrm{H}}\Delta\mathbf{G}$ is a diagonal matrix. In practice, it is sufficient for $\Delta\mathbf{G}^{\mathrm{H}}\Delta\mathbf{G}$ to be diagonally dominant, as it corresponds to measured data and therefore it is not expected for the non-diagonal terms to be identically 0.

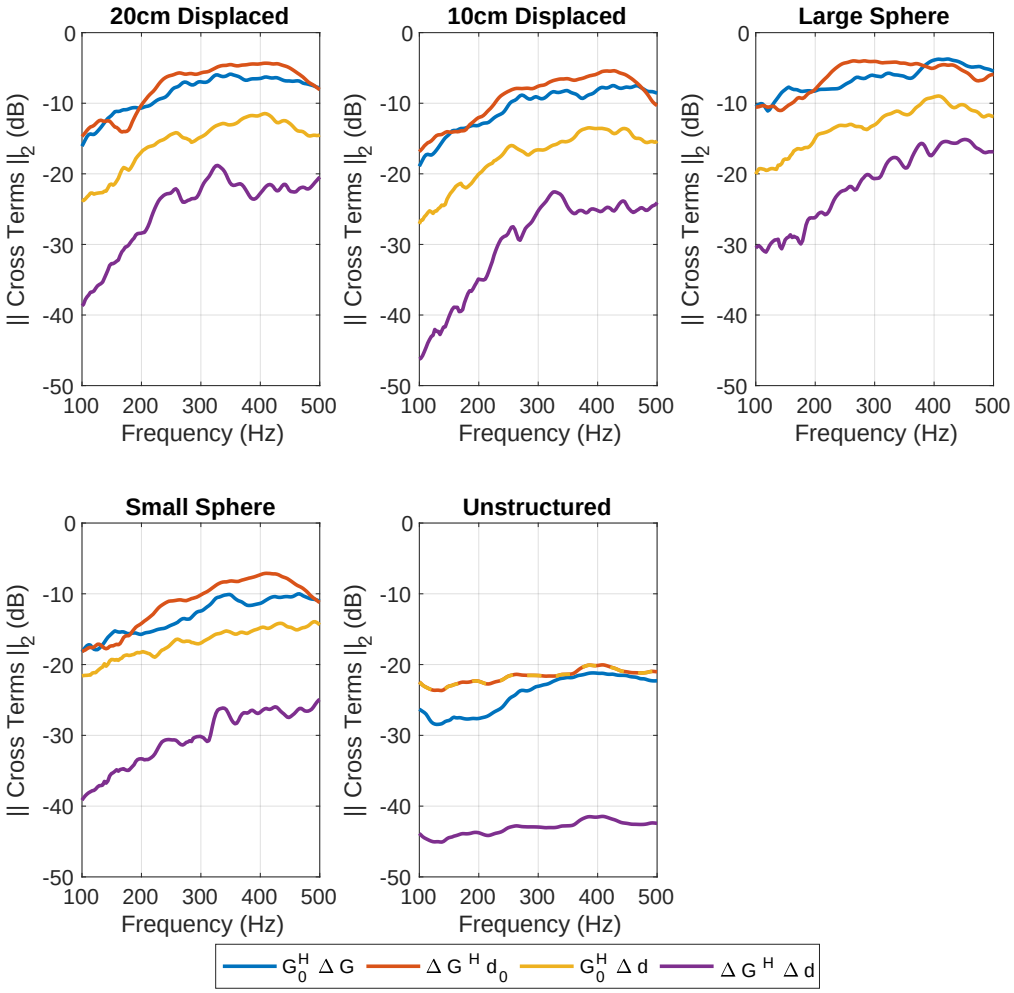

Figure 3.3: Plots showing the 2-norm of the cross-terms in Equation 3.9, relative to the 2-norm of their respective nominal terms.

A matrix $\mathbf{a} = a_{ij}$ can be said to be diagonally dominant [58] if, for every row of the matrix,

$$|a_{ii}| - \sum_{j,j\neq i} |a_{ij}| \geq 0. \tag{3.23}$$

For each perturbation condition, and over a range of frequencies, the diagonal dominance of the matrix $\Delta\mathbf{G}^{\mathrm{H}}\Delta\mathbf{G}$ has been calculated according to Equation 3.23 and averaged across every row in the matrix. These results are presented in Figure 3.4. It can be seen from Figure 3.4 that the condition shown in Equation 3.23 is not true at any frequency for any of the structured perturbation conditions and, in fact, the sum of the off-diagonal terms is greater than the diagonal terms such that the left-hand side of Equation 3.23 is negative. Therefore, $\Delta\mathbf{G}^{\mathrm{H}}\Delta\mathbf{G}$ can not be said to be diagonally dominant for the structured perturbations considered in this study. However, in the case of unstructured perturbations, the condition shown in Equation 3.23 is true and, therefore, the matrix can be considered to be diagonally dominant across the bandwidth investigated.

To provide further insight, the magnitude of the terms in the matrix $\Delta\mathbf{G}^{\mathrm{H}}\Delta\mathbf{G}$ have been av-

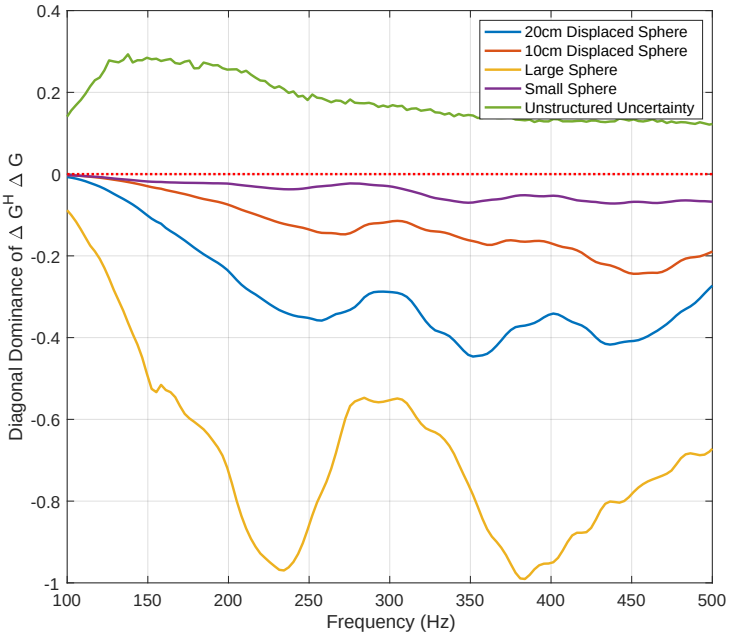

Figure 3.4: Plot showing the diagonal dominance of the matrix $\Delta\mathbf{G}^{\mathrm{H}}\Delta\mathbf{G}$ across frequency, for each perturbation condition.

eraged over frequency, and are presented in Figure 3.5 for each perturbation condition. As the magnitude of $\Delta\mathbf{G}$ varies significantly between each perturbation condition, the scales of the colorbars in Figure 3.5 are not consistent across the four plots and, therefore, each of the plots presented in Figure 3.5 can only be compared to itself. Figure 3.5 shows that, whilst $\Delta\mathbf{G}^{\mathrm{H}}\Delta\mathbf{G}$ is not diagonally dominant according to the definition shown in Equation 3.23 for the cases of structured uncertainty considered in this study, it has strong diagonal components. The criteria for diagonal dominance shown in Equation 3.23 is quite strict as, for the given matrix to be considered diagonally dominant, the magnitude of each of the off-diagonal terms in each row would have to be less than 3.1% of the magnitude of the diagonal term, on average. It can also be seen from Figure 3.5 that, in the case of structured uncertainty, $\Delta\mathbf{G}^{\mathrm{H}}\Delta\mathbf{G}$ is more consistent with a banded matrix [58] than with a diagonal matrix, as it appears to have significant non-zero terms on the superdiagonal ($i = j+1$) and the subdiagonal ($i = j - 1$), as well as the diagonal ($i = j$).

This section has presented an investigation into the validity of the assumptions shown in Equations 3.10 to 3.15 which, if valid, would allow the full formulation for the optimal source strengths for the perturbed system to be approximated by a regularised form of the optimal source strengths for the nominal system. This would allow a robust system to be designed which would be able to maintain acoustic cloaking performance over a range of perturbations, as may be required for a practical system. For this to be possible, the cross-terms shown in Equation 3.9 would be neglected, and the $\Delta\mathbf{G}^{\mathrm{H}}\Delta\mathbf{G}$ term would be approximated by a scaled identity matrix. The above study has shown that, in the case of random unstructured uncertainty, the assumptions described in Equations 3.10 to 3.15 are valid and therefore the robust solution for the optimal source strengths is given by Equation 3.16. In the case of the specific structured perturbations considered in this study, whilst it may be reasonable to

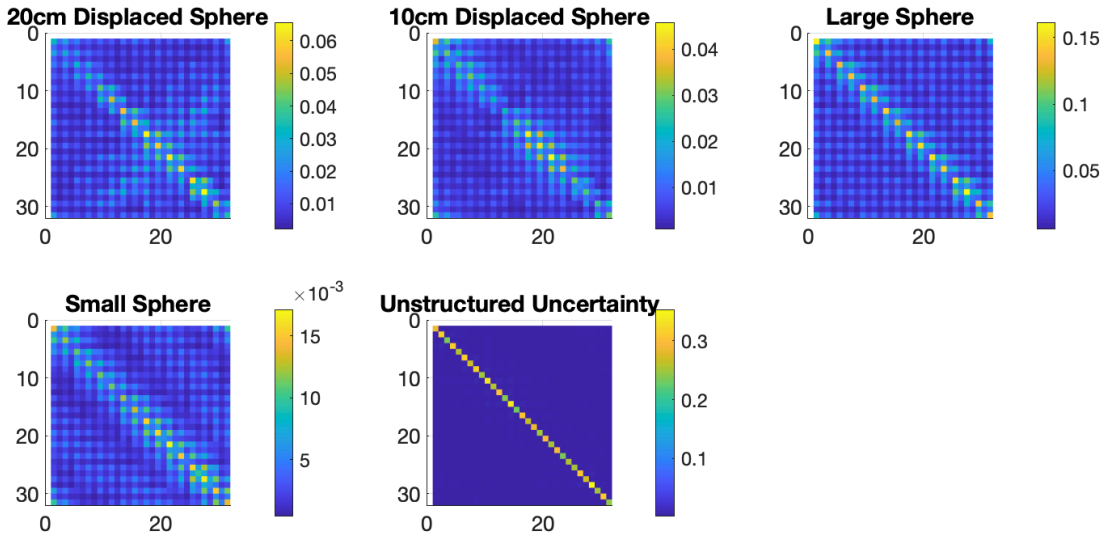

Figure 3.5: Contour plots showing the magnitude of $\Delta\mathbf{G}^{\mathrm{H}}\Delta\mathbf{G}$, averaged over frequency, for each perturbation condition.

neglect the cross-terms related to the perturbations in the disturbance signals, $\mathbf{G}_0^{\mathrm{H}}\Delta\mathbf{d}_s$ and $\Delta\mathbf{G}^{\mathrm{H}}\Delta\mathbf{d}_s$, the cross-terms related to the perturbations in the plant response matrix, $\mathbf{G}_0^{\mathrm{H}}\Delta\mathbf{G}$ and $\Delta\mathbf{G}^{\mathrm{H}}\mathbf{d}_{s0}$, are significant and, therefore, neglecting them is expected to have a significant effect on the acoustic cloaking performance. The above study has also shown that whilst the $\Delta\mathbf{G}^{\mathrm{H}}\Delta\mathbf{G}$ matrix has strong diagonal components, it is not diagonally dominant and, therefore, approximating it by an identity matrix may be inaccurate.

Although it has been shown that the simplifying assumptions do not hold for the considered forms of structured perturbation, it is still interesting to investigate the control performance when utilising Tikhonov regularisation, as in Equation 3.16, since this has been demonstrated to offer improved robustness in many practical active noise control applications. The following sections will discuss various methods to select the regularisation parameter β, and will present an investigation into its effect on the performance of the active acoustic cloaking system.

3.3 Robustness to Unstructured Perturbations

This section will present an investigation into the effect of unstructured uncertainty on the control strategy described in Chapter 2. The performance of the control system can be evaluated in terms of the cost function defined in Equation 3.6 which can be related to the scattered acoustic power, W_s, as shown in Equation 2.7. This metric has been calculated before and after the implementation of active control, allowing the attenuation in the scattered acoustic power caused by the controller to be quantified. Figure 3.6 shows the attenuation in the scattered acoustic power achieved by the active control system, over a range of frequencies and with increasing values of the regularisation parameter, β. The optimal source strengths have been calculated using Equation 3.16, which assumes that the perturbations are random and uncorrelated and, therefore, lead to Tikhonov regularisation, and the scattered acoustic pressure after control has been calculated using Equation 3.4. For clarity, the

colour bar in Figure 3.6 has been scaled to only show positive levels of attenuation, so that dark blue corresponds to 0 dB attenuation or enhancement in the scattered power. Figure 3.6 shows that, as discussed in Chapter 2, the performance of the controller in the nominal case is unaffected by the amount of regularisation until it reaches approximately $\beta = 10^{-4}$. As the regularisation is increased above this point, the performance decreases and the system can be said to be over-regularised. The effect of over-regularisation can also be seen in the second plot in Figure 3.6, showing the attenuation in the scattered field when the system contains unstructured uncertainty. This plot shows a slight deterioration in the acoustic cloaking performance, when compared to the nominal case, especially at low frequency and when using a small value of regularisation, however when the system containing uncertainty is regularised to approximately $\beta = 10^{-3}$, the performance degradation, when compared to the nominal case, is minimal.

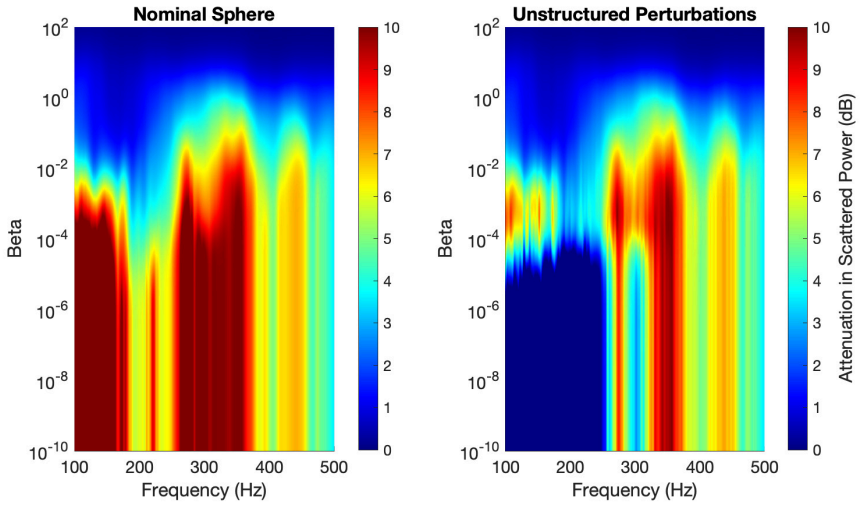

Figure 3.6: Contour plots showing the attenuation that the control system is able to achieve in the scattered sound power over frequency and a range of values of β, for the nominal case and when the system is subject to unstructured uncertainty.

To observe the effect of unstructured uncertainty on the acoustic cloaking performance more clearly, Figure 3.7 shows a plot of the attenuation achieved by the controller in the nominal case, and in the case where the system includes unstructured uncertainty, when regularised with a value of $\beta = 10^{-3}$. For comparison, the nominal performance when the control source strengths have been calculated without regularisation, $\beta = 0$, is also included in Figure 3.12, which shows the level of control that can be achieved by the active acoustic cloaking system when robustness is not considered. It can be seen from Figure 3.7 that, with this value of regularisation, the active control system achieves almost identical results whether the unstructured uncertainty is present in the system responses or not. There is a very slight performance deterioration at low frequencies, but the difference is less than 1 dB and is therefore not considered to be significant. It is interesting to note that, whilst regularising the system with a value of $\beta = 10^{-3}$ almost completely eliminates the effect of the unstructured uncertainty considered in this study, it does result in a significant performance deterioration when compared to the unregularised nominal case where, below approximately 150 Hz, the regularised controller is achieving 10 dB less control than the unregularised controller. This tradeoff should be considered on a case-by-case basis when designing a practical active acoustic cloaking system, and the level of robustness required in the system should be bal-

anced against the reduction in performance in the nominal case.

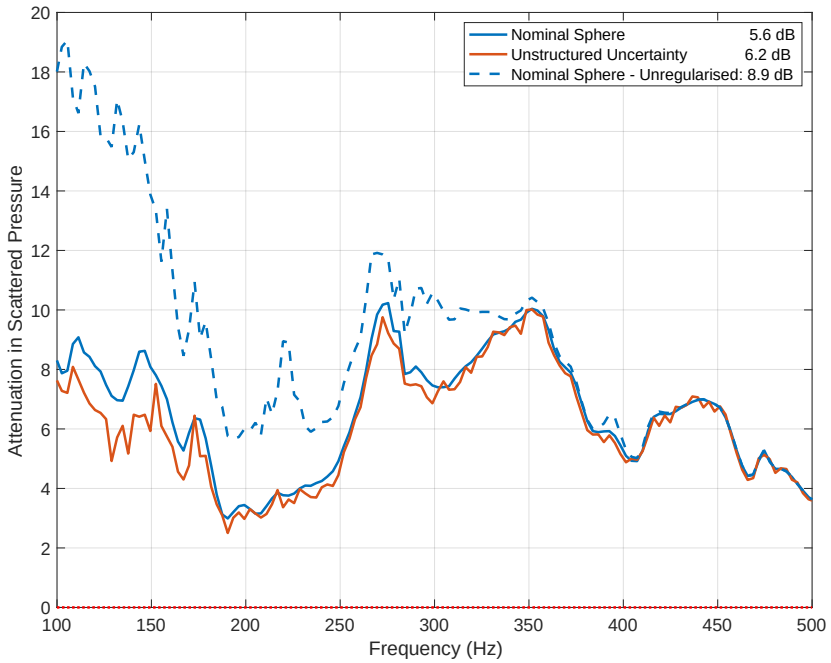

Figure 3.7: A plot showing the level of attenuation in the scattered sound power that the control system is able to achieve when regularised with a value of $\beta = 1 \times 10^{-3}$ in the nominal case, and with unstructured uncertainty. The un-regularised nominal performance is also included as a dashed line for comparison. The frequency averaged attenuation value for each condition is given in the legend

3.4 Robustness to Uncertainty in the Size of the Scattering Object

This section will present an investigation into the effect of uncertainty in the size of the scattering sphere on the control strategy described in Chapter 2, using experimental data. As in the previous study, the attenuation in the scattered acoustic power achieved by the active control system optimised for the nominal sphere size over a range of frequencies and with increasing values of the regularisation parameter, β, has been calculated in the nominal case, and with uncertainty in the size of the scattering sphere. These results are presented in Figure 3.8, showing the attenuation in the scattered field for the nominal sized sphere, the r_+ and r_- spheres respectively. These plots show that uncertainty in the size of the scattering object results in a significantly lower level of acoustic cloaking performance when compared to the nominal case, regardless of the level of regularisation used. The active acoustic cloaking system is still able to achieve a moderate level of attenuation with the small sphere, mainly above 250 Hz, however, in the case of the large sphere, the control system is only able to achieve control over a narrow range of frequencies and is also relatively sensitive to the setting of the regularisation parameter, β. This difference in the acoustic cloaking performance can be explained by the relative magnitudes of the perturbations in the plant response and the disturbance field, $\Delta\mathbf{G}$ and $\Delta\mathbf{d}_s$, for each sphere size, as shown in Figure 3.2.

To show the effect of varying the size of the scattering object more clearly, Figure 3.9 presents

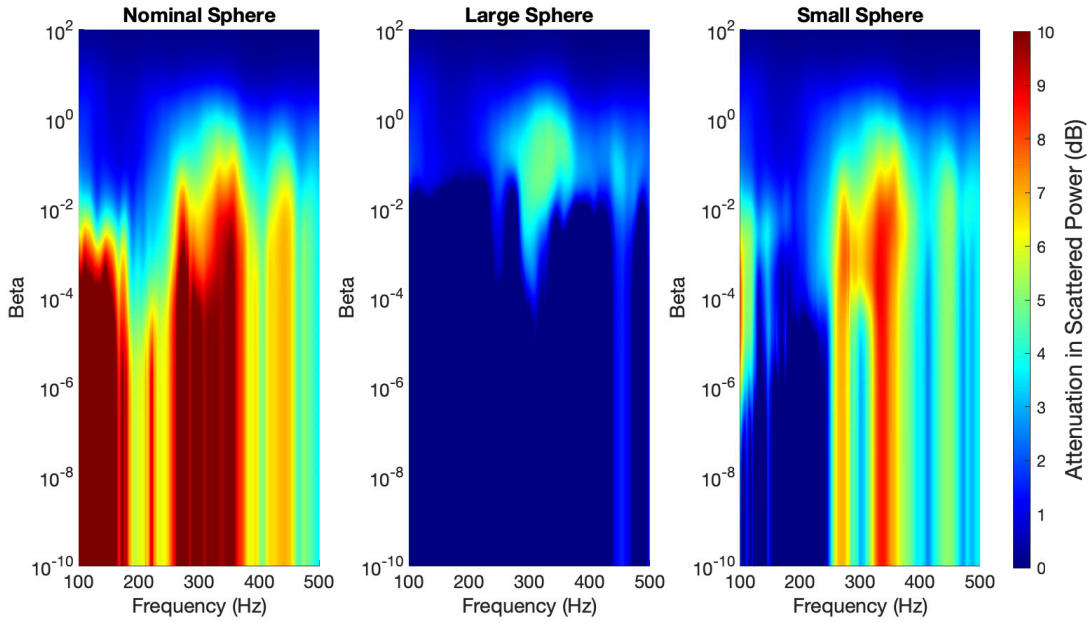

Figure 3.8: Contour plots showing the attenuation that the control system is able to achieve in the scattered sound power over frequency and a range of values of β, for the nominal case and each of the perturbed cases.

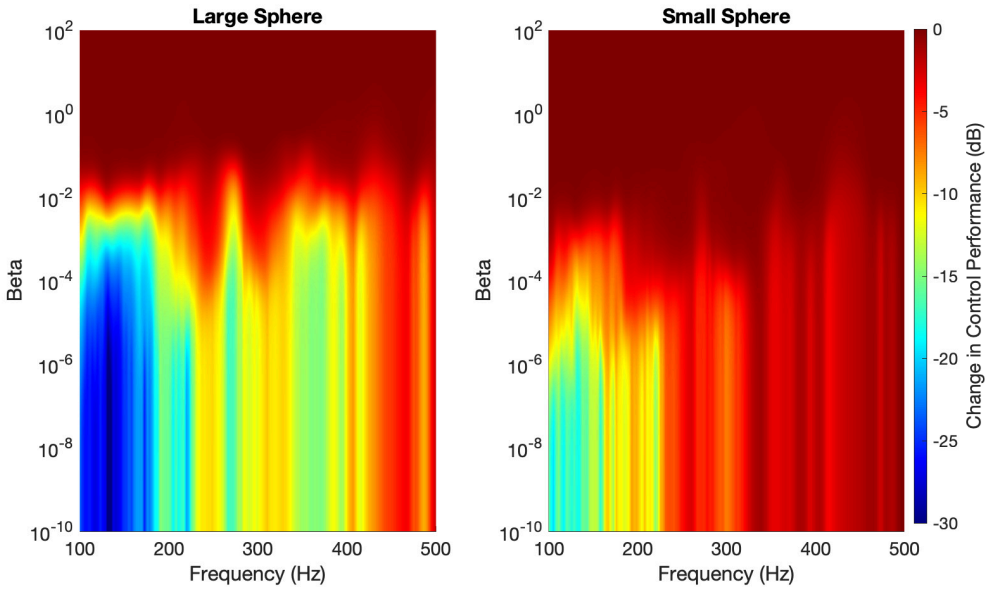

Figure 3.9: Contour plots showing the difference in the attenuation achieved by the nominal control system for each of the perturbed sphere sizes compared with the nominal case, over frequency and a range of values of β.

the deterioration in the acoustic cloaking performance when compared to the nominal case. Figure 3.9 clearly shows that when the control system is not over-regularised, varying the size of the scattering object results in a large deterioration in the acoustic cloaking performance at low frequencies, with a performance degradation of up to 30 dB below approximately 250 Hz in the case of the large sphere. This is less pronounced at higher frequencies, with both spheres showing a performance degradation of less than 10 dB above approximately 400 Hz, but as shown by the nominal performance plot in Figure 3.8, the nominal performance itself decreases at higher frequencies.

The variation in the deterioration of the active cloaking performance over frequency can be directly associated with the condition number of the matrix inversion. As shown in Equation 3.16, the matrix $\mathbf{G}^{\mathrm{H}}\mathbf{G}+\beta\mathbf{I}$ has to be inverted to calculate the optimal source strengths, and if this matrix is poorly conditioned then the resulting performance will be less robust and uncertainties in the system will have a significant effect on the performance. The condition number of the matrix $\mathbf{G}^{\mathrm{H}}\mathbf{G}+\beta\mathbf{I}$ was calculated over a range of frequencies and plotted in Chapter 2, however is repeated for convenience in Figure 3.10. By comparing Figures 3.9 and 3.10 it is clear that the frequencies with the highest condition number are the least robust to changes in the size of the scattering body. Increasing the value of regularisation in Equation 3.16 reduces the condition number and, therefore, increases the robustness, but at the cost of a deterioration in the nominal performance.

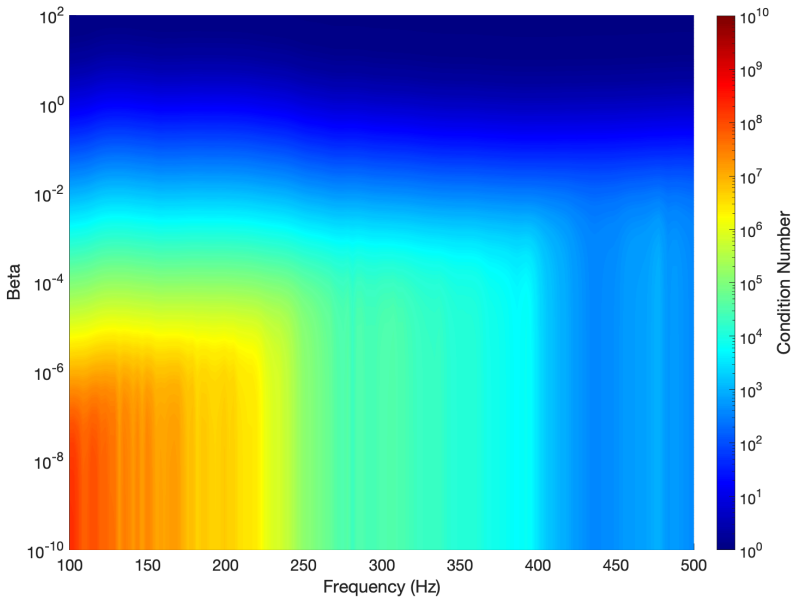

Figure 3.10: Contour plot showing the condition number of the matrix $\mathbf{G}^{\mathrm{H}}\mathbf{G}+\beta\mathbf{I}$ over frequency and a range of values of β.

From the series of results presented above, it is clear that the selection of the regularisation value, β, is highly significant. A high value of β will result in a system that is very robust to changes, but that performs poorly in every case. A control system with a low value of β will achieve significant attenuation in the nominal case but will have poor robustness to any changes in the system responses. To provide further insight into this trade-off, Figure 3.11 shows the frequency averaged attenuation for each sphere size, across a range of regularisation values when the control sources are, again, optimised using the nominal responses.

The average performance across all three sphere sizes is also included as a dashed line for comparison. Figure 3.11 shows that, as shown in Figure 3.8, the control performance remains constant at low values of β for all three cases. The performance in the nominal case starts to noticeably deteriorate as the regularisation is increased above approximately $\beta = 10^{-4}$, however, the plots corresponding to the performance of the largest and smallest spheres show that the performance of the acoustic cloaking system increases with regularisation to reach a maxima at $\beta = 2 \times 10^{-1}$ and $\beta = 3 \times 10^{-3}$ respectively. As regularisation is increased above this point, the performance in all three cases falls to zero as the systems become over-regularised. For the active control system to achieve a robust performance across the range of uncertainties investigated in this paper, the regularisation value corresponding to the peak in the dashed line should be used. However, this level of regularisation has a significant impact on the nominal performance, approximately halving the level of frequency averaged attenuation from 9 dB to just over 4 dB. It is, perhaps, unsurprising that Tikhonov regularisation has less of an effect with the structured perturbations considered here, when compared to the study presented in Section 3.3 which considered unstructured perturbations, as the form of the structured uncertainties do not approximate an identity matrix or zeros, as discussed in Section 3.2. In a practical environment, this tradeoff would have to be evaluated on a case-by-case basis to ascertain how robust the system needs to be, and what the minimum allowable level of nominal performance is.

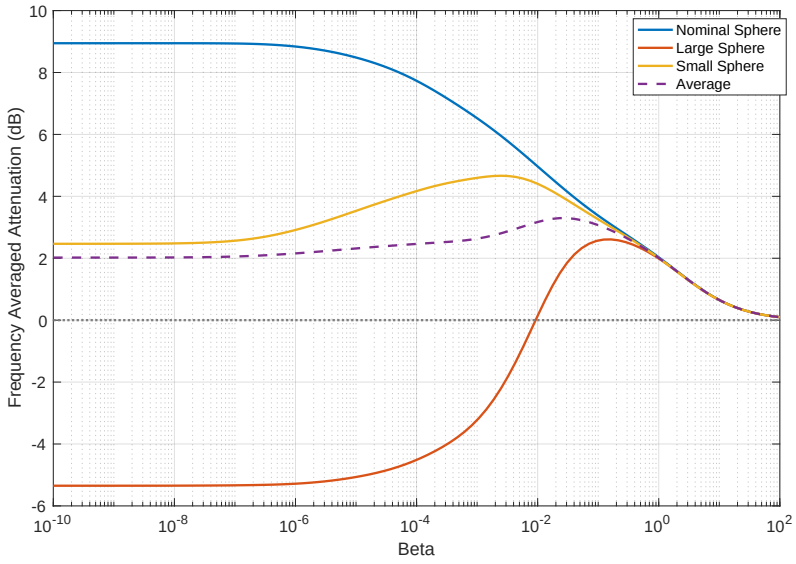

Figure 3.11: A plot showing the frequency averaged attenuation in the scattered sound power that the control system is able to achieve with increasing values of regularisation for the nominal case, and in each of the perturbed cases. The average of these three cases is also included as a dashed line.

According to the results presented in Figure 3.11, a value of $\beta = 2 \times 10^{-2}$ provides the highest level of frequency averaged attenuation on average across all of the perturbation conditions. Using this value of regularisation, the optimal control source strengths for the nominal sphere were calculated according to Equation 3.16, and the resulting control performance for all three sphere sizes was calculated according to Equation 3.4. The resulting control performance is presented over frequency in Figure 3.12. For reference, the acoustic cloaking performance of the unregularised nominal case is also included. It can be seen from the results presented in Figure 3.12 that, with the given level of regularisation, the per-

formance difference between the nominal and small spheres is negligible, with both systems achieving between 2 dB and 8 dB of attenuation over the presented frequency range. The control system is able to achieve limited control of the acoustic scattering from the large sphere at frequencies above 250 Hz, but cannot achieve control below this; instead causing enhancement in the acoustic scattered field. The performance difference between the large and small spheres can be explained by the relative magnitudes of the uncertainty in each case, as shown in Figure 3.2.

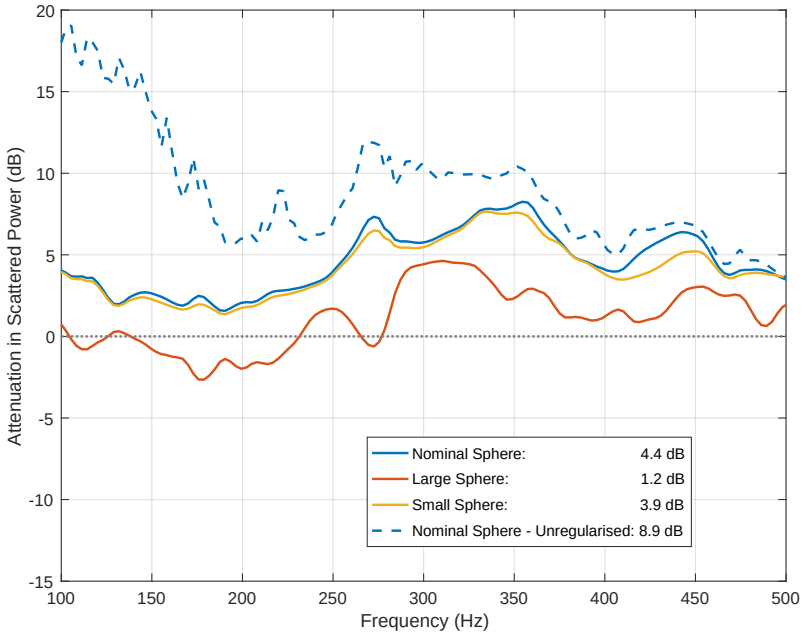

Figure 3.12: A plot showing the level of attenuation in the scattered sound power that the control system is able to achieve when regularised with a value of $\beta = 1 \times 10^{-2}$ in the nominal case, and in each of the perturbed cases. The un-regularised nominal performance is also included as a dashed line for comparison. The frequency averaged attenuation value for each perturbation is given in the legend.

3.4.1 Sensitivity to Perturbations in Either the Plant Response or the Disturbance Field

When active acoustic cloaking is implemented in a practical environment, fluctuations in the environmental conditions will result in variations in both the plant response and the disturbance field and, therefore, the above study has investigated the robustness of the active acoustic cloaking system to uncertainties in both of these parameters, as described in Equations 3.1 and 3.2. In practice, however, it may be possible for the active control system to obtain knowledge of the perturbations in either of these parameters and to adjust the control signals appropriately. Online identification of the acoustic plant response is an active area of research, and various methods have been presented in the literature [67, 68]. If such a method was incorporated into the active acoustic cloaking system described above, then the controller could be updated to account for perturbations in the plant response, reducing $\Delta\mathbf{G}$ in Equation 3.2 and therefore reducing the effects of uncertainty on the acoustic cloaking performance. Similarly, the incorporation of an adaptive algorithm into the active acoustic cloaking system, such as the Filtered-X Least Mean Square (FXLMS) algorithm, could track variations in the disturbance field and therefore reduce the $\Delta\mathbf{d}_s$ term in Equation 3.1. The

following section will develop the study presented above by investigating the robustness of the active acoustic cloaking system when the controller has knowledge of the perturbations in the plant response, the disturbance field, or both.

Using Equation 3.16, the optimal control source strengths have been calculated to minimise the far-field acoustic scattered pressure for four different scenarios:

1. No Knowledge of the perturbations: $\mathbf{G} = \mathbf{G}_0$ $\mathbf{d}_s = \mathbf{d}_{s_0}$
2. Knowledge of perturbations in $\mathbf{G}$: $\mathbf{G} = \mathbf{G}_0 + \Delta\mathbf{G}$ $\mathbf{d}_s = \mathbf{d}_{s_0}$
3. Knowledge of perturbations in $\mathbf{d}_s$: $\mathbf{G} = \mathbf{G}_0$ $\mathbf{d}_s = \mathbf{d}_{s_0} + \Delta\mathbf{d}_s$
4. Knowledge of perturbations in $\mathbf{G}$ and $\mathbf{d}_s$: $\mathbf{G} = \mathbf{G}_0 + \Delta\mathbf{G}$ $\mathbf{d}_s = \mathbf{d}_{s_0} + \Delta\mathbf{d}_s$

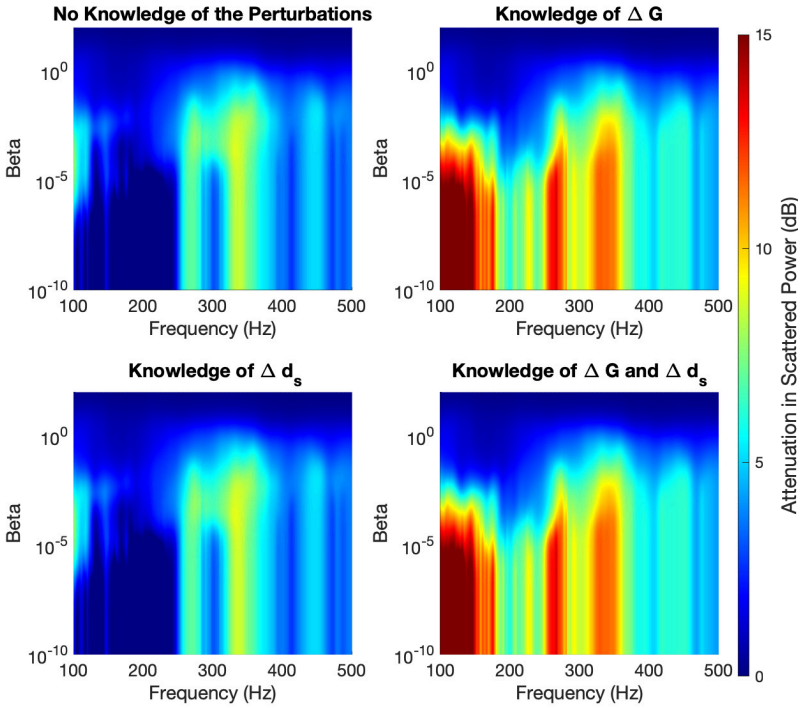

Figure 3.13: Contour plots showing the attenuation that the control system is able to achieve in the scattered sound power over frequency and a range of values of β, when the size of the scattering sphere is reduced and the controller has different levels of knowledge of the perturbations.

The control signals in each case have been calculated over a range of values of β and, for each condition, the scattered acoustic pressure after control has been calculated using Equation 3.5. The resulting levels of attenuation in the scattered acoustic field are plotted in Figure 3.13 when the size of the scattering sphere is reduced to r_-, and in Figure 3.14 when the size of the scattering sphere is increased to r_+. Figures 3.13 and 3.14 both show that knowledge of the perturbations in the disturbance field seem to have minimal effect on the level of acoustic cloaking that can be achieved by the controller, as the acoustic cloaking performance with no knowledge of the perturbations very closely matches the performance when the controller has perfect knowledge of the perturbed disturbance field. In contrast to this, when the controller has perfect knowledge of the plant response, but the perturbations in the disturbance field are not known, the controller is able to achieve comparable levels of acoustic cloaking performance to the unperturbed results presented in Figure 3.8, and in

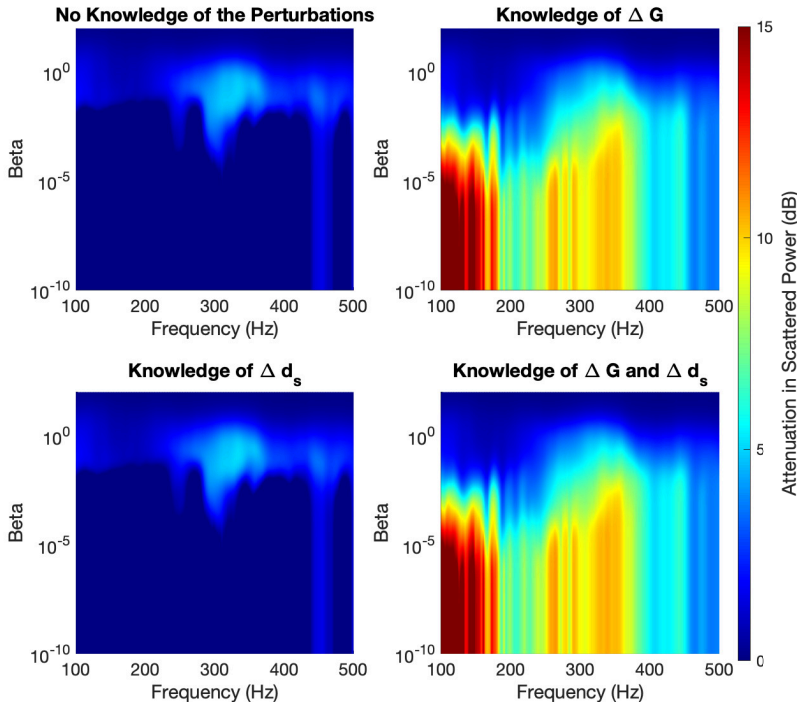

Figure 3.14: Contour plots showing the attenuation that the control system is able to achieve in the scattered sound power over frequency and a range of values of β, when the size of the scattering sphere is increased and the controller has different levels of knowledge of the perturbations.

fact achieves very similar performance to the case shown in Figures 3.13 and 3.14 in which perfect knowledge of both the disturbance and plant response changes is assumed. The level of attenuation presented in Figure 3.13 is higher, across most frequencies and values of β, than the level of attenuation presented in Figure 3.14, which can be attributed to the magnitude of the perturbations in sphere size.

Based on the investigation into the characteristics of the plant and disturbance perturbations presented in Section 3.2, it is unsurprising that the perturbed active acoustic cloaking system with knowledge of $\Delta\mathbf{G}$ achieves significantly higher levels of control than when it has knowledge of $\Delta\mathbf{d}_s$. The results presented in Figure 3.3 show that the plant perturbation terms, $\Delta\mathbf{G}$, in the full solution for optimal source strengths, given by Equation 3.9, are multiple orders of magnitude greater than the disturbance perturbation terms,$\Delta\mathbf{d}_s$, in the same equation. In the present study it is assumed that Equation 3.16 is used to calculate control source strengths with knowledge of the plant perturbations, $\Delta\mathbf{G}$, which is equivalent to using Equation 3.9 and including all of the $\Delta\mathbf{G}$ terms. In this instance, the only source of error in Equation 3.9 is due to assuming that the $\Delta\mathbf{d}_s$ terms are equal to zero, however it has been shown previously that they are relatively small and therefore the error introduced by this assumption is minimal.

In addition to the fact that the plant perturbation terms in Equation 3.9 are significantly greater than the disturbance perturbation terms, they are also included in the required matrix inversion. Nelson and Yoon [69] present a mathematical investigation into the effect of uncertainty on a matrix inversion, and show that the error in the resulting system is equal to the perturbation level multiplied by the condition number of the matrix inversion. As shown in Figure 3.10, the condition number for the system considered in this Chapter reaches 10^{10} at low

frequencies when the regularisation term is small, therefore, a small perturbation in the plant response will result in an error 10^{10} larger than the perturbation. In contrast, uncertainty in the disturbance field does not result in this large multiplier and, therefore, the performance of the control system is far less dependent on perturbations in the disturbance field than it is to perturbations in the plant response.

In a similar process to that presented in Section 3.4, the acoustic cloaking performance presented in Figures 3.13 and 3.14 has been averaged over frequency to show the effect of regularisation on the broadband acoustic cloaking performance, and is presented in Figure 3.15 over a range of values of β. Figure 3.15 supports the observations made above, and shows that the frequency averaged attenuation in the scattered sound power does not change significantly whether the controller has knowledge of the change in the disturbance field or not. When the controller has knowledge of the perturbed plant response, however, the active acoustic cloaking system is able to achieve comparable levels of control to the nominal case.

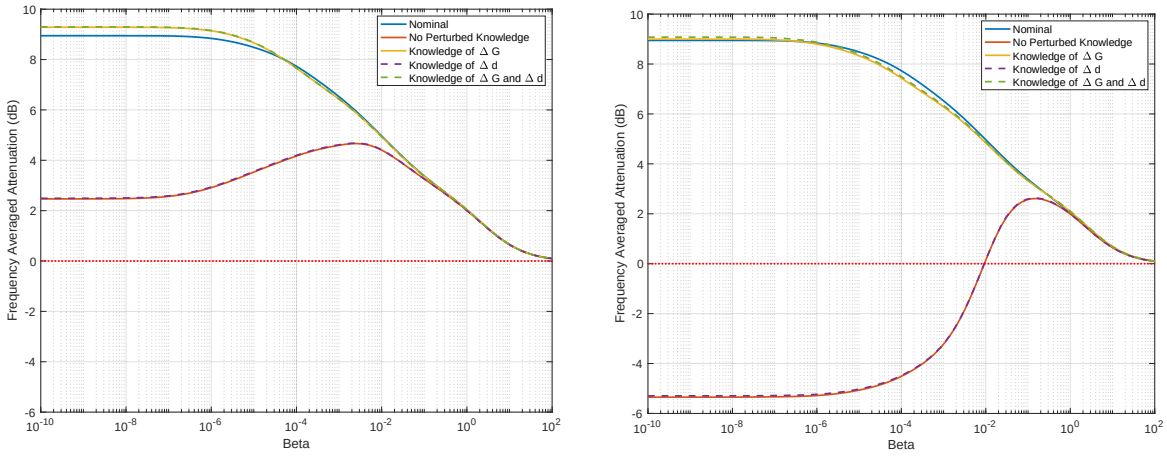

(a) Sphere Radius $= r_-$ *(b) Sphere Radius $= r_+$*

Figure 3.15: A plot showing the frequency averaged attenuation in the scattered sound power that the control system is able to achieve with increasing values of regularisation for the nominal case, and when the size of the scattering sphere is varied and the controller has different levels of knowledge of the perturbations.

3.5 Robustness to Uncertainty in the Position of the Scattering Object

The above study has investigated the robustness of the active acoustic cloaking system to variations in the size of the scattering sphere, however in a practical scenario it is perhaps more likely for the position of the scattering object to vary and, therefore, the following section will present a study into the robustness of the active acoustic cloaking system to changes in the position of the scattering object. As shown in Figure 3.1b, the acoustic plant response and disturbance field have been measured when the r_0 sized scattering sphere is displaced, in the direction of the primary acoustic source, by 10 cm and 20 cm.

As in the previous study, the measured acoustic responses of the sphere in its nominal position, and perturbed by 10 cm and 20 cm, have been used to implement an offline optimal tonal control strategy. The optimal source strengths have been calculated using Equation 3.16, and the scattered acoustic pressure after control has been calculated using Equation 3.5. The attenuation in the scattered acoustic power achieved by the active control system over a range of frequencies and with increasing values of the regularisation parameter, β, is presented in Figure 3.16 for all three sphere positions. The deterioration in the acoustic cloaking performance when compared to the nominal case has also been calculated and plotted, as in the previous study, and is presented in Figure 3.17.

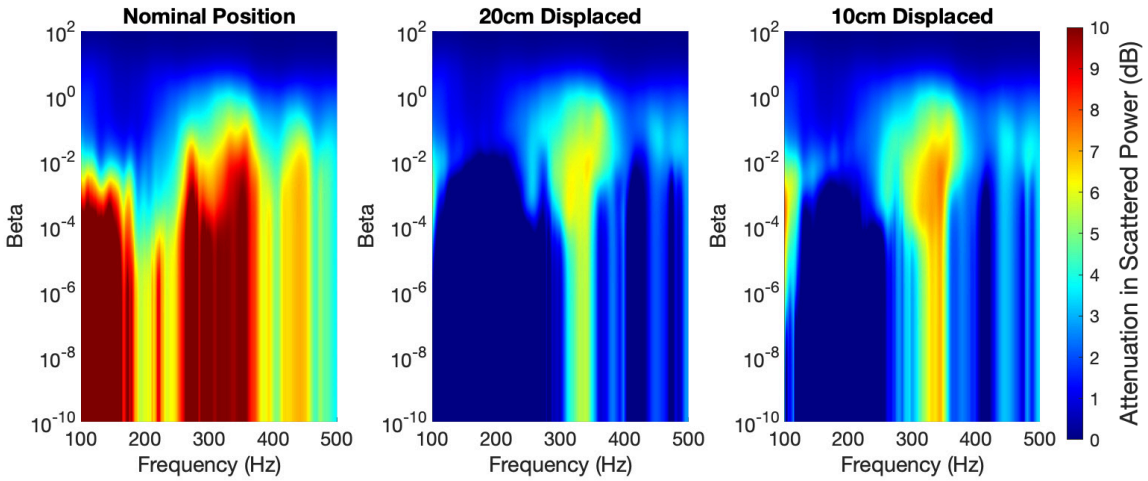

Figure 3.16: Contour plots showing the attenuation that the control system is able to achieve in the scattered sound power over frequency and a range of values of β, for the nominal case and each of the perturbed cases.

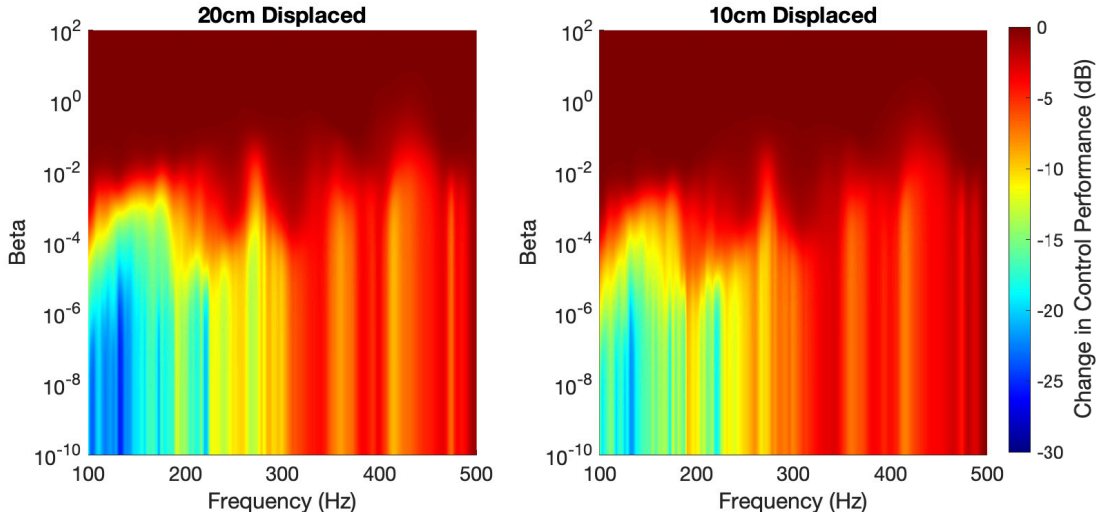

Figure 3.17: Contour plots showing the difference in the attenuation achieved by the nominal control system for each of the perturbed sphere sizes compared with the nominal case, over frequency and a range of values of β.

Figures 3.16 and 3.17 show that, as is the case when changing the size of the scattering object, changing the position of the scattering object causes a significant deterioration in the acoustic cloaking performance, even when the sphere is only perturbed by 10 cm. The largest reduction in the acoustic cloaking performance is at low frequencies and with low values of regularisation, where the perturbations lead to a reduction in performance of up to 30 dB, which can again be explained by the condition number of the acoustic plant response presented in Figure 3.10. All of the results presented in this Chapter show a frequency band centred at approximately 330 Hz at which the active control system achieves a local maxima in the performance. This frequency has a wavelength corresponding to twice the radius of the far-field sensor array.

To provide further insight into the trade-off between nominal performance and robustness, Figure 3.18 presents the frequency averaged attenuation for each perturbation across a range of regularisation values. The average performance across all three cases is also included as a dashed line for comparison. Figure 3.18 shows that, as shown in Figure 3.16, the control performance remains constant at low values of β in every case. As discussed previously, the performance of the nominal sphere starts to noticeably decrease as the regularisation is increased above approximately $\beta = 10^{-5}$, however the acoustic cloaking performance with either of the displaced spheres begins to increase at this same value of β. The control performance with the sphere displaced by 10 cm reaches its maximum of 3.5 dB at approximately $\beta = 1 \times 10^{-2}$, whilst the control performance with the sphere displaced by 20 cm reaches its maximum of 2.8 dB at approximately $\beta = 5 \times 10^{-2}$. As in the previous study, the regularisation value corresponding to the peak in the dashed line, $\beta = 1 \times 10^{-2}$, should be selected to ensure that the active control system is able to achieve a robust performance whilst allowing the scattering object to move by up to 20 cm. However, this level of regularisation has a significant impact on the nominal performance, reducing it by approximately 2 dB. As mentioned in Section 3.4, it is perhaps unsurprising that Tikhonov regularisation does not reduce the effects of uncertainties to the same extent that it did with the unstructured uncertainty, discussed in Section 3.3, as the form of the structured uncertainties investigated in this section do not approximate an identity matrix or zeros, as discussed in Section 3.2. In a practical environment, this tradeoff would have to be evaluated on a case-by-case basis to ascertain how robust the system needs to be, and what the minimum allowable level of nominal performance is.

The performance of the robust active acoustic cloaking system will now be presented over frequency. According to the results presented in Figure 3.18, a value of $\beta = 1 \times 10^{-2}$ has been selected which corresponds to maximising the attenuation averaged across all frequencies and perturbations. The optimal control source strengths for the nominal sphere were calculated according to Equation 3.16, and the resulting control performance for all three sphere positions was calculated according to Equation 3.4. The results are presented over frequency in Figure 3.19. For comparison, the nominal performance when the control source strengths have been calculated with $\beta = 0$ is also included in Figure 3.19, showing the level of control that can be achieved by the active acoustic cloaking system if robustness does not need to be considered. It can be seen from these results that, with the given level of regularisation, the controller is unable to achieve more than 8 dB of attenuation even in the nominal case, and this reduces to 7 dB and 6 dB as the sphere is displaced by 10 cm and 20 cm respectively. However, despite the significant deterioration in nominal performance caused by the level of regularisation used, Figure 3.19 shows relatively consistent results when the sphere

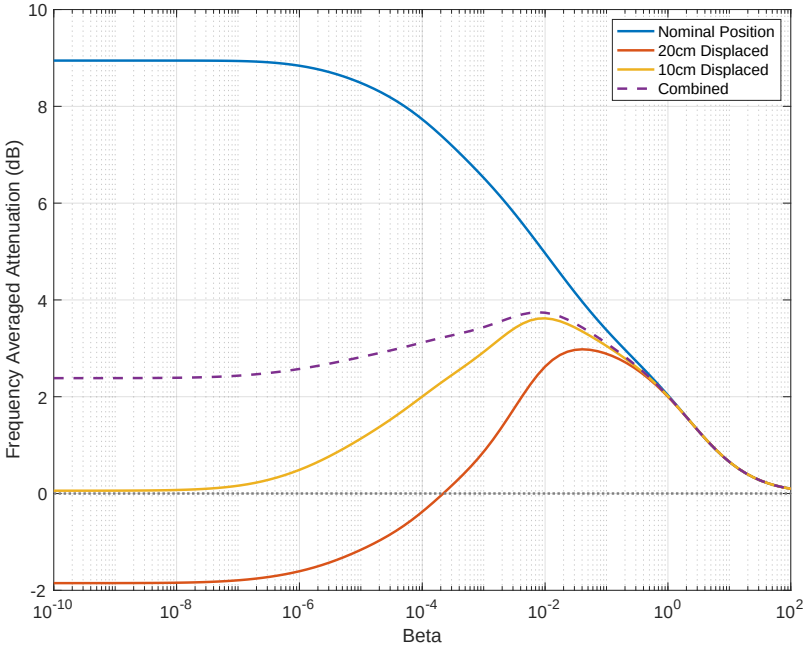

Figure 3.18: A plot showing the frequency averaged attenuation in the scattered sound power that the control system is able to achieve with increasing values of regularisation for the nominal case, and in each of the perturbed cases. The average of these three cases is also included as a dashed line.

is perturbed. When regularised with value of $\beta = 1 \times 10^{-2}$, the acoustic cloaking system is able to attenuate the broadband scattered acoustic power by up to approximately 3 dB, even when the scattering sphere is displaced by 20 cm.

As discussed in Section 3.4.1, the effect of monitoring and tracking the variation in either the plant response or the disturbance field to reduce the effects of uncertainty on the acoustic cloaking performance has been investigated. The conclusions of this study were identical to those presented in Section 3.4.1; that is knowledge of perturbations in the plant response can significantly reduce the effect of uncertainties on the acoustic cloaking performance, whereas knowledge of perturbations in the disturbance field make little difference to the performance. As these results provide no further insight to those presented in Section 3.4.1, and in the interest of succinctness, this study has not been included in the main part of this thesis, however the plots are included in Appendix E.

3.6 Implementation of Frequency Dependent Regularisation to Improve Robustness

A thorough investigation into the robustness of the active acoustic cloaking strategy, presented in Chapter 2, to perturbations in the size and position of the scattering object has been presented in Sections 3.4 and 3.5. It has been shown throughout these studies that a suitable regularisation value is highly important, and allows for a tradeoff between nominal performance and robustness. The study presented above has investigated the effect of frequency independent regularisation on the robustness of the acoustic cloaking system, however, the system may be able to achieve a more favourable tradeoff between nominal per-

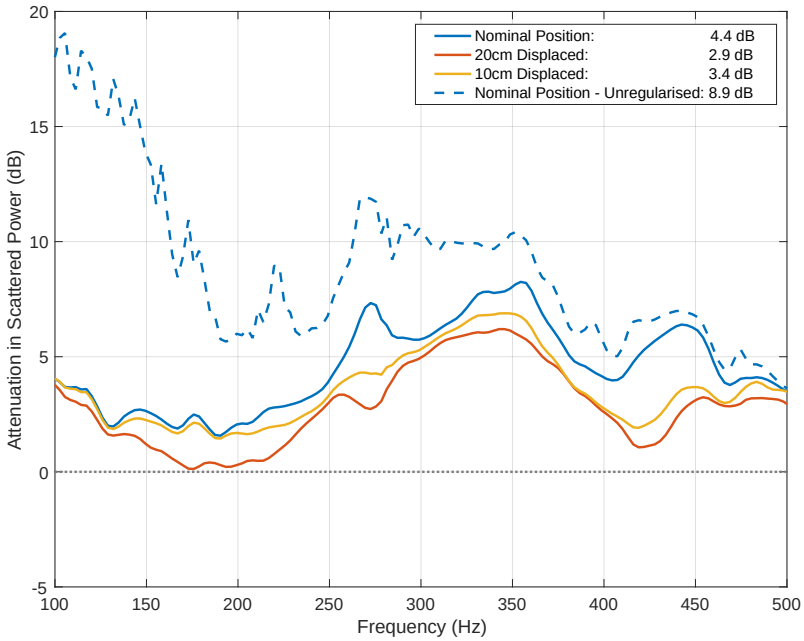

Figure 3.19: A plot showing the level of attenuation in the scattered sound power that the control system is able to achieve when regularised with a value of $\beta = 1 \times 10^{-2}$ in the nominal case, and in each of the perturbed cases. The un-regularised nominal performance is also included as a dashed line for comparison. The frequency averaged attenuation value for each perturbation is given in the legend.

formance and robustness if β was allowed to vary with frequency. This section will present an investigation into the effect of frequency dependent regularisation on the active acoustic cloaking system, and will outline a method of calculating a frequency dependent value of β that maximises robust performance.

Using Figures 3.8 and 3.16, the value of β which achieves the maximum level of attenuation in the scattered sound power for each perturbation condition has been extracted at each frequency and has been plotted in Figure 3.20. The dashed line in Figure 3.20 shows the median regularisation value across all perturbations. The optimal value of β for the nominal case has not been included in Figure 3.20 as the lack of uncertainty means the performance is monotonically increasing as regularisation decreases. Figure 3.20 shows that, as can be seen in the previous plots, the amount of regularisation required depends on the level of perturbation. The largest perturbations, corresponding to the measurements with the r_+ sphere or displacing the r_0 sphere by 20 cm, require significantly higher values of β than the smaller perturbations, regardless of frequency. It can also be seen from Figure 3.20 that the optimal value of regularisation for a given perturbation varies significantly across frequency, with most of the perturbation sets showing a variation of over 10^2 across the bandwidth investigated. This suggests that the implementation of frequency dependent regularisation will provide performance and robustness benefits when compared to frequency independent regularisation. However, it is worth noting that using this method to select the appropriate level of frequency dependent regularisation requires some a priori knowledge of the perturbations, which may not be faesible in practice.

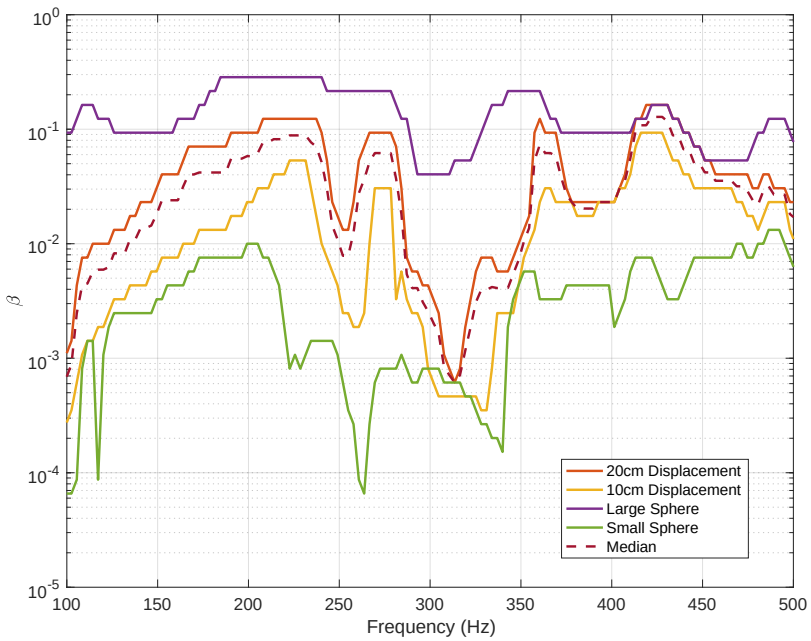

Figure 3.20: A plot showing, for each perturbation, the value of regularisation which achieves the best acoustic cloaking performance across frequency. The dashed line represents the median value of β across all of the perturbation cases.

To observe the effect of frequency dependent regularisation on the acoustic cloaking performance, the attenuation in the scattered sound power has been calculated using the largest frequency dependent regularisation function shown in Figure 3.20, corresponding to the r_+ sphere, the smallest frequency dependent regularisation function shown in Figure 3.20, corresponding to the r_- sphere, and the median frequency dependent regularisation function shown in Figure 3.20. The optimal control source strengths have been calculated in each case according to Equation 3.16, and the acoustic cloaking performance has been calculated according to Equation 3.4. The results are presented over frequency in Figure 3.21, with the frequency averaged attenuation level provided for reference in the caption. As in the previous results, the nominal unregularised performance is also included to demonstrate the performance trade-off required to improve robustness.

It can be seen from the results presented in Figure 3.21a that the use of the median frequency dependent regularisation function provides a more favourable tradeoff between the nominal performance and robustness than achieved by the frequency independent results presented in Figures 3.12 and 3.19. Specifically, the performance with frequency dependent regularisation achieves equal or greater frequency averaged attenuation performance for every perturbation condition when compared to the equivalent frequency independent regularisation cases. Whilst this frequency dependent regularisation function does result in enhancement in the scattered sound power with the r_+ sphere at frequencies below 150 Hz, this is relatively small and the cost is probably outweighed by the performance increase across the rest of the frequency range. Figure 3.21b shows that the largest frequency dependent regularisation function shown in Figure 3.20, corresponding to the r_+ sphere, achieves a high level of consistency across all of the perturbations investigated, with minimal performance deterioration when the system is perturbed. This is achieved at the detriment of the nominal case, however, where the broadband performance is reduced by over 5dB compared to

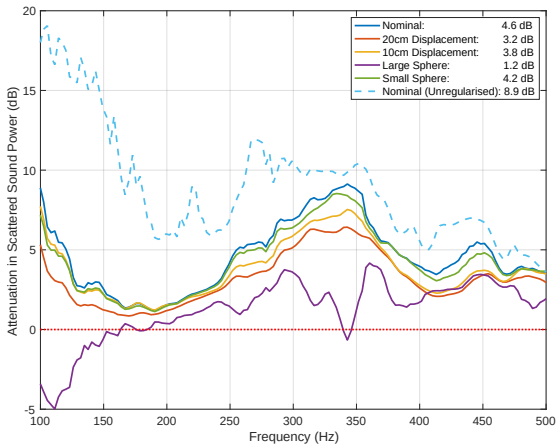

(a) Median Frequency Dependent Regularisation Function

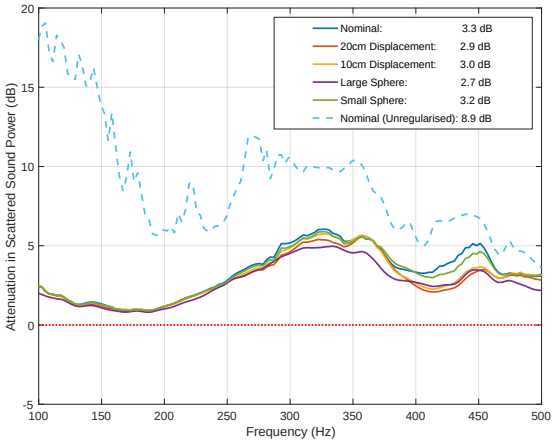

(b) Largest Frequency Dependent Regularisation Function

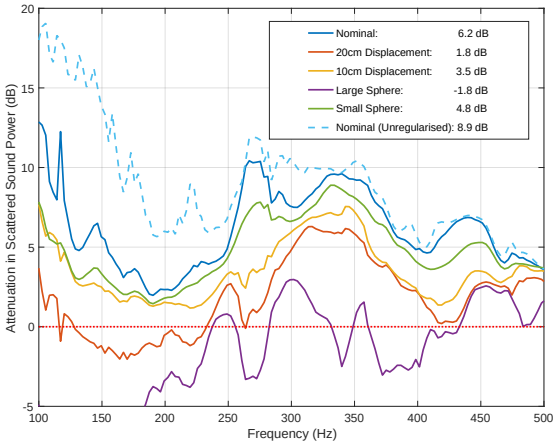

(c) Smallest Frequency Dependent Regularisation Function

Figure 3.21: A series of plots showing the attenuation in the scattered sound power achieved by the acoustic cloaking system for each perturbation, when regularised with different frequency dependent regularisation functions from Figure 3.20. The frequency averaged attenuation value for each perturbation is given in the legend.

the unregularised system. Figure 3.21c presents the acoustic cloaking performance when the controller is regularised using the smallest frequency dependent regularisation function shown in Figure 3.20, corresponding to the r_- sphere which, due to the low level of regularisation, shows a high level of variability in the acoustic cloaking performance when the spheres are perturbed. Whilst the performance with the nominal sphere is comparable to the unregularised case above approximately 250 Hz, minimal performance is achieved with the r_+ sphere which, instead, causes significant enhancement in the scattered sound power across a large portion of the considered frequency range.

The results presented in Figure 3.21 show that the use of frequency dependent regularisation can provide increased robustness with a smaller reduction in nominal performance when compared to the results presented in Section 3.4 using frequency independent regularisation. A number of frequency dependent regularisation functions have been investigated, corresponding to the optimal values of β for each of the perturbation cases, and will henceforth be referred to as *Method 1*. It was found that the median of these optimal values provides a good tradeoff between nominal performance and robustness. An alternative approach to calculating the frequency dependent regularisation function will now be presented. At each frequency and for each value of β, the attenuation in the scattered sound power presented in Figures 3.8 and 3.16 has been averaged across all five perturbation conditions to give a single surface plot corresponding to the performance of the system when exposed to a range of uncertainties, and is presented in Figure 3.22. At each frequency, the value of β that corresponds to the largest average attenuation has been extracted and is plotted as a red line in Figure 3.22. Figure 3.22 shows that, as in Figure 3.20, the value of β changes significantly with frequency, justifying the use of frequency dependent regularisation. The red trace in Figure 3.22 shows that the frequency dependent regularisation function calculated using this method, *Method 2*, follows a noticeably different shape to the frequency dependent regularisation functions shown in Figure 3.20, which were calculated according to *Method 1*.

To observe the performance of the frequency dependent regularisation function calculated according to *Method 2*, the optimal control source strengths have been calculated using Equation 3.16 with the regularisation function shown in Figure 3.22. The acoustic cloaking performance has been calculated according to Equation 3.4, and is presented over frequency in Figure 3.23. As in the previous results, the performance of the nominal sphere when it is unregularised is included for reference, and the frequency averaged attenuation values for each perturbation case are included in the legend. It can be seen that the performance of the acoustic cloaking system using frequency dependent regularisation calculated according to *Method 2* is similar to the acoustic cloaking performance achieved using the median frequency dependent regularisation function. To enable a clearer comparison between these two regularisation methods, and to benchmark their performance against the other regularisation methods, the frequency averaged attenuation values for every regularisation method and perturbation are presented in Table 3.1. It can be seen that the performance of the frequency dependent regularisation function calculated according to *Method 2* is very similar to the performance achieved using the median frequency dependent regularisation function calculated according to *Method 1*, with both methods achieving performance within 0.2 dB of one another across all of the perturbation conditions. When compared to the frequency independent regularisation value of $\beta = 10^{-2}$, both of the frequency dependent methods achieve superior performance under every perturbation condition. The average frequency averaged attenuation across all perturbation conditions has also been calculated and included in Table

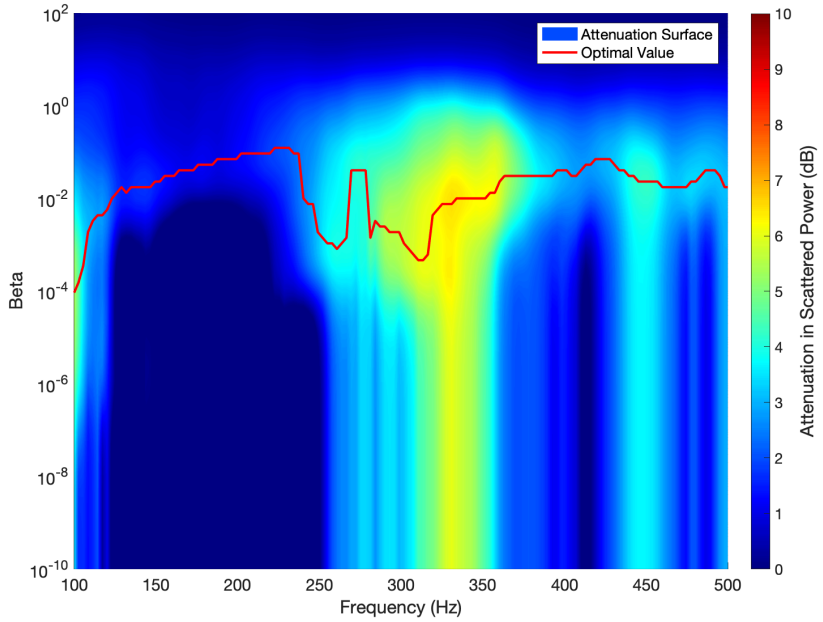

Figure 3.22: A contour plot showing the attenuation that the control system is able to achieve in the scattered sound power over frequency and a range of values of β, averaged across all five perturbation conditions. The red line depicts the value of β at each frequency which achieves the largest average attenuation.

3.1 and this shows that, to maintain robustness across all five of the perturbation conditions investigated in this chapter whilst maximising the acoustic cloaking performance in each case, frequency dependent regularisation should be used, calculated using *Method 2*. With the exception of the unregularised nominal case, this method achieves similar or greater levels of control to every other regularisation method investigated and, as shown in Figure 3.23, only results in significant enhancement of the scattered sound power below approximately 120 Hz. It is worth noting that choosing this regularisation method for a practical system would require the perturbations to be investigated in advance.

Perturbation	$\beta = 0$	$\beta = 10^{-2}$	**Median FDR 1**	**Large FDR 1**	**Small FDR 1**	**FDR 2**
Nominal	**8.9**	4.4	4.6	3.3	6.2	4.8
r_+ Sphere	-5.3	1.2	1.2	**2.7**	-1.8	1.2
r_- Sphere	2.5	3.9	4.2	3.2	**4.8**	4.3
20cm Displaced	-1.9	2.9	**3.2**	2.9	1.8	3.1
10cm Displaced	0.1	3.4	**3.8**	3.0	3.5	**3.8**
Average	0.86	3.16	3.40	3.02	2.90	**3.44**

Table 3.1: A table showing a summary of the broadband average attenuation values (in dB) for each regularisation and perturbation case.

3.7 Conclusions

This Chapter has presented a thorough investigation into the effects of uncertainty on active acoustic cloaking. An array of acoustic control sources was used to minimise the scattered acoustic pressure at a far-field microphone array using an optimal harmonic control formulation. Using this configuration it has been shown that between 5 dB and 19 dB of attenuation

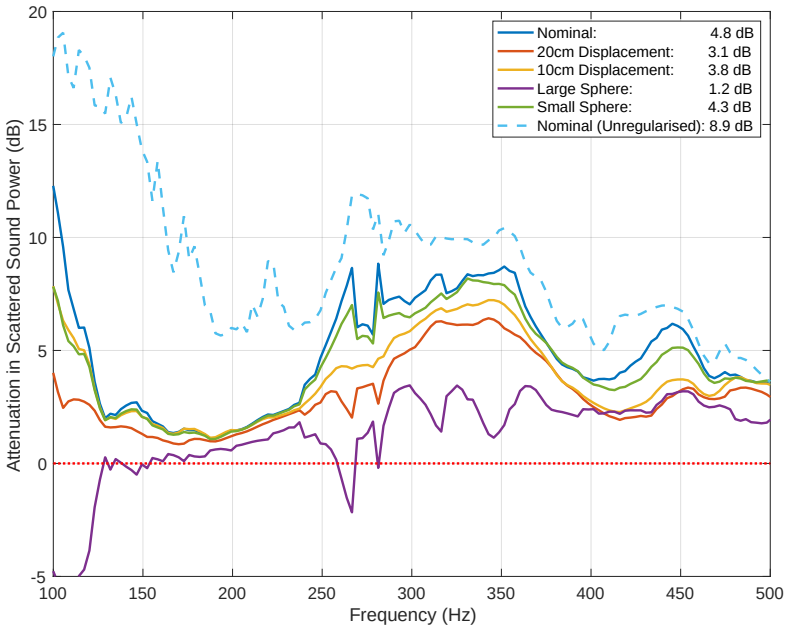

Figure 3.23: A plot showing the attenuation in scattered sound power achieved by the acoustic cloaking system for each perturbation, when regularised with the frequency dependent regularisation function shown in Figure 3.22. The frequency averaged attenuation value for each perturbation is given in the legend.

in the far-field scattered acoustic power can be achieved across the bandwidth investigated when there is no uncertainty in the system. The formulation for optimal source strengths in the presence of uncertainty has been derived, and compared to the regularised formulation for the source strengths in the nominal case. It has been shown that, if the perturbations are random and uncorrelated with one another, the cross-terms in the full formulation can be neglected and the $\Delta\mathbf{G}^{\mathrm{H}}\Delta\mathbf{G}$ term can be approximated by a scaled identity matrix. These assumptions have been thoroughly investigated, and it has been shown that they are valid in the case of random unstructured uncertainty, however they are not valid for the specific structured perturbations considered in this study. In spite of this, the regularised formulation for the source strengths in the nominal case has been shown to be sufficient to provide a robust solution to random unstructured uncertainty, to uncertainty in the size of the scattering object, and to uncertainty in the position of the scattering object.

It was shown that the performance decrease due to uncertainty in the system was greatest when the plant response matrix was poorly conditioned, which is most significant at low frequencies, and the importance of choosing an appropriate value of regularisation was shown. When regularised to maximise the robustness of the system, the difference between the nominal and small spheres, a reduction in radius of 26%, resulted in minimal performance degradation, whereas the difference between the nominal and the large sphere, an increase in radius of 66%, caused significant performance degradation. Similarly, when appropriately regularised, perturbing the sphere by 10 cm or 20 cm results in only a small degradation when compared to the nominal performance, however, this level of regularisation significantly reduces the nominal performance by 3 dB when compared to the unregularised case.

The importance of tracking any variation in the acoustic plant response was demonstrated,

and it was shown that uncertainty in the plant response resulted in significantly higher deterioration in the acoustic cloaking performance than uncertainty in the disturbance field. This has been explained in terms of the relative magnitudes of $\Delta\mathbf{G}$ and $\Delta\mathbf{d}_s$ and by considering the fact that the plant response needs to be inverted, which is not the case for the disturbance field. The effect of frequency dependent regularisation was investigated, and it was shown that using a frequency dependent regularisation method can significantly improve the tradeoff between nominal performance and robustness, and multiple methods of calculating the frequency dependent values of β have been presented and compared.

This chapter has made use of an optimal harmonic control strategy and it was assumed that the scattered acoustic pressure could be directly measured at the far-field microphone array. In practice this is not possible and, therefore, additional signal-processing steps will be required to obtain a disturbance signal in real-time. A potential method to achieve this is presented in Chapter 5. The optimal harmonic controller used in this chapter neglects the real-world implementation challenges of causality and obtaining a suitable reference signal, both of which are discussed in Chapters 4 and 7, and the use of a rigid scattering object removes the additional complexities of resonant scattering which will be discussed further in Chapters 6 and 7.

Chapter 4

A Broadband Time Domain Active Acoustic Cloaking System, Applied to a Rigid Sphere

The previous chapters have presented investigations into the effect of active acoustic cloaking on the scattered acoustic field from a rigid sphere, and have discussed the robustness of such a system to perturbations. All of the previous chapters have used an optimal harmonic control strategy which assumes that the disturbance is tonal and, therefore, the selection of a reference signal and the practical constraint of causality can both be neglected. It is beneficial to consider this control strategy as it allows the performance of an active control system to be assessed in the best-case scenario, however, a tonal control architecture will not be suitable for a practical application in which the disturbance is non-tonal.

This chapter will present an investigation into the use of a broadband time-domain active control strategy, and the performance will be assessed using the data measured with the experimental setup presented in Chapter 2, which utilises the rigid spherical scatterer. The broadband optimal control problem will be formulated in the time-domain in Section 4.1. The level of acoustic cloaking that can be achieved by the controller, for the considered experimental system, will then be assessed in Section 4.2. The choice of reference signal and the effect of varying the number of taps in the control filter will be discussed, and finally a brief investigation into the robustness of the system to perturbations in the position of the scattering object will be presented.

4.1 Formulation of the Optimal Broadband Controller

This section will present a formulation of the optimal controller, which will lead to the derivation of the corresponding optimal control filters that will minimise the broadband acoustic scattered power. In practice, when anything but tonal disturbance signals are being considered, it is necessary to constrain the control filters to be causal and the optimal filter responses in this case can be derived in the time-domain, as described in [37] for the standard feedforward active noise control system. To this end, the scattered acoustic pressure measured at the l-th error microphone after control can be expressed at the n-th time step as

$$e_{s_l}(n) = d_{s_l}(n) + \sum_{m=1}^{M}\sum_{j=0}^{J-1}\sum_{k=1}^{K}\sum_{i=0}^{I-1} g_{lmj} w_{mki} x_k(n-i-j), \tag{4.1}$$

where $d_{s_l}(n)$ is the scattered pressure at the l-th error sensor due to the primary disturbance, g_{lmj} is the j-th coefficient of the J-th order FIR filter approximating the plant response between the m-th control source and the l-th error sensor, w_{mki} is the i-th coefficient of the I-th order FIR control filter corresponding to the m-th control source and the k-th reference signal, and x_k is the k-th reference signal. By assuming the controller is time invariant, Equation 4.1 can be rewritten as

$$e_{s_l}(n) = d_{s_l}(n) + \sum_{m=1}^{M}\sum_{k=1}^{K}\sum_{i=0}^{I-1} w_{mki} r_{lmk}(n-i), \tag{4.2}$$

where r_{lmk} is the k-th reference signal filtered by the plant response between the m-th control source and the l-th error microphone. The filtered reference signal can be expressed as

$$r_{lmk}(n) = \sum_{j=0}^{J-1} g_{lmj} x_k(n-j). \tag{4.3}$$

For convenience, Equation 4.2 can be expressed in vector form as

$$e_{s_l}(n) = d_{s_l}(n) + \sum_{i=0}^{l-1} \mathbf{w}_i^{\mathrm{T}} \mathbf{r}_l(n-i), \tag{4.4}$$

where $\mathbf{w}_i$ and $\mathbf{r}_l(n)$ are defined as

$$\mathbf{w}_i = [w_{11i}, w_{12i}, \ldots, w_{1Ki}, w_{21i}, \ldots w_{MKi}]^{\mathrm{T}} \tag{4.5}$$

$$\mathbf{r}_l(n) = [r_{l11}(n), r_{l12}(n), \ldots, r_{l1K}(n), r_{l21}(n), \ldots, r_{lMK}(n)]^{\mathrm{T}}. \tag{4.6}$$

The multichannel control problem can then be formulated by expressing the vector of L error signals in the time domain as

$$\mathbf{e}_s(n) = \mathbf{d}_s(n) + \mathbf{R}(n)\mathbf{w}, \tag{4.7}$$

where

$$\mathbf{e}_s(n) = [e_{s_1}(n), \ldots, e_{s_L}(n)]^{\mathrm{T}}, \tag{4.8}$$

$$\mathbf{d}_s(n) = [d_{s_l}(n), \ldots, d_{s_L}(n)]^{\mathrm{T}}, \tag{4.9}$$

$$\mathbf{R}(n) = \begin{bmatrix} \mathbf{r}_1(n)^{\mathrm{T}} & \mathbf{r}_1(n-1)^{\mathrm{T}} & \dots & \mathbf{r}_1(n-I+1)^{\mathrm{T}} \\ \mathbf{r}_2(n)^{\mathrm{T}} & \mathbf{r}_2(n-1)^{\mathrm{T}} & \dots & \mathbf{r}_2(n-I+1)^{\mathrm{T}} \\ \vdots & \vdots & & \vdots \\ \mathbf{r}_L(n)^{\mathrm{T}} & \mathbf{r}_L(n-1)^{\mathrm{T}} & \dots & \mathbf{r}_L(n-I+1)^{\mathrm{T}} \end{bmatrix}, \tag{4.10}$$

and the MKI vector of control filter coefficients is defined as

$$\mathbf{w} = \left[\mathbf{w}_0^{\mathrm{T}}, \mathbf{w}_1^{\mathrm{T}} \dots \mathbf{w}_{I-1}^{\mathrm{T}}\right]. \tag{4.11}$$

As stated in the previous Chapters, the cost function, in the context of acoustic cloaking, is defined as

$$J = \mathrm{E}\left[\mathbf{e}_s(n)^{\mathrm{H}}\mathbf{e}_s(n) + \beta\mathbf{w}^H\mathbf{w}\right], \tag{4.12}$$

where β is a positive real effort-weighting parameter to constrain the magnitude of the source strengths. Substituting Equation 4.7 into Equation 4.12 gives the quadratic cost function as

$$J = \mathbf{w}^{\mathrm{T}}\mathrm{E}\left[\mathbf{R}^{\mathrm{T}}(n)\mathbf{R}(n) + \beta\mathbf{w}^H\mathbf{w}\right]\mathbf{w} + 2\mathbf{w}^{\mathrm{T}}\mathrm{E}\left[\mathbf{R}^{\mathrm{T}}(n)\mathbf{d}_s(n)\right] + \mathrm{E}\left[\mathbf{d}_s^{\mathrm{T}}(n)\mathbf{d}_s(n)\right]. \tag{4.13}$$

Assuming that $\mathrm{E}\left[\mathbf{R}^{\mathrm{T}}(n)\mathbf{R}(n)\right]$ is positive definite, this cost function has a unique global minimum and the optimal set of control filters that minimises the scattered acoustic field at the error sensors is given as

$$\mathbf{w}_{opt} = -\left[\mathrm{E}\left[\mathbf{R}^{\mathrm{T}}(n)\mathbf{R}(n) + \beta\mathbf{I}\right]\right]^{-1}\mathrm{E}\left[\mathbf{R}^{\mathrm{T}}(n)\mathbf{d}_s(n)\right]. \tag{4.14}$$

Tikhonov regularisation has been included into Equation 4.14 to introduce a constraint on the control effort and to improve the conditioning of the matrix inversion, via the regularisation parameter β.

4.2 Acoustic Cloaking Performance

The performance of the broadband active acoustic cloaking control system described in the previous section will be investigated using the measurement responses corresponding to the system described in detail in Chapter 2. In summary, the scattered acoustic pressure from a rigid sphere has been measured at a far-field microphone array, as shown in Figures 4.1 and 4.3, and forms the vector of disturbance signals, $\mathbf{d}_s$. The matrix of transfer responses between 32 acoustic control sources and the far-field microphone array has also been measured, and forms the matrix of plant responses $\mathbf{G}$. In the following section, this measurement data will be used to investigate the acoustic cloaking performance that can be achieved by the causally constrained, broadband controller described in Section 4.1. The selection of a suitable reference signal will be discussed, the effect of varying the length of the control filters will be presented, and the robustness of the system to perturbations in the position of the scattering object will investigated.

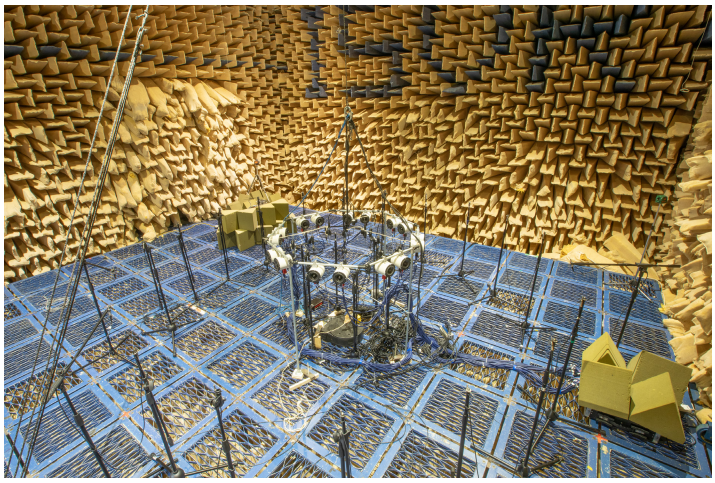

Figure 4.1: A photograph of the experimental setup, showing the microphone and loudspeaker arrays arranged in the anechoic chamber.

4.2.1 Effect of Reference Signal Selection

The performance of a broadband causally constrained control system is dependent on the availability of a suitable reference signal. In general, the reference signal(s) should be coherent with, and time-advanced compared to, the error signal(s). In the case of the measurement setup described in Chapter 2, the drive signal for the loudspeaker generating the primary disturbance can be utilised as the reference signal. By definition, this will be time advanced compared to, and coherent with, the scattered acoustic pressure and, therefore, this can be considered a perfect reference signal. It should be noted that whilst it will often be infeasible to obtain the signal driving the incident field in a real-world practical system, doing so in the present study will provide insight into the level of attenuation that can be achieved by the controller in ideal conditions.

The vector of measured disturbance signals, $\mathbf{d}_s$, and the matrix of measured plant responses, $\mathbf{G}$, have been used to calculate optimal control filters over a range of regularisation values according to Equation 4.14, with a filter length of $I = 512$, and using the perfect reference signal described above. The effect of varying the filter length will be investigated in more detail in Section 4.2.2. The resulting levels of attenuation achieved by the controller are presented in Figure 4.2, which can be directly compared to the equivalent plot for the tonal controller presented in Figure 2.7. As with the previous results, the colour axis has been limited to only show positive values of attenuation. It can be seen by comparing Figures 4.2 and 2.7 that the performance of the optimal causally constrained broadband controller is significantly poorer than the performance of the optimal harmonic controller discussed in Chapter 2. At low frequencies, and with low values of regularisation, the controller is unable to achieve control and actually results in a significant enhancement in the acoustic scattering. This is likely due to the matrix of plant responses being ill-conditioned, as shown in Figure 2.8, and therefore prone to numerical inaccuracies. Figure 4.2 shows a clear sweet-spot in the regularisation at approximately $\beta = 1 \times 10^{-7}$ where the control performance reaches a maxima. With this value of regularisation, the controller is able to achieve between 3 dB and 15 dB of attenuation in the scattered acoustic field across the investigated frequency range.

The results presented in figure 4.2 provide insight into the level of acoustic cloaking per-

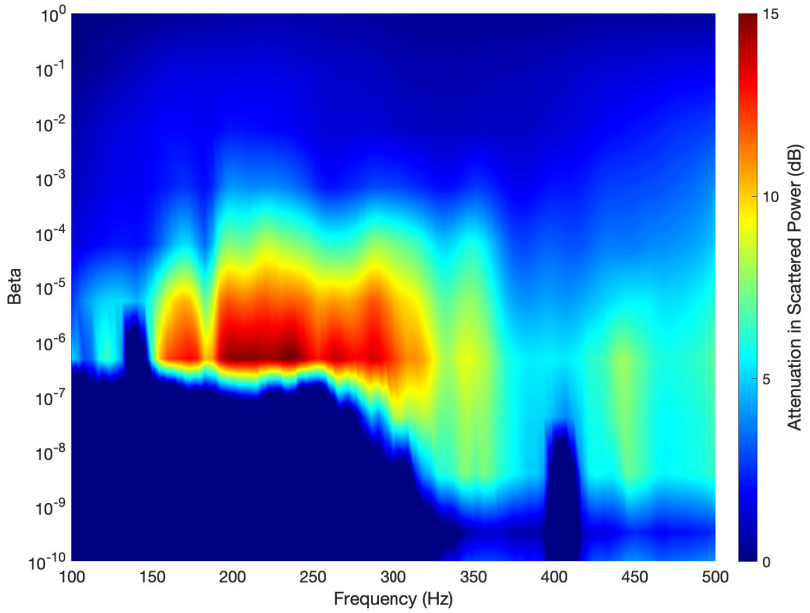

Figure 4.2: A Contour plot showing the attenuation that the broadband, causally constrained control system is able to achieve in the scattered sound power over frequency and a range of values of β when using a perfect reference signal and a control filter length of $I = 512$.

formance that can be achieved when a perfect reference signal is available. However, as discussed previously, this reference signal is unlikely to be available in a practical sytem implementation as, in the case of active cloaking, the primary source generating the incident pressure field is often unknown and, therefore, cannot be accessed to provide a reference signal. Therefore, the following analysis will investigate the performance of the acoustic cloaking system using a reference signal that is potentially accessible in a greater variety of applications. There are three obvious candidate signals for this: the incident acoustic pressure, the scattered acoustic pressure, or the total acoustic pressure. The latter two of these signals will both be affected by the control sources, and to use them in a practical setup would therefore require a control architecture including a secondary path cancellation loop, which the former would not require. As has been thoroughly discussed in previous chapters, it is not straightforward to directly measure the scattered acoustic pressure and, therefore, utilising this as a reference signal would also require additional signal processing steps. For these reasons, the incident acoustic pressure field has been selected as the reference signal for the following analysis.

Figure 4.3 shows the geometry of the measurement setup previously discussed in Chapter 2. It can be seen from Figure 4.3 that the sensor directly in front of the incident disturbance has been selected as the reference sensor, as this provides the largest time-advance relative to the error signal and, therefore, the incident acoustic pressure measured at this sensor will be used as the reference signal. It should be noted that in a practical implementation the Direction of Arrival (DOA) of the incident field may not be known. In this case, multiple reference sensors could be used [70] to ensure that at least one remains time-advanced compared to the disturbance, or a DOA estimation technique could be used, however, neither of these additional challenges will be considered in the following study.

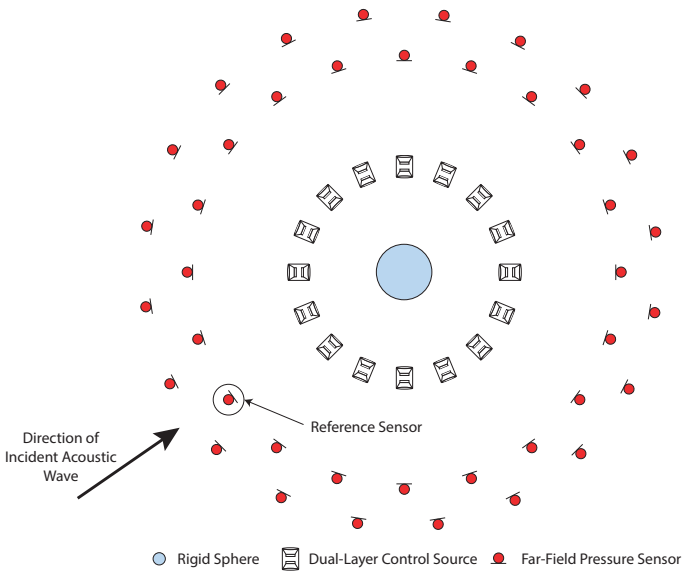

Figure 4.3: Schematic diagram showing the source/sensor arrangement and the scattering sphere, with the position of the reference sensor marked.

As with the results presented in Figure 4.2, Equation 4.14 has been used to calculate optimal control filters over a range of regularisation values, with a filter length of $I = 512$, and using the incident pressure measured directly in front of the primary disturbance as the reference signal. The attenuation achieved by the controller is presented in Figure 4.4 and, as with the previous results, the colour axis has been limited to only show positive values of attenuation. Figure 4.4 shows a broadly similar trend to the results presented in Figure 4.2. The attenuation that can be achieved is slightly reduced relative to the results using a perfect reference signal, especially above approximately 325 Hz and with smaller values of regularisation where the controller using the practical reference signal is unable to achieve control. As with the results presented in Figure 4.2, the active control system is unable to achieve control at low frequencies and with low values of regularisation, however both sets of results show an optimal value of regularisation of approximately $\beta = 1 \times 10^{-7}$ where the control performance reaches a maxima.

To enable a clearer comparison of the acoustic cloaking performance between the two reference signals, the attenuation performance using each signal, when regularised with a value of $\beta = 1 \times 10^{-7}$, has been plotted over frequency in Figure 4.5. Figure 4.5 shows that the overall spectral shape of the attenuation is similar when using either a perfect reference signal or the incident pressure measured in front of the primary disturbance, however the latter achieves between 1 dB and 2 dB less than the former across the majority of the frequency range. There is a notch in the acoustic cloaking performance when using the perfect reference signal, at approximately 130 Hz which corresponds to a wavelength of approximately 2.6 m. The distance between the loudspeaker generating the incident field and the surface of the scattering sphere is 2.6 m and, therefore, this notch in performance is likely to be due to the formation of standing waves in the experimental setup.

The results presented in Figures 4.2, 4.4 and 4.5 provide insight into the effect of the refer-

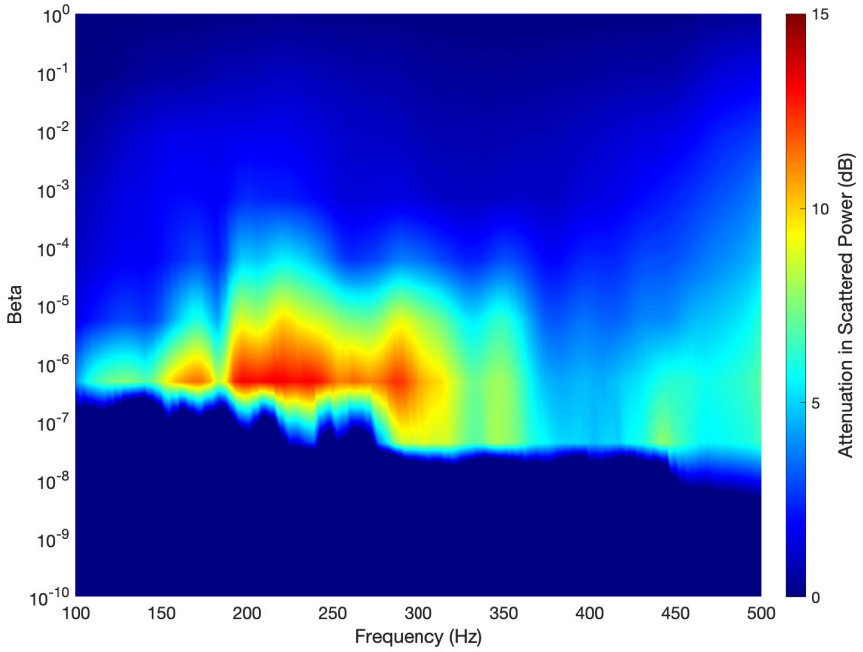

Figure 4.4: A Contour plot showing the attenuation that the broadband, causally constrained control system is able to achieve in the scattered sound power over frequency and a range of values of β when using the incident pressure measured in front of the primary loudspeaker as a reference signal and a control filter length of $I = 512$.

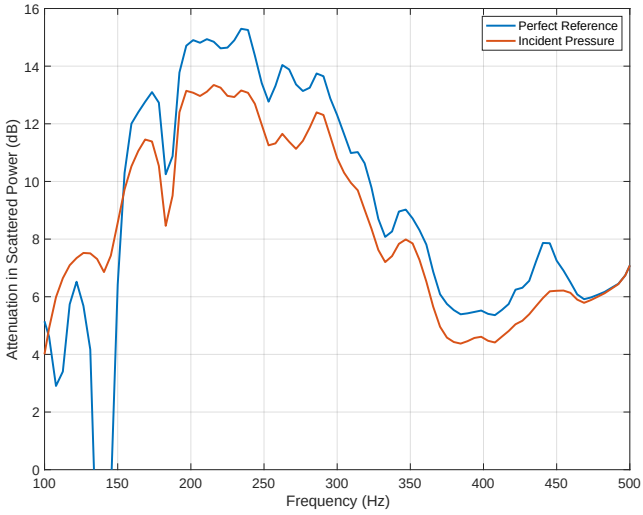

Figure 4.5: A plot showing the attenuation that the broadband, causally constrained control system is able to achieve in the scattered sound power over frequency when using a regularisation value of $\beta = 1 \times 10^{-7}$ and a control filter length of $I = 512$ for both reference signals.

ence signal on the control performance. The performance of a broadband control system is also heavily dependent on ensuring that the control filters are of a suitable length to capture sufficient information about the system. This requirement will be investigated in the following section.

4.2.2 Effect of Control Filter Length

The following section will investigate how the performance of the acoustic cloaking system is related to the length of the control filters. The length of the control filters is a key parameter to investigate when designing broadband control systems as it allows for a trade-off between computational load and control performance and, therefore, it is of interest to investigate how the acoustic cloaking performance of the proposed system varies with different lengths of control filters.

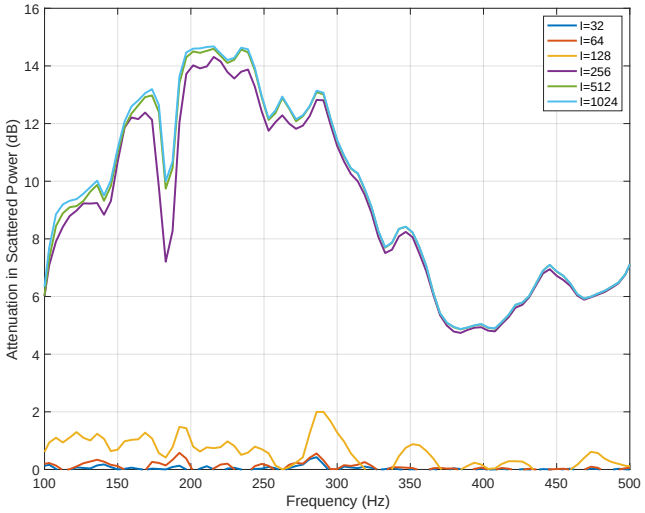

Figure 4.6: A plot showing the attenuation that the broadband, causally constrained control system is able to achieve in the scattered sound power over frequency, with a range of values for the control filter length, I, when regularised to achieve the maximum possible performance and using the incident pressure measured in front of the primary loudspeaker as a reference signal.

To investigate this, Equation 4.14 has been used to calculate optimal control source strengths with increasing filters lengths from $I = 32$ to $I = 1024$ when using the incident pressure measured in front of the primary loudspeaker as a reference signal. In each case, the attenuation performance was calculated for a range of different values of regularisation, and the optimal regularisation value was selected. The data acquired at a sample rate of $f_s = 48\text{kHz}$ was used, rather than the down-sampled data at $f_s = 2.4\text{kHz}$, to provide greater temporal resolution for this study. The attenuation for each controller configuration is presented over frequency in Figure 4.6, and the corresponding control filters are plotted in Figure 4.7. Figure 4.6 shows that, as expected, the acoustic cloaking performance increases with increasing control filter length. However, what is perhaps more surprising is the sharpness of this performance increase. There appears to be a threshold of $I = 256$, below which the acoustic cloaking performance is extremely limited, and above which the acoustic cloaking performance reaches a plateau and is relatively unaffected by further increases in the filter length. This can be explained by the plots presented in Figure 4.7, which show that the peak of the impulse response is at approximately 159 samples and, therefore, to ensure that the

control filters contain sufficient information to be effective their length must be greater than 159 samples. This time delay corresponds to a distance of approximately 1.14 m, which is equivalent to the distance between the sensor array and the outer ring of the control source array.

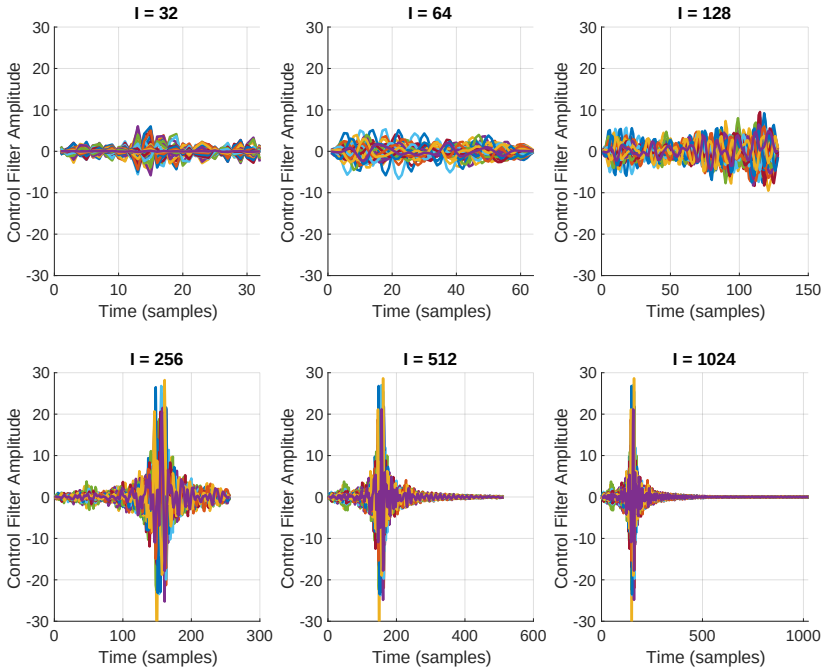

Figure 4.7: A plot showing the impulse responses of the causally constrained control filters, calculated with a range of values for the control filter length,I, when regularised to achieve the maximum possible performance and using the incident pressure measured in front of the primary loudspeaker as a reference signal.

The results presented so far in this Chapter have shown that the broadband, causally constrained controller formulated in Section 4.1 is effective at acoustically cloaking the rigid sphere using the measurement setup shown in Figure 4.1 if the control filters are long enough and a suitable reference signal is used. However, as discussed thoroughly in Chapter 3, the performance of an active acoustic cloaking system can be severely limited when perturbations are introduced. Therefore, the following section will present an investigation into the robustness of the broadband, causally constrained controller presented in Section 4.1.

4.2.3 Robustness to Perturbations

It is important to consider the robustness of a practical active control system, as discussed in Chapter 3, as it is often the case that variations in the physical system can introduce uncertainties in the plant response or disturbance field. It was shown in Chapter 3 that the selection of the regularisation parameter, β, is highly significant; a large value of β will result in a system that is very robust to changes, but that performs poorly in every case, whereas a control system with a low value of β will achieve significant attenuation in the nominal case but will have poor robustness to any changes in the system responses. The following section will investigate the robustness of the proposed broadband active acoustic cloaking strategy to variations in the position of the scattering sphere.

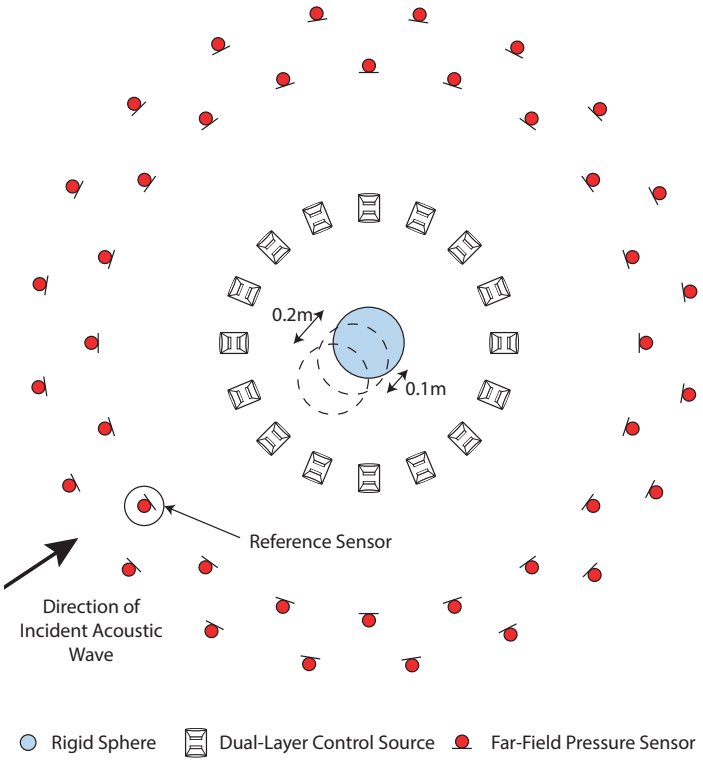

Figure 4.8: A schematic diagram showing the source/sensor arrangement and the scattering sphere in the nominal and perturbed positions.

This study will consider perturbations in the position of the scattering object of 10 cm and 20 cm in the direction of the incident acoustic wave, as shown in Figure 4.8. This is consistent with the robustness study presented for the tonal controller in Section 3.5. The broadband control formulation presented above has been implemented using the measured acoustic responses of the sphere in its nominal position, and perturbed by 10 cm and 20 cm. Optimal control filters have been calculated using Equation 4.14, when using the incident acoustic pressure measured in front of the primary loudspeaker as the reference signal and a control filter length of $I = 512$. The scattered acoustic pressure after control has been calculated using Equation 4.7. The attenuation in the scattered acoustic power has been calculated over a range of frequencies and with increasing values of the regularisation parameter, β, and is presented in Figure 4.9 for all three sphere positions. The results shown in Figure 4.9 are consistent with the results for the optimal tonal controller shown in Figure 3.16, in that there is a significant performance degradation when the sphere is perturbed from the nominal position, and the level of performance degradation can be linked to the magnitude of the perturbation.

It can be seen from Figure 4.9 that, as concluded in Chapter 3, appropriate selection of the regularisation parameter, β, can enable the active acoustic cloaking to be robust to the perturbations considered in this study, however regularising to this level will result in decreased performance when the sphere is in the nominal position. To provide further insight into this trade-off, the results presented in Figure 4.9 have been averaged over frequency to quantify the broadband attenuation that can be achieved for each sphere position over a range of values of β. These results are presented in Figure 4.10 and, as with the robustness analy-

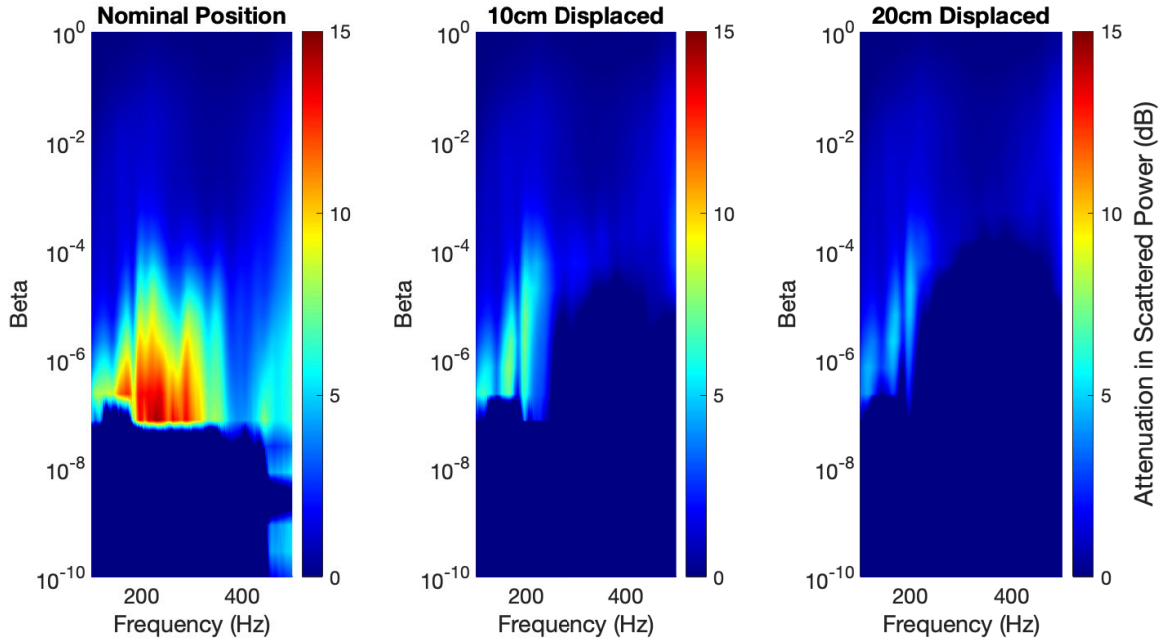

Figure 4.9: Contour plots showing the attenuation that the broadband, causally constrained control system is able to achieve in the scattered sound power over frequency and a range of values of β, for the nominal case and each of the perturbed cases, using a control filter length of $I = 512$ and when using the incident acoustic pressure measured in front of the primary loudspeaker as the reference signal.

sis presented in Chapter 3, the average of the nominal and perturbed conditions has been included as a dashed line. It can be seen from Figure 4.10 that when the controller is regularised with a value of β less than approximately 5×10^{-8}, the controller is unable to achieve any control; consistent with the results presented in Figure 4.9. In this case, the system is under-regularised and therefore the inversion of the $\mathbf{R}^{\mathrm{T}}(n)\mathbf{R}(n)$ matrix shown in Equation 4.14 is ill-conditioned and prone to numerical inaccuracy. The attenuation performance in the nominal case reaches a maxima of 14 dB at $\beta = 2 \times 10^{-7}$ and, as would be expected, the performance deteriorates as regularisation is increased above this point and the system can be said to be over-regularised. In each of the perturbed conditions, however, minimal attenuation is achieved with low values of β and the performance maxima for the 10 cm and 20 cm conditions are at values of $\beta = 1 \times 10^{-3}$ and $\beta = 5 \times 10^{-3}$ respectively. To ensure that the active acoustic cloaking system is robust to all of the perturbation conditions considered in this study, a value of β corresponding to the maxima in the dashed line should be selected. In this case the control system is able to achieve control in the acoustic scattering regardless of whether the sphere is perturbed or not, however the performance when the sphere is in the nominal position is reduced from approximately 14 dB to approximately 7 dB. These results show that, as has been discussed previously, the value of β should be carefully selected, and consideration should be given to the range of perturbations which can reasonably be expected in the physical system.

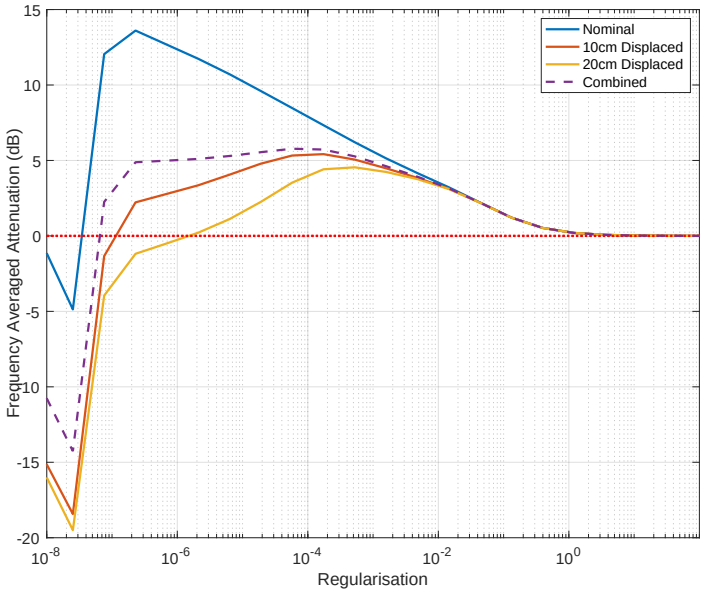

Figure 4.10: A plot showing the frequency averaged attenuation that can be achieved by the active acoustic cloaking system when the sphere is in the nominal position, and when the sphere is perturbed by 10 cm and 20 cm, with a range of values of the regularisation parameter β. The system is configured to use the incident pressure measured in front of the primary loudspeaker as a reference signal and a control filter length of $I = 512$.

4.3 Conclusions

This Chapter has presented a broadband, causally-constrained, formulation for the set of optimal control filters to minimise the acoustic scattering from an object. Measured data corresponding to a rigid sphere was used to analyse the performance of the proposed formulation, and it was shown that up to 15 dB of attenuation could be achieved in ideal conditions. The choice of a reference signal was investigated, and it was shown that up to 14 dB of attenuation can be achieved when using the incident pressure measured directly in front of the primary disturbance as a reference. It should be noted, however, that this arrangement requires a priori knowledge of the DOA of the incident acoustic wave and, therefore, in a practical environment either multiple reference sensors or a DOA estimation technique would be required.

The requirements in terms of control filter length were investigated and it was found that, for the given dataset, the control filters have to be at least 168 samples long to achieve significant levels of control. It was shown that there is negligible benefit when using control filters lengths of longer than 256 samples, as the results when using 512 and 1024 samples were almost identical to those using control filters of 256 samples. The robustness of the control system to perturbations in the position of the scattering object was also investigated, and it was shown that the value of the regularisation parameter was significant in ensuring robust performance. When robustness is not considered, the controller is able to achieve a frequency averaged attenuation value of 14 dB, however minimal control is achieved when the position of the scattering sphere is perturbed. When the value of regularisation is selected to maximise the average performance across all perturbation conditions, over 4 dB of attenuation can be achieved in the perturbed cases, however, the performance in the nominal case is reduced to 7 dB. When designing a practical active control system, the requirements

of robustness and nominal performance should be considered, and an appropriate value of regularisation should be selected; this has previously been investigated in more detail in Chapter 3.

The control strategies presented in this chapter, as well as in all of the previous chapters, have assumed that the scattered acoustic pressure can be directly measured at each microphone in the sensor array to provide the error signals to be minimised. As discussed in Chapter 1, this is not possible in a practical setup and, therefore, other methods should be considered to allow the scattered acoustic pressure to be estimated from a measurable quantity. A virtual sensing approach will, therefore, be formulated in Chapter 5, which will allow the far-field scattered acoustic pressure to be estimated from near-field total acoustic pressure measurements and will thus address this challenge. The studies presented so far consider a rigid spherical scattering object, however, in practice it is known that the acoustic scattering from resonant structures is far more complex [11, 71]. Chapter 7 will investigate the performance of the broadband active acoustic cloaking strategy presented in this Chapter applied to a flexible aluminium cylinder, to allow an investigation into the effects of resonant scattering on the acoustic cloaking performance. Building on this, Chapter 6 will present an alternative acoustic cloaking approach to minimise the effects of resonant scattering from a flexible structure.

Chapter 5

A Virtual Sensing Strategy for the Real-Time Estimation of the Acoustic Scattering from a Rigid Sphere

The use of active control to reduce the acoustic scattering from an object has significant potential as an acoustic cloaking strategy, however, the practical implementation of such a system is currently limited due to the fact that the scattered acoustic pressure cannot be directly measured and, therefore, cannot be used as an error signal in an active control system. Active acoustic cloaking systems have been demonstrated successfully in the simulation domain [38, 59, 60], however, these systems all assume prior knowledge of the scattered acoustic pressure. Various methods of estimating the scattered acoustic pressure from a directly measurable quantity have been presented in the literature, including numerical modelling [62] and wave decomposition based approaches [40], however, these methods only consider the control of tonal disturbances. Furthermore, the performance of the numerical modelling approach proposed by Testa et al [62] is dependent on the accuracy of the numerical model, whilst the wave decomposition approach proposed by Friot et al [40] requires a large number of sensors positioned around the scattering object, which may not be practical for many applications.

The broadband, causally constrained control strategy presented in Chapter 4 achieved a significant level of control of the scattered acoustic field, however, it was assumed that the scattered acoustic pressure was known in the far-field of the scattering object, which provided the control algorithm with the necessary error and reference signals. In a practical scenario, however, it is likely that positioning sensors in the far-field of the scattering object will not be practical for a variety of the considered use cases and, regardless of where the sensors are positioned, they will still only provide a measurement of the total acoustic pressure, rather than the scattered component in isolation.

This chapter will propose a virtual-sensing algorithm, which can be combined with the control algorithm presented in Chapter 4 to resolve some of the issues associated with far-field sensor placement, and the detection of the scattered acoustic field. The proposed virtual sensing method is based on an adaptation of the Remote Microphone Technique [72] that has previously been used in active noise control applications. The proposed method esti-

mates the far-field scattered acoustic pressure by filtering near-field measurements of the total acoustic pressure using an optimally designed observation filter. This chapter builds upon a frequency-domain implementation of the proposed method [61] by formulating it in the time-domain, and then combining it with the broadband, causally constrained controller presented in Chapter 4.

Section 5.1 will layout the proposed virtual sensing strategy and present a derivation of the filter coefficients for the optimal observation filters in the time domain. Section 5.2 will asses the accuracy of the virtual sensing method using the measured data corresponding to a rigid spherical scattering object, described in Chapter 2. Section 5.3 will quantify the acoustic cloaking performance that can be achieved by combining the virtual sensing algorithm with the broadband, causally constrained control algorithm, and the robustness of the system will also be considered.

5.1 Formulation

As noted in the introduction to this chapter, the proposed virtual sensing strategy estimates the far-field scattered pressures from measurements of the total acoustic pressure in the near-field of the scattering object. The far-field scattered pressures are estimated by filtering the near-field pressure signals via an observation filter. This section will derive an expression to calculate the J filter coefficients of the optimal observation filters, $\mathbf{O}_{\text{opt}}$. In practice, when anything but tonal disturbance signals are being considered, it is necessary to constrain the observation filters to be causal and the optimal filter responses in this case can be derived in the time-domain, as described in [37, 73] for the standard remote microphone technique. The experimental setup shown in Figure 5.1 will be used to motivate the proposed strategy, although the derivation for the optimal observation filters is not necessarily dependent on a specific arrangement of sensors.

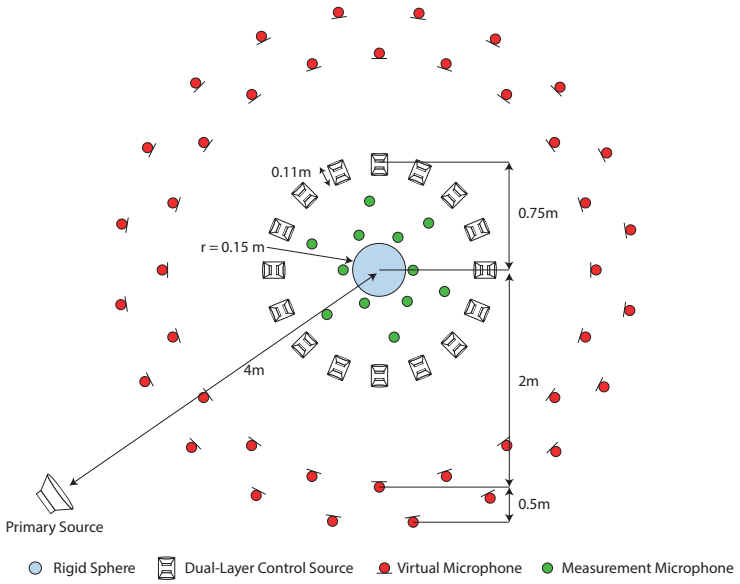

Figure 5.1: A schematic diagram showing the position of the sources and sensors in the experimental setup.

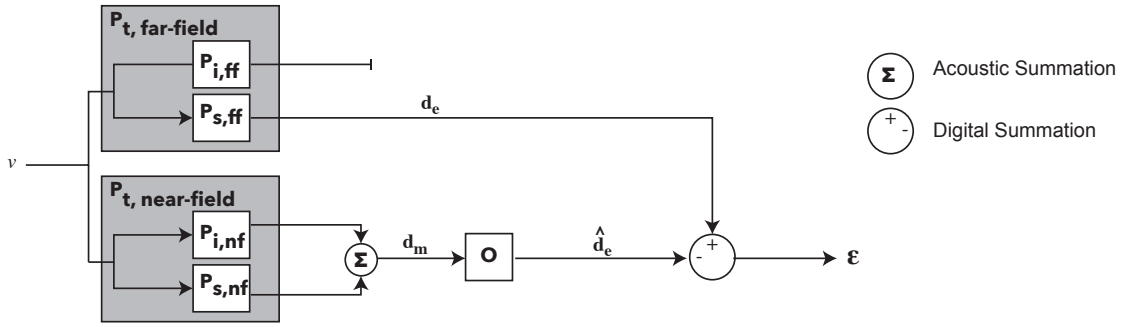

Figure 5.2: Block diagram showing the formulation of the virtual-sensing system where v is the primary source strength, $\mathbf{d}_m$ is the vector of total acoustic pressures at the measurement microphone positions, $\mathbf{d}_e$ is the vector of scattered acoustic pressures at the estimation sensor positions, $\mathbf{O}$ is the matrix of observation filters, $\widehat{\mathbf{d}_e}$ is the vector of estimated scattered acoustic pressures at the estimation sensor positions, and ϵ is the vector of estimation errors.

Figure 5.1 shows a schematic of the experimental setup described in Chapter 2, with the addition of a near-field sensor array. The far-field sensor array of $N_e = 40$ measurements of the scattered acoustic pressure, indicated in red in Figure 5.1, will form the virtual sensors, whilst the near-field sensor array of $N_m = 12$ measurements of the total acoustic pressure, indicated in green in Figure 5.1 will form the measurement sensors. Following the standard Remote Microphone Technique, a matrix of observation filters, $\mathbf{O}$, will be calculated such that the signals from the measurement sensors, when filtered by the observation filters, give an estimate of the signals at the virtual sensors, as shown in Figure 5.2.

The $JN_e \times 1$ vector of current and past disturbance signals at the virtual sensors, $\mathbf{d}_e(n)$, and the $JN_m \times 1$ vector of current and past disturbance signals at the measurement sensors, $\mathbf{d}_m(n)$, are defined as

$$\mathbf{d}_e(n) = \left[\mathbf{d}_{e_1}^{\mathrm{T}}(n), \mathbf{d}_{e_2}^{\mathrm{T}}(n) \dots \mathbf{d}_{e_{N_e}}^{\mathrm{T}}(n)\right]^{\mathrm{T}} \tag{5.1}$$

$$\mathbf{d}_m(n) = \left[\mathbf{d}_{m_1}^{\mathrm{T}}(n), \mathbf{d}_{m_2}^{\mathrm{T}}(n) \dots \mathbf{d}_{m_{N_m}}^{\mathrm{T}}(n)\right]^{\mathrm{T}}, \tag{5.2}$$

where

$$\mathbf{d}_{e_{ne}}(n) = \left[\mathbf{d}_{e_{ne}}(n), \mathbf{d}_{e_{ne}}(n-1) \dots \mathbf{d}_{e_{ne}}(n-J-1)\right]^{\mathrm{T}} \tag{5.3}$$

$$\mathbf{d}_{m_{nm}}(n) = \left[\mathbf{d}_{m_{nm}}(n), \mathbf{d}_{m_{nm}}(n-1) \dots \mathbf{d}_{m_{nm}}(n-J-1)\right]^{\mathrm{T}}. \tag{5.4}$$

According to the virtual sensing strategy, the $JN_e \times 1$ vector of estimated current and past disturbance signals at the virtual sensors, $\widehat{\mathbf{d}_e}(n)$, is given by filtering the measurement sensor signals, $\mathbf{d}_m$, as

$$\widehat{\mathbf{d}_e}(n) = \mathbf{O}\mathbf{d}_m(n), \tag{5.5}$$

where $\mathbf{O}$ is the matrix of observation filter coefficients, defined as

$$\mathbf{O} = \left[\mathbf{O}_1^{\mathrm{T}}, \mathbf{O}_2^{\mathrm{T}} \dots \mathbf{O}_{N_e}^{\mathrm{T}}\right]^{\mathrm{T}}, \tag{5.6}$$

where

$$\mathbf{O}_{n_e} = \left[\mathbf{O}_{n_e 1}^{\mathrm{T}}, \mathbf{O}_{n_e 2}^{\mathrm{T}} \dots \mathbf{O}_{n_e N_m}^{\mathrm{T}}\right]^{\mathrm{T}}, \tag{5.7}$$

and $\mathbf{O}_{n_e n_m}$ is the observation filter between the n_mth measurement microphone and the n_eth virtual microphone, modelled by a Jth order FIR filter given as

$$\mathbf{O}_{n_e n_m} = \left[\mathbf{O}_{n_e n_m 0}, \mathbf{O}_{n_e n_m 1} \dots \mathbf{O}_{n_e n_m (J-1)}\right]^{\mathrm{T}}. \tag{5.8}$$

The estimation error, ϵ, is defined as the difference between the disturbance signals measured at the virtual sensors, $\mathbf{d}_e$, and the estimated signals at these locations, $\widehat{\mathbf{d}_e}$, which gives

$$\epsilon(\mathbf{n}) = \mathbf{d}_e(n) - \widehat{\mathbf{d}_e}(n). \tag{5.9}$$

Substituting Equation 5.5 into Equation 5.9 gives the estimation error as

$$\epsilon(\mathbf{n}) = \mathbf{d}_e(n) - \mathbf{O}\mathbf{d}_m(n). \tag{5.10}$$

The matrix of optimal observation filters, $\mathbf{O}_{\mathrm{opt}}$, can then be found by minimising the sum of the squared estimation errors and, therefore, the cost function, $\mathbf{J}$, can be expressed as

$$J = \mathrm{trace}\left[E\left[\epsilon(\mathbf{n})\epsilon(\mathbf{n})^{\mathrm{T}} + \beta_{\mathrm{est}}\mathbf{O}\mathbf{O}^{\mathrm{T}}\right]\right] \tag{5.11}$$

where $\beta_{\mathrm{est}}\mathbf{O}\mathbf{O}^{\mathrm{T}}$ is included to constrain the magnitude of the observation filters. By combining Equations 5.10 and 5.11, the cost function can be expressed as

$$J = \mathrm{trace}\left[E\left[\left(\mathbf{d}_e(n) - \mathbf{O}\mathbf{d}_m(n)\right)\left(\mathbf{d}_e(n) - \mathbf{O}\mathbf{d}_m(n)\right)^{\mathrm{T}} + \beta_{\mathrm{est}}\mathbf{O}\mathbf{O}^{\mathrm{T}}\right]\right]. \tag{5.12}$$

The cost function given in Equation 5.12 can be minimised following the process outlined in [37, 73], giving the optimal matrix of observation filters, $\mathbf{O}_{\mathrm{opt}}$, as

$$\mathbf{O}_{\mathrm{opt}} = \left(\left[E\left[\mathbf{d}_m(n)\mathbf{d}_m^{\mathrm{T}}(n) + \beta_{\mathrm{est}}\mathbf{I}\right]\right]^{-1} E\left[\mathbf{d}_m(n)\mathbf{d}_e^{\mathrm{T}}(n)\right]\right)^{\mathrm{T}} \tag{5.13}$$

It should be noted that the solution shown in Equation 5.13 is true for the overdetermined case, where $N_m > N_e$. For the specific geometry considered in this study, shown in Figure 5.1, this is not the case and in fact the system is severely underdetermined. As detailed in [37], the solution shown in Equation 5.13 can be considered to be an 'engineering approximation' in the underdetermined case and, therefore, the minimum mean square error that can be achieved by the virtual sensing technique will be non-zero. It is proposed, in a practical implementation of the virtual sensing system, that the observation filters would be calculated in an initial setup phase; during which the scattered acoustic pressure can be measured at a far-field sensor array using, for example, the process described in Section 2.1. After the observation filters have been calculated, according to Equation 5.13, the far-field sensor array is no longer required and the virtual sensing method can be used to estimate the far-field scattered acoustic pressure. It is assumed, in this case, that the transfer responses of the system are time-invariant and, therefore, the observation filters will remain accurate. The addition of the regularisation term β_{est} will limit the magnitude of the observation filters, and ensure a certain level of robustness of the estimation system to variations in the response of the system, and this is discussed in more detail in Section 5.3.1.

5.2 Virtual Sensing Performance

The performance of the virtual sensing algorithm described in the previous section will be investigated using the measured responses corresponding to the system described in detail in Chapter 2 and shown in Figure 5.1. The total acoustic pressure at the array of 12 near-field sensors will provide the vector of measurement signals, $\mathbf{d}_m$, and the scattered acoustic pressure at the array of 40 far-field sensors will provide the vector of virtual signals, $\mathbf{d}_e$. In the following section, this measured data will be used to investigate the accuracy of the proposed virtual sensing strategy, and the effect of varying the length of the observation filters will be discussed. In Section 5.3, the virtual sensing strategy described in Section 5.1 will be combined with the broadband, causally constrained controller presented in Chapter 4, and the acoustic cloaking performance of the combined system will be analysed. The robustness of the combined virtual sensing and control system to perturbations in the position of the scattering object will also be investigated.

To investigate the accuracy of the virtual sensing method, optimal observation filters have been calculated according to Equation 5.13, and the subsequent estimation error, ϵ, has been calculated according to Equation 5.10. To allow the overall estimation performance to be quantified, the estimation error has been averaged over the 40 far-field microphones, and is presented in Figure 5.3 over a range of frequencies and values of the regularisation parameter β_{est}, when using an observation filter length of $J = 256$. It can be seen from Figure 5.3 that the estimation error of the virtual sensing system is relatively consistent across the frequency range presented, and is primarily governed by the level of regularisation. There is a slight inconsistency between 250 Hz and 300 Hz, mostly noticeable between $\beta_{\text{est}} = 1 \times 10^{-10}$ and $\beta_{\text{est}} = 1 \times 10^{-2}$, that shows an increased estimation error. This frequency range equates to wavelengths between 1.3 m and 1.1 m, which corresponds to approximately half of the radius of the far-field microphone array, as well as the distance from the sphere to the far-field array. Therefore, this is likely caused by limitations in the experimental setup, specifically a combination of spatial-aliasing and interaction between the sphere and sensor arrays. When the system is regularised with a value of approximately $\beta_{\text{est}} = 1 \times 10^{-18}$ or lower, the virtual sensing performance is limited by the accuracy of the solution given in Equation 5.13 which, due to the system being undetermined, is non-perfect.

As Figure 5.3 shows that the estimation error is monotonically decreasing with regularisation, there is no optimal value of β_{est} to select. As previously discussed, however, the use of regularisation can ensure that the system remains robust to physical changes and, therefore, whilst there is no optimal value in the nominal case, there will be a clearer benefit of regularisation when perturbations are introduced. The following analysis will use an arbitrary value of $\beta_{\text{est}} = 1 \times 10^{-4}$, however, the robustness of the virtual sensing system and the effect of regularisation will be discussed further in Section 5.3.1. The average estimation error of the virtual sensing system, when regularised with a value of $\beta_{\text{est}} = 1 \times 10^{-4}$ and when using an observation filter length of $J = 256$, is presented over frequency in Figure 5.4. Figure 5.4 clearly shows the performance decrease between 250 Hz and 300 Hz, as discussed above. The frequency smearing of this performance decrease is caused by the far-field array consisting of two concentric rings of sensors which, due to slight inaccuracies in the measurement setup, will be subject to small positioning errors.

To provide further insight into the performance of the virtual sensing strategy, Figure 5.5

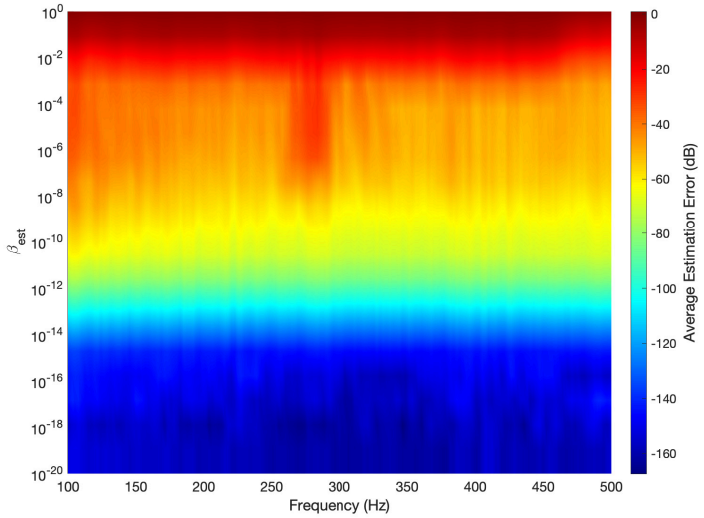

Figure 5.3: A contour plot showing the estimation error of the proposed virtual sensing strategy, averaged over all 40 far-field microphones, when using an observation filter length $J = 256$ and a range of estimation regularisation values.

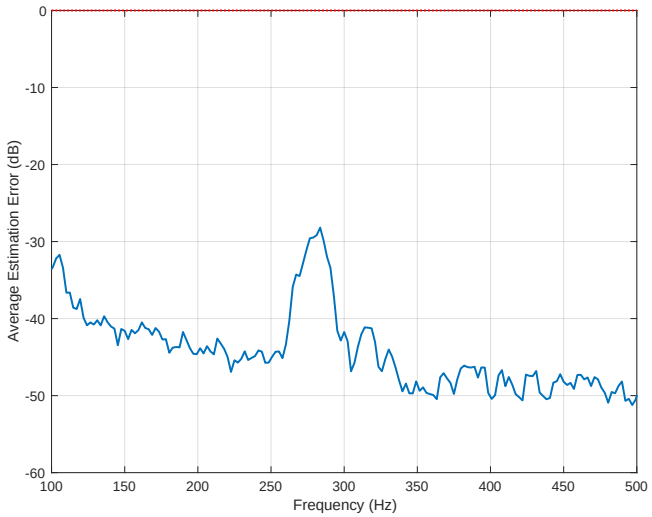

Figure 5.4: A plot showing the estimation error of the proposed virtual sensing strategy, averaged over all 40 far-field microphones, when regularised with a value of $\beta = 1 \times 10^{-4}$ and using a filter length of $J = 256$.

presents a plot showing the real and estimated scattered acoustic pressure at a subset of the far-field sensor positions when regularisation is set to $\beta_{\text{est}} = 1 \times 10^{-4}$. The responses at 6 of the sensor locations have been included in Figure 5.5 for clarity, selected to be evenly distributed around the sensor array to given an overview of the estimation behaviour, however the responses at the other 34 sensors show a similar trend. It can be seen from the results presented in Figure 5.5 that the virtual sensing strategy is providing an accurate estimate of the scattered acoustic pressure at each sensor location, with the dashed and solid lines showing highly consistent results across the frequency range. There are noticeable errors in the blue set of results shown in Figure 5.4, with the estimation error reaching a maximum value of 10 dB at 125 Hz, however the virtual sensing algorithm is still able to accurately predict the overall shape of the response. The proposed virtual sensing approach is similar conceptually to the approach proposed in [41], where 'Scattering Filters' are formulated to estimate the scattered acoustic pressure from measurements of the total acoustic pressure, however the current study builds upon the work by Friot et al as it formulates the observation filters in the time domain, without assuming a tonal disturbance field.

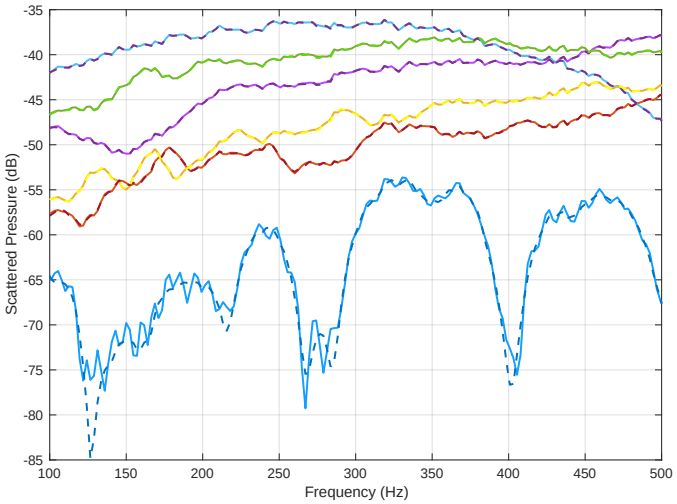

Figure 5.5: A plot showing the real scattered acoustic pressure (solid), and the estimated scattered acoustic pressure (dashed), at a number of the far-field sensor locations when the virtual sensing strategy is regularised with a value of $\beta = 1 \times 10^{-4}$ and using a filter length of $J = 256$.

The results presented in Figures 5.4 and 5.5 show the accuracy of the virtual sensing system when there is no uncertainty in the system responses, and when using a set of observation filters of length $J = 256$. The performance of a virtual sensing system is heavily dependent on ensuring that the observation filters are of a suitable length to capture sufficient information about the system. This requirement will be investigated in the following section.

5.2.1 Effect of Observation Filter Length

The following section will investigate how the performance of the virtual sensing system is related to the length of the observation filters. The length of the observation filters is a key parameter to investigate when designing virtual sensing systems as it allows for a trade-off between computational load and estimation performance and, therefore, it is of interest to investigate how the estimation performance of the proposed system varies with different lengths of control filters.

To investigate this, Equation 5.13 has been used to calculate optimal observation filters with increasing filter lengths from $J = 32$ to $J = 1024$, in a similar manner to the investigation into control filter lengths presented in Section 4.2.2. In each case, the regularisation was selected so as to ensure that the maximum peak of the estimation FIRs are of equal magnitude. The data acquired at a sample rate of $f_s = 48\text{kHz}$ was used, rather than the down-sampled data at $f_s = 2.4\text{kHz}$, to provide greater temporal resolution for this study. The estimation error, averaged over all 40 far-field sensors, is presented over frequency in Figure 5.6 and the corresponding observation filters are plotted in Figure 5.7. Figure 5.6 shows that, as expected, the virtual sensing accuracy increases with increasing observation filter length. As was the case for the active control filters discussed in Section 4.2.2, there appears to be a threshold of $J = 256$, below which the accuracy of the virtual sensing algorithm is severely limited, and above which the estimation error reaches a plateau and is relatively unaffected by further increases in the filter length. This behaviour can be explained by the impulse response plots presented in Figure 5.7, which show that the main peak of the impulse responses is at approximately 174 samples and, therefore, to ensure that the observation filters contain sufficient information to be effective their length must be greater than 174 samples. This time delay corresponds to a distance of approximately 1.25 m, which is equivalent to the distance between the sensor array and the control source array.

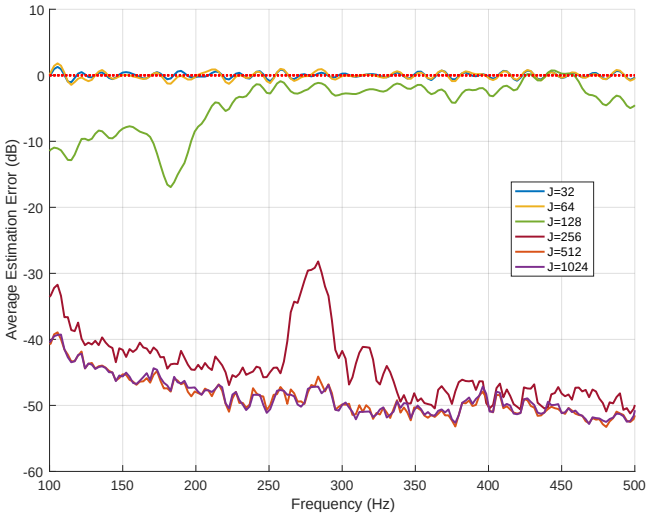

Figure 5.6: A plot showing the estimation error of the proposed virtual sensing strategy, averaged over all of the sensors in the far-field array, with increasing values of J and when regularised such that the peak in the observation filters is of equivalent magnitude.

5.2.2 Robustness of Virtual Sensing Method

This section will present an investigation into the robustness of the proposed active acoustic cloaking system to perturbations in the position of the scattering object. To be consistent with the robustness studies presented previously in this thesis in Chapter 3 and Section 4.2.3, the scattering sphere has been displaced by 10 cm and 20 cm in the direction of the incident acoustic field. Equation 5.13 was used to calculate the optimal observation filters with the sphere in the nominal position, and the performance of the virtual sensing system was calculated with the sphere in the perturbed positions. As with the robustness studies presented previously, the accuracy of the proposed system has been calculated over a range of regularisation values, and is presented as a contour plot in Figure 5.8.

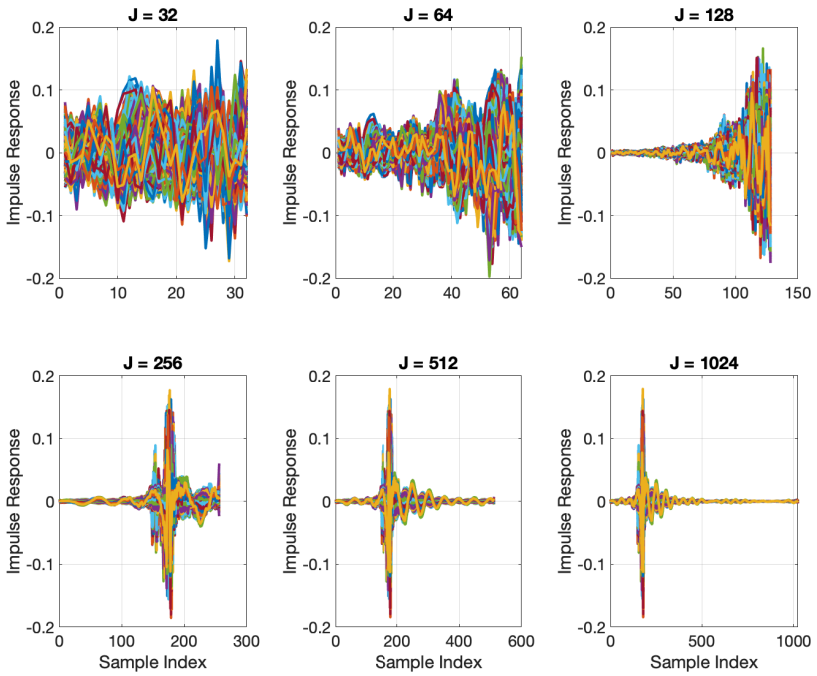

Figure 5.7: A plot showing the impulse responses of the observation filters, with increasing values of J, when regularised to have the same magnitude peak.

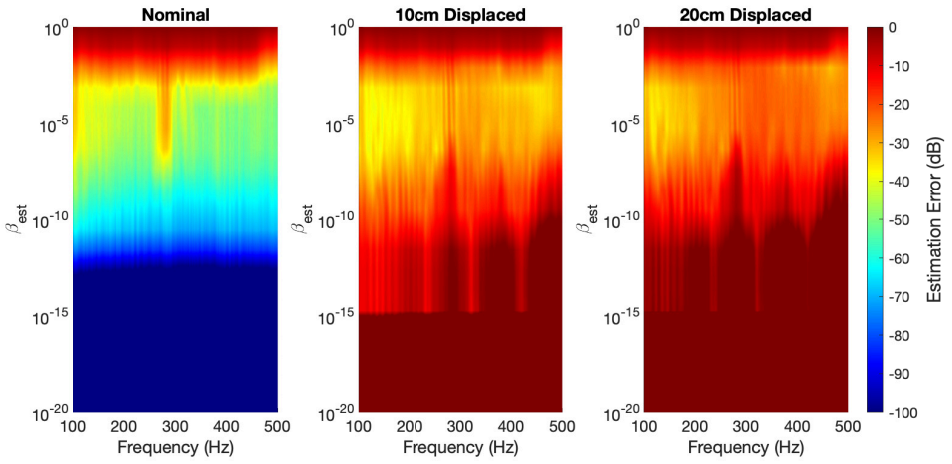

Figure 5.8: Contour plots showing the estimation error of the proposed virtual sensing strategy over frequency and a range of values of β_{est}, for the nominal case and each of the perturbed cases.

It can be seen from Figure 5.8 that, whilst the estimation error in the nominal case is monotonically decreasing with decreasing regularisation, this is not the case for the perturbed conditions and there is a clear optimal range of regularisation values at approximately $\beta_{\text{est}} = 1 \times 10^{-4}$ at which the virtual sensing system achieves similar accuracy in both the nominal and perturbed conditions. To display this more clearly and, again, consistent with the regularisation studies presented previously, the estimation error has been averaged across frequency to give an indication of the broadband accuracy of the virtual sensing algorithm, and this can be seen in Figure 5.9 for the nominal and perturbed cases. It is clear from the

results presented in Figure 5.9 that there is a narrow range of values of β_{est} which achieve a negative estimation error in the perturbed case, with an optimal point at approximately $\beta_{\text{est}} = 1 \times 10^{-4}$ where the virtual sensing approach is able to achieve -24 dB of estimation error in the perturbed cases, and -44 dB in the nominal case. It is also interesting to note that there is little difference in the estimation error between perturbing the sphere by 10 cm or 20 cm, in contrast to the results presented previously which show a greater effect.

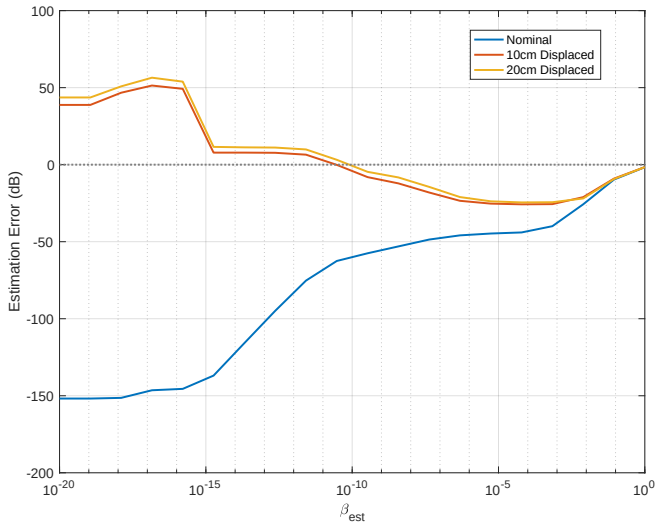

Figure 5.9: A plot showing the frequency averaged estimation error of the virtual sensing system with increasing values of regularisation for the nominal case, and in each of the perturbed cases.

From the results presented in Figures 5.8 and 5.9, it can be seen that a regularisation value of approximately $\beta_{\text{est}} = 1 \times 10^{-4}$ provides a reasonable level of performance in the nominal case whilst ensuring that the performance does not deteriorate significantly when perturbations are introduced. Figure 5.10 shows the estimation error for the nominal case, and the two perturbed conditions, when using a regularisation value of $\beta_{\text{est}} = 1 \times 10^{-4}$. It can be seen from Figure 5.10 that, as shown in the previous plots, including uncertainty results in an increase in estimation error, however, as the regularisation value has been selected appropriately this increase is fairly modest. Above 300 Hz, perturbing the sphere by 10 cm and 20 cm results in an increase in the estimation error by approximately 20 dB and 30 dB respectively. Below 200 Hz, the effect of the perturbations is reduced as the level of perturbation becomes small compared to the acoustic wavelength. It is interesting to note that the increase in estimation error seen in the nominal case between 250 Hz and 300 Hz is almost completely removed for both of the perturbation conditions, with only a slight discontinuity being visible within this frequency range. This is, perhaps, unsurprising as the inclusion of uncertainty in the formulation of optimal observation filters has the same effect as adding regularisation to the system, as shown in Section 3.1 and in the literature [63–65].

The results presented in Figures 5.3 to 5.7 show that, with an appropriate value of regularisation and a suitable length of observation filters, the proposed virtual sensing strategy is able to accurately estimate the far-field scattered acoustic pressure, at a number of sensor locations, from near-field measurements of the total acoustic pressure. Whilst this is interesting in its own right, the following section will combine the virtual sensing strategy with the broadband, causally constrained controller described in Chapter 4 to form an active acoustic

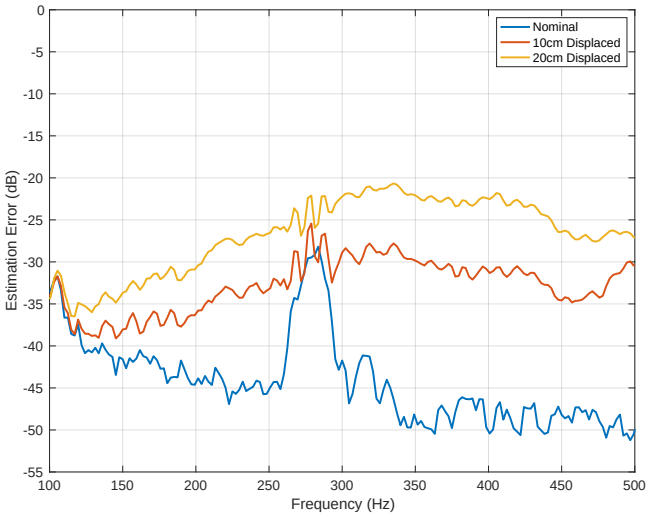

Figure 5.10: A plot showing the estimation error of the proposed virtual sensing strategy with the sphere in the nominal position, and with the sphere perturbed by 10 cm and 20 cm, averaged over all 40 far-field microphones when using an observation filter length $J = 256$ and an estimation regularisation value of $\beta_{\text{est}} = 1 \times 10^{-4}$.

cloaking system that does not require real-time knowledge of the scattered acoustic pressure.

5.3 Acoustic Cloaking Performance with Virtual Sensing

This section will combine the virtual sensing strategy described in Section 5.1 with the broadband control strategy described in Chapter 4. The array of microphones in the near-field of the scattering sphere has been used to measure the total acoustic pressure at each sensor location. Optimal observation filters have been calculated, according to Equation 5.13, which give an estimate of the scattered acoustic pressure at each of the far-field sensor locations. Equation 4.14 is used to calculate optimal control source strengths to minimise the vector of estimated scattered acoustic pressures, and the acoustic cloaking performance of this system is calculated according to Equation 4.7. A schematic of the proposed system is presented in Figure 5.11.

The performance of the active acoustic cloaking system presented in Figure 5.11 has been investigated using the measured data corresponding to the acoustic scattering from a rigid sphere, discussed in Chapter 2. Based on the investigations presented in Sections 4.2 and 5.2, filter lengths of $I = 512$ and $J = 256$ will be used for the control filters and observation filters respectively. A regularisation value of $\beta = 1 \times 10^{-6}$ will be used in the calculation of optimal control source strengths, and a regularisation value of $\beta_{\text{est}} = 1 \times 10^{-4}$ will be used in the calculation of the optimal observation filters. The incident acoustic pressure measured in front of the primary loudspeaker will be used as the reference signal. The performance of the proposed acoustic cloaking strategy is presented in Figure 5.12 and, for reference, the attenuation that can be achieved if the acoustic scattering is directly controlled is also included. It can be seen from Figure 5.12 that controlling the estimate of the scattered pressure, rather than directly controlling the scattered pressure, reduces the acoustic cloaking performance by less than 2 dB across the considered frequency range. The largest degradation in control

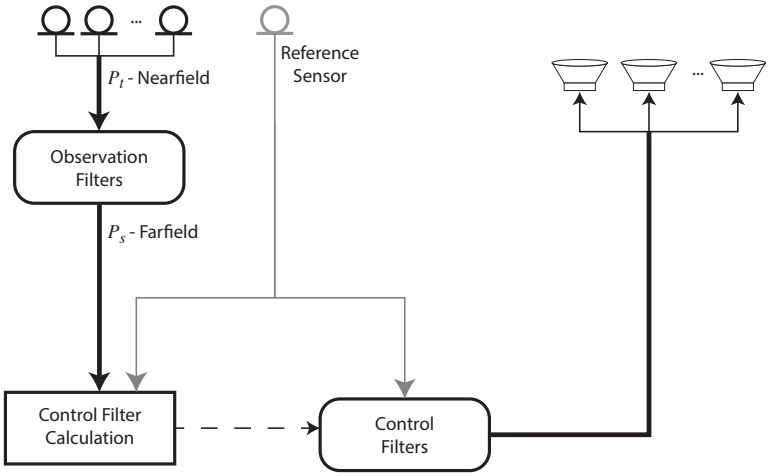

Figure 5.11: A schematic showing the proposed active acoustic cloaking system, including virtual sensing and active control FIRs.

performance is between 250 Hz and 300 Hz, which is explained by the peak in the estimation error shown in Figure 5.4, caused by spatial-aliasing of the far-field microphone array.

As shown in Figure 5.3, the accuracy of the virtual sensing approach is largely dependent on the level of regularisation, with lower values of regularisation resulting in more accurate estimations. However, it is known from the literature [53, 64, 72], as well as the study presented in Chapter 3, that low values of regularisation may result in a poorly conditioned matrix inverse which, in turn, significantly reduces the robustness of the solution. Therefore, although using a lower value of regularisation in Equation 5.13 may result in superior performance in the nominal case, the robustness of the observation filters will be reduced. This will be investigated in the following section.

5.3.1 Robustness of Active Acoustic Cloaking System Using Virtual Sensing

The results presented in Figure 5.10 show that perturbing the scattering body reduces the estimation accuracy by up to 30 dB, however, it is perhaps more insightful to consider what effect this has on the acoustic cloaking performance. As in the previous sets of results, and as shown in Figure 5.11, Equation 5.13 has been used to calculate the optimal observation filters to estimate the far-field scattered acoustic pressure from measurements of the near-field total acoustic pressure, with the sphere in the nominal position. The near-field total acoustic pressure, with the sphere in each of the perturbed conditions, has then been used with the observation filters calculated previously to provide an estimate of the far-field scattered acoustic pressure. Equation 4.14 has been used to calculate the optimal control source strengths to minimise the vector of estimated scattered acoustic pressures. The acoustic cloaking performance, with the sphere in the nominal position and in each of the perturbed positions, has been calculated according to Equation 4.7 and is presented in Figure 5.13. It can be seen from Figure 5.13 that, although the inclusion of uncertainty in the position of the scattering object significantly reduces the accuracy of the virtual sensing system, as shown in Figure 5.10, the level of attenuation in the far-field scattered response that can

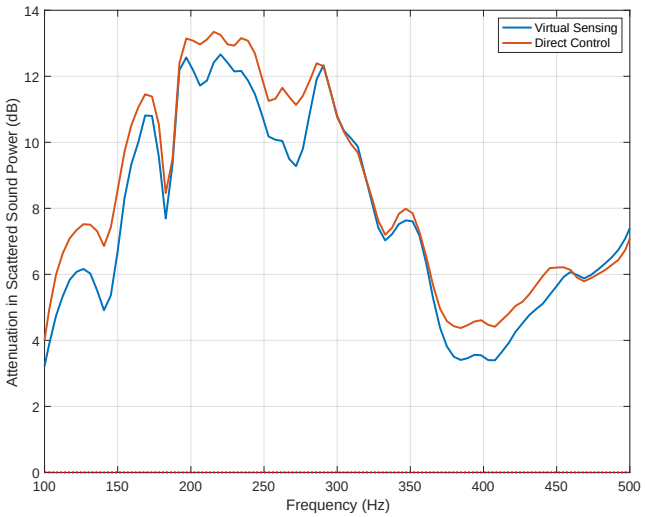

Figure 5.12: A plot showing the attenuation that the control system is able to achieve in the scattered sound power over frequency when directly minimising the scattered pressure at each microphone location, and when minimising an estimate of the scattered pressure using the proposed virtual sensing method. The system was configured with a control regularisation value of $\beta = 1 \times 10^{-6}$, a virtual sensing regularisation value of $\beta_{\text{est}} = 1 \times 10^{-4}$, a control filter length of $I = 512$, an observation filter length of $J = 256$ and the incident pressure measured in front of the primary loudspeaker as a reference signal.

be achieved remains relatively unchanged below approximately 250 Hz. Above 250 Hz the degradation in performance caused by the inclusion of uncertainty is less than 5 dB across the presented frequency range. This is, perhaps, unsurprising as it was shown in [61, 73] that the estimation error of a virtual sensing system is directly relatable to the level of control that can be achieved. For example, a virtual sensing system that can achieve -10 dB of estimation error will limit the performance of an active controller to a maximum attenuation of 10 dB. Therefore, based on the results shown in Figure 5.10, this would limit the maximum attenuation achievable by the acoustic cloaking system to 35 dB across the majority of the frequency range, with the sphere in the nominal position. The results shown in Figures 4.5 and 5.12 show that this is clearly not the case and, therefore, it is apparent that, with the experimental data described in Chapter 2 and the acoustic cloaking system shown in Figure 5.11, the active acoustic cloaking system is more limited by the controllability of the physical system rather than by the accuracy of the virtual sensing method. Perturbing the system reduces the accuracy of the virtual sensing approach, but not by so much that it becomes dominant compared to the performance limitations imposed by the physical system.

5.4 Conclusions

This Chapter has presented a method to estimate the far-field scattered acoustic pressure based on measurements in the near-field of a scattering body of the total acoustic pressure. This approach, based on virtual sensing, is an important step to achieving a practical active acoustic cloaking system for two reasons. Primarily, it addresses the problem discussed in the previous chapters, which have all assumed that a measure of the scattered acoustic pressure is available. In practice, it is not possible to directly measure the scattered acoustic pressure and, therefore, a method is required to estimate it based on a directly measurable

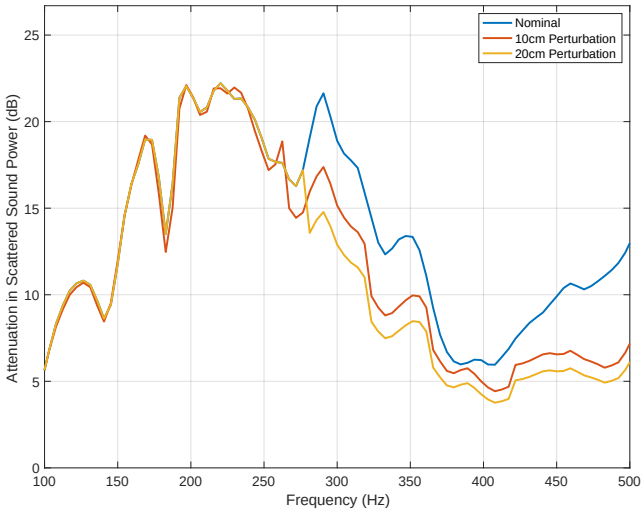

Figure 5.13: A plot showing the attenuation that the control system is able to achieve in the scattered sound power over frequency when minimising an estimate of the scattered pressure using the proposed virtual sensing method with the sphere in the nominal position, and with the sphere perturbed by 10 cm and 20 cm. The system was configured with a control regularisation value of $\beta = 1 \times 10^{-6}$, a virtual sensing regularisation value of $\beta_{\text{est}} = 1 \times 10^{-4}$, a control filter length of $I = 512$, an observation filter length of $J = 256$ and the incident pressure measured infront of the primary loudspeaker as a reference signal.

quantity; in this case, the total acoustic pressure. The second contribution of the proposed virtual sensing approach is that it only requires near-field acoustic sensors. In a practical implementation of active acoustic cloaking, it will often be impractical to have sensors in the far-field of the scattering object and, therefore, having a method to estimate the far-field values from near-field measurements is beneficial.

To address the scattered field detection problem, a formulation to calculate the optimal observation filters has been presented, and the estimation accuracy has been quantified using measured data corresponding to the acoustic scattering from a rigid sphere, with various values of regularisation. The effect of varying the length of the observation filters was discussed and it was shown that, to achieve an accurate estimate, the filter length must be longer than 0.073 s. The virtual sensing system was combined with the active control system discussed previously, and it was shown that the acoustic cloaking performance using the virtual sensing approach is only slightly lower than the acoustic cloaking performance when directly minimising the scattered acoustic pressure. The robustness of the virtual sensing system to perturbations in the position of the scattering object has been investigated and it was shown that, for the given system, the acoustic cloaking performance is mostly limited by the controllability of the system rather than the accuracy of the virtual sensing method and, therefore, perturbing the system resulted in minimal deterioration of the acoustic cloaking performance.

The system presented in this chapter makes a significant contribution towards the realisation of a practical active acoustic cloaking system, by addressing two of the key implementation challenges. However, the method still requires an initial setup phase where the far-field scattered acoustic pressure is measured by measuring acoustic responses with and without the

scattering object present. For some applications of active acoustic cloaking, this may not be practical and it may, therefore, be of interest to investigate whether numerical methods could be used to calculate observation filters. It has also been noted that the analysis in this Chapter has assumed that the position of the source generating the incident acoustic field is known, and that it is not time-varying. In a practical implementation this may not be the case and, therefore, it would be insightful to consider whether the matrix of observation filters depends on the direction of the incident acoustic field.

Chapter 6

The Effect of Active Vibration Control on the Acoustic Scattering from a Flexible Cylinder

The previous chapters have considered a physical system consisting of a rigid spherical scattering object surrounded by two microphone arrays and a loudspeaker array. In practice, it is possible that the scattering object will be non-rigid and, therefore, resonant scattering will need to be considered. The following two chapters will consider the acoustic scattering from a flexible, thin-walled aluminium cylinder. Rather than using acoustic loudspeakers as control sources and pressure microphones as error sensors, structural sensing and actuation will be used and the challenges that this introduces will be considered and investigated. Chapter 6 will investigate the effects of Active Vibration Control on the acoustic scattered field, and Chapter 7 will present an investigation into the performance limitations introduced by using structural actuation as an acoustic cloaking method.

It has been thoroughly discussed throughout the preceding chapters that the real-time estimation of scattered acoustic pressure is one of the most significant challenges to overcome when implementing active acoustic cloaking in a practical setting. Chapter 5 has presented a possible solution to this, however, the presented virtual sensing approach relies on transfer responses measured during an initial setup phase which, in a practical scenario, may vary over time. This chapter will investigate an alternative control approach, which may have the effect of reducing the acoustic scattering from a flexible body without relying on any pre-measured acoustic or structural-acoustic transfer responses. This chapter will present an investigation into the effect of implementing Active Vibration Control (AVC) on the soundfield scattered from a flexible cylinder. It is known from the work by Bobrovnitskii [20] that the acoustic scattering from a flexible object is increased when the object is excited on resonance. Therefore, if an active control system can be designed such that the structural resonances of the scattering object are heavily damped, it is reasonable to expect this to reduce the acoustic scattering, however this has not been presented in literature to date. This Chapter presents both a simulation and experimental investigation into the effects of AVC on the acoustic scattering from a flexible cylinder in air. It should be noted that the implementation of AVC will only effect the acoustic scattering on-resonance and will result in minimal difference to the rigid component of the acoustic scattered pressure, however this may be sufficient to reduce the characteristic signature of the scattered soundfield. Parts of this work

have been published in [74].

6.1 Simulation Study

To investigate the effect of AVC on the acoustic scattering from a cylindrical shell, a hollow aluminium cylinder will be considered as shown in Figure 6.1. The cylinder will initially be considered as having free boundary conditions, and both the external and internal domains will be defined as air. To provide insight into this system, and to enable an investigation into the effect of AVC on the acoustic scattering from a cylindrical shell, a numerical model has been developed and will be presented in this section. The modelling environment and methodology will first be outlined, and then the structural and acoustic characteristics of the cylindrical shell will be presented. Finally, the model will be used to investigate the implementation of AVC and its effect on the acoustic scattering from the cylinder.

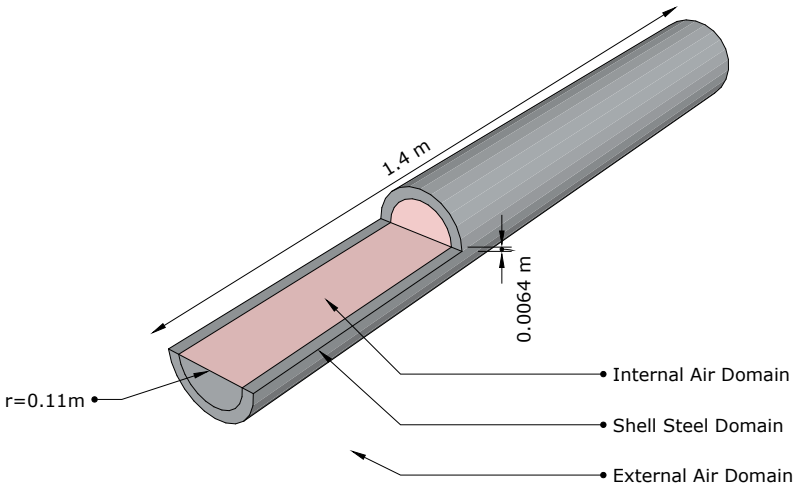

Figure 6.1: A diagram showing the geometry of the acoustic scattering object

6.1.1 Modelling Environment

This section will outline the numerical model which has been used to investigate the effect of AVC on the acoustic scattering from a cylindrical shell. Consistent with the other numerical simulations throughout this thesis, COMSOL Multiphysics has been selected as the software in which to develop the model. A numerical model has been selected over an analytical model as it makes it relatively simple to introduce additional aspects of a real-world implementation, such as finite sized control sources, mass loading of the structure, and various boundary conditions.

COMSOL's Acoustic-Structure boundary coupling feature can be used to model the interaction between the acoustic domains inside and outside of the sphere, and the response of the structural shell. The boundary conditions of the cylinder are modelled as having no net force on them except for that imposed by the acoustic plane wave. Therefore, the boundary load, F, imposed on the cylinder at any given node is

$$F = p\boldsymbol{n}, \tag{6.1}$$

where $\boldsymbol{n}$ is the surface normal and p is the acoustic pressure [75]. This couples the acoustic response into the structure. The structure is then coupled back into the fluid by equating the particle acceleration of the fluid and the structural acceleration of the shell in the radial direction at each mesh point, which gives

$$-\boldsymbol{n} \cdot \left(\frac{-1}{\rho_0} \left(\Delta p - \mathbf{q} \right) \right) = a_n, \tag{6.2}$$

where $\boldsymbol{n}$ and p are as defined above, $\mathbf{q}$ is the equivalent dipole source strength, and a_n is the normal acceleration vector, given by $a_n = 0$ for the case of a rigid enclosure, or $a_n = (\mathbf{n} \cdot \mathbf{u})\,\omega^2$ for a fully coupled system, where $\mathbf{u}$ is the harmonic displacement vector of the solid structure, and ω is the angular frequency.

As the model outlined in Figure 6.1 is unbounded, the incident plane wave will propagate from and to infinity, without a defined computational domain. Within COMSOL, there are two approaches to solving the infinite domain problem. The first is to bound a finite domain using a Perfectly Matched Layer (PML) [76], mesh the domain and the PML and solve using the Finite Element Method (FEM). The second approach utilises the Boundary Element Method (BEM), which only requires the boundaries to be meshed; the radiated field is then calculated by re-formulating the plane wave equation (describing the acoustic pressure within a domain) into an integral equation using Green's functions. This formulation calculates the pressure received at any given point in space from a unit source on the boundary of the domain. [77]. Other methods to handle this problem are also available, although not implemented within COMSOL, such as infinite elements [78].

For large problem sizes, especially unbounded problems such as the one in question, BEM is known to have a significant computational advantage over FEM due to there not being a need to mesh the entire volume, but rather only the boundaries of the solid object [79]. However, the numerical solvers required for computing a BEM solution are far more complex than those for FEM [80] and, therefore, BEM can be slower than FEM for small problem sizes. Therefore, the air domain inside the hollow cylinder was solved using FEM. Finite Element Analysis was also used to model the structural dynamics of the cylinder's shell, and all three methods (Acoustical FEM, Acoustical BEM and Structural FEM) were fully coupled, as discussed by Fritze et al [81].

The coupled BEM-FEM model was meshed with a free tetrahedral mesh over the cylindrical shell, with a minimum of 6 elements per wavelength. A convergence study was carried out, as shown in Appendix F, which verified that 6 elements per wavelength is sufficient to obtain accurate results over the considered frequency range. The external air domain does not need to be meshed due to the use of BEM rather than FEM. The cylindrical shell geometry can be implemented in one of two ways: either using a pair of concentric cylinders and using the intersection geometry tool to generate the shell volume, or by modelling a single cylinder and using an analytical shell model [82], implemented within COMSOL using Lagrange basis functions [83], to simulate the desired thickness. The latter was used in this case, as it prevented the need to generate a full volumetric mesh in the relatively thin aluminium

domain and, instead, a simple surface mesh could be used. This mesh is shown in Figure 6.2 at four separate frequencies, which correspond to different modes of the fully coupled structural-acoustic system that will be discussed in the following section.

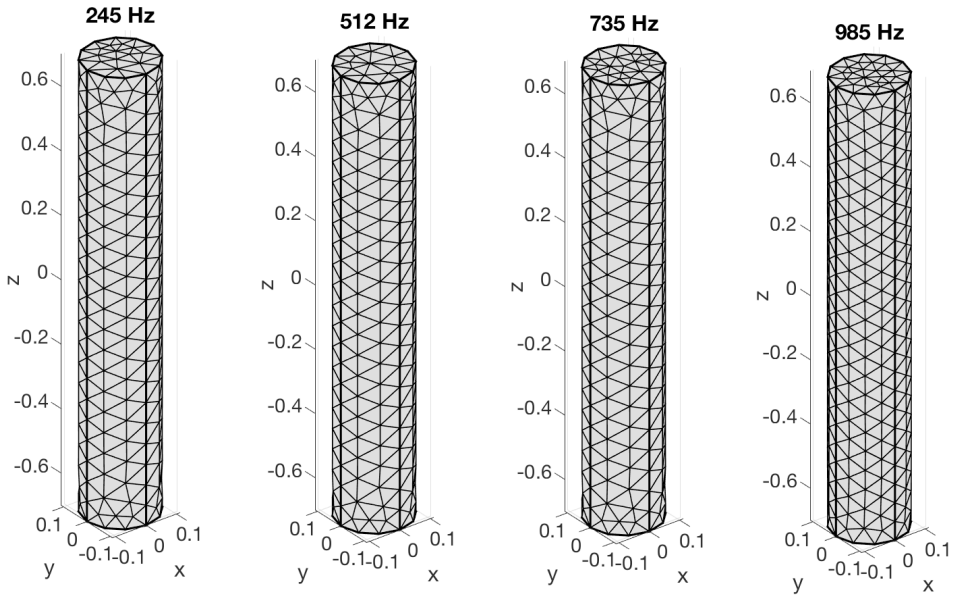

Figure 6.2: Mesh, generated by COMSOL to solve the coupled acoustic scattering model, at 245 Hz, 517 Hz, 735 Hz and 988 Hz

The cylinder is excited by an incident acoustic plane wave, propagating from a $\theta = 45°$ $\phi = 45°$ angle, as shown in Figure 6.3. The model outlined above has been solved over a range of frequencies between 100 Hz and 1 kHz with 1 Hz resolution and, due to the computational time involved, the IRIDIS Compute Cluster was used. The following analysis will utilise this model to investigate the acoustic scattering from the cylindrical shell and to observe the effect of implementing AVC on this.

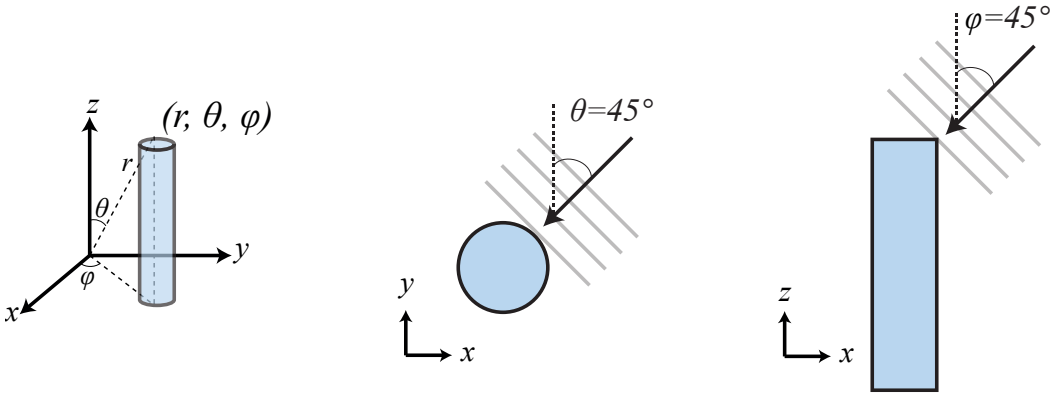

Figure 6.3: Schematic diagram showing the direction of the incident plane wave, in both plan view and front projection.

6.1.2 Structural Response

Modal Analysis

It is known that the vibration of the cylinder will be greatest when excited at resonance, and the work by Bobrovnitskii [20] and Williams [11] shows that the acoustic scattering of a structure may also increase around these resonant frequencies. With the coupled system outlined above, both the shell and the hollow interior will introduce their own resonances, however, the coupling between them will cause these resonances to shift slightly when compared to the resonances of either the invacuo structure or the rigid walled acoustic enclosure. To effectively investigate the mode shapes and corresponding eigenfrequencies of this coupled system, an eigenfrequency analysis was carried out using COMSOL Multiphysics.

The modal frequencies of the coupled model below 1 kHz are shown in Table 6.1, whilst the corresponding mode shapes are shown in Figure 6.4. Axisymmetric repeated modes have only been included once and are symbolised in bold. Table 6.1 also shows the frequencies corresponding to the equivalent mode shapes of either an uncoupled invacuo rigid cylinder, or an uncoupled rigid walled acoustic cavity [84].

Coupled Mode (Hz)	**Invacuo Structural Mode** (Hz)	**Rigid Acoustic Cavity Mode** (Hz)
122	-	123
245	-	245
339	353	-
367	-	368
490	-	490
517	513	-
574	549	-
612	-	613
735	-	735
857	-	858
879	-	947
887	861	-
900	948	-
912	-	914
937	981	-
951	1273	-
967	-	980
988	-	1103

Table 6.1: Modal frequencies from the coupled structural-acoustic model below 1 kHz, and the equivalent uncoupled modal frequencies. Bold font represents an axis-symmetric repeated mode.

The eigenfrequencies from the modal analysis are useful when investigating the vibro-acoustic behaviour of the cylindrical shell, as they will correspond to local maxima in the structural response of the cylindrical shell when excited by a suitable disturbance signal; although not every mode will be excited by every disturbance signal. Nevertheless, since the level of structural vibration will be large at these resonant frequencies, it is shown by Williams [11] and Bobrovnitskii [20] that acoustic scattering is increased at these frequencies. It is also useful to consider the mode shapes shown in Figure 6.4 when designing an AVC system to ensure that the disturbance is both observable, and controllable. Any error sensors and

control forces should be located at anti-nodes rather than within nodal regions to ensure detection and excitation of the structure respectively.

As noted by Bobrovnitskii [20], a strong structural resonance may result in enhanced acoustic scattering and, therefore, it is insightful to assess which modes, outlined in Table 6.1, result in a strong structural response for a given acoustic excitation. To quantify the structural response of the cylinder to an acoustic excitation, and to provide a vector of error signals for the AVC system discussed in the following sections, an array of 97 accelerometers, each measuring the radial component of the surface acceleration, has been simulated over the cylindrical shell as shown in Figure 6.5. The sum of the squared responses at these sensors is plotted over frequency in Figure 6.6. It can be seen from Figure 6.6 that there are 6 main resonances in the structural response over the presented frequency range which, when compared to the mode shapes shown in Figure 6.4, all correspond to structural bending or acoustic breathing modes of the cylinder. In the following section, this insight into the structural response will be linked to the acoustic scattering from the cylinder.

6.1.3 Scattered Acoustic Pressure

As the aim of this chapter is to investigate the relationship between structural vibration and acoustic scattering, and ultimately how controlling the former influences the latter, the scattered pressure field must be analysed as well as the structural response, which has been considered in the previous section. Figure 6.7 shows the predicted total acoustic pressure field when the cylinder is excited by an incident plane wave at 339 Hz, 517 Hz, 574 Hz and 887 Hz, which correspond to the modes with the largest structural response determined in the previous section. The angle of incidence of the plane wave is marked in each of the plots in Figure 6.7. The shadowing effect of the cylinder can clearly be seen in the 574 Hz plots, where the amplitude of the total field downstream of the cylinder is greatly reduced when compared with the amplitude of the total pressure upstream of the cylinder. Specular backscattering is shown by the rippling in the 887 Hz plots, orthogonal to the angle of incidence, however, it is difficult to clearly see details of the soundfield scattered by the cylinder from the total pressure plots, particularly at lower frequencies. Therefore, the scattered acoustic field, p_s, can be calculated from the difference between the incident acoustic field, p_i, and the total acoustic field, p_t, as

$$p_s = p_t - p_i. \tag{6.3}$$

This can be used to visualise the effect that the scattering object has on a given soundfield. Figure 6.8 shows the scattered acoustic pressure field in both plan view and front elevation, when the cylinder is excited by an acoustic plane wave impinging from $\theta = 45^\circ$ $\phi = 45^\circ$ at the four frequencies considered above. The angle of incidence of the plane wave is once again marked on the plots. Figure 6.8 clearly shows a beam of energy reflected from the cylinder, perpendicular to the incident wave, as well as the component of the scattered field that represents the acoustic shadowing, as discussed previously.

To accurately assess how the acoustic scattering is affected by the structural resonances of the cylinder, and to further benchmark the performance once AVC is simulated, the scattered sound power, W_{scat}, is calculated as an integral of the scattered sound pressure over a far-field sphere enclosing the cylinder [54], as

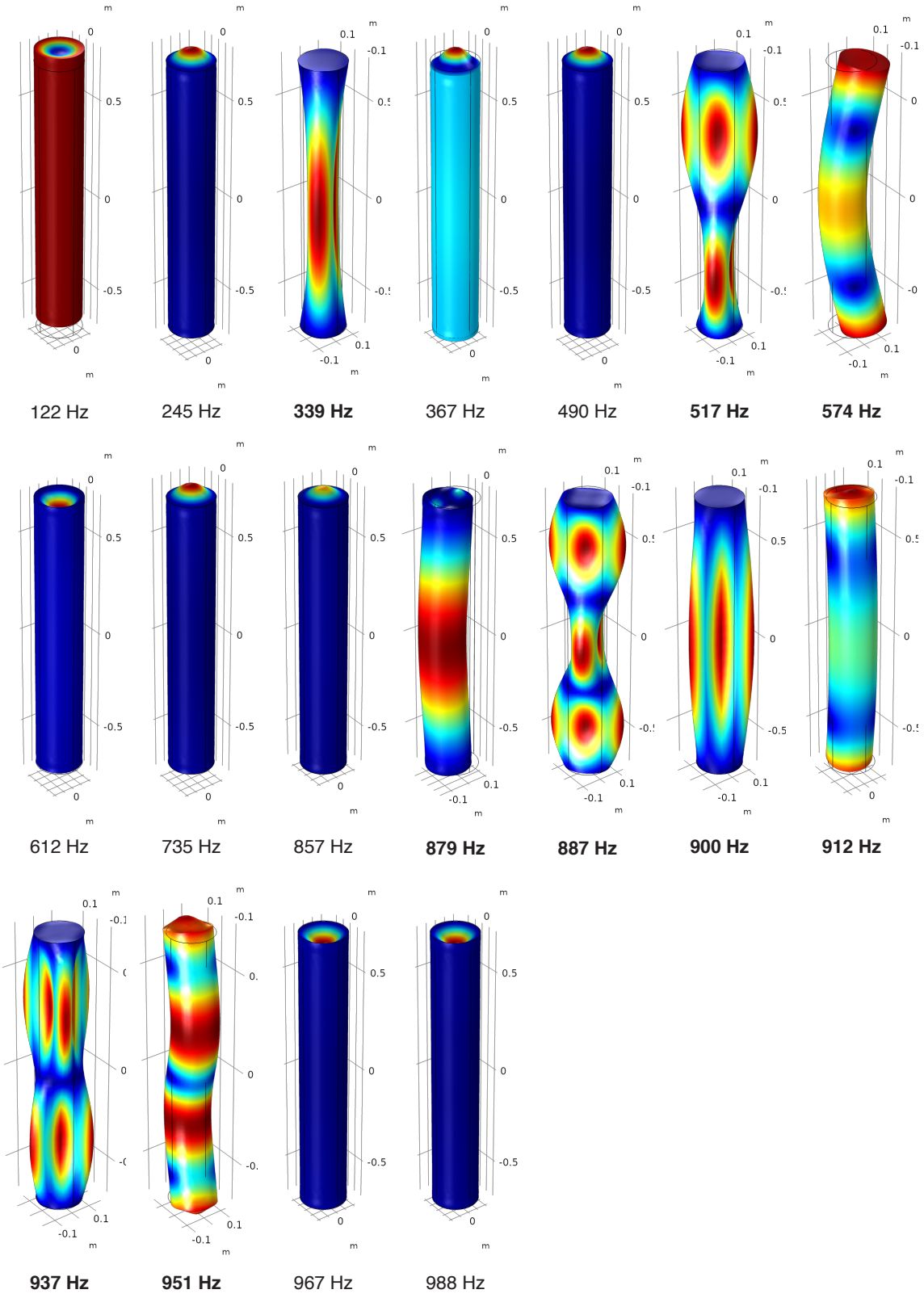

Figure 6.4: Modal frequencies and corresponding mode shapes of the cylinder. Frequencies in bold denote repeated axisymmetric modes.

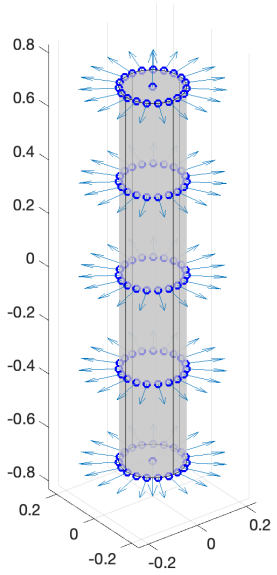

Figure 6.5: Location of the structural sensors on the surface of the cylinder. The arrows indicate the normal direction to the surface at each sensor.

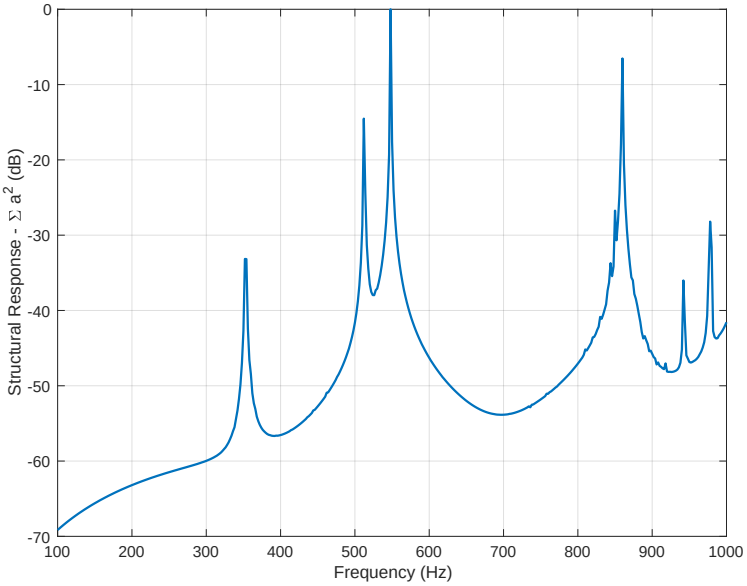

Figure 6.6: Sum of the squared accelerometer signals when the cylinder is excited by a plane wave from $\theta = 45°$ $\phi = 45°$

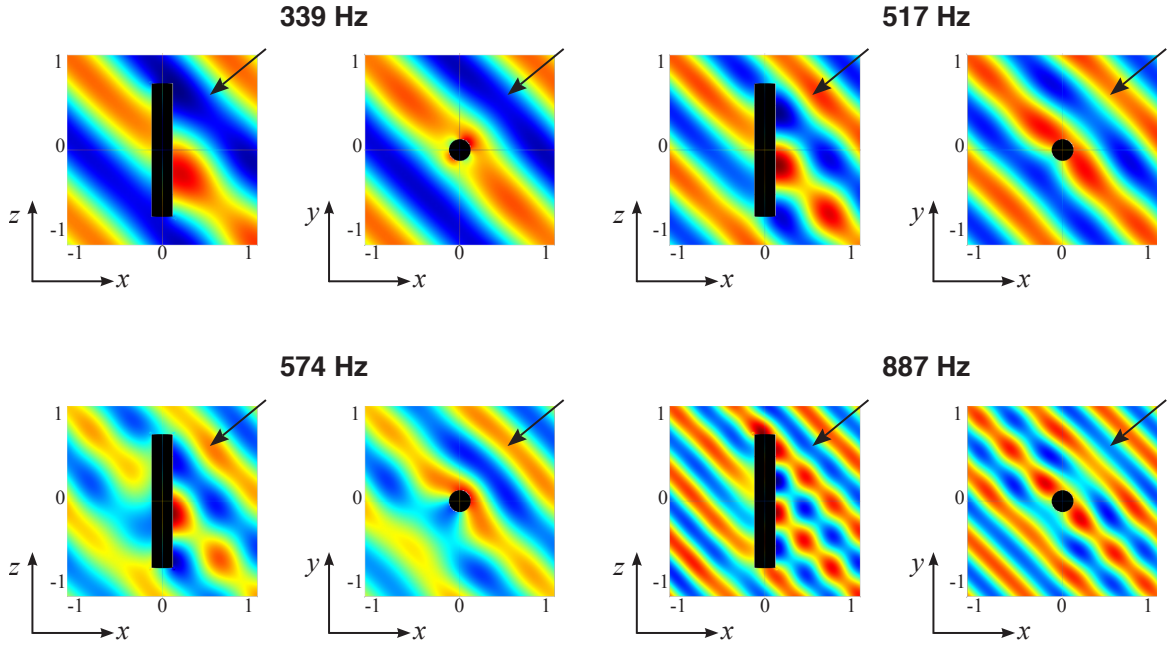

Figure 6.7: Predicted total acoustic pressure field when the cylinder is excited by an incident plane wave at 339 Hz, 517 Hz, 574 Hz and 887 Hz. The angle of incidence of the plane wave is shown by the arrow.

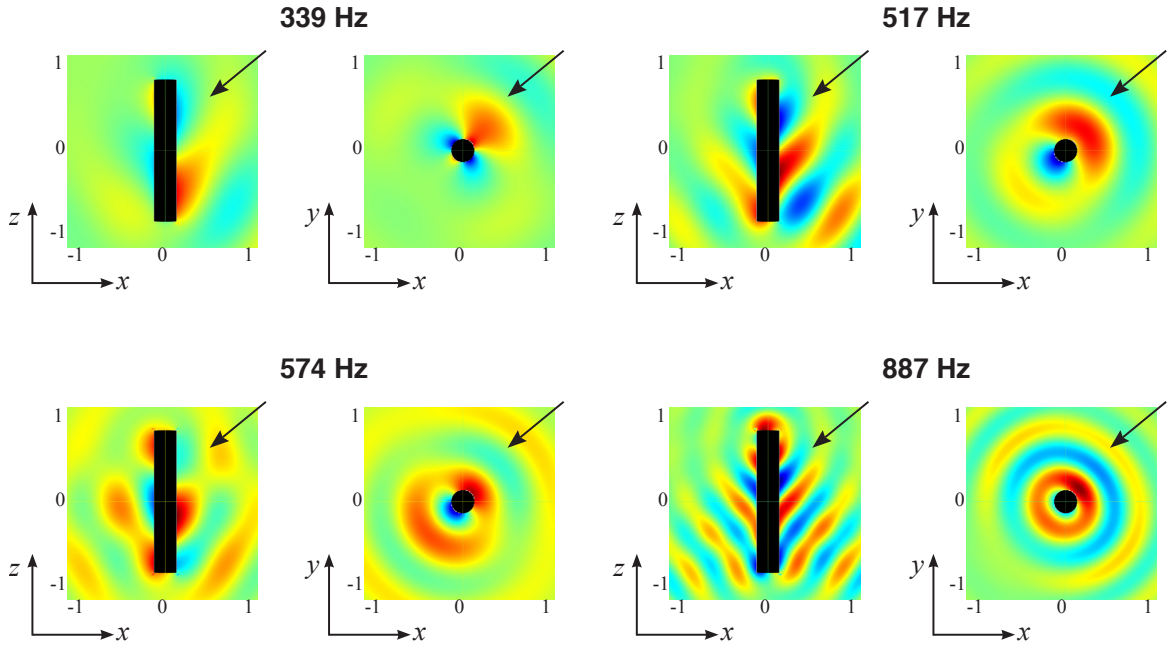

Figure 6.8: Predicted scattered acoustic pressure field when the cylinder is excited by an incident plane wave at 339 Hz, 517 Hz, 574 Hz and 887 Hz. The angle of incidence of the plane wave is shown by the arrow.

$$W_{scat} = \int_S \frac{|p_s^2|}{2\rho_0 c_0}. \tag{6.4}$$

The scattered sound power has been calculated and plotted over the frequency range of interest, as shown in Figure 6.9. In order to investigate the effects of resonant scattering, the scattered sound power given by Equation 6.4 was calculated for a rigid cylinder, which was also modelled in COMSOL and the results are included in Figure 6.9 as a dashed line. The bottom two plots in Figure 6.9 show enlarged sections of the top plot, each over a narrower bandwidth. Figure 6.9 shows that, although the structural response of the cylinder shows a number of resonances over frequency, the scattered sound power of the flexible cylinder has only one significant resonance at 574 Hz, corresponding to the first bending mode of the cylinder. Away from this resonance the scattered sound power is almost identical to that of a rigid cylinder.

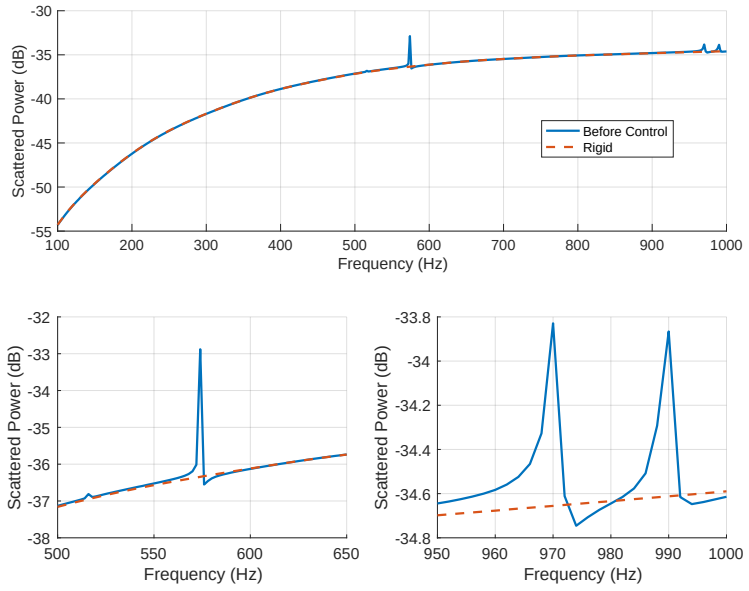

Figure 6.9: Total scattered sound power as a function of frequency, when excited by a plane wave from $\theta = 45°$ $\phi = 45°$. The bottom plots are zoomed in on two different frequency ranges to display the resonances of interest.

The results presented in Figure 6.9 are consistent with analytical results of underwater cylinders shown in the literature [20, 85, 86], which show that the scattered pressure from a rigid cylinder is similar to that from a flexible cylinder except at specific resonance peaks. A similar study to that presented above has also been carried out using a steel cylindrical shell, rather than the aluminium cylindrical shell discussed here. The results are presented in [74], and show the same trend as presented in Figure 6.9 with a 5 dB resonance at the breathing mode. In the case of the steel cylindrical shell study, the effect of varying the angle of incidence of the incoming acoustic wave was also investigated. Whilst the angle of incidence changed the relative magnitudes of the structural and acoustic modes, the scattered power was similar to that presented in Figure 6.9, and so this study has been omitted from inclusion in this thesis.

It is interesting to note that, for the cylinder considered in the present study, significant resonant scattering is only observed at the breathing mode. It is known from [87, 88] that the mechanism for resonant scattering to occur is by insonification of the structure, which then re-radiates acoustic energy. It can be seen from Figure 6.6 that the structural response, when the cylinder is excited acoustically at the 574 Hz resonance, is significantly greater than at any other frequency. It can, therefore, be assumed that the vibroacosutic coupling of the system is efficient at this frequency, which results in significant resonant scattering. In the following section, the effect of increasing the vibroacoustic coupling will be investigated.

6.1.4 Underwater Scattered Acoustic Pressure

It is clear from Figures 6.6 and 6.9 that the resonances in the scattered sound power correspond to peaks in the structural response of the cylinder, which can be related to the coupling efficiency between the structure and the external fluid. In the case of a cylinder submerged in water, as is likely for many of the potential uses of Active Acoustic Cloaking, the structural-acoustic coupling between the scattering object and the external fluid is much greater and, therefore, it is of interest to consider the acoustic scattering in this case. To investigate this, the computational model described above has been adjusted to consider an air-filled thin-walled aluminium cylinder submerged in water. The properties of the cylinder remain unchanged from the previous set of results. Whereas, in the previous set of results, the angle of incidence of the acoustic plane wave had little effect on the scattered acoustic power, this is not the case in the underwater simulated results and, therefore, three angles of incident plane wave have been investigated. These correspond to a $\theta = 45^\circ$ $\phi = 45^\circ$ angle as shown in Figure 6.3, a broadside disturbance from $\theta = 45^\circ$ $\phi = 90^\circ$, and an end-cap disturbance from $\theta = 45^\circ$ $\phi = 0^\circ$. The scattered sound power was calculated using Equation 6.4 for each angle of incidence, and is plotted in Figure 6.10 against frequency. As in the previous results, the scattered acoustic power for a rigid cylinder has also been plotted for comparison.

It can be seen from Figure 6.10 that that there are a number of resonances in the scattered sound power, which are excited to varying amounts by the different angles of incident acoustic wave. It is clear by comparing Figures 6.9 and 6.10 that the structural-acoustic coupling is much greater in water, as the difference between the scattered sound power for the flexible and rigid cylinders is far greater in water than in air. There are six significant peaks in the scattered sound power, all of which are greater than 20 dB in magnitude. As in the previous study, a modal analysis of the submerged cylinder has been implemented and the mode shapes corresponding to the peaks in the scattered sound power are presented in Figure 6.11. It is interesting to note that lowest significant resonant peak in the scattered sound power in both the and and water simulations corresponds to the first bending mode of the cylinder, whilst one of the end-cap modes also causes resonant scattering in both cases.

Whilst the scattered sound power from the cylinder in air exhibits one significant resonance of approximately 5 dB, the scattered sound power from the cylinder in water shows six significant peaks, each greater than 20 dB. Whilst, for experimental convenience, the remainder of this chapter will consider a cylinder in air, it has been noted that the implementation of AVC will have a far greater impact on the scattered sound power when the cylinder is submerged in a fluid with a greater acoustic coupling efficiency.

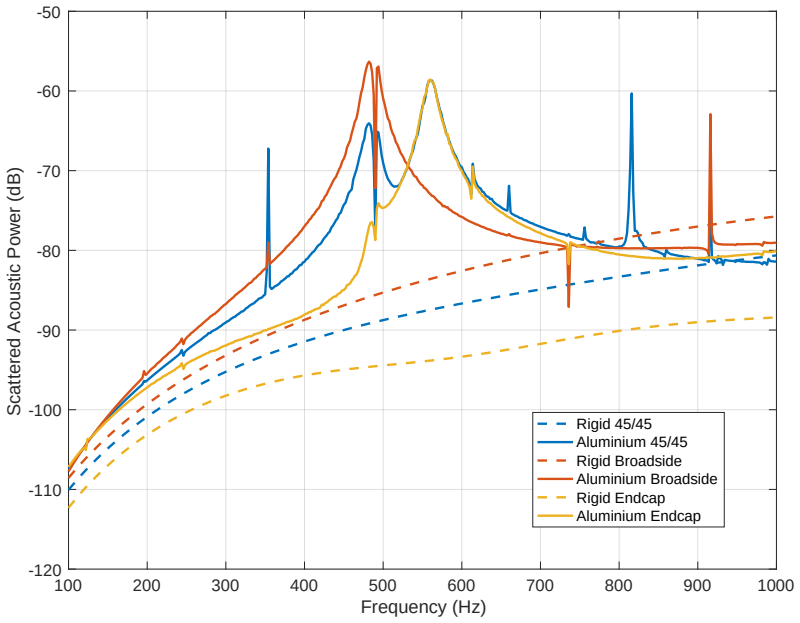

Figure 6.10: Total underwater scattered sound power as a function of frequency, when excited by a plane wave from $\theta = 45° \ \phi = 45°$

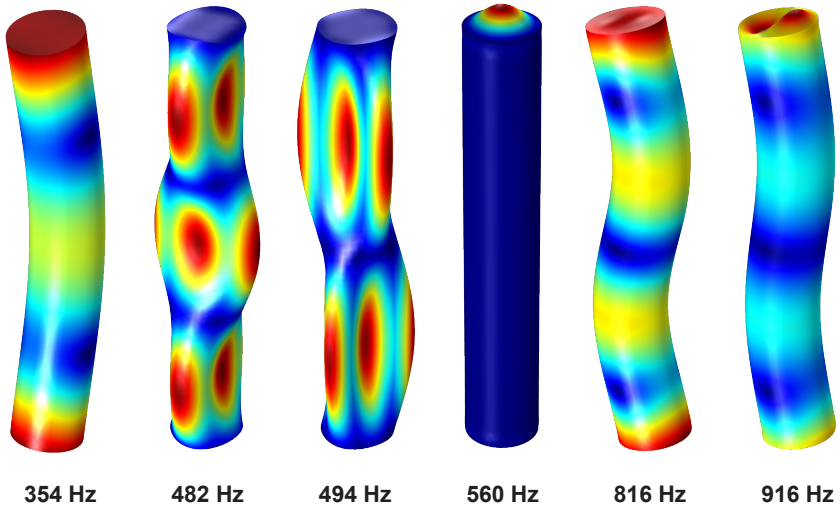

Figure 6.11: Mode shapes, corresponding to a submerged cylinder, which cause resonant scattering to occur.

6.1.5 Implementation of Active Control

It has been shown in the previous section that the scattered field from a flexible cylinder in air exhibits peaks in the scattered sound power, which do not occur in the case of a rigid scattering body. These peaks in the scattered response have been shown to correspond to frequencies of specific structural modes. Considering some of the use-cases of active acoustic cloaking described in Chapter 1, it is likely that these sharp peaks in the scattered response would be undesirable. Therefore, this section will investigate how the scattered acoustic field can be influenced by the implementation of an AVC system designed to minimise the vibration of the cylinder and, thus, force it to behave as if it were rigid.

Control Methodology

The proposed AVC system consists of an array of 97 accelerometers mounted on the surface of the cylinder detecting the radial component of the surface acceleration, as shown in Figure 6.5, and an array of 23 structural control forces as shown in Figure 6.12. In addition to the disturbance signals, in order to simulate the behaviour of an AVC system, it is also necessary to obtain the plant responses between the array of control forces and the array of structural error sensors. This has been achieved by driving each control force in turn with a 1N excitation in the inwards normal direction, and evaluating the response at each of the structural error sensors. These responses have then been combined to form the plant matrix of complex transfer impedances, $\mathbf{G}$.

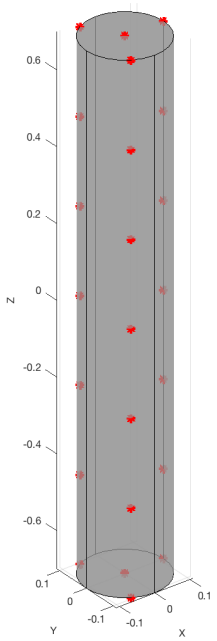

Figure 6.12: Location of the control forces on the surface of the cylinder. Each force acts inwards, in the radial direction.

An optimal harmonic feedforward controller has been formulated, which assumes that a

perfect reference signal is available, that the disturbance is tonal and, therefore, perfectly deterministic, and that there is no constraint on the causality of the controller. Based on these assumptions, a vector of optimal control forces can be calculated at each frequency as [37]

$$\mathbf{f_{opt}} = -\left(\mathbf{G}^H\mathbf{G} + \beta\mathbf{I}\right)^{-1}\mathbf{G}^H\mathbf{d}, \tag{6.5}$$

where β is a regularisation parameter and $\mathbf{I}$ is the identity matrix. Tikhonov regularisation has been included in Equation 6.5 to reduce the effects of ill-conditioning on the matrix inversion of $\mathbf{G}^H\mathbf{G}$ and to constrain the control effort of the control signals. The vibration of the cylinder after control, or the error signal, $\mathbf{e}$, is given as

$$\mathbf{e} = \mathbf{d} + \mathbf{G}\mathbf{f_{opt}}. \tag{6.6}$$

Control Performance

The vector of optimal control forces has been calculated using Equation 6.5, and the resulting error signals have been computed using Equation 6.6. The regularisation value β was set in proportion to the condition number, and the results are presented in Figure 6.13. From these results it can be seen that a significant reduction in the average structural acceleration across the entire frequency range has been predicted. The sum of the squared acceleration signals is reduced at all frequencies, with the AVC system effectively eliminating the resonant peaks completely. Although the structure is still vibrating, the magnitude of vibration is significantly reduced, such that it can be compared to a rigid body.

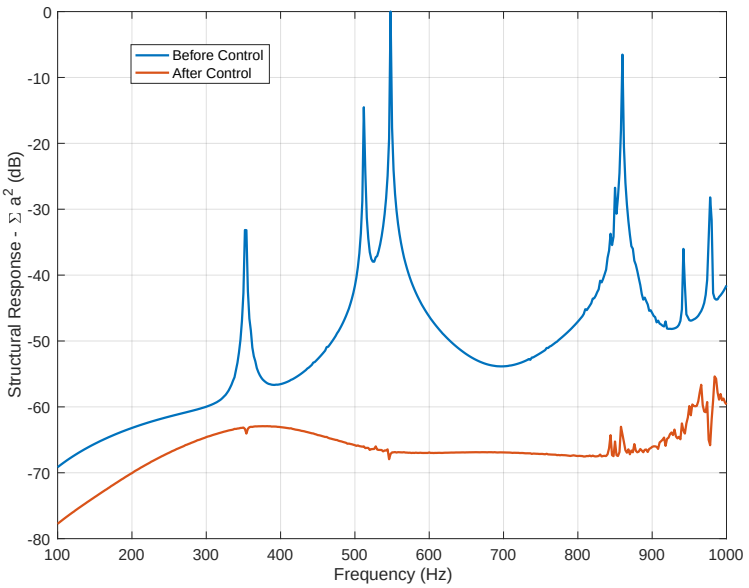

Figure 6.13: Mean square acceleration before and after active vibration control.

Using Equation 6.4, the scattered sound power has been computed with and without AVC and the results are presented in Figure 6.14. The acoustic scattered field before AVC shows

clear peaks in the spectrum at the first bending mode, and at two higher frequency modes. These peaks in the scattered spectrum have been reduced to the rigid response by the AVC system and thus, as expected, the scattering from the controlled cylinder is consistent with the rigid cylinder results, which are also presented in Figure 6.13 for reference.

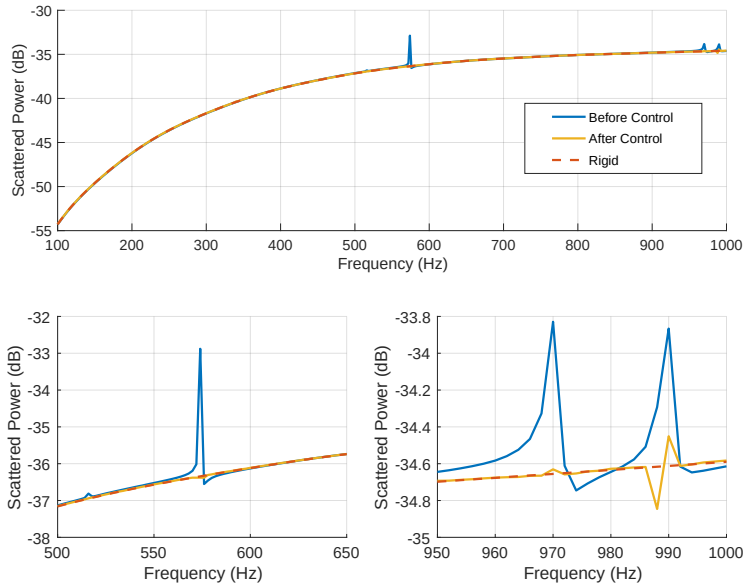

Figure 6.14: Scattered sound power before and after active vibration control

These results give an initial understanding of the level of attenuation in acoustic scattering that can be achieved by implementing AVC, for the given setup. Whilst the structure cannot be considered acoustically transparent, as the rigid body scattering is unaffected by this control strategy, the characteristic signature of the scattering is eliminated, which may be sufficient for some applications. If the structural-acoustic coupling was higher (for example, a cylinder submerged in water), or if the structure was more compliant or lightly damped, then it is expected that the level of reduction would be greater. The control methodology outlined above is considered a 'best case' controller, as it assumes that a perfect reference signal is available, and neglects any real-world considerations such as filter causality or variation in the plant response. Despite these assumptions, the current study gives valuable insight into the effects of AVC on acoustic scattering, and provides insight into the physical system.

6.2 Experimental Study

This section will use experimental data in an attempt to validate the simulation study described above into the effects of AVC on the acoustic scattering from a cylindrical shell. Initially, the experimental method will be described, and the scattering structure will be characterised and compared to the numerical results. The AVC system outlined above will then be implemented offline using the experimental data, and the control performance will be compared to the performance predicted from the simulated data.

6.2.1 Experimental Setup & Structural Characterisation

An aluminium cylinder has been designed and manufactured such that it is comparable in geometry to the simulated cylinder shown in Figure 6.1, with removable end-caps so that the control actuators can be mounted inside the structure. The construction of the cylinder is summarised in Figure 6.15, and detailed manufacturing drawings are included in Appendix G. It is known from the modelling presented earlier in this chapter that only specific modes

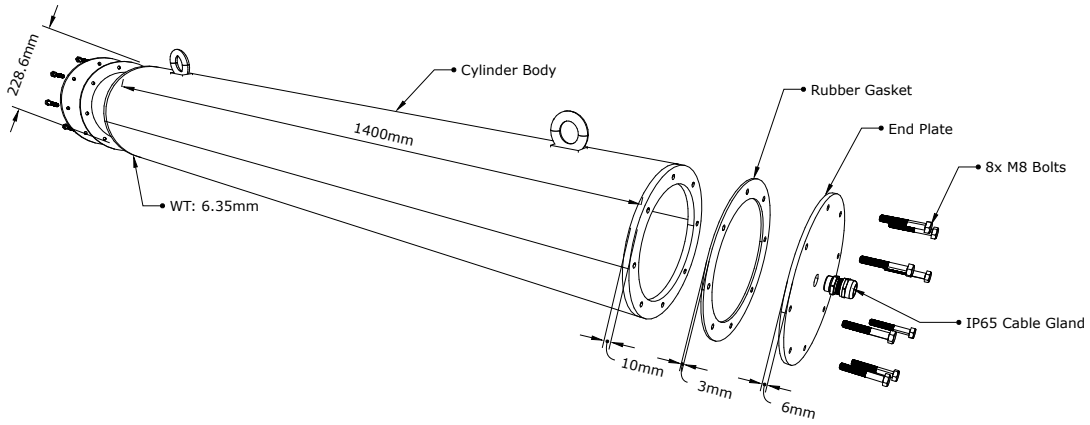

Figure 6.15: Construction of the aluminium cylinder

of the cylinder cause an increase in acoustic scattering. Therefore, the structural response of the experimental cylinder has first been characterised to identify the modal frequencies of the structure. For the purposes of these initial measurements, the cylinder was suspended on a rigid steel frame from two mounting points, as shown in Figures 6.15 and 6.16.

An array of 10 control actuators (Tectonic Elements TEAX32C30-4/B) was distributed over the inside of the cylinder, glued to the inner wall of the shell using epoxy resin [89] as shown in Figure 6.16, with one of the 10 actuators stuck to the end cap. A second array of 12 accelerometers was placed onto the cylinder, arranged in a single line parallel to its central axis. The transfer function between each accelerometer and each control shaker was measured, before moving the accelerometer array by 45 degrees radially around the central axis of the cylinder and repeating. This was carried out for all 45 degree increments, resulting in 96 total measurement positions.

The dSpace DSP platform was chosen to perform the measurements as it allows for the future implementation of a realtime processing loop, such as an AVC system. A dSpace Autobox RTI1005 was connected to a DS2103 DAC card and a DS2003 ADC card, set to a sampling frequency of 2.1 kHz. These were configured to generate gaussian white noise, and to output it through each secondary shaker in turn via a Benchmaster 21M Kemo low-pass filter (cutoff at 1000 Hz) and a Monacor STA1508 power amplifier. The structural response was measured by 12 x PCB A352/C67 accelerometers, which were powered by a PCB481 signal conditioner. A loudspeaker was used as the primary disturbance, and was also driven with broadband noise through a Benchmaster 21M Kemo low-pass filter (cutoff at 1000 Hz) and a Monacor STA1508 power amplifier. A 60 s measurement was carried out,

with the level normalised such that the loudspeaker achieved 100 dBA at the surface of the cylinder. The loudspeaker was positioned at the $\theta = 45°$ $\phi = 45°$ position, as detailed in Figure 6.3. An overview of the measurement signal chain can be seen in Figure 6.17, and images of the experimental setup are shown in Figure 6.16. All of the serial numbers for the transducers used in this set of experiments can be found in Appendix H.

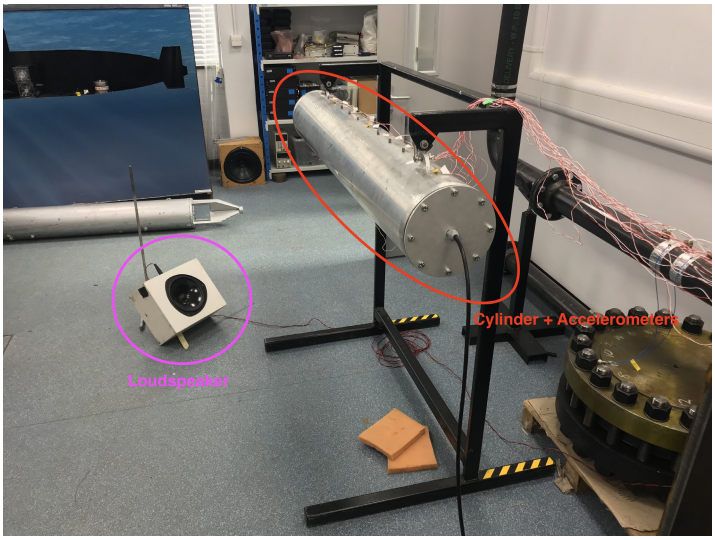

(a) A photograph of the experimental setup, showing the cylinder, loudspeaker, control actuators and accelerometers.

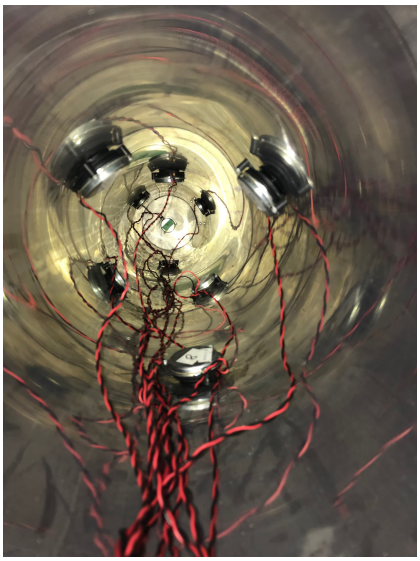

(b) A photograph showing the location of the actuators, stuck to the inside of the cylindrical shell.

Figure 6.16: Images of the experimental setup

The experimental setup outlined above was used to generate a 96x10 matrix of plant responses between 10 structural excitation positions and 96 accelerometer positions, and a 96x1 matrix of plant responses between one acoustic source and 96 accelerometer positions. The overall structural frequency response of the cylinder has been represented by averaging the squared magnitude of the transfer responses over every shaker/accelerometer combination, to give a single frequency response plot, as shown in Figure 6.18. For reference, the structural response from the computational model presented previously in this chapter is also shown in Figure 6.18.

Figure 6.18 shows consistent results between the modelled and measured responses, with the frequency of the first mode being almost exactly identified by the model. The two modes around 500 Hz are closer together in the measurements than the model whilst larger differences between the measured and simulated responses can be observed at the higher frequency resonances. Whilst Figure 6.18 shows the response of the structure to a structural excitation, the response of the structure to an acoustic excitation has also been calculated (using the loudspeaker as the primary disturbance), but has not been presented as it shows an almost identical result to those shown in Figure 6.18 but with a slightly higher noise floor.

There are differences between the measured and modelled responses presented in Figure 6.18, with small errors being observed in the relative magnitude and frequency of the lower modes, but much more significant differences being observed at higher frequencies. Whilst

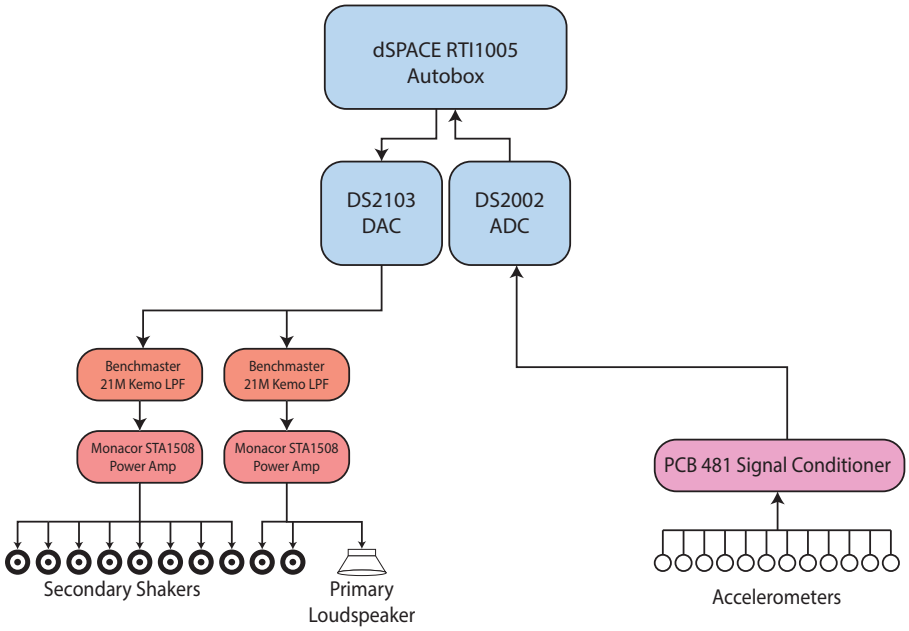

Figure 6.17: Frequency response measurement signal chain

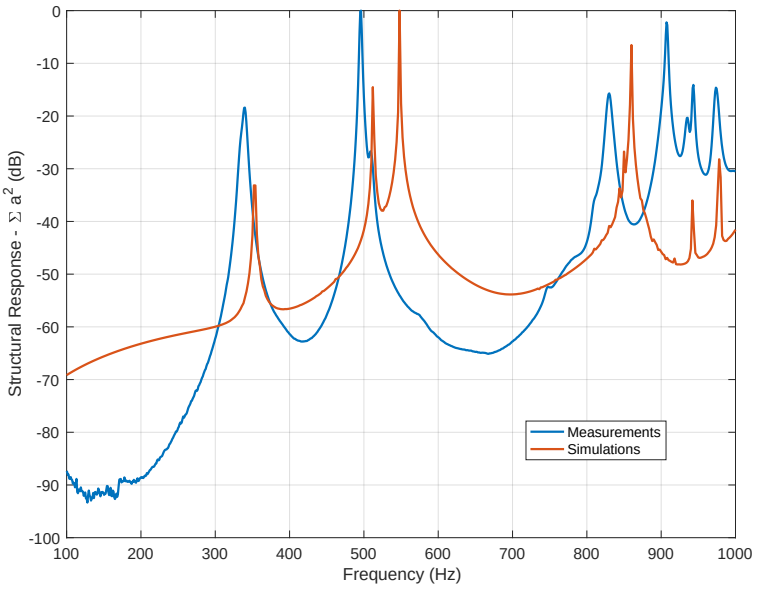

Figure 6.18: Measured frequency response of the cylinder, averaged over excitation position and measurement position. The simulated frequency response is also included.

these could be due to slight inconsistencies in the exact properties of the aluminium material used in the model, or the fact that the model assumes free boundary conditions whereas the real-life cylinder is suspended at two points, as shown in Figure 6.16, it could also be caused by the annulus structure. The model assumes a perfect cylinder, whereas in real-life the removable end caps require an annulus to be welded to the end of the cylindrical shell for them to bolt into. There is also a rubber gasket between the end caps and the annulus, to prevent non-linear interactions between the two hard surfaces, which will add damping in the real-life system. Additionally, the presence of the 10 actuators shown in Figure 6.16 will act like Tuned Mass Damper (TMD)s tuned to the fundamental resonance of the actuators. A discussion of this, and other potential discrepancies between the simulations and experiments discussed in this chapter, is presented in Appendix I.

To explore the experimental structural responses in more detail and understand how each resonance shown by the responses presented in Figure 6.18 relates to the modes of the structure, the magnitude of the measured acceleration (at a given frequency) from the primary acoustic excitation was plotted as a colormap onto the surface of a cylinder. Figure 6.19 shows a selection of the measured acceleration profiles, and their corresponding mode shapes from the computational model. Figure 6.19 shows that the computational model is accurately identifying the first 4 mode shapes of the cylinder to within 65 Hz of their true value, with the largest error occurring in the identification of the bending mode. This is to be expected, as the bending mode has antinodes at the two ends of the cylinder, and these are the locations where both the presence of the annulus and the suspension points will have the greatest effect on the structural response. In addition, the accelerometer array used for these measurements did not extend right to the end of the cylinder, and so it is possible that the acceleration at the very tip of the cylinder is significantly greater than presented in Figure 6.19. A discussion of potential discrepancies between the simulations and experiments discussed in this Chapter is presented in Appendix I

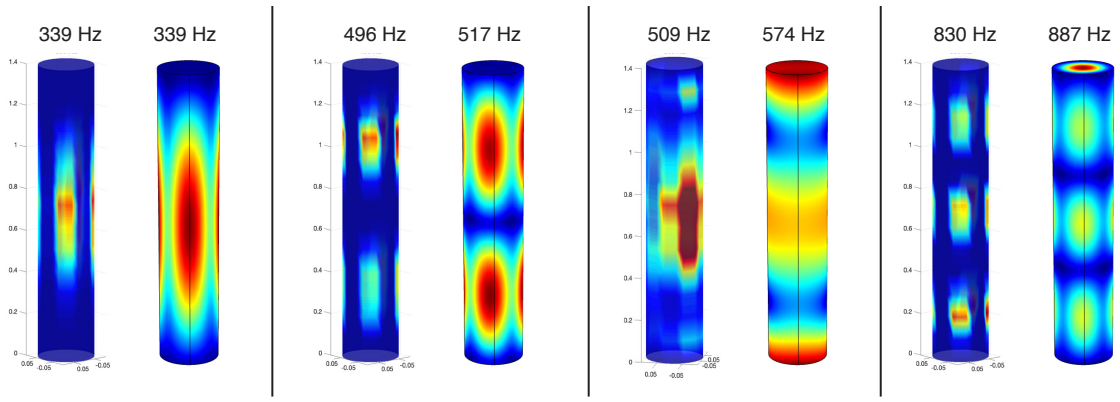

Figure 6.19: A set of surface plots comparing the operational deflection shapes of the measured resonances of the cylinder with the mode shapes from the computational model

6.2.2 Control Performance

To investigate the effect of AVC on the scattered acoustic field, a practical AVC system was designed and implemented using the dSPACE DSP platform. Due to the complex operational deflection shapes shown in Figure 6.19, it was decided that a Multiple Input Multiple

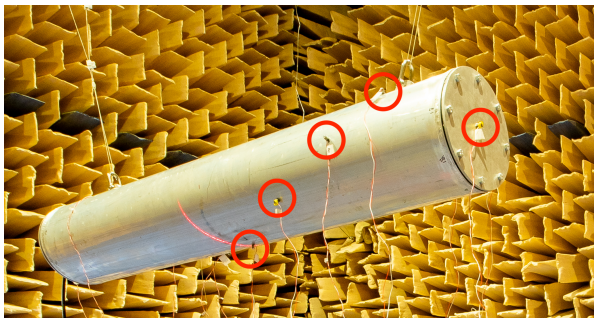

Figure 6.20: Photograph of the experimental setup, showing the accelerometers mounted to the cylinder.

Output (MIMO) system should be used, enabling global control to be achieved at higher frequencies. Although, in the previous section, 96 accelerometer positions were used, it is clearly impractical to realise this many sensors on a small scale structure such as the cylinder in question; and this would also result in an extremely high computational demand for the active control system. Therefore, a spiral array of 12 accelerometers was implemented on the cylinder as shown in Figure 6.20. Whilst a spiral pattern is unlikely to be the optimal arrangement of accelerometers for any of the frequencies discussed here, it can be seen from Figure 6.4 that a spiral arrangement will ensure that at least 6 accelerometers will fall outside of nodal regions across the bandwidth being investigated.

The aluminium cylinder has been suspended in an anechoic chamber, with an array of 20 PCB 130F20 ICP Microphones surrounding it, as shown in Figure 6.21. It was shown in the modelling discussed previously in this Chapter that the scattering is fairly consistent around the vertical plane of the cylinder and, therefore, a simple 2-dimensional evaluation of the scattered field should be sufficient. As only planar power measurements are required, it was decided that a ring of microphones would be used rather than a fully enclosing sphere of microphone positions, as defined in ISO3745 [90]. To ensure that the alignment of all of the microphones and loudspeaker positions was consistent, a digital turntable was placed at the centre of the array and used to measure each angle to an accuracy of $\pm 0.01°$. A laser level was secured to the turntable, and used to trace out a radius (with the angle set by the turntable) along which the loudspeaker or microphone should sit. Precise positioning of all of the transducers used in the experiment allows for more in depth post-processing (creating accurate directivity plots for example), and improves the repeatability of the measurements. The measurement microphones were powered by a rack of Fylde 256ac IEPE amplifiers, before going into the dSPACE DSP System. The equipment used for the structural characterisation measurements, shown in Figure 6.17, remains the same. A list of serial numbers for all of the equipment can be found in Appendix H.

The sound power W of a source can be estimated from n far-field acoustic pressure measurements in an anechoic environment as [54]

$$W = \sum_{n} \frac{|p^2|}{2\rho_0 c_0}. \tag{6.7}$$

Therefore, an estimate of the scattered sound power from an object can be calculated by

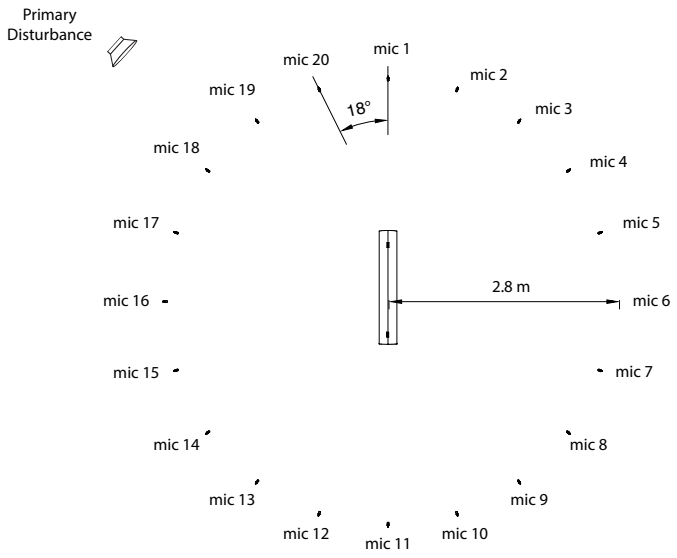

Figure 6.21: Diagram showing the positions of the microphones and loudspeakers used to conduct the scattered sound power measurements

combining Equations 6.3 and 6.7, giving

$$W_s = \sum_n \frac{\left|(p_t - p_i)^2\right|}{2\rho_0 c_0}. \tag{6.8}$$

To provide an accurate comparison to the modelled data, which used an incident sound field with a perfectly flat spectrum, the scattered sound power is normalised by the incident sound power in all measurement results presented in this Chapter.

Figure 6.22 shows the equipment setup in the anechoic chamber. The cylinder was suspended in the chamber to remove any scattering caused by the support structure. All of the measurements were carried out by driving the primary disturbance loudspeaker for 300 s with white noise, band limited to between 100 Hz and 900 Hz, with the level calibrated to achieve 100 dBa at the midpoint of the cylinder.

All of the microphones were calibrated using a Larson Davis CAL250 class 1 Calibrator, and background noise measurements were taken. The incident field was measured initially, without the presence of the cylinder. The response at all of the microphones was measured to give a vector of incident acoustic pressures, $\mathbf{p}_i$. The cylinder was then placed into the chamber, and the measurement was repeated to provide a vector of total acoustic pressures, $\mathbf{p}_t$. From this, Equation 6.8 can be used to calculate the scattered sound power from the cylinder, W_s. The transfer functions between each control shaker, each microphone and each accelerometer were also measured using 300s of broadband noise, to enable AVC to be investigated offline.

To ensure the repeatability of the measurement procedure, a repeatability study was conducted. The process detailed above was carried out three times, and each time the cylinder was removed and carefully re-positioned in the chamber. The three separate scattered sound

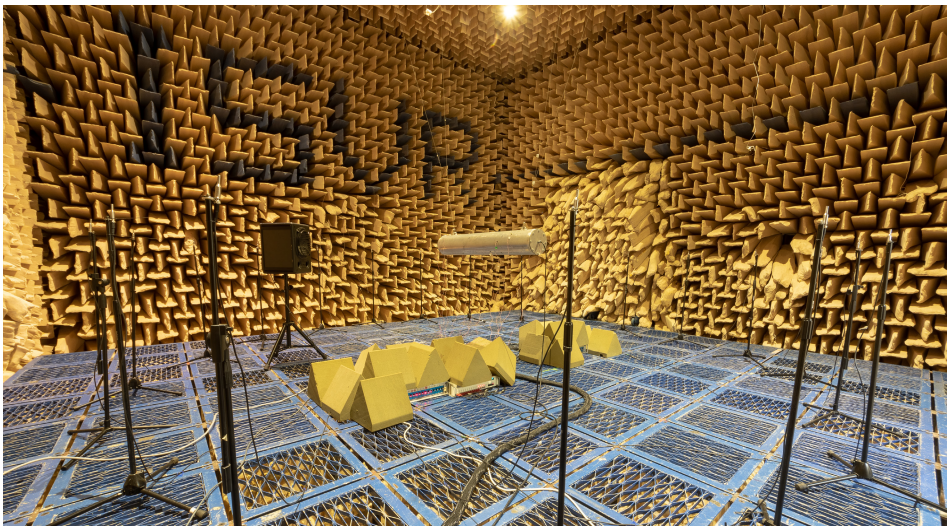

Figure 6.22: A photograph of the equipment setup in the anechoic chamber.

power plots are presented in Figure 6.23. Figure 6.23 shows that the three separate measurements are almost identical, with a maximum variation between them of $< 1\mathrm{dB}$ above 200 Hz. This repeatability study shows that the scattered power being measured is not simply measurement noise or artefact, but is in fact a physical phenomenon.

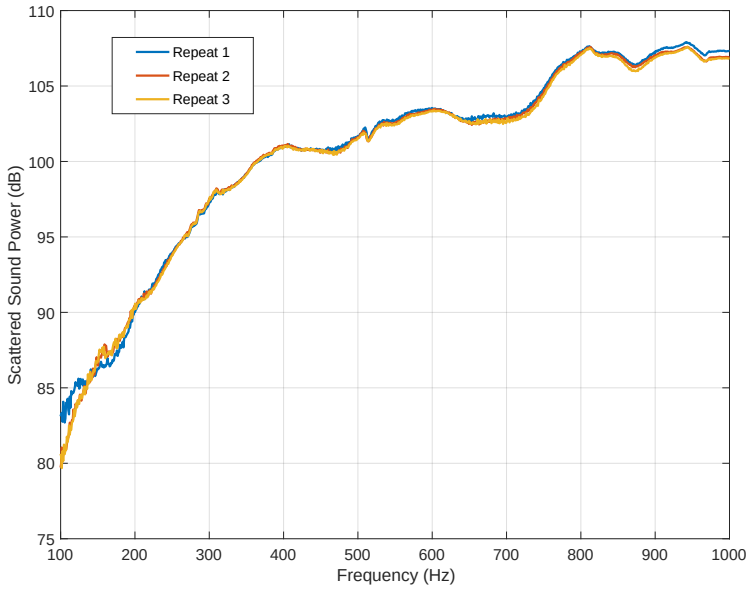

Figure 6.23: A plot showing the scattered sound power from the cylinder, measured on three separate occasions to assess the repeatability of the measurement procedure.

6.2.3 Acoustic Scattered Field

The measured scattered sound power for the system shown in Figure 6.21 is shown in Figure 6.24, when normalised relative to the incident sound power level. Figure 6.24 shows that whilst the general shape is consistent with the predicted sound power shown in Figure 6.9, and there is a slight discontinuity at 509 Hz, corresponding to the first bending mode, there

are no significant peaks in the scattered power. This is thought to be due to a lower level of structural-acoustic coupling, which may be due to a low level of compliance in the measured structure compared to the simulated structure. This may be due to the annulus structure, which was not included in the model, practical variations from the assumed material properties, or due to the differences in the boundary conditions. A lower level of structural-acoustic coupling will result in reduced structural excitation from the incident sound field and, therefore, reduced resonant scattering.

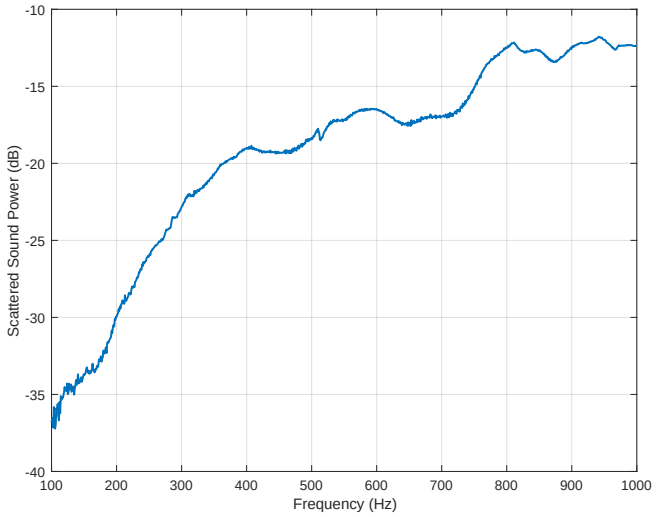

Figure 6.24: Measured scattered sound power, normalised to the incident sound power level.

The polar patterns of the scattered sound pressure at the 4 largest resonances of the cylinder are shown in Figure 6.25, with a grey rectangle identifying the location of the cylinder, and a grey arrow indicating the direction of the incident acoustic wave. The results shown in Figure 6.25 support the modelling results shown in Figure 6.8, with large areas of high acoustic scattering behind the cylinder caused by acoustic shadowing, and areas of high scattering in front of the cylinder caused by acoustic reflections. In general, the reflections become larger at higher frequencies, as the wavelength of the incident acoustic field becomes significantly smaller than the size of the cylinder. This is both consistent with the computational modelling, and with results presented in the literature on acoustic scattering [14, 16, 17, 91].

6.2.4 Effect of AVC on the Scattered Acoustic Field

An optimal harmonic feedforward AVC system has been implemented, as formulated in Section 6.1.5, using the measured transfer functions between the accelerometers and the control actuators, following the same approach used for the simulation results presented in Section 6.1.5. Using Equations 6.5 and 6.6, optimal control forces were calculated at each frequency and the resultant error at each accelerometer was calculated, and is plotted in Figure 6.26. Figure 6.26 show that the AVC system is performing well across the bandwidth, with significant attenuation being achieved at every frequency, and over 15 dB of attenuation at the first bending mode. Whilst the attenuation from the experimental results, shown in Figure 6.26, is lower than the attenuation achieved with the simulated results, shown in Figure 6.13, they cannot be directly compared as the latter had significantly more error sensors and control sources than the former.

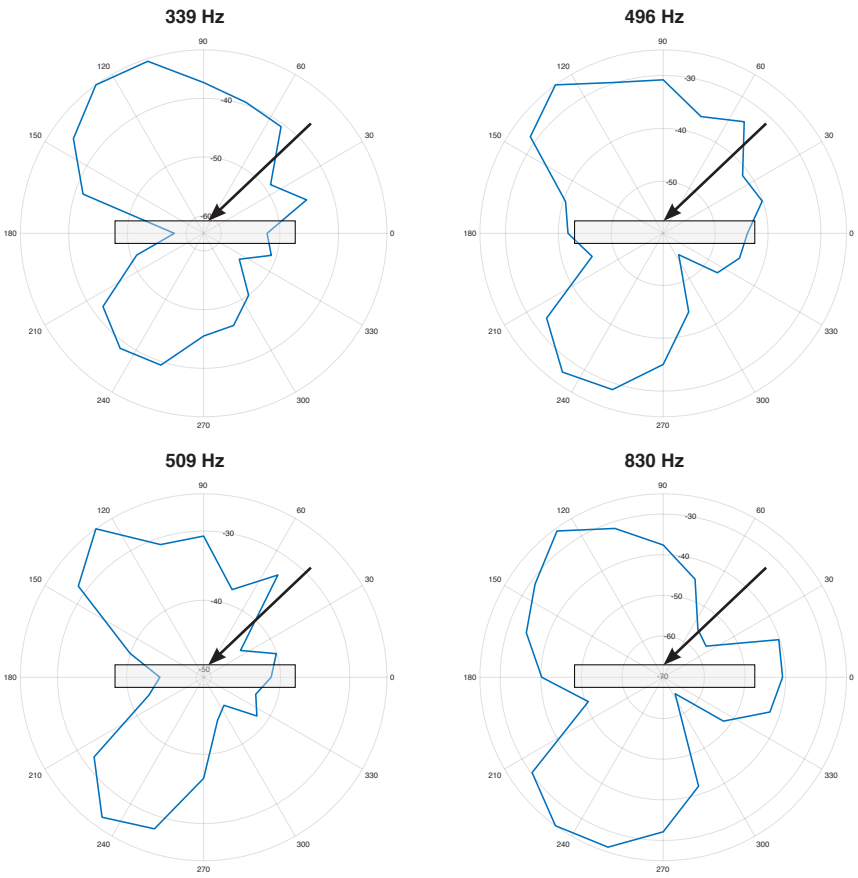

Figure 6.25: Polar plots of the measured scattered sound pressure when the cylinder is excited at the 4 largest structural resonances, whose operational deflection patterns are shown in Figure 6.19. A grey rectangle identifies the location of the cylinder, and a grey arrow indicates the direction of the incident acoustic wave.

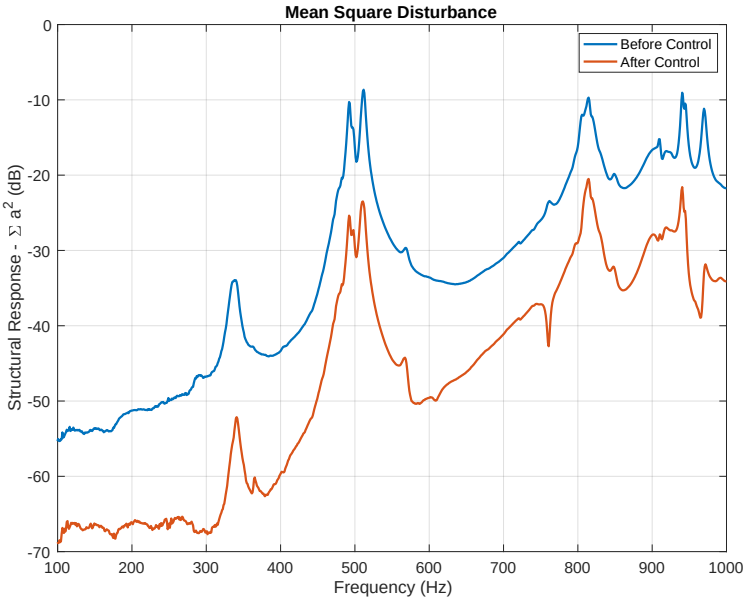

Figure 6.26: Structural response from the experimental cylinder before and after the implementation of AVC

The effect of the AVC system on the acoustic scattered field will now be investigated. The measured responses between the control actuators and the measurement microphones have been combined with the the optimal control signals calculated in the previous section to calculate the vector of pressures after control, $\mathbf{e}_s$, as

$$\mathbf{e}_s = \mathbf{d}_s + \mathbf{G}_a\mathbf{u} \tag{6.9}$$

where $\mathbf{G}_a$ is the structural-acoustic plant matrix between each control shaker and each microphone, and $\mathbf{u}$ is the vector of optimal control sources. Equations 6.7 and 6.8 were then used to calculate the scattered sound power after control, and the achieved attenuation in scattered sound power is presented in Figure 6.27.

Figure 6.27 shows negligible attenuation in the scattered sound power as a result of the AVC system. Whilst there is no significant enhancement, the AVC system appears to have little effect on the scattered sound power. The computational results presented in Section 6.1.5 show how the implementation of an AVC system can successfully reduce the resonant components of the acoustic scattered sound field; however, it was also shown how AVC has minimal effect on the rigid components of the scattered sound field. Figure 6.24 shows that the experimental cylinder is not exhibiting significant resonant scattering and, therefore, it is understandable that the implementation of AVC makes little difference. There are a number of reasons which might prevent significant levels of resonant scattering from occurring in the measured dataset, despite it being predicted from the computational model. These reasons are discussed in detail in Appendix I, and various refinements are made to the model to attempt to quantify these differences.

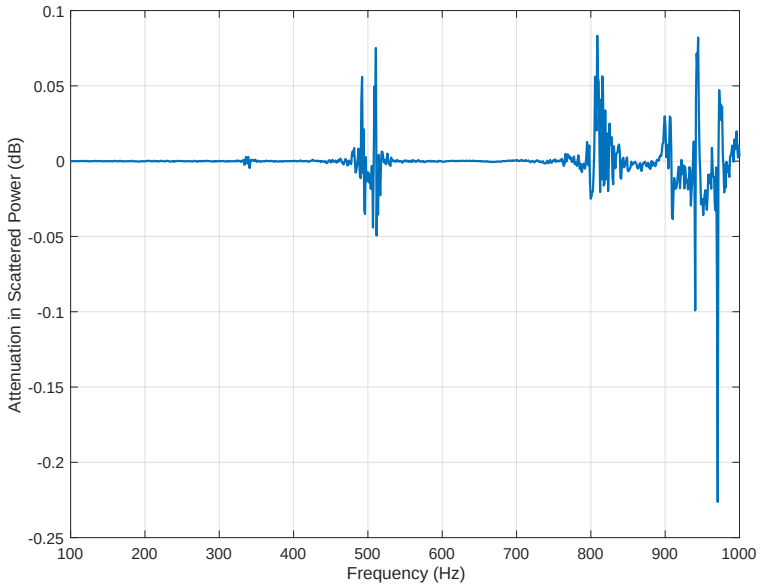

Figure 6.27: Attenuation in the scattered sound power by implementing Active Vibration Control.

6.3 Conclusions

It is known from the literature [11, 71] that the acoustic scattering from a resonant structure can be decomposed into rigid and flexible components. It therefore follows that the implementation of AVC can reduce the resonant component of the acoustic scattering from a flexible body, however this has not previously been demonstrated either experimentally or in simulation. This chapter has presented an investigation into the effect of AVC on the scattered field from a flexible cylindrical scatterer using both computational and experimental studies. The computational dataset was generated using a coupled BEM-FEM model of a flexible aluminium cylindrical shell, implemented in COMSOL Multiphysics. A similar cylinder was manufactured, and suspended in an anechoic chamber with an array of accelerometers stuck to it, and an array of microphones located in the far-field to provide the experimental dataset corresponding to the numerical model. The structural response of the cylinder was characterised in both experimental and computational domains, and it was shown that the model was able to accurately predict the frequencies of the four dominant structural resonances within the bandwidth of interest.

In simulation, the scattered sound power was calculated and it was found that there was a peak in the scattered soundfield when the structure is excited at the resonant frequency corresponding to its first bending mode. In order to potentially control this, AVC was implemented on the simulated cylinder with the direct aim of reducing its structural response to an acoustic excitation. It was shown that, by implementing AVC, the structural response of the cylinder can be significantly attenuated over a wide bandwidth. This had the effect of attenuating the resonant peaks in the scattered sound power such that the acoustic scattering was consistent with that from a rigid cylinder, with no resonant characteristics. It was shown that the rigid component of the acoustic scattering is not influenced by the AVC system and, therefore, the cylinder cannot be considered to be acoustically cloaked. The rigid body com-

ponent of the scattering is still present, however, by reducing the peaks in the scattered field the characteristic properties of the acoustic response are reduced, and the remaining rigid component of the scattered field may be less important in certain applications.

A similar study into the effects of AVC on acoustic scattering was conducted using the experimental dataset. These measurements displayed no significant resonant scattering behaviour within the bandwidth considered, contrary to the predictions from the numerical model, and this was discussed with a more comprehensive investigation being presented in Appendix I. Nevertheless, AVC was implemented and resulted in a significant level of attenuation in the structural response of the cylinder, achieving a 15 dB reduction in structural excitation at the mode which exhibited resonant scattering in simulation. No effect on the scattered sound power was observed, however, due to the lack of resonant scattering in the uncontrolled case. Potential differences between the measured and modelled transfer responses, which may explain the lack of resonant scattering in the measured results, are outlined and discussed in Appendix I.

Chapter 7

Active Structural Acoustic Cloaking, Applied to a Flexible Cylinder

This Chapter will build upon the direct-minimisation acoustic cloaking approach discussed in Chapter 2, and the implementation of active control using structural actuation discussed in Chapter 6, and will present an investigation into the implementation of an Active Structural Acoustic Cloaking (ASACL) system on a flexible cylindrical scatterer. Chapter 2 presented acoustic cloaking results using an optimal harmonic control strategy and, therefore, assumed that a perfect reference signal was available and that there was no constraint on the causality of the controller. Chapter 2, therefore, shows physical insight into the controllability problem, but does not provide an indication as to the level of acoustic cloaking that can be achieved in a realistic implementation.

The use of structural actuation as a control mechanism to minimise acoustic scattering has been previously proposed in the literature [20, 71, 92, 93], with Eggler et al [92] comparing it to Active Structural Acoustic Control (ASAC) systems and referring to it as ASACL. Eggler et al used analytical simulations to investigate the difference in the active acoustic cloaking performance that can be achieved when using either acoustic or structural control sources. This work demonstrated that, for an infinite elastic cylinder, structural point forces are able to achieve higher levels of attenuation in the scattered acoustic field than when using acoustic monopole control sources. This simulation based study investigated the physical limitations of different control actuation arrangements, however, it was assumed that a perfect reference signal was available and that there was no constraint on the causality of the controller.

The current chapter will build upon both the published work by Eggler et al [92], and the previous chapters in this thesis, by presenting an investigation into the practical limitations of an ASACL system using practical reference signals for non-tonal disturbances. An Internal Model Control (IMC) architecture will be used to obtain a suitable reference signal, and the effects of causally constraining the control filters will be explored, as this is required for the control of broadband signals in practice. Additionally, the influence of the active acoustic cloaking strategy on the structural response is investigated, and the requirements in terms of the number of control actuators is also investigated for the realistic structure. Elements of this chapter have been previously published in [94].

7.1 Experimental Setup

In order to investigate the practical limits on ASACL, a series of both structural and acoustic measurements have been carried out in the Large Anechoic Chamber at the Institute of Sound & Vibration Research. A thorough description of the experimental procedure and the exact details of the equipment used are presented in Chapter 6, although the following section will briefly summarise these details. As shown in Figure 7.1, the scattering body utilised during this study consisted of a hollow aluminium cylindrical shell of length 1.4 m, radius 0.23 m and wall thickness 6.4 mm, which was suspended inside the anechoic chamber on a pair of flexible mounts. Full details of the geometry of the cylinder are presented in Appendix G.

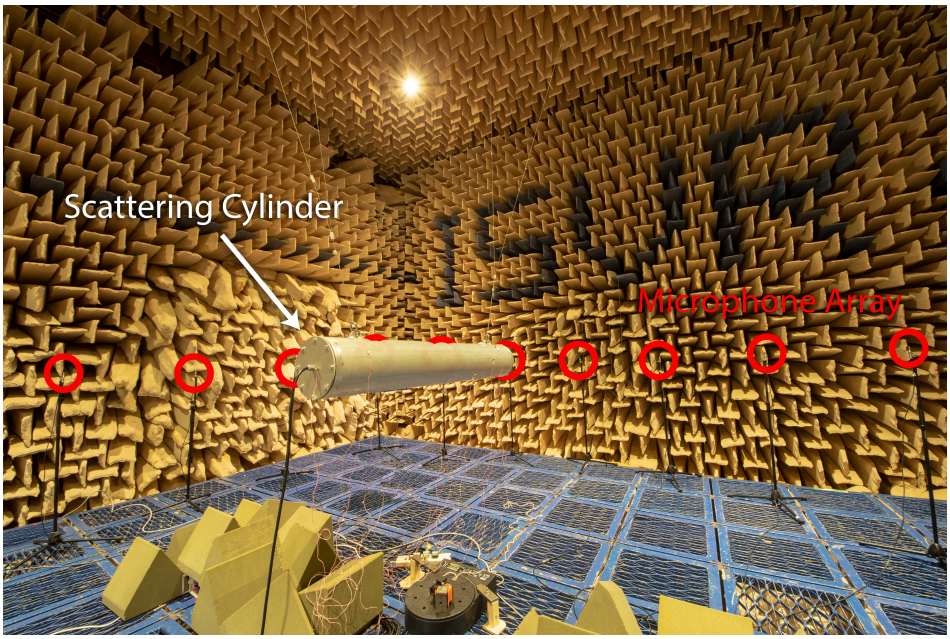

Figure 7.1: Photograph of the experimental setup, showing the cylinder and far-field microphones.

When designing a control system, it is important to ensure that the disturbance to be reduced is both controllable and observable [95]. That is, the error sensors should be located such that they are able to fully characterise the disturbance to be controlled, and the control sources should be located such that they are able to reduce the unwanted disturbance. An exhaustive set of structural measurements and computational simulations have been carried out to accurately characterise the structural response of the experimental scattering object, which were presented in detail in Chapter 6. The full structural response was presented in Figure 6.6, which shows four dominant modes within the considered bandwidth of 100 Hz to 1 kHz. The experimentally identified operational deflection shapes for these modal frequencies have been re-plotted in Figure 7.2, along with the corresponding modal frequencies from the computational model presented in Chapter 6. It can be seen from Figure 7.2 that there is a strong correlation between the numerical and experimental results, with both datasets showing consistent mode shapes for the four dominant modes below 1 kHz. As described in Chapter 6, knowledge of these mode shapes informed the placement of accelerometers and control actuators, as shown in Figures 6.16 and 6.20. A summary of the source/sensor arrangement described in Chapter 6 is shown in Figure 7.3, and the measured data corresponding to this arrangement will be used in the subsequent analysis.

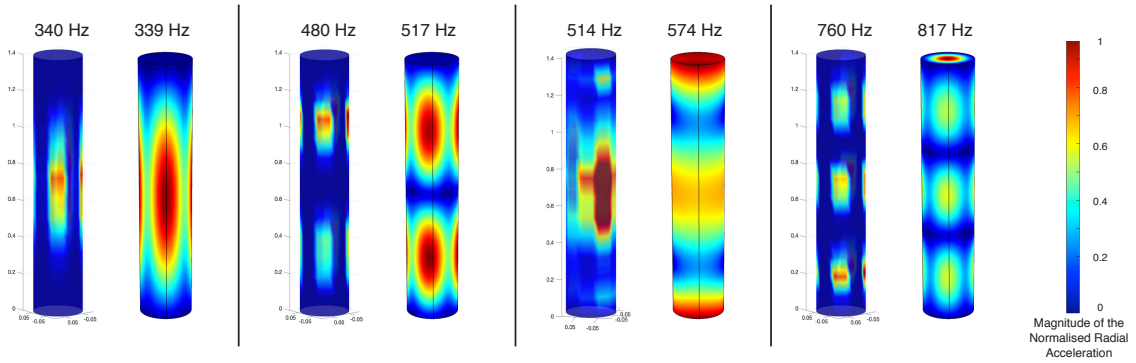

Figure 7.2: The mode shapes and eigenfrequencies of the four dominant structural modes of the cylinder below 1kHz. The left-hand plot in each case shows the measured data and the right-hand plot shows the corresponding results calculated using a numerical model.

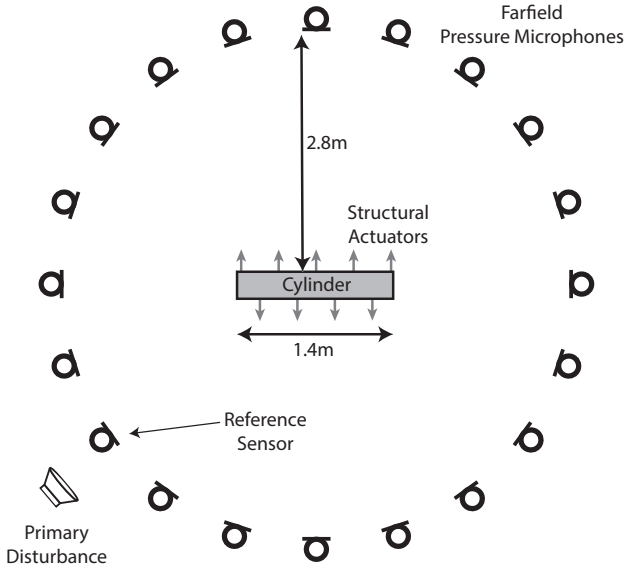

Figure 7.3: Diagram of the experimental layout, showing the scattering cylinder, far-field pressure microphones, structural actuators and primary disturbance location.

The experimental setup shown in Figure 7.3 has been used to obtain the acoustic and structural transfer responses, which will subsequently be used to investigate the performance of ASACL. Transfer responses between each source (1 primary acoustic source and 9 structural control sources) and each structural and acoustic sensor have been measured with the cylinder present in the anechoic chamber. Under this condition, the responses measured at each microphone when the primary source is driven give the vector of total acoustic pressures, $\mathbf{d}_t$, which can be expressed in terms of the linear summation of the vector of incident, $\mathbf{d}_i$, and scattered, $\mathbf{d}_s$, pressures as

To extract the scattered pressures from these measurements, it is necessary to remove the

cylinder and measure the transfer responses between the primary source and the array of microphones, which provides a direct measure of the incident pressures at each microphone location, $\mathbf{d}_i$. According to Equation 7.1, the scattered acoustic pressure can then be calculated at each microphone location by subtracting the vector of incident pressures, $\mathbf{d}_i$, from the vector total pressures, $\mathbf{d}_t$. Although this method provides a measure of the scattered acoustic field that can be utilised to implement an active acoustic cloaking system in a stationary sound field, it is clearly not a practical solution for the implementation of a real-time controller in the presence of changes in the primary disturbance or the acoustic environment. Chapter 5 presents a method to provide a real-time estimation of the acoustic scattered pressure, and alternative methods are presented in the literature [41, 62, 92], however all of these methods rely on knowledge of the acoustic field with and without the scattering body present during a setup stage. The present Chapter focuses on the effectiveness of structural actuation as a control mechanism for active acoustic cloaking and the limitations imposed by a practical causally constrained controller and, therefore, insight can be provided to the control strategy without directly addressing the scattered field detection issue. In the following formulations, the full multi-channel solutions will be presented, which assume that M control sources are used to minimise the scattered pressures at L error sensors, using K reference signals, and a control filter with a tap-length of I samples

7.2 Broadband Control Formulations

This section will describe the feedforward control strategy that will be used to implement an ASACL system. The block diagram showing the architecture of the controller is presented in Figure 7.4, from which it can be seen that the adopted strategy is a feedforward filtered reference system, with an IMC architecture providing the reference signal. One of the areas of novelty of this study is the combination of an IMC architecture with a broadband controller, as the majority of studies presented in the literature implement tonal control strategies which avoid both the problems of causality, and of finding a suitable reference signal. In order to understand the limits on the control performance, the optimal broadband control filters will be derived in this section both with and without causality constraints and these optimal filters will be utilised later in the chapter in conjunction with the measured transfer responses discussed above.

The vector of total acoustic pressures at the array of L error microphones before control, $\mathbf{d}_t$, can be expressed in terms of the summation of the vectors of incident pressures, $\mathbf{d}_i$, and scattered pressures, $\mathbf{d}_s$, at the error microphones which, at a single frequency, gives

$$\mathbf{d}_t = \mathbf{d}_i + \mathbf{d}_s. \tag{7.1}$$

As shown in Figure 7.4, the total pressure at the error microphones after control, $\mathbf{e}_t$, is given by the linear superposition of the total disturbance, $\mathbf{d}_t$, and the pressures at the error microphones due to control, which gives

$$\mathbf{e}_t = \mathbf{d}_t + \mathbf{G}\mathbf{u}, \tag{7.2}$$

where $\mathbf{G}$ is the matrix of complex transfer responses between the M control sources and

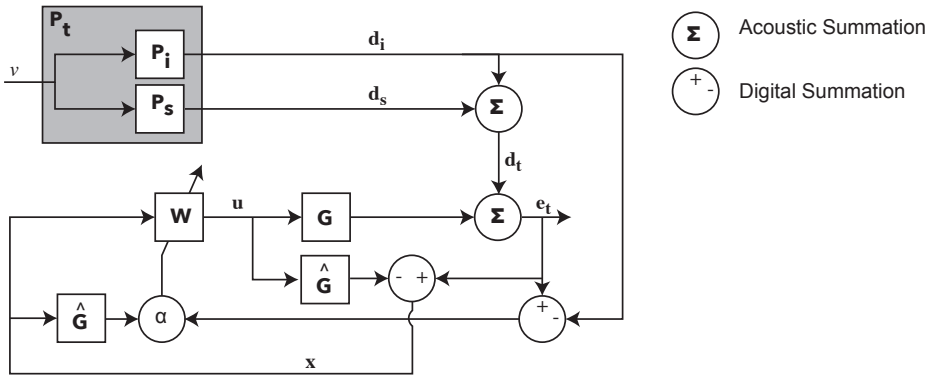

Figure 7.4: Block diagram showing the formulation of the IMC Filtered-Reference Least Mean Squares (FxLMS) active control system where v is the primary source strength, $\mathbf{d}_i$ $\mathbf{d}_s$ and $\mathbf{d}_t$ are the vectors of incident, scattered, and total acoustic pressures at the measurement microphone positions, x is the reference signal, $\mathbf{G}$ is the matrix of vibroacoustic plant responses, and $\mathbf{u}$ is a vector of control signals.

the error microphones, and $\mathbf{u}$ is the vector of M control signals. As shown in Figure 7.4, the control signals are calculated by filtering the vector of K reference signals, $\mathbf{x}$, via the matrix of $(M \times K)$ control filters, $\mathbf{W}$, which gives

$$\mathbf{u} = \mathbf{W}\mathbf{x}. \tag{7.3}$$

The choice of reference signals is critical to the operation of active noise control systems and, in general, the reference signal should be coherent with the error signals and provide some time-advance for the control system to operate. In the case of active cloaking, the primary source generating the incident pressure field is usually unknown and, therefore, cannot be accessed to provide a reference signal. However, as discussed in the introduction, the scattered field, which forms the error signals to be cancelled, is effectively generated by the scattering object. Therefore, it may be possible to position the reference sensors in close proximity to the scattering body to provide some time advance between the reference signals and the outgoing scattered field to be controlled. This is discussed in more detail in Section 7.3.4, where the effect of moving the reference sensor is investigated using computational data. In the present study, a single layer of error microphones is employed, as shown in Figures 7.1 and 7.3, in conjunction with a filtered-reference least mean squares (FxLMS) adaptive algorithm and an IMC structure [96]. Using this control architecture, the reference signals, $\mathbf{x}$, are provided by estimates of the disturbance signals at the error microphones. Although this may somewhat limit the time advance between the reference and error signals, it provides a highly coherent reference signal and has been shown to be an effective strategy in a variety of practical applications [97, 98]. An estimate of the vector of total pressures at the error microphones before control, $\hat{\mathbf{d}}_t$, can be calculated as shown in Figure 7.4 by compensating for the control source contributions at the error microphones, which gives

$$\hat{\mathbf{d}}_t = \mathbf{e}_t - \hat{\mathbf{G}}\mathbf{u}, \tag{7.4}$$

where $\hat{\mathbf{G}}$ is an estimate of the matrix of plant responses. This estimate will form the vector reference signals $\mathbf{x}$. In the present study, it is assumed that the plant response $\mathbf{G}$ is perfectly

known such that $\mathbf{G} = \hat{\mathbf{G}}$ and, therefore, the control architecture show in Figure 7.4 simplifies to a standard feedforward controller.

In the context of active acoustic cloaking, the aim of the controller is to generate a control field such that the sound field after control is equal to the incident sound field, thus cloaking the scattering body. By substituting Equation 7.1 into Equation 7.2, it can be seen that the total pressure at the error sensors after control is given by

$$\mathbf{e}_t = \mathbf{d}_i + \mathbf{d}_s + \mathbf{G}\mathbf{u}, \tag{7.5}$$

which is the summation of the incident, scattered and control sound fields. Therefore, by cancelling the scattered pressures using the control sources, the total pressure after control becomes equal to the incident field and the scattering body will be effectively cloaked. Minimisation of the scattered acoustic field can be expressed in terms of the space-averaged mean square scattered pressure in the far-field, which can be approximated by the cost function defined as

$$J = \mathrm{E}\left[\mathbf{e}_s^{\mathrm{H}}\mathbf{e}_s\right], \tag{7.6}$$

where E is the expectation operator and $\mathbf{e}_s$ is scattered acoustic pressure at the error sensors after control which can be expressed as

$$\mathbf{e}_s = \mathbf{d}_s + \mathbf{G}\mathbf{u}. \tag{7.7}$$

As shown in Figure 7.4, it is assumed that this can be calculated from the directly measured error signals, $\mathbf{e}_t$, as

$$\mathbf{e}_s = \mathbf{e}_t - \mathbf{d}_i, \tag{7.8}$$

where the incident disturbance signals have been identified a priori.

In the following two sections, the optimal control filters will be calculated that minimise the cost function defined in Equation 7.6, firstly with no constraint on the causality and subsequently when a causality constraint is introduced. The full multi-channel formulations will be presented, which assume that M control sources are used to minimise the scattered pressures at L error sensors, using K reference signals, and a control filter with a tap-length of I samples.

7.2.1 Causally Unconstrained Optimal Controller

The causally unconstrained controller can be derived in the frequency domain. Firstly, combining Equations 7.3, 7.6 and 7.7 gives the cost function to be minimised in Hermitian quadratic form as

$$J = \mathrm{trace}\left[\mathrm{E}\left[\mathbf{G}\mathbf{W}\mathbf{x}\mathbf{x}^{\mathrm{H}}\mathbf{W}^{\mathrm{H}}\mathbf{G}^{\mathrm{H}} + \mathbf{G}\mathbf{W}\mathbf{x}\mathbf{d}_s^{\mathrm{H}} + \mathbf{d}_\mathbf{s}\mathbf{x}^{\mathrm{H}}\mathbf{W}^{\mathrm{H}}\mathbf{G}^{\mathrm{H}} + \mathbf{d}_s\mathbf{d}_\mathbf{s}^{\mathrm{H}}\right]\right]. \tag{7.9}$$

By defining the matrices of power and cross spectral densities between the reference and disturbance signals as

$$\mathbf{S}_{xx} = \mathrm{E}\left[\mathbf{x}\mathbf{x}^{\mathrm{H}}\right], \tag{7.10}$$

$$\mathbf{S}_{xd} = \mathrm{E}\left[\mathbf{d}_s\mathbf{x}^{\mathrm{H}}\right], \tag{7.11}$$

$$\mathbf{S}_{dd} = \mathrm{E}\left[\mathbf{d}_s\mathbf{d}_s^{\mathrm{H}}\right], \tag{7.12}$$

the cost function can be simplified to give

$$J = \mathrm{trace}\left[\mathbf{G}\mathbf{W}\mathbf{S}_{xx}\mathbf{W}^{\mathrm{H}}\mathbf{G}^{\mathrm{H}} + \mathbf{G}\mathbf{W}\mathbf{S}_{xd}^{\mathrm{H}} + \mathbf{S}_{xd}\mathbf{W}^{\mathrm{H}}\mathbf{G}^{\mathrm{H}} + \mathbf{S}_{dd}\right]. \tag{7.13}$$

By differentiating Equation 7.13 with respect to the real and imaginary parts of the matrix of control filter coefficients, and setting the result to zero as detailed in [37], the matrix of optimal control filters is given as

$$\mathbf{W_{opt}} = -\left[\mathbf{G}^{\mathrm{H}}\mathbf{G} + \beta\mathbf{I}\right]^{-1}\mathbf{G}^{\mathrm{H}}\mathbf{S}_{xd}\mathbf{S}_{xx}^{-1}, \tag{7.14}$$

where $\mathbf{I}$ is an identity matrix, and it is assumed that both $\mathbf{G}^{\mathrm{H}}\mathbf{G}$ and $\mathbf{S_{xx}}$ are invertible. To constrain the control effort, and to reduce the effect of poor conditioning on the matrix inversion, Tikhonov regularisation [53] has been included and can be adjusted with the regularisation parameter β to reach a trade-off between nominal performance and robustness.

7.2.2 Causally Constrained Optimal Controller

In practice, when anything but tonal disturbance signals are being considered, it is necessary to constrain the broadband control filters to be causal and the optimal filter responses in this case can be derived in the time-domain, as in [37] for the standard feedforward active noise control system. The following derivation is similar to the formulation presented in Chapter 4, however is repeated here for completeness. The scattered acoustic pressure measured at the l-th error microphone after control can be expressed at the n-th time step as

$$e_{s_l}(n) = d_{s_l}(n) + \sum_{m=1}^{M}\sum_{j=0}^{J-1}\sum_{k=1}^{K}\sum_{i=0}^{I-1} g_{lmj}w_{mki}x_k(n-i-j), \tag{7.15}$$

where $d_{s_l}(n)$ is the scattered pressure at the l-th error sensor due to the primary disturbance, g_{lmj} is the j-th coefficient of the J-th order FIR filter approximating the plant response between the m-th control source and the l-th error sensor, w_{mki} is the i-th coefficient of the I-th order FIR control filter corresponding to the m-th control source and the k-th reference signal, and x_k is the k-th reference signal. By assuming the controller is time invariant, Equation 7.15 can be rewritten as

$$e_{s_l}(n) = d_{s_l}(n) + \sum_{m=1}^{M}\sum_{k=1}^{K}\sum_{i=0}^{I-1} w_{mki}r_{lmk}(n-i), \tag{7.16}$$

where r_{lmk} is the k-th reference signal filtered by the plant response between the m-th control source and the l-th error microphone. The filtered reference signal can be expressed as

$$r_{lmk}(n) = \sum_{j=0}^{J-1} g_{lmj} x_k(n-j). \tag{7.17}$$

For convenience, Equation 7.16 can be expressed in vector form as

$$e_{s_l}(n) = d_{s_l}(n) + \sum_{i=0}^{l-1} \mathbf{w}_i^{\mathrm{T}} \mathbf{r}_l(n-i), \tag{7.18}$$

where $\mathbf{w}_i$ and $\mathbf{r}_l(n)$ are defined as

$$\mathbf{w}_i = [w_{11i}, w_{12i}, \ldots, w_{1Ki}, w_{21i}, \ldots w_{MKi}]^{\mathrm{T}} \tag{7.19}$$

$$\mathbf{r}_l(n) = [r_{l11}(n), r_{l12}(n), \ldots, r_{l1K}(n), r_{l21}(n), \ldots, r_{lMK}(n)]^{\mathrm{T}}. \tag{7.20}$$

The multichannel control problem can then be formulated by expressing the vector of L error signals in the time domain as

$$\mathbf{e}_s(n) = \mathbf{d}_s(n) + \mathbf{R}(n)\mathbf{w}, \tag{7.21}$$

where

$$\mathbf{e}_s(n) = [e_{s_1}(n), \ldots, e_{s_L}(n)]^{\mathrm{T}}, \tag{7.22}$$

$$\mathbf{d}_s(n) = [d_{s_1}(n), \ldots, d_{s_L}(n)]^{\mathrm{T}}, \tag{7.23}$$

$$\mathbf{R}(n) = \begin{bmatrix} \mathbf{r}_1(n)^{\mathrm{T}} & \mathbf{r}_1(n-1)^{\mathrm{T}} & \ldots & \mathbf{r}_1(n-I+1)^{\mathrm{T}} \\ \mathbf{r}_2(n)^{\mathrm{T}} & \mathbf{r}_2(n-1)^{\mathrm{T}} & \ldots & \mathbf{r}_2(n-I+1)^{\mathrm{T}} \\ \vdots & \vdots & & \vdots \\ \mathbf{r}_L(n)^{\mathrm{T}} & \mathbf{r}_L(n-1)^{\mathrm{T}} & \ldots & \mathbf{r}_L(n-I+1)^{\mathrm{T}} \end{bmatrix}, \tag{7.24}$$

and the MKI vector of control filter coefficients is defined as

$$\mathbf{w} = \left[\mathbf{w}_0^{\mathrm{T}}, \mathbf{w}_1^{\mathrm{T}} \ldots \mathbf{w}_{I-1}^{\mathrm{T}}\right]. \tag{7.25}$$

As in the case of the causally unconstrained controller, the cost function is defined by Equation 7.6. Substituting Equation 7.21 into Equation 7.6 gives the quadratic cost function as

$$J = \mathbf{w}^{\mathrm{T}} \mathrm{E}\left[\mathbf{R}^{\mathrm{T}}(n)\mathbf{R}(n)\right]\mathbf{w} + 2\mathbf{w}^{\mathrm{T}} \mathrm{E}\left[\mathbf{R}^{\mathrm{T}}(n)\mathbf{d}_s(n)\right] + \mathrm{E}\left[\mathbf{d}_s^{\mathrm{T}}(n)\mathbf{d}_s(n)\right]. \tag{7.26}$$

Assuming that $\mathrm{E}\left[\mathbf{R}^{\mathrm{T}}(n)\mathbf{R}(n)\right]$ is positive definite, this cost function has a unique global minimum and the optimal set of control filters that minimises the scattered acoustic field at the error sensors is given as

$$\mathbf{w}_{opt} = -\left[\mathrm{E}\left[\mathbf{R}^{\mathrm{T}}(n)\mathbf{R}(n) + \beta\mathbf{I}\right]\right]^{-1}\mathrm{E}\left[\mathbf{R}^{\mathrm{T}}(n)\mathbf{d}_s(n)\right]. \tag{7.27}$$

As with the causally unconstrained solution given by Equation 7.14, Tikhonov regularisation has been included, which introduces a constraint on the control effort, via the regularisation parameter β.

7.3 Experimental Investigation of Active Structural Acoustic Cloaking Limitations

In the following analysis, the acoustic measurements described above will be used to investigate the performance limitations of the proposed feedforward control strategy both with and without a constraint on the causality. As shown in Figure 7.3, the total pressure measured at the microphone directly in-front of the primary disturbance will be used to provide the reference signal, which will be calculated using the IMC structure shown in Figure 7.4. In practice it would not necessarily be known where the primary disturbance is relative to the scattering object and, therefore, it may be necessary to use a DOA estimation process to select the most suitable reference signal or signals to use. The FxLMS controller will be implemented using $M = 9$ control actuators to minimise the scattered acoustic pressure at $L = 20$ far-field microphones using a control filter of length $I = 512$ samples at a sampling frequency of $f_s = 2500$ Hz. In the present study, the regularisation parameters in each case have been selected so as to ensure that the magnitude of the dominant peak in the control filter impulse responses are approximately equal between the causally constrained and causally unconstrained control filters to enable a sensible comparison between the two configurations; however, it should be noted that an alternative approach would be to regularise both controllers such that the overall power of the impulse responses are equal.

7.3.1 Limits Due to Causality

In order to understand the limits on the performance of the ASACL control system described above, this section will compare the performance of the causally constrained and unconstrained controllers in order to provide insight into the limits imposed by both enforcing causality and the proposed method of obtaining a time-advanced reference signal. The performance of the control systems can be evaluated in terms of the cost function defined in Equation 7.6 and, provided that the error microphones are positioned in the far-field, this can be related to the scattered sound power as [54]

$$W_s = \frac{J}{2\rho_0 c_0} \tag{7.28}$$

where ρ_0 is the fluid density and c_0 is the speed of sound in the fluid.

The scattered sound power has been calculated for both the causally unconstrained and constrained controllers, and is presented in Figure 7.5, along with the scattered sound power

before control. From these results it can be seen that the causally constrained controller is able to achieve between 5 and 10 dB of attenuation across the presented bandwidth. By removing the constraint on the causality of the control filter, it can be seen that performance at frequencies below around 400 Hz is significantly increased, with an attenuation of around 20 dB at 100 Hz. At frequencies above approximately 500 Hz, however, the difference between the causally constrained and unconstrained controllers is less than 1 dB.

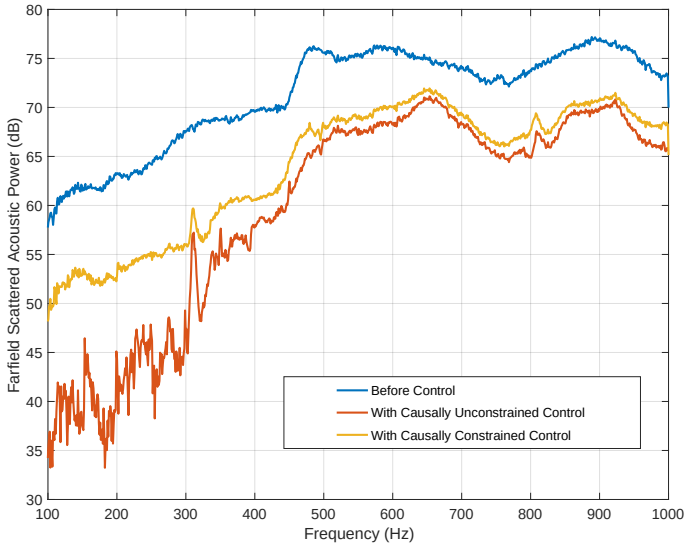

Figure 7.5: The scattered power before control, with broadband unconstrained control, and with broadband causally constrained control.

The difference in performance achieved between the causally constrained and unconstrained controllers can be explained by evaluating the time-advance provided by the reference signal. This can be evaluated in terms of the group delay [99] between the reference signal, calculated according to Equation 7.4, and the scattered pressure error signal at the same microphone position, given by Equation 7.7. The calculated group delay is shown in Figure 7.6 as a function of frequency and, from these results, it is shown that the proposed reference signal provides a time advance compared to the error signal of around 6 ms over the considered bandwidth. There is a slight increase in the group delay with frequency, but importantly, at lower frequencies the time advance is not much greater than the period of oscillation, and this limits the achievable control performance at lower frequencies when causality is enforced, as shown in Figure 7.5. For reference, the impulse response of the control filter corresponding to the first actuator for the causally constrained and unconstrained control strategies is presented in Figure 7.7, and this shows the significant non-causal component in the unconstrained filters. It is interesting to note that the impulse response for the causally constrained controller, shown in Figure 7.7, has significantly higher levels of energy throughout the tail of the response, whereas the response for the causally unconstrained controller decays to negligible levels rapidly after the main peak. This may suggest that the controller is utilising the modal response of the structure, which is periodic and, therefore, predictable, to achieve enhanced control without requiring acausal components. The control filter responses for all 9 actuators are consistent in form to the examples presented in Figure 7.7.

Whilst Figure 7.5 presents the performance of the two control algorithms over frequency, it is also insightful to observe how the control strategies affect the directivity of the acoustic scat-

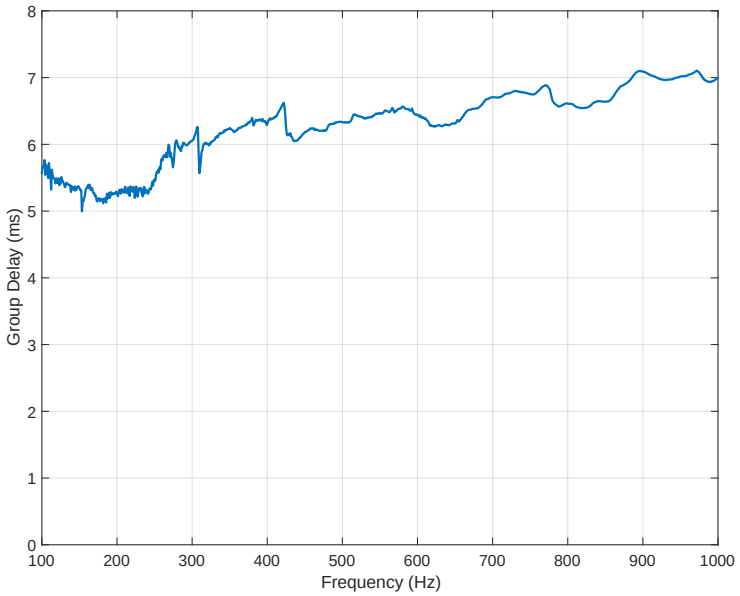

Figure 7.6: The group delay between the reference signal and the scattered pressure error signal at the reference microphone, as shown in Figure 7.3.

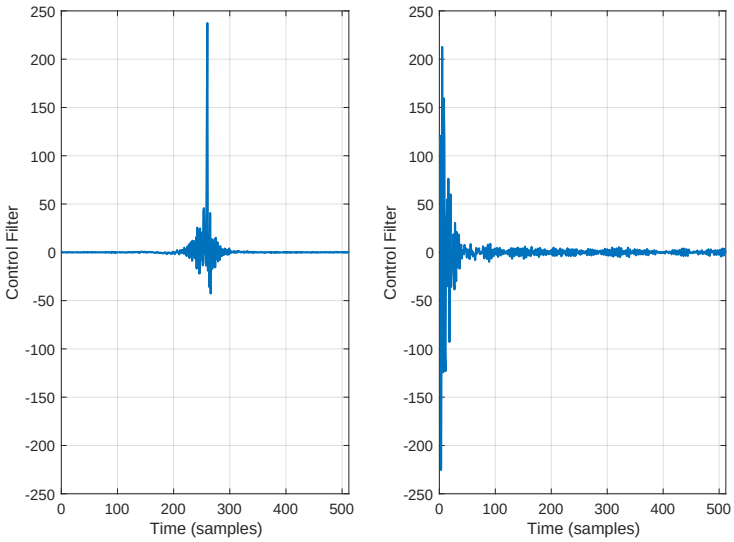

Figure 7.7: The impulse responses of the control filter for the first actuator, with both the causally unconstrained (left) and causally constrained (right) controllers.

tered pressure. Figure 7.8 shows the directivity of the scattered pressure at the frequencies corresponding to each of the four dominant modes of the structure, as identified in Figure 7.2. The directivities of the scattered pressure are shown both before control, and after control using the causally constrained and unconstrained control strategies. For reference, the orientation of the cylinder has been marked on each plot in Figure 7.8 and the direction of propagation of the incident field is indicated by the arrow. The 480 Hz and 514 Hz plots in Figure 7.8 clearly show the two main lobes of the scattered pressure field, with the specular back-scattering occurring in the 120° direction and the scattered field that results in acoustic shadowing being most prominent in the 240° direction. It is interesting to note that while the ASACL strategies are effective at achieving significant reductions in the acoustic scattered power, as shown by the results presented in Figure 7.5, it is clear from the results in Figure 7.8 that both constrained and unconstrained controllers produce some enhancement in the acoustic scattered pressure in certain directions. In general, these enhancements occur in directions where the uncontrolled scattered field is low in level and, therefore, the controllers are effectively trading off the enhancement to achieve significant reductions in directions where the uncontrolled scattered field is dominant.

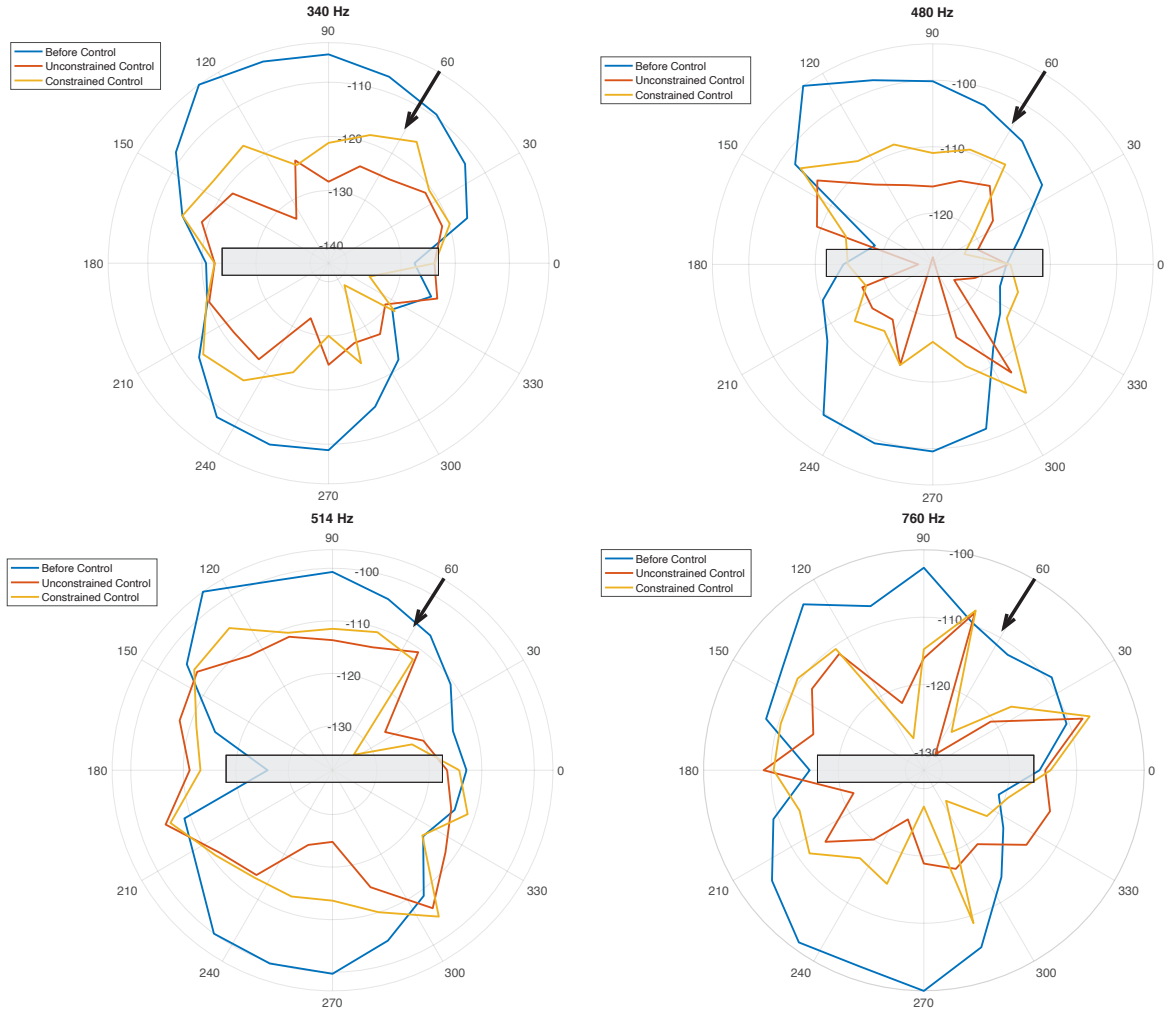

Figure 7.8: Polar plots showing the directivity of the scattered pressure field at the frequencies corresponding to the four dominant modes of the cylinder before control, with broadband unconstrained control, and with broadband causally constrained control. The direction of the incident wave is marked with an arrow.

To provide more insight into the effects of constraining the causality of the control system, the control effort for each controller has been calculated as

$$\mathrm{CE} = 10 \log_{10} \left[\mathbf{u}^{\mathrm{H}} \mathbf{u} \right] . \tag{7.29}$$

The control effort provides an indication of the power required by a control system and the results for the causally constrained and unconstrained controllers are presented over frequency in Figure 7.9. These results show that the causally constrained controller requires significantly more energy at low frequencies, despite achieving a lower level of reduction in the scattered power. Above approximately 800 Hz, both the causally unconstrained and causally constrained controllers are almost identical in terms of both performance and control effort. It is worth noting that the performance of any practical system will be limited by the maximum force output of the control actuators, and it should be ensured that the required control effort is within the linear operating range of the actuators.

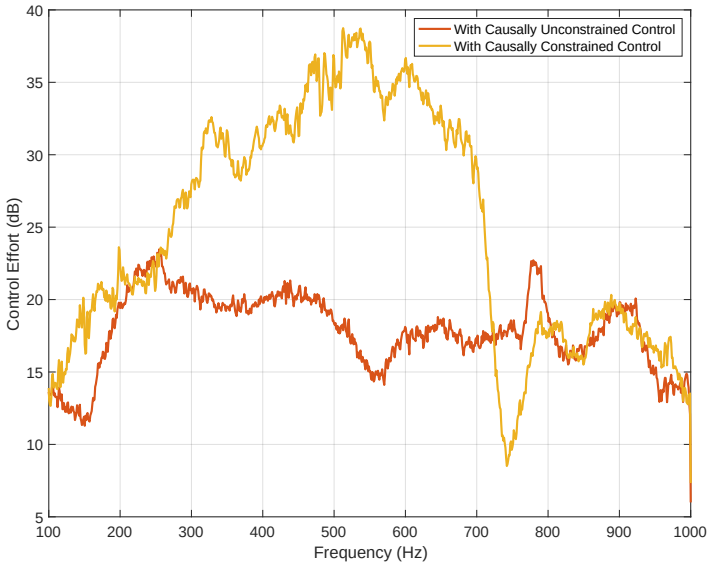

Figure 7.9: The control effort in decibels plotted against frequency for both the causally unconstrained and causally constrained controllers.

7.3.2 Effect of Active Cloaking on the Structural Response

In addition to investigating the effect of ASACL on the scattered acoustic field, it is also insightful and of practical interest to investigate how the structural response of the cylinder is affected by the active cloaking strategy. In certain applications, an ASACL system that significantly increases the vibration of the structure would not be acceptable and, therefore, it may be necessary to constrain the levels of structural enhancement or adopt alternative control methods.

As described previously, and as shown in Chapter 6.20, an array of 12 accelerometers was attached to the cylinder to measure the radial component of the cylinder vibration when excited by the incident acoustic wave. Figure 7.10 shows the sum of the squared accelerometer signals when the cylinder is excited by the primary acoustic field, and when acoustic scattering is controlled using the two control formulations. Figure 7.10 clearly shows the four main

structural resonances of the cylinder, corresponding to the dominant modes outlined in Figure 7.2. From these results it can be seen that both control strategies result in a significant increase in the structural vibration across the presented frequency range. This indicates that the structure is effectively being used as an acoustic radiator to achieve the acoustic control, as in the case of active structural acoustic control systems [100–104]. This result also indicates that rather than the active cloaking system driving the structure to behave as an acoustically rigid body which scatters less on resonance than an elastic body [20, 74], as discussed in Chapter 6, the structure is being driven in a more complex manner to maximise the reduction in the scattered acoustic field. The differences between the causally constrained and causally unconstrained results shown in Figure 7.10 can be related to the corresponding differences between the control efforts in each case, as shown in Figure 7.9.

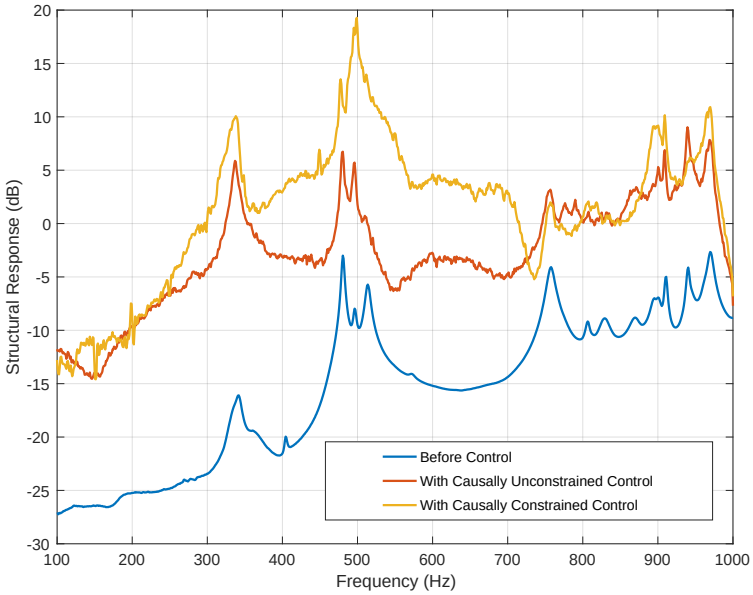

Figure 7.10: The structural response of the cylinder when it is excited by the incident acoustic field without control, and with both causally unconstrained control and causally constrained control.

7.3.3 Limits Due to Number of Control Actuators

It has been shown in the previous sections that the structural actuator array is able to effectively reduce the scattering from the finite-sized cylinder and the limits due to the use of a practical reference signal and imposing causality on the controller have also been demonstrated. However, in most practical applications, it is beneficial for the active control system to be as light weight and low-cost as possible. This can be achieved by minimising the number of control actuators required. For this reason, an investigation into the reliance of the implemented ASACL system on the number of control actuators has been carried out. Although a similar study into the effect of the number of control actuators was carried out by Eggler et al [92], this previous study investigated a cylinder of infinite length via numerical simulations. Therefore, it is of interest to investigate the influence of the number of structural control actuators for the experimental configuration presented here.

The performance of the ASACL system in terms of the broadband average attenuation in

the scattered sound power has been calculated for increasing numbers of actuators between 1 and 9. In each case, the optimal configuration of actuators was selected through an exhaustive search. Due to the computational complexity of an exhaustive search, only the performance of the causally unconstrained controller has been investigated; however, these results are expected to be consistent regardless of the causality of the controller. Figure 7.11 presents the scattered sound power over frequency before control and with the causally unconstrained controller for an increasing number of control actuators. From these results it can be seen that with a single control actuator, reduction in the scattered acoustic pressure can only be achieved at frequencies below around 250 Hz. As the number of control actuators is increased, the control bandwidth also increases, and with 5 control actuators significant levels of control are achieved across the presented bandwidth. Increasing the number of control actuators further offers some further improvements in the level of control achieved across the presented bandwidth, but the difference in performance between five, seven and nine actuators at frequencies above 500 Hz is less than 3 dB.

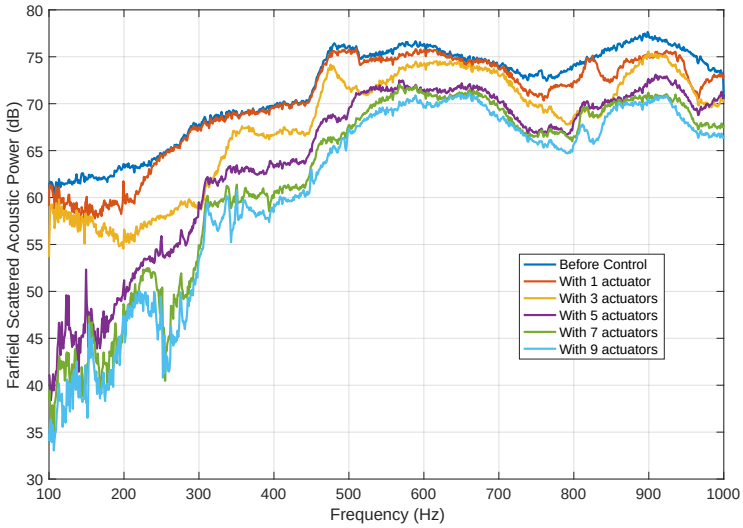

Figure 7.11: The scattered power before control, and with broadband unconstrained control with increasing numbers of control actuators.

To provide further insight into the influence of the number of control actuators used, the performance presented in Figure 7.11 has been averaged over three frequency bands and the frequency averaged attenuation has been plotted against the number of control actuators in Figure 7.12. From these results it can be seen that, whilst the performance has not fully converged in any of the three frequency bands, it has reached a point where the increase in performance achieved by adding additional actuators is less than 1 dB. For example, increasing the number of actuators from 8 to 9 provides a broadband increase in performance of 0.7 dB, 0.8 dB and 0.3 dB in the three bandwidths respectively. It is interesting to note that to achieve a broadband average attenuation of around 6 dB requires 2 actuators up to 250 Hz, 4 actuators up to 500 Hz and 7 actuators up to 1 kHz, suggesting a doubling in bandwidth approximately requires a doubling in the number of control actuators.

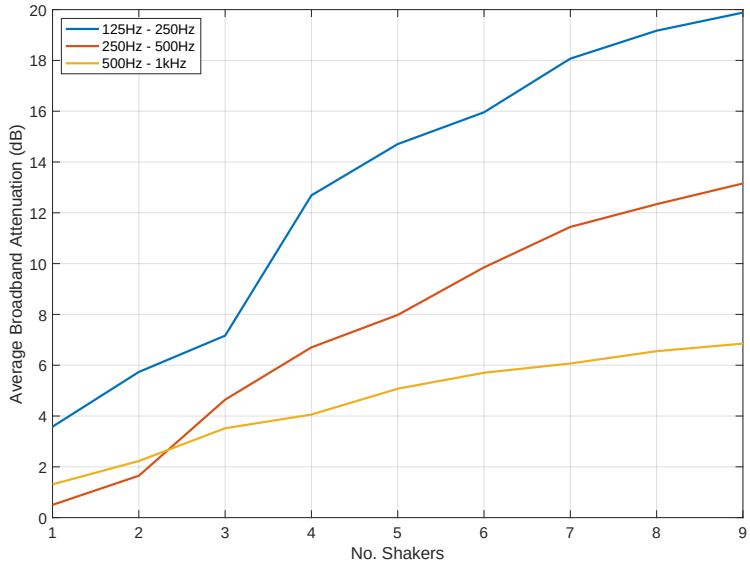

Figure 7.12: The frequency averaged attenuation within three frequency bands, for increasing numbers of control actuators

7.3.4 Limits Due to the Reference Signal

It is well known that, in the case of causally-constrained broadband active control, the performance of the controller is heavily dependent on the suitability of the reference signal(s). As has been discussed previously, the reference signal must be both time advanced compared to, and coherent with, the disturbance signal. This study has made use of an IMC structure to obtain a reference signal for the controller, as shown in Figure 7.4, and it was shown in Figures 7.5 and 7.6 that the low-frequency performance of the proposed system is limited by the time-advance provided by the reference signal. Due to experimental constraints, this practical study used one of the sensors from the far-field microphone array as the reference sensor, however this is unlikely to be the optimal location to obtain a reference signal due to its distance from the scattering object, and the limited time advance that this results in.

To investigate the effect that the position of the reference sensor has on the performance of the ASACL system, the computational FEM-BEM model described in Chapter 6 was used. As described in Chapter 6, this model simulates a flexible thin-walled aluminium cylinder of nominally the same geometry as in the experimental case. A far-field microphone array has been simulated within the computational model, with each sensor positioned consistently with the experimental setup described in Figure 7.3, and an array of structural point forces are simulated on the surface of the cylinder, located to match the experimental setup shown in Figure 6.16. Further to the far-field microphone array, a dedicated reference microphone has been implemented, and its location can move radially on-axis with the incident field. As in Chapter 6, this model has been solved over a range of frequencies between 100 Hz and 1 kHz, and over a range of reference sensor positions between $r = 1.2$ m and $r = 3$ m. The data from this model was then used, in conjunction with Equation 7.27 to simulate a causally-constrained broadband ASACL system for each position of the reference sensor.

The attenuation achieved by the controller is presented in Figure 7.13 for a range of reference sensor positions, plotted at a range of discrete frequencies. It can be seen that, in general,

the performance of the ASACL system deteriorates as the distance between the reference sensor and the scattering object increases, and therefore as the time-advance of the reference signal decreases. This is more obvious at lower frequencies, as the time-advance provided by the reference signal becomes equivalent to, or even less than, the period of oscillation of the scattered wave.

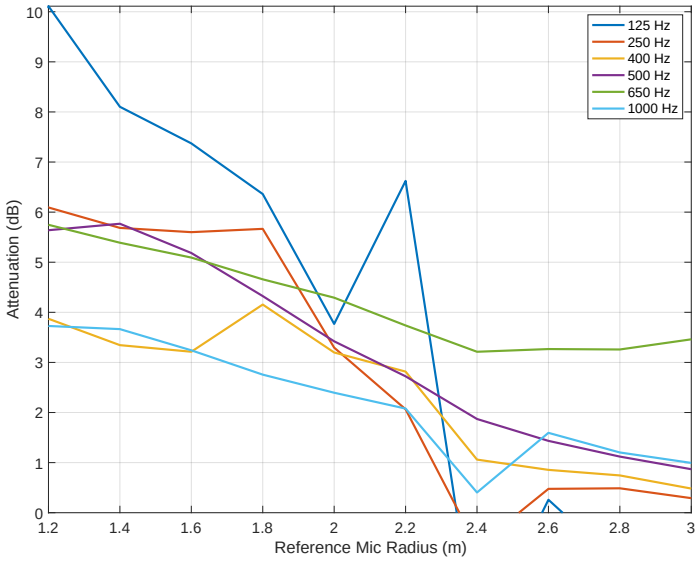

Figure 7.13: The attenuation achieved by the ASACL system for a range of reference sensor positions, plotted at discrete frequencies.

7.4 Conclusions

This chapter has built on the previous work presented in this thesis by applying an Active Acoustic Cloaking system to a practical structure; in this case a flexible aluminium cylinder. Building on previous literature of ASACL, a broadband control strategy has been implemented, using an IMC structure to obtain a reference signal, and the causality of the control filters has been investigated. Using this configuration, it has been shown that at least 10 dB of attenuation in the far-field scattered sound power can be achieved across the bandwidth investigated. The impact of causally constraining the control filters was investigated, and it has been shown that the causality constraint required in broadband control systems limits the performance of the controller, particularly at low frequencies where the time-advance provided by the proposed reference signal is small compared to the period of oscillation, however this can be overcome if the reference sensor can be located in the near-field of the scattering object. It has also been shown that the control effort required by the causally constrained controller is significantly greater than that required by the causally unconstrained controller and this can be related to a reduction in the efficiency of control. The effect of the ASACL system on the structural response of the scattering structure has also been investigated for the first time, and it has been shown that the structural response is significantly enhanced. This may need to be considered in real-world applications, where an enhanced level of structural vibration may not be acceptable. The influence of the number of control actuators on performance has also been investigated, and it has been shown how the number of structural control actuators required for successful acoustic cloaking increases as the bandwidth of control increases, with a doubling in control bandwidth approximately corre-

sponding to a doubling in the number of required actuators.

The presented results provide new insight into the practicability of using structural actuation to minimise the acoustic scattering from an object. However, challenges to the realisation of fully practical active acoustic cloaking strategies that are capable of operating in non-stationary environments are still outstanding. For instance, in a practical active acoustic cloaking system the formulation described in this chapter would need to be combined with the virtual sensing technique described in Chapter 5 so as to avoid relying on unrealistic a priori information about the scattered soundfield. In addition to the real-time estimation of the scattered acoustic pressure, it is necessary to obtain a real-time reference signal. In this chapter, a reference signal has been calculated using an IMC architecture and the signal provided by a microphone located in the direction of the primary source. In a practical implementation, the direction of arrival of the incident wave may not be known and, therefore, multiple reference microphones would need to be used to ensure that at least one reference signal is time-advanced compared to the scattered wave [70].

Chapter 8

Conclusions

In many applications, there is an interest in reducing the acoustic scattering from both rigid and flexible objects subject to an incident soundfield, often referred to as acoustic cloaking. Passive and active methods of acoustic cloaking have been discussed in the literature, however, the latter is the focus of this thesis. The main challenge with implementing an active acoustic cloaking system is the lack of availability of a suitable error signal. Ideally, such a system would directly minimise the scattered acoustic pressure measured in the far-field of the scattering object. However, a microphone placed in the scattered soundfield will provide a signal proportional to the total acoustic pressure, which contains both the scattered and incident components. In addition, placing sensors in the far-field of the scattering object may not be practical for many implementations. There are also a number of other practical challenges associated with implementing an active acoustic cloak in practice, which include considerations of robustness and controller design.

This thesis has primarily focussed on the challenges associated with practically implementing an active acoustic cloaking system, and has addressed the scattered field detection problem, as well as considering alternative control approaches that may not require measuring this in real-time. The robustness of the active acoustic cloaking systems has been investigated, and both rigid and non-rigid scattering objects have been considered. The main conclusions from each of these investigations are reviewed below.

8.1 Active Acoustic Cloaking of a Rigid Sphere

It is known from the literature that the acoustic scattering from an object can be considered to consist of a rigid and flexible component. The work described in Chapters 2 to 5 of this thesis considers the former of these problems, and experimentally investigates the acoustic scattering from a rigid spherical object.

In the first instance, Chapter 2 has described the experimental setup for the investigation of active acoustic cloaking of the rigid sphere, and an optimal tonal control strategy is used to directly minimise the measured scattered acoustic pressure using the transfer responses of the measured system. This work forms the foundation for the remainder of the thesis by highlighting some of the limitations of practical active acoustic cloaking. In particular, although it was shown that the given active acoustic cloaking system was able to achieve up to 18 dB

of attenuation in the scattered sound power, this performance was dependent on both the control source and error sensor arrangements. This is consistent with active control systems in general, with the control source arrangement determining the controllability and the error sensors determining the observability.

The work presented in Chapter 2 extends the literature simply by presenting an experimental investigation into the performance of active acoustic cloaking, and goes beyond the previous work of Friot et al [40, 41] by considering both backscatter and shadowing effects. When designing a practical active acoustic cloaking system, it is valuable to consider the robustness of the system to uncertainties. Over time, it is likely that the physical plant responses and the disturbance sound field will vary and, therefore, it should be ensured that the active acoustic cloaking system is sufficiently robust to handle these uncertainties. To provide insight into this challenge, Chapter 3 has presented an investigation into the robustness of the optimal tonal control strategy. This study considered the effects of both structured uncertainty, in the form of variations in the size of the scattering sphere and variations in the position of the scattering sphere, and random unstructured uncertainty. It was shown that a robust solution could be achieved by including regularisation in the formulation of the optimal source strengths on two conditions: that the magnitude of the cross-terms shown in Equation 3.9 could be neglected, and that the matrix $\Delta\mathbf{G}^{\mathrm{H}}\Delta\mathbf{G}$, where $\Delta\mathbf{G}$ is the matrix of plant uncertainties, is diagonally dominant. However, it was shown that, for the considered structured uncertainties, the magnitude of the cross-terms related to perturbations in the plant response were significant and, therefore, neglecting them would be inaccurate. In contrast, the magnitude of the cross-terms related to the disturbance field, and unstructured uncertainty in both the disturbance field and plant response, were small and, therefore, it may be valid to neglect them. It was also shown that the matrix $\Delta\mathbf{G}^{\mathrm{H}}\Delta\mathbf{G}$ is not diagonally dominant for any of the structured uncertainties considered in this study, however, it is diagonally dominant in the case of the unstructured uncertainty.

Despite the perturbations corresponding to the structured uncertainties not meeting the conditions described above, it remains practically insightful to consider what effect regularisation would have and, therefore, the effect of including regularisation in the formulation of the optimal source strengths has also been investigated. It was shown that for the unstructured uncertainties, including regularisation results in minimal degradation to the performance when compared to the nominal case. Based on the previous investigation that showed that the unstructured uncertainty satisfied the two conditions needed for regularisation to be effective, this is, perhaps, unsurprising. However, what is less obvious is the effect of including regularisation in the control source formulation when using the responses containing structured uncertainty. Whilst the performance is significantly degraded compared to the nominal case, some level of control was achieved with all of the structured perturbations considered in this study, when using a suitable value of regularisation. It was also shown that, across all perturbation conditions, uncertainty in the plant responses has the biggest influence on performance and, by comparison, uncertainty in the measured disturbance signal causes far less degradation in performance.

In summary, the robustness study presented in Chapter 3 showed that the optimal tonal active control system is able to achieve robust performance across the considered perturbations. However, to achieve this, the regularisation factor, whether frequency dependent or independent, requires careful tuning with consideration of the expected levels and forms

of uncertainty and so expected uncertainties would need to be characterised for a practical realisation.

In many implementations of active acoustic cloaking, there may be an interest in cloaking the scattering object from non-tonal incident fields. Therefore, the performance of a time-domain, broadband active acoustic cloaking strategy was investigated, using the experimental data obtained from the rigid spherical scattering object described previously, and the results of this study were presented in Chapter 4. In the first instance, it was assumed that a perfect reference signal was available and, in this case, the broadband active acoustic cloaking method was shown to achieve a similar reduction in the scattered sound power as provided by the optimal tonal controller. However, since the ideal reference signal is unlikely to be available in practice, the performance of the broadband controller was subsequently investigated when the incident pressure measured at the microphone directly infront of the primary loudspeaker was used as the reference signal. This resulted in some small deterioration in the level of acoustic cloaking performance compared to the idealised reference case, but still remains some way from a practical solution. Nevertheless, a brief investigation into the robustness of the broadband active acoustic cloaking system to perturbations in the position of the scattering object was presented, and it was again demonstrated that suitable selection of the regularisation value was able to provide a robust solution, at the cost of reduced performance in the nominal case.

In the work summarised to this point, it was assumed that a real-time measure of the scattered acoustic pressure was available for the controller to minimise. In practice, it is not possible to directly measure the scattered acoustic pressure and, therefore, a novel virtual sensing approach based on the Remote Microphone Technique [72] has been proposed in Chapter 5. This sensing strategy is able to estimate the far-field scattered acoustic pressure from near-field measurements of the total acoustic pressure. This broadband approach has been formulated in the time domain, and has again been validated using the measured data corresponding to the rigid spherical scatterer. The proposed strategy satisfies two requirements for a practical active acoustic cloaking system: it provides a real-time estimate of the far-field scattered acoustic pressure, and it only requires measurements in the near-field of the scattering object. It was shown, using the measured data, that the virtual sensing approach is able to accurately estimate the far-field scattered acoustic pressure, achieving an average estimation error of approximately -40 dB. Whilst the results presented in Chapter 5 show that the virtual sensing system may be able to achieve lower values of estimation error, the robustness of the estimation should also be considered and, therefore, the regularisation used in the calculation of the observation filters should be chosen with a consideration of uncertainties. When the virtual sensing strategy is integrated into the broadband active control strategy, it was shown that this system is able to achieve comparable levels of performance to when the controller directly minimises the far-field scattered acoustic pressure; the performance difference between the former and the latter is shown to be less than 2 dB across the frequency range investigated. The robustness of the virtual sensing system was considered and it was shown that, for the regularisation value used in this study, uncertainty in the position of the scattering object resulted in an increase in the estimation error but not to such an extent that it had a significant effect on the control performance.

8.2 Active Acoustic Cloaking of a Flexible Cylinder

All of the work summarised in Section 8.1 was motivated by the use-case of implementing an active acoustic cloaking system on a rigid spherical object, using acoustic control sources. In practice, many applications of active acoustic cloaking will be applied to non-rigid objects, and it is known that the scattering behaviour of a flexible object has additional complexities due to the presence of both resonant and rigid scattering components. Therefore, Chapters 6 and 7 of this thesis have investigated the potential of using active technologies to cloak a hollow aluminium cylinder. In this case, structural actuation is used to provide the control sources rather than loudspeakers, and the sensing arrays include both structural and acoustic sensors.

Since a flexible scattering body will contain both rigid and resonant scattering components, it can be theorised that forcing a flexible object to behave rigidly will reduce the resonant scattering component and leave the rigid scattering component relatively unaffected. An investigation into the validity of this theory was presented in the thesis, considering a hollow aluminium cylinder. The effect of AVC on the acoustic scattering from the cylinder was investigated via both numerical simulations and experiments. In the simulation study it was shown that, by minimising the structural response with the implementation of AVC, a reduction in the resonant scattering was realised. However, resonant scattering was not apparent in the measured datasets. A thorough investigation into possible causes for the discrepancies between the simulation and experimental results has been presented in Appendix I, and it is thought that the most likely cause for the discrepancy is the presence of additional damping in the experimental setup. AVC was successfully implemented, achieving significant reductions in the structural response of the cylinder, however, as resonant scattering was not present before the implementation of AVC, the control resulted in a negligible change to the scattered sound power. Whilst the results from this experimental study do not disprove the concept of AVC reducing resonant scattering from a flexible body, the experimental setup considered in this study was not able to show it. Refinements to the experimental setup have been suggested, however, and these are recommended in Section 8.3.

In order to realise acoustic cloaking of the flexible structure, and particularly control of both resonant and rigid body scattering, Chapter 7 presents an investigation into an active structural acoustic cloaking strategy. It was shown that this control strategy was able to achieve over 5 dB of attenuation in the scattered sound power across the bandwidth considered. A study into the effect of reducing the number of structural control actuators was also conducted, and this demonstrated that to achieve a doubling in the control bandwidth approximately requires a doubling in the number of control actuators for the considered system, however, generalising this has been left for future work. Finally, it was shown that the ASACL system using structural actuation resulted in a significant increase in the structural response of the cylinder, leading to the conclusion that the controller is using the cylinder as a surface with which to radiate acoustic energy. In practice, this may raise concerns of structural fatigue and the system designer should be aware of this side-effect of ASACL.

8.3 Recommendations for Future Work

The work presented in this thesis has highlighted a number of areas for potential future work, which are summarised in this section.

Whilst the robustness study presented in Chapter 3 provided significant insight into the robustness of the proposed active acoustic cloaking system to the four perturbation conditions considered in the study, it may be of interest to consider additional sources of uncertainty. In the use-case of an Autonomous Underwater Vehicle (AUV), for example, the plant responses of the system may change as the depth of the AUV varies due to changes in the temperature and pressure of the surrounding fluid. It may be possible to predict this effect and apply a correction to the plant responses based on a depth sensor, however, this would require additional work to assess its feasibility.

The work presented in Chapter 3 concluded that the active acoustic cloaking system is relatively robust to structured uncertainty in the disturbance field, but that uncertainty in the plant responses had a more significant effect on the cloaking performance. Various methods have been presented in the literature for the real-time update of the plant responses in a control system [67, 68]. An approach such as this could be incorporated into the active acoustic cloaking system to reduce the effect of uncertainty in the plant responses and, therefore, increase the robustness of the system.

Many of the control approaches discussed in this thesis have assumed prior knowledge of the DOA of the incident acoustic wave. The broadband control strategies utilised the incident pressure measured in front of the primary source as the reference signal, and the observation filters used in the virtual sensing algorithm will also be dependent on the angle of incidence of the incoming wave. In a practical implementation of active acoustic cloaking, it is possible that the DOA will not be known and, therefore, a DOA estimation technique [105–108] may need to be introduced into the control architecture. Whilst the study presented in Chapter 4 investigated the suitability of various reference signals, it is important to consider how this could be found in practice and, for this reason, a feedback control architecture may be beneficial [109].

The numerical investigation, presented in Chapter 6, into the effect of AVC on the acoustic scattering from a cylinder showed a potential reduction in the resonant scattering behaviour, however, this could not be validated experimentally. This is likely due to experimental limitations, which had the effect of damping the resonances to the point that the resonant scattering behaviour could not be observed for the considered structure in air. It would be insightful for these experiments to be repeated, possibly underwater where the fluid-structure coupling would be greater, to see if AVC can, in fact, be used to reduce resonant scattering as demonstrated numerically in this thesis.

It was assumed when designing the ASACL system presented in Chapter 7 that the scattered acoustic pressure at the far-field sensor array was known. This would not be the case for a practical implementation and, therefore, it would be insightful to integrate a scattered field detection approach, such as that presented in Chapter 5, into the ASACL system. As the experimental setup considered in Chapter 7 contains an array of accelerometers rather than a near-field array of microphones, a study into the accuracy of the virtual sensing approach when the cylinder is excited off-resonance would be beneficial, and would greatly improve the practicability of the ASACL system presented in Chapter 7.

Appendices

Appendix A

Serial Numbers for Equipment for the Rigid Sphere Measurements

- Microphone Preamplifier - Yamaha MLA8
- ADC - Tascam ML32D, SN 1860049
- DAC - Dante AVIO
- DAC & Control Source Power Amplifier - Innosonix MA32LP - SN 300118000098
- Primary Source Power Amplifier - Behringer iNuke NU1000 - SN S1200159AEM
- Primary Loudspeaker - Tannoy CPA12
- Control Loudspeaker - Visaton B80 (in custom enclosure)
- Near-Field Measurement Microphones - 16 x NTI M4261
    1. SN 2320
    2. SN 1892
    3. SN 2291
    4. SN 2327
    5. SN 2328
    6. SN 2005
    7. SN 2322
    8. SN 2329
    9. SN 2323
    10. SN 2289
    11. SN 1871
    12. SN 2292
    13. SN 2002
    14. SN 2332

15. SN 2326
16. SN 2006

- Far-Field Measurement Microphones - 20 x PCB 130F20 ICP Measurement Microphones
    1. SN 50328
    2. SN 50330
    3. SN 50352
    4. SN 50333
    5. SN 50337
    6. SN 50326
    7. SN 50349
    8. SN 50335
    9. SN 50353
    10. SN 50351
    11. SN 50329
    12. SN 50325
    13. SN 50327
    14. SN 50350
    15. SN 50334
    16. SN 50442
    17. SN 50348
    18. SN 50331
    19. SN 50354
    20. SN 50336
- Acoustic Intensity Probe - Microflown PU Regular - SN PR901011
- Acoustic Calibrator - Larson Davis CAL250 - SN 0122

Appendix B

Manufacturing Drawings for the Visaton B80 Control Loudspeakers

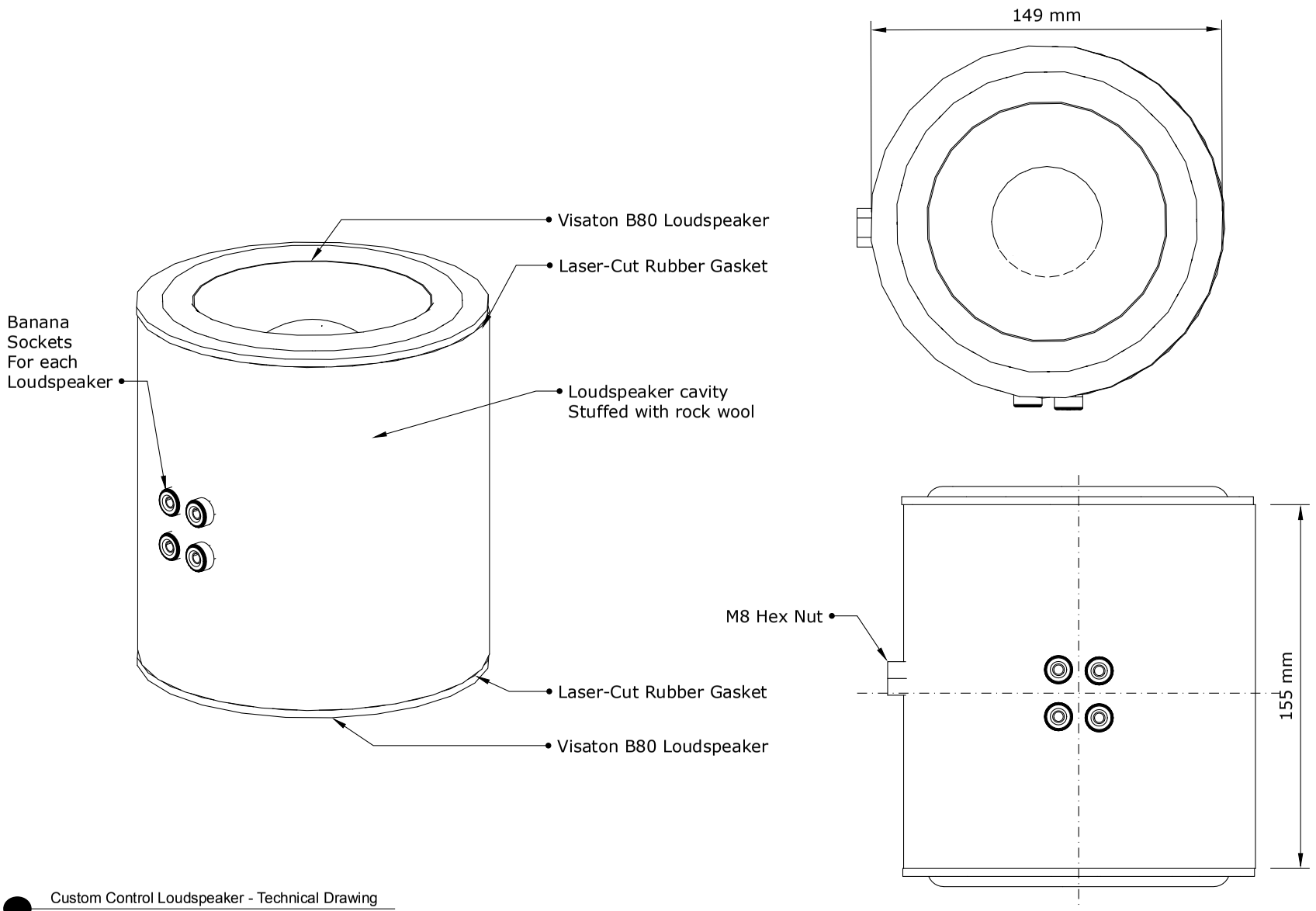

Custom Control Loudspeaker - Technical Drawing

Scale: 1mm : 2mm

Drawn By: Charlie House - c.house@soton.ac.uk

Appendix C

On-Axis Acoustic Response of the Visaton B80 Control Loudspeakers

This appendix will present the on-axis acoustic response measurements of one pair of control loudspeakers used for the acoustic cloaking measurements in Chapters 2 to 5. The physical details of the control loudspeakers are presented in Appendix B.

One of the loudspeaker pairs was mounted on a stand at a height of 1 m in the Large Anechoic Chamber at the Institute of Sound & Vibration Research, University of Southampton, as shown in Figure C.1. An NTI M4261 measurement microphone (Serial Number 2292) was mounted on a microphone stand on-axis with the loudspeaker, at a distance of 1 m. The loudspeaker was powered via a Monacor STA1508 power amplifier, and a Focusrite 2i4 USB Soundcard was used as the ADC/DAC. As shown in Appendix B, each control loudspeaker unit consists of a pair of Visaton B80 loudspeakers, mounted coaxially and in opposite directions from one another. These loudspeakers were driven individually with a broadband sine sweep, which was then de-convolved with the inverse sweep to calculate the transfer response [51]. The measured acoustic transfer response is presented in Figure C.2.

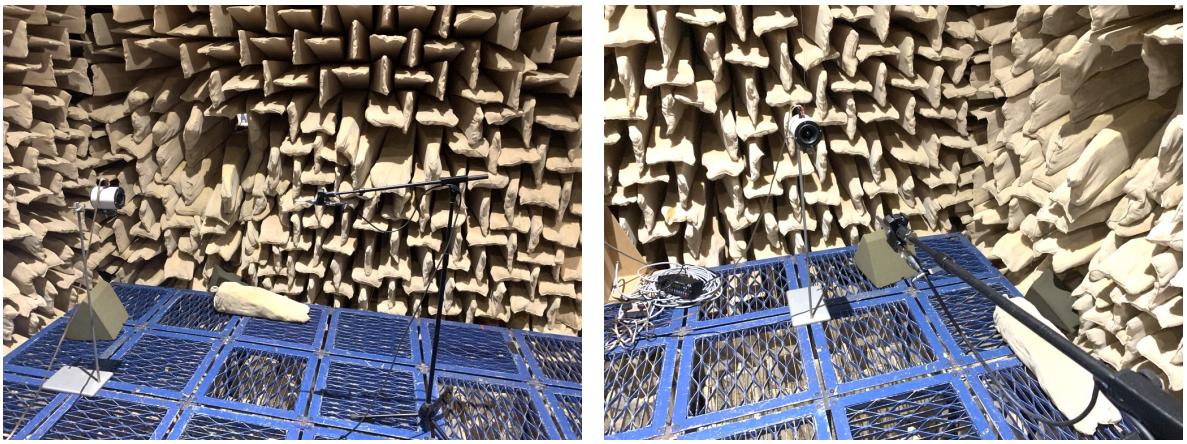

Figure C.1: Photograph showing the measurement setup to characterise the on-axis response of the loudspeakers.

The acoustic response presented in Figure C.2 shows that both loudspeakers have a low frequency roll off below approximately 120 Hz, but a reasonably flat response at frequencies above this. The rear loudspeaker has a slightly lower broadband response to the front loudspeaker, which can be attributed to variability in the manufacturer supplied components. Above approximately 1 kHz, the response from the rear loudspeaker begins to significantly reduce as acoustic shadowing effects, from the enclosure and front loudspeaker, begin to become significant. As the experimental studies presented in this thesis that make use of these loudspeakers are focussed on the 100 Hz - 500 Hz bandwidth, it can be concluded from this set of results that the proposed loudspeaker design is fit for purpose. Whilst the variability between individual loudspeakers is not significant enough to cause a problem, it should be considered and corrected for in the post-processing of any subsequent experimental setups. It should also be noted that these loudspeakers are inefficient below approximately 120 Hz and, therefore, any acoustic excitation within this bandwidth will be at a lower amplitude.

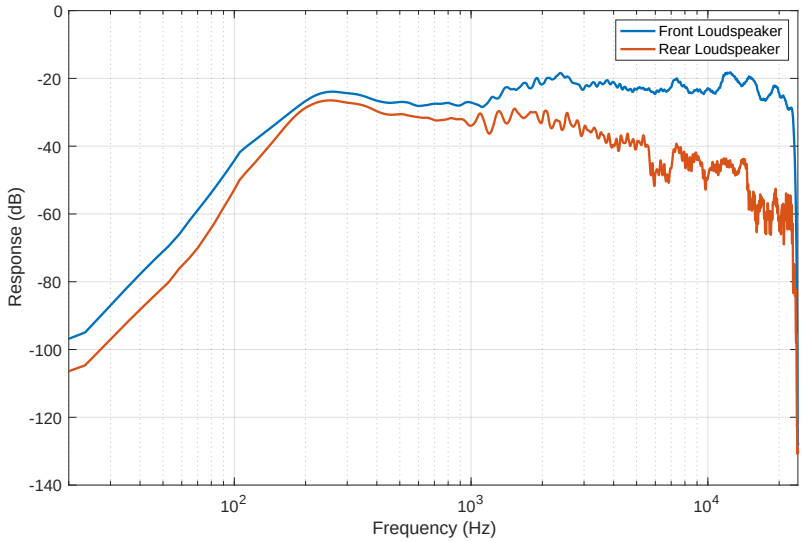

Figure C.2: Plot showing the measured acoustic response from each loudspeaker to the measurement microphone.

Appendix D

Transducer Datasheets

B 80 - 8 Ohm

Art. No. 1261

8 cm (3,3") High-End-Breitband-Lautsprecher mit hervorragend ausgeglichenem Übertragungsverhalten. Durch das Zusammenspiel der beschichteten Papiermembran, der hinterlüfteten Zentrierspinne, dem Phaseplug, sowie dem sehr starken, aber gleichzeitig leichten Neodymantrieb konnte ein äußerst ausgeglichener Frequenzgang mit sehr geringen Verzerrungen und mechanischen Verlusten geschaffen werden. Der B 80 - 8 Ohm ist ideal einsetzbar für kleine High-End-Regalboxen oder als Mittelhochtöner in hochwertigen Mehrwegkombinationen.

8 cm (3.3") high-end full-range loudspeaker with excellent balanced response characteristics. Due to perfect accordance of the coated paper cone, the rear ventilated damper and the phase plug, as well as the strong and lightweight neodymium magnet, an extremely well-balanced frequency response with very low harmonic distortion and lowest possible mechanical losses comes into being. The B 80 8 OHM is ideal for small high-end shelf speakers or as a mid-high-range unit in high-end multi-way speakers.

VISATON GmbH • Ohligser Straße 29-31 • D-42781 Haan • Tel.: 02129/552-0 • Fax 02129/552-10 • E-Mail: visaton@visaton.com

B 80 - 8 Ohm

Art. No. 1261

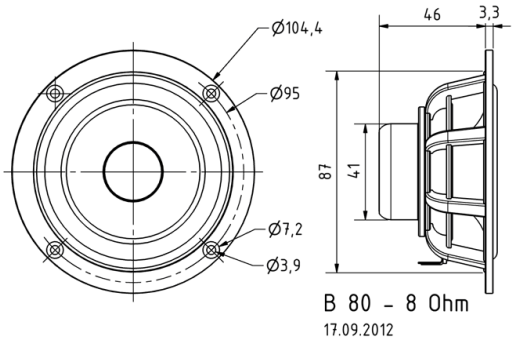

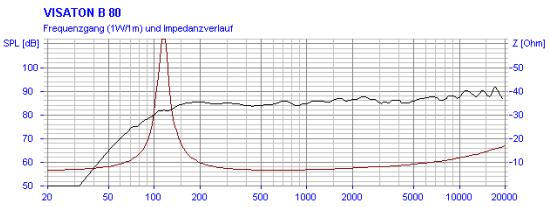

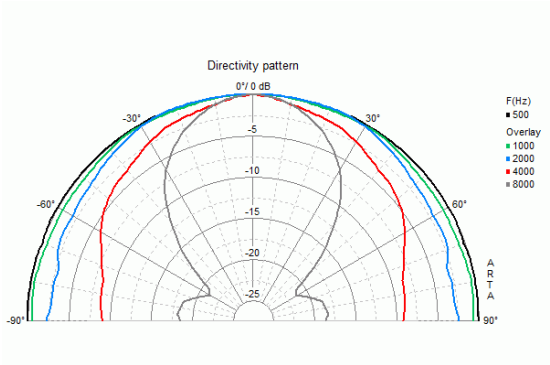

Technische Daten / **Technical data**

Membrannachgiebigkeit Cm Cm	0,87 mm/N
Nennbelastbarkeit Rated power	30 W
Musikbelastbarkeit Maximum power	50 W
Nennimpedanz Z Nominal impedance Z	8 Ohm
Übertragungsbereich Frequency response	80–20000 Hz
Mittlerer Schalldruckpegel Mean sound pressure level	85 dB (1 W/1 m)
Abstrahlwinkel (-6 dB) Opening angle (-6 dB)	119°/4000 Hz
Maximaler linearer Hub Maximum linear displacement	2,2 mm
Resonanzfrequenz fs Resonance frequency fs	110 Hz
Magnetische Induktion Magnetic induction	1,17 T
Magnetischer Fluss Magnetic flux	290 µWb
Obere Polplattenhöhe Height of front pole-plate	3 mm
Schwingspulendurchmesser Voice coil diameter	25 mm
Wickelhöhe Height of winding	7,5 mm
Schallwandöffnung Cutout diameter	89 mm
Gewicht netto Net weight	0,32 kg
Gleichstromwiderstand Rdc D.C. resistance Rdc	6,6 Ohm
Mechanischer Q-Faktor Qms Mechanical Q factor Qms	6,53
Elektrischer Q-Faktor Qes Electrical Q factor Qes	0,69
Gesamt-Q-Faktor Qts Total Q factor Qts	0,63
Äquivalentes Luftnachgiebigkeitsvolumen Vas	

08.06.2016

GERMANY VISATON®

Equivalent volume Vas	1,8 l
Effektive Membranfläche Sd Effective piston area Sd	38,5 cm²
Dynamische bewegte Masse Mms Dynamically moved mass Mms	2,8 g
Antriebsfaktor Bxl Force factor Bxl	4,15 Tm
Anschlüsse Connections	5,1 x 0,5 mm (+) 2,8 x 0,5 mm (–)

VISATON GmbH • Ohligser Straße 29-31 • D-42781 Haan • Tel.: 02129/552-0 • Fax 02129/552-10 • E-Mail: visaton@visaton.com

Model 130F20

ICP® Electret Array Microphone

Installation and Operating Manual

**For assistance with the operation of this product,
contact PCB Piezotronics, Inc.**

Toll-free: 800-828-8840
24-hour SensorLine: 716-684-0001
Fax: 716-684-0987
E-mail: info@pcb.com
Web: www.pcb.com

PCB PIEZOTRONICS INC.

Service, Repair, and Return Policies and Instructions

The information contained in this document supersedes all similar information that may be found elsewhere in this manual.

Service – Due to the sophisticated nature of the sensors and associated instrumentation provided by PCB Piezotronics, user servicing or repair is not recommended and, if attempted, may void the factory warranty. Routine maintenance, such as the cleaning of electrical connectors, housings, and mounting surfaces with solutions and techniques that will not harm the physical material of construction, is acceptable. Caution should be observed to ensure that liquids are not permitted to migrate into devices that are not hermetically sealed. Such devices should only be wiped with a dampened cloth and never submerged or have liquids poured upon them.

Repair – In the event that equipment becomes damaged or ceases to operate, arrangements should be made to return the equipment to PCB Piezotronics for repair. User servicing or repair is not recommended and, if attempted, may void the factory warranty.

Calibration – Routine calibration of sensors and associated instrumentation is recommended as this helps build confidence in measurement accuracy and acquired data. Equipment calibration cycles are typically established by the users own quality regimen. When in doubt about a calibration cycle, a good "rule of thumb" is to recalibrate on an annual basis. It is also good practice to recalibrate after exposure to any severe temperature extreme, shock, load, or other environmental influence, or prior to any critical test.

PCB Piezotronics maintains an ISO-9001 certified metrology laboratory and offers calibration services, which are accredited by A2LA to ISO/IEC 17025, with full traceability to SI through N.I.S.T. In addition to the normally supplied calibration, special testing is also available, such as: sensitivity at elevated or cryogenic temperatures, phase response, extended high or low frequency response, extended range, leak testing, hydrostatic pressure testing, and others. For information on standard recalibration services or special testing, contact your local PCB Piezotronics distributor, sales representative, or factory customer service representative.

Returning Equipment – *Following these procedures will ensure that your returned materials are handled in the most expedient manner*. Before returning any equipment to PCB Piezotronics, contact your local distributor, sales representative, or factory customer service representative to obtain a Return **Warranty, Service, Repair, and Return Policies and Instructions** Materials Authorization (RMA) Number. This RMA number should be clearly marked on the outside of all package(s) and on the packing

list(s) accompanying the shipment. A detailed account of the nature of the problem(s) being experienced with the equipment should also be included inside the package(s) containing any returned materials.

A Purchase Order, included with the returned materials, will expedite the turn-around of serviced equipment. It is recommended to include authorization on the Purchase Order for PCB to proceed with any repairs, as long as they do not exceed 50% of the replacement cost of the returned item(s). PCB will provide a price quotation or replacement recommendation for any item whose repair costs would exceed 50% of replacement cost, or any item that is not economically feasible to repair. For routine calibration services, the Purchase Order should include authorization to proceed and return at current pricing, which can be obtained from a factory customer service representative.

Contact Information – International customers should direct all inquiries to their local distributor or sales office. A complete list of distributors and offices can be found at www.pcb.com. Customers within the United States may contact their local sales representative or a factory customer service representative. A complete list of sales representatives can be found at www.pcb.com. Toll-free telephone numbers for a factory customer service representative, in the division responsible for this product, can be found on the title page at the front of this manual. Our ship to address and general contact numbers are:

PCB Piezotronics, Inc.
3425 Walden Ave.
Depew, NY14043 USA
Toll-free: (800) 828-8840
24-hour SensorLine[SM]: (716) 684-0001
Website: www.pcb.com
E-mail: info@pcb.com

PCB工业监视和测量设备 - 中国RoHS2公布表
PCB Industrial Monitoring and Measuring Equipment - China RoHS 2 Disclosure Table

部件名称	有害物质					
	铅 (Pb)	汞 (Hg)	镉 (Cd)	六价铬 (Cr(VI))	多溴联苯 (PBB)	多溴二苯醚 (PBDE)
住房	O	O	O	O	O	O
PCB板	X	O	O	O	O	O
电气连接器	O	O	O	O	O	O
压电晶体	X	O	O	O	O	O
环氧	O	O	O	O	O	O
铁氟龙	O	O	O	O	O	O
电子	O	O	O	O	O	O
厚膜基板	O	O	X	O	O	O
电线	O	O	O	O	O	O
电缆	X	O	O	O	O	O
塑料	O	O	O	O	O	O
焊接	X	O	O	O	O	O
铜合金/黄铜	X	O	O	O	O	O

本表格依据 SJ/T 11364 的规定编制。

O： 表示该有害物质在该部件所有均质材料中的含量均在 GB/T 26572 规定的限量要求以下。

X： 表示该有害物质至少在该部件的某一均质材料中的含量超出 GB/T 26572 规定的限量要求。
铅是欧洲RoHS指令2011/65/ EU附件三和附件四目前由于允许的豁免。

CHINA RoHS COMPLIANCE

Component Name	Hazardous Substances					
	Lead (Pb)	Mercury (Hg)	Cadmium (Cd)	Chromium VI Compounds (Cr(VI))	Polybrominated Biphenyls (PBB)	Polybrominated Diphenyl Ethers (PBDE)
Housing	O	O	O	O	O	O
PCB Board	X	O	O	O	O	O
Electrical Connectors	O	O	O	O	O	O
Piezoelectric Crystals	X	O	O	O	O	O
Epoxy	O	O	O	O	O	O
Teflon	O	O	O	O	O	O
Electronics	O	O	O	O	O	O
Thick Film Substrate	O	O	X	O	O	O
Wires	O	O	O	O	O	O
Cables	X	O	O	O	O	O
Plastic	O	O	O	O	O	O
Solder	X	O	O	O	O	O
Copper Alloy/Brass	X	O	O	O	O	O

This table is prepared in accordance with the provisions of SJ/T 11364.

O: Indicates that said hazardous substance contained in all of the homogeneous materials for this part is below the limit requirement of GB/T 26572.

X: Indicates that said hazardous substance contained in at least one of the homogeneous materials for this part is above the limit requirement of GB/T 26572.
Lead is present due to allowed exemption in Annex III or Annex IV of the European RoHS Directive 2011/65/EU.

PCB PIEZOTRONICS INC.

OPERATING GUIDE FOR 130 SERIES MICROPHONES

Contents:

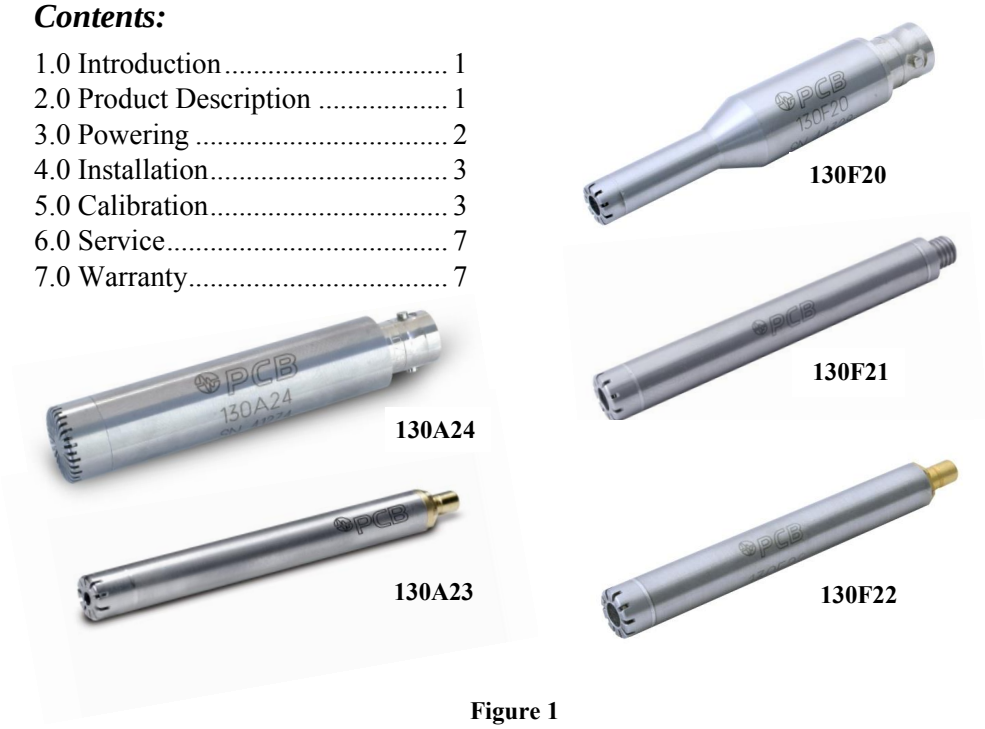

Figure 1

1.0 Introduction

PCB® 130 series ICP® array microphones provide an extremely cost-effective method for large channel count sound pressure measurements. Multiple array microphones with their excellent phase characteristics can be combined with the appropriate software to perform measurements that are not possible with a single microphone. Typical applications include sound pressure mapping, beamforming, acoustic mode analysis, near-field acoustic holography, or sound intensity measurments. To ensure the best performance from your 130 series microphone follow the installation and operating procedures in this guide. If you have additional questions concerning the microphone system or applications, call a factory Application Engineer at 716-684-0001, or your nearest PCB® Field Application Engineer.

2.0 Product Description

PCB®'s 130 series ICP® Array are integrated systems that include a built-in preamplifier. Models 130F20, 130F21, and 130F22 are all ¼-inch microphones that provide a 45 mV/Pa output over an extended 120dB dynamic range. They are ideal for use at frequencies from 20 Hz to 10 kHz (± 2dB) or 20 kHz (± 5dB). All models are of rugged, stainless steel construction .

These microphones all have the same performance specifications but are fitted with different electrical connectors to make them suitable for differing applications. Model 130F20 features a BNC connector while Model 130F21 uses a 10-32 coaxial jack connector. Model 130F22 terminates in a SMB connector. These models are shown in Figure 1.

The 130A23 and 130A24 are designed for high amplitude applications with an upper dynamic range of 150 dB. Model 130A23 terminates in a SMB electrical connector. The 130A24 is an enhanced, rugged, water and dust resistant design, and terminates in a BNC electrical connector. Model 130A24 has a lower sensitivity (10 mV/Pa) than the 130A23 (14 mV/Pa), but otherwise the performance specifications are the same.

All 130 Series array microphones include TEDS capable digital memory and communitation electronics compliant with IEEE 1451.4. These microphones are easy to operate and interface with many PCB® ICP® constant current signal conditioners and other data acquisition and recording instruments available on the market today. In a complete microphone system, low-impedance cables couple the microphone and signal conditioner to customer supplied read-out instruments. The use of low impedance cables enables signals to be driven long distances with negligible signal loss.

3.0 Powering

All ICP® powered microphones require constant-current excitation for proper operation. For this reason, use only PCB constant-current signal conditioners or other approved constant-current sources. The signal conditioner provides an AC-coupled output signal that is compatible with most standard readout devices. Signal conditioners consist of a regulated 2-20mA, 18-30 VDC source. They are available in single or multi channel, battery or line powered configurataions. Battery powered devices offer versatility for portable low noise measurements, whereas line powered units provide the capability for continuous monitoring. A typical system schematic is shown in Figure 2.

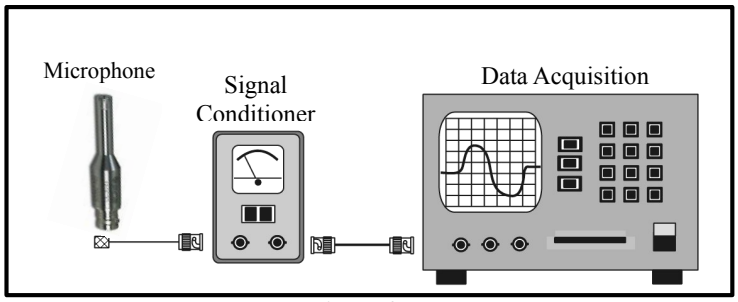

Figure 2

Signal conditioners have meters or LEDS, which enable users to monitor the bias voltage output signal, check microphone operation, and detect cable faults. Typically yellow denotes an open circuit; green indicates normal operation and red indicates a short circuit. Many FFT analyzers, data acquisition modules, and data collectors have the proper constant-current excitation built-in for direct use with ICP® microphones. Before using this feature, care should be taken to assure the proper supply voltage and constant current excitation are provided. Check the enclosed specification sheet to make sure the supply voltage and current are within acceptable limits for your particular microphone.

4.0 Installation

There are many ways to mount the microphone, from simply placing the microphone in a clip to using a two-dimensional array stand. A diagram of an array configuration is provided in Figure 3. For installation of this type, remove the microphone from its package, connect the appropriate cable between the signal conditioner and the microphone, and connect a second cable between the signal conditioner and the data acquisition device. Cabling may consist of standard low-impedance coax cables. Desired electrical connectors would be dependent on the 130 series microphone used and the input of the signal conditioner and read-out instrument. PCB® offers these cables in a variety of standard or customer specified lengths.

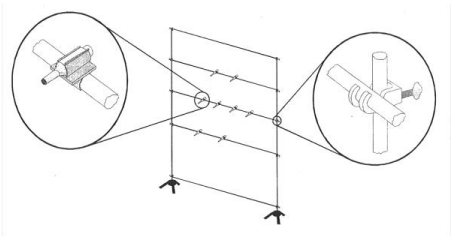

Figure 3

The 130A24 microphone features a removable grid cap and replaceable protective cover. This allows the 130A24 to withstand harsh environments while extending the lifespan of critical sensitive components. If the water and dust resistant cover is damaged, having a removable grid cap allows the user to replace this protective cover quickly and easily.

To replace a grid cap, first unthread the grid cap from the housing. Next, peel off the existing cover from the end of the housing. Sharp edged tools can be used to aid in cover removal, but it is important to keep the tool at a shallow angle. DO NOT make contact with the microphone's delicate diaphragm (right hand side of Figure 4). To ensure a proper seal, gently wipe the top of the microphone housing to remove any moisture or debris. Do not use solvent when removing debirs from the housing because solvents have the potential to damage the microphone. Apply the replacement water resistant patch to the end of the housing (left hand side of Figure 4) while keeping it centered. Finally, assemble the grid cap back onto the housing. Additional 079A46 five-pack replacement water resistant pads can be ordered separately.

Figure 4

5.0 Calibration

All microphones are supplied with calibration documentation showing the free field frequency response and the conditions under which the calibration was performed. Calibrations are performed with reference microphones traceable to national laboratories specializing in acoustic measurements (NIST, PTB, or DFM). PCB is ISO 10012-1 and ISO 9001-2008 certified. Calibration methods used by PCB for acoustic pressure have been audited for proficiency and accredited for compliance with ISO/IEC 17025:2005; ANSI/NCSL Z540-1-1994 & ANSI/NCSL Z540.3. Sample calibration certificates are provided in Figure 5, Figure 6, and Figure 7 for the 130F series, 130A23, and 130A24, respectively.

All 130 series array microphones are designed for use in a free field environment. A free field environment is one without reflections. Anechoic rooms and outdoor spaces without structures are good examples of a free field environment. The free field response is the voltage response with respect to the pressure when exposed to a plane progressive sound wave. A free field microphone has a flat frequency response with respect to any source whose primary direction is collinear with the axis of the microphone.

Calibration of free field microphone occurs at a zero degree angle of incidence. This means that the frequency response reported on the calibration certificate is valid when the microphone is directed straight at the sound source. If the microphone is directed at an angle with respect to the source the response may vary depending on the angle and the frequency of operation.

After completing the system set-up, turn on the the signal conditioner and allow 1 to 2 minutes for the system to stabilize. If the system doesn't appear to be functioning correctly check all system connections and try to isolate and individually check functionality of all system components, or consider replacing system components one at a time. If the system still does not operate properly, consult a PCB Application Engineer.

Under normal conditions, microphones offer a very stable response. However, the microphone output may be affected by harsh environments, such as moisture, dirt, mechanical shock, or other unusual conditions. This may manifest itself in a number of ways, ranging from a loss in frequency range to failure of the built-in microelectronic circuits. To assure sensors characteristics are known PCB® recommends that a recalibration cycle be established for each microphone. Customers should determine a calibration cycle best suited for their needs as the cycle is based upon a variety of factors, such as frequency of use, exposure to harsh environmentals, accuracy requirements, trend information obtained from previous calibration records, contractual regulations, and risk associated with incorrect readings. PCB® recommends 12 to 24 month calibration intervals but as stated, this interval is at the discretion of the customer and is based on customer needs. It is also best practice to perform verification both before and after each test. PCB's CAL 250 acoustic calibrator (sold separately) is a handheld calibration instrument ideal for field or quick sensor operational evaluation purposes.

6.0 Service

See the supplemental sheet for information on our service, repair and return policies, procedures and instructions. If an unexpected problem arises, call our 24-Hour SensorLine℠ (716-684-0001) to discuss your dynamic instrumentation needs with a PCB® Application Engineer.

7.0 Warranty

PCB's 130 Series Microphones are covered by a limited warranty against defective material and workmanship. Visit http://www.pcb.com/terms_conditions for a complete statement of our warranty.

3425 Walden Avenue, Depew, NY 14043-2495
E-Mail: info@pcb.com
Website: www.pcb.com

24-hour SensorLine[SM]: 716-684-0001
Fax: 716-684-0987
Toll-free: 800-828-8840

ISO 9001 CERTIFIED • AS9100 CERTIFIED

In the interest of constant product improvement, specifications are subject to change without notice.

Manual Number: 64548
Manual Revision: NR
ECO# 45478
Printed in the U.S.A.

Model Number	ICP® ELECTRET ARRAY MICROPHONE	Revision: NR
130F20		ECN #: 45478

Performance	ENGLISH	SI	
Nominal Microphone Diameter	1/4"	1/4"	
Frequency Response Characteristic(at 0° incidence)	Free-Field	Free-Field	
Frequency Response(± 2 dB)	20 to 10,000 Hz	20 to 10,000 Hz	
Frequency Response(± 3 dB)	10 to 16,000 Hz	10 to 16,000 Hz	
Frequency Response(± 4 dB)	10 to 20,000 Hz	10 to 20,000 Hz	
Phase Match(100 Hz to 3 kHz)	± 3 °	± 3 °	[1]
Phase Match(50 Hz to 5 kHz)	± 5 °	± 5 °	[1]
Phase Match(5 kHz to 10 kHz)	± 10 °	± 10 °	[1]
Sensitivity	45 mV/Pa	45 mV/Pa	
Sensitivity(+/-3)(@ 250 Hz)	-26.9 dB re 1 V/Pa	-26.9 dB re 1 V/Pa	
Inherent Noise(Linear)	29 dB re 20 µPa	29 dB re 20 µPa	[1]
Inherent Noise(A Weighted)	<26 dB(A) re 20 µPa	<26 dB(A) re 20 µPa	
Inherent Noise(A Weighted)	24 dB(A) re 20 µPa	24 dB(A) re 20 µPa	[1]
Dynamic Range(3% Distortion Limit)	>122 dB re 20 µPa	>122 dB re 20 µPa	
TEDS Compliant	Yes	Yes	[2]
Environmental			
Temperature Range(Operating)	+14 to +122 °F	-10 to +50 °C	
Temperature Effect on Output(-10 to +50 °C)	0.7 dB	0.7 dB	[1]
Electrical			
Excitation Voltage	18 to 30 VDC	18 to 30 VDC	
Constant Current Excitation	2 to 20 mA	2 to 20 mA	
Output Bias Voltage	5.5 to 14 VDC	5.5 to 14 VDC	
Output Impedance	<150 Ohm	<150 Ohm	
Physical			
Housing Material	Stainless Steel	Stainless Steel	
Electrical Connector(Output)	BNC Jack	BNC Jack	
Size (Diameter x Length)(overall)	0.5 in x 2.63 in	12.7 mm x 66.8 mm	
Size (Diameter x Length)(head)	0.28 in x .87 in	7 mm x 22.1 mm	
Weight	0.90 oz	25.5 gm	[1]

CE[3]

All specifications are at room temperature unless otherwise specified.
In the interest of constant product improvement, we reserve the right to change specifications without notice.
ICP® is a registered trademark of PCB Group, Inc.

OPTIONAL VERSIONS

Optional versions have identical specifications and accessories as listed for the standard model except where noted below. More than one option may be used.

NOTES:
[1]Typical.
[2]TEDS Capable Digital Communication, compliant with IEEE 1451.4
[3]See PCB Declaration of Conformance PS023 for details.

Entered: LK	Engineer: TP	Sales: MV	Approved: MT	Spec Number:
Date: 6/21/2016	Date: 6/21/2016	Date: 6/21/2016	Date: 6/21/2016	63460

PCB PIEZOTRONICS
3425 Walden Avenue, Depew, NY 14043
Phone: 716-684-0001
Fax: 716-684-0987
E-Mail: info@pcb.com

63459

REVISIONS		
REV	DESCRIPTION	DIN
NR	RELEASED TO DRAFTING	45478

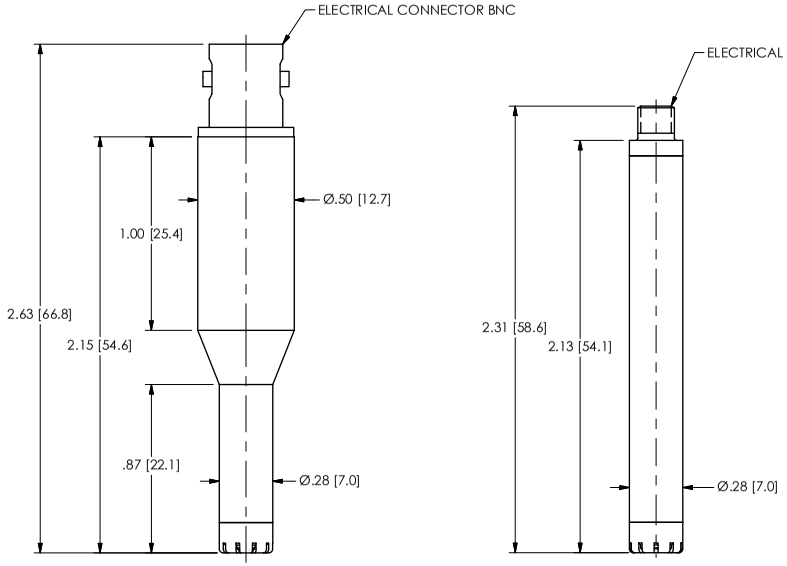

MODEL 130F20

MODEL 130F21

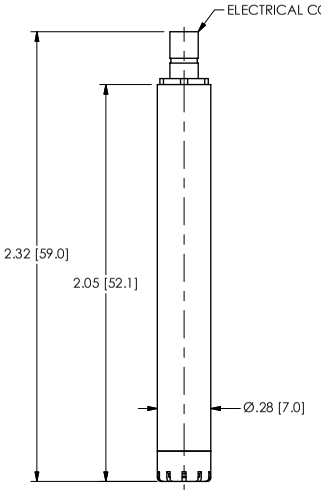

MODEL 130F22

UNLESS OTHERWISE SPECIFIED TOLERANCES ARE:		DRAWN		CHECKED		ENGINEER	
DIMENSIONS IN INCHES	DIMENSIONS IN MILLIMETERS [IN BRACKETS]	KRM	6/15/16	ECB	6/15/16	NJL	6/15/16
DECIMALS XX ±.03 XXX ±.010 ANGLES ± 2 DEGREES	DECIMALS X ± 0.8 XX ± 0.25 ANGLES ± 2 DEGREES	TITLE: OUTLINE DRAWING MODEL 130F SERIES ICP MICROPHONE					
FILLETS AND RADII .003 - .005	FILLETS AND RADII 0.07 - 0.13						

PCB PIEZOTRONICS
3425 WALDEN AVE. DEPEW, NY 14043
(716) 684-0001 E-MAIL: sales@pcb.com

CODE IDENT. NO.	DWG. NO.
52681	63459
SCALE: 2X	SHEET 1 OF 1

Technical Data Measurement Microphones

	M2230 Class 1 Certified	M2230-WP Class 1 Outdoor Microphone (M2230+WP30)	M2211 Frequency Response Class 1	M2215 High SPL Frequency Response Class 1	M4261 Class 2
Consisting of	PreAmplfier MA220 + MC230 or MC230A Capsule	PreAmplfier MA220 + MC230 or MC230A Capsule + WP30	PreAmplfier MA220 + M2211 Capsule	PreAmplfier MA220 + M2215 Capsule	M4261 microphone with permanently installed capsule
Microphone Type	Omnidirectional, pre-polarized condenser, free field microphone				
Classification according IEC 61672 and ANSI S1.4	Class 1 Certified	Class 1	Frequency Response Class 1		Class 2
Capsule / Transducer	1/2" detachable with 60UNS2 thread, type WS2F according IEC 61094-4				1/4" permanently installed
PreAmplifier Type	MA220				-
Flatness tolerance bands typical	±1 dB @ 5 Hz - 20 Hz ±1 dB @ >20 Hz - 4 kHz ±1.5 dB @ >4 kHz - 10 kHz ±2 dB @ >10 kHz - 16 kHz ±3 dB @ >16 kHz - 20 kHz				+1/-4.5 dB @ 5 Hz - 20 Hz ±1.5 dB @ >20 Hz - 4 kHz ±3 dB @ >4 kHz - 10 kHz ±4.5 dB @ >10 kHz - 16 kHz ±5 dB @ >16 kHz - 20 kHz
Actual Frequency Response	freely available as Excel-data, register microphone at My NTi Audio and contact info@nti-audio.com				
Frequency Range	5 Hz - 20 kHz				
Residual Noise Floor typical	16 dB(A)		21 dB(A)	25 dB(A)	27 dB(A)
Maximum SPL @THD 3%, 1 kHz	137 dBSPL		144 dBSPL	153 dBSPL	142 dBSPL

	M2230 Class 1 Certified	M2230-WP Class 1 Outdoor Microphone (M2230+WP30)	M2211 Frequency Response Class 1	M2215 High SPL Frequency Response Class 1	M4261 Class 2
Sensitivity typical @ 1 kHz	-27.5 dBV/Pa ±2 dB (42 mV/Pa)		-34 dBV/Pa ±3 dB (20 mV/Pa)	-42 dBV/Pa ±3 dB (8 mV/Pa)	-36 dBV/Pa ±3 dB (16 mV/Pa)
Temperature Coefficient	< -0.01 dB / °C		< ±0.015 dB / °C		< ±0.02 dB / °C
Temperature Range	-10°C to +50°C (14°F to 122°F)				0°C to +40°C (32°F to 104°F)
Pressure Coefficient	-0.005 dB / kPa		-0.02 dB / kPa		-0.04 dB / kPa
Influence of Humidity (non-condensing)	< ±0.05 dB				< ±0.4 dB
Humidity	5% to 90% RH, non-condensing				
Long Term Stability	> 250 years / dB				-
Power Supply	48 VDC phantom power				
Current Consumption	2.3 mA typical				1.7 mA typical
Electronic Data Sheet	NTi Audio ASD in accordance with IEEE P1451.4 V1.0, Class 2, Template 27				
Output Impedance	100 Ohm balanced				
Connector	Balanced 3-pole XLR				
Diameter Dimensions	20.5 mm (0.8")	36 mm (1.4")	20.5 mm (0.8")		
Length Dimensions	154 mm (6.1")	378 mm (14.9")	150 mm (5.9")		
Weight	100 g, 3.53 oz	430 g, 15.17 oz	100 g, 3.53 oz		83 g, 2.93 oz
Environmental Protection	IP51	IP54 in vertical position	IP51		
NTi Audio #	600 040 050	600 040 055	600 040 022	600 040 045	600 040 070

Typical Frequency Response of Measurement Microphones

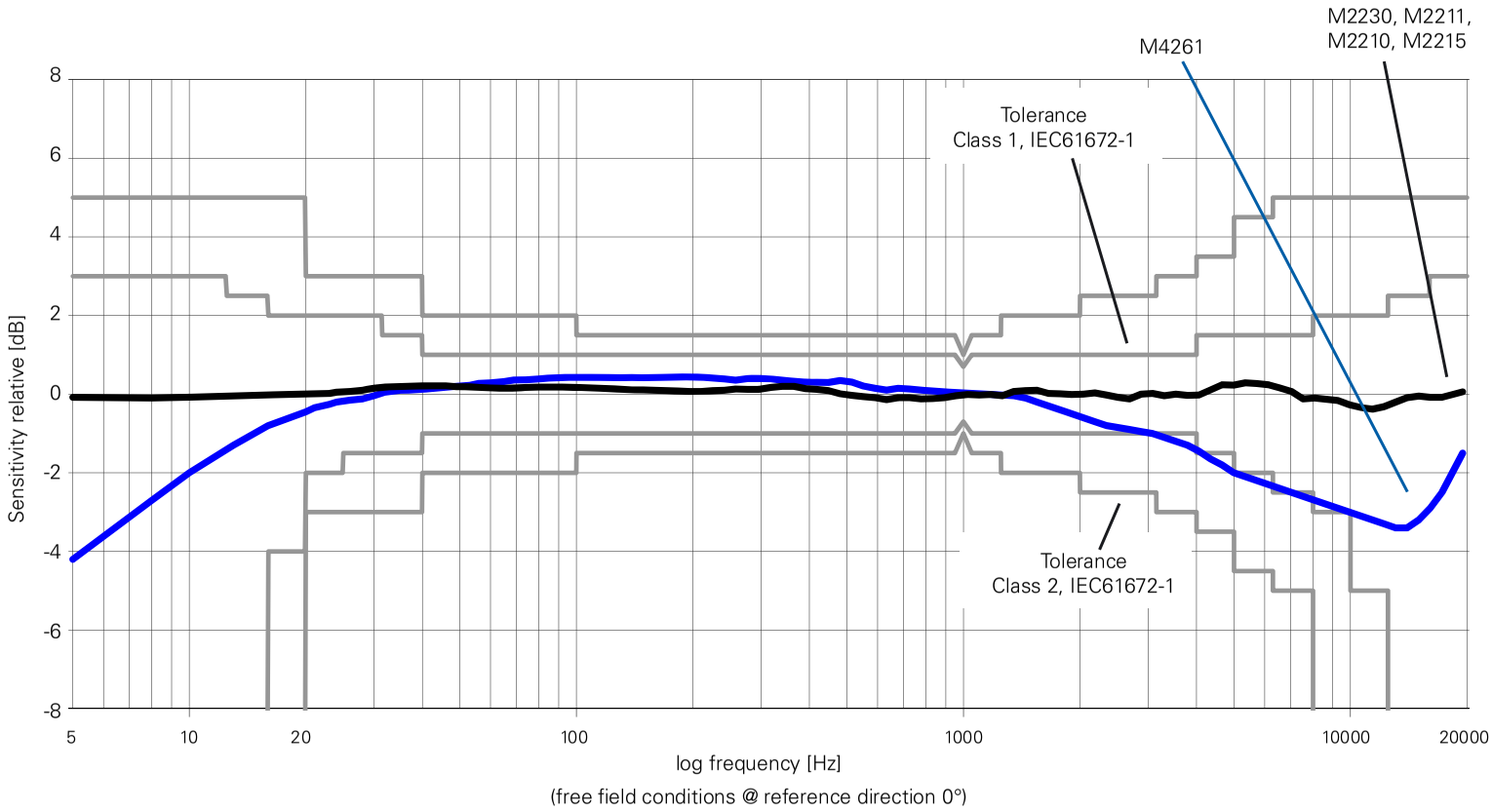

Free Field - Pressure Correction Factors

If a measurement microphone is held in a free-field environment, then the measurement microphone acts at high frequencies like a reflector. The sound pressure increases in front of the microphone capsule membrane. M2230, M2211 and M2215 are free-field equalized measurement microphones, they compensate for the increased pressure internally.

The calibrator offers no longer free-field conditions. Therefore, the free-field equalization of the microphone must be compensated. This needs to be considered prior the calibration. The correction value needs to be added to the pressure response of the microphone.

Example:

- During the calibration, the XL2 measures the sound level in the calibrator. If the B&K4226 calibrator is used and it is set to 16 kHz, then the XL2+M2230 reads just 86.7 dBA.
- The free-field sound level is calculated by summing the XL2 measurement value and the correction value (= 86.7 dB + 7.3 dB = 94.0 dB).

The following corrections apply with the B&K4226 calibrator:

Nominal Frequency [Hz]	M2230 Measurement Microphone [dB]	M2211 Measurement Microphone [dB]	M2215 Measurement Microphone [dB]	Measurement Uncertainty U [dB]
31.5	0.0	0.0	0.0	0.3
63	0.0	0.0	0.0	0.3
125	0.0	0.0	0.0	0.3
250	0.0	0.0	0.0	0.3
500	0.0	0.1	0.0	0.3
1000	0.0	0.1	0.0	0.3
2000	0.3	0.6	0.2	0.3
4000	0.7	1.7	1.2	0.3
8000	2.6	4.2	3.9	0.4
12500	6.0	7.3	6.7	0.7
16000	7.3	9.2	9.0	0.8

Correction values for other calibrators for M2230:

Type	Correction Value	Calibration Frequency	Calibration Level
NTi Audio CAL200	0.1	1 kHz	114 dB
B&K 4231	0.2	1 kHz	114 dB
Norsonic Nor-1251	0.2	1 kHz	114 dB

Diffuse Field Correction Factors

A diffuse sound field is characterized by the sound arriving at the receiver from all directions with more or less equal probability. The M2230, M2211, M2215 and M4261 are free-field equalized measurement microphones. The default frequency response refers to a 0° sound incidence. The diffuse-field frequency response is calculated by averaging the directional characteristics; this results in a reduction at the high frequencies. The individual third-octave band correction values for diffuse-field conditions are documented in the following table. The directional response of the M2230 is described in the appendix.

Example:

- The sound pressure level in a diffuse sound field shall be determined. The display of the XL2 with the M2230 reads 80.0 dBA for the 20 kHz third-octave band.
- The diffuse sound level is now calculated from the sum of the XL2 measurement value and the correction value (80.0 dB + 8.7 dB = 88.7 dB).

This correction is not necessary using a diffuse field equalized measurement microphone.

Nominal Frequency [Hz]	1/2" Microphone M2230, M2211, M2215 [dB]	1/4" Microphone M4261 [dB]
<63	0.0	0.0
63	0.0	0.0
80	0.0	0.0
100	0.0	0.0
125	0.0	0.0
160	0.0	0.0
200	0.0	0.0
250	0.1	0.0
315	0.1	0.0
400	0.1	0.0
500	0.1	0.1
630	0.1	0.1
800	0.2	0.1
1000	0.2	0.1
1250	0.3	0.1
1600	0.4	0.1
2000	0.5	0.1
2500	0.6	0.2
3150	0.8	0.2
4000	1.1	0.3
5000	1.4	0.5
6300	1.9	0.7
8000	2.5	1.0
10000	3.4	1.4
12500	4.6	1.9
16000	6.4	2.5
20000	8.7	3.2

M2230 Frequency Response for Free Field, Diffuse Field and Pressure

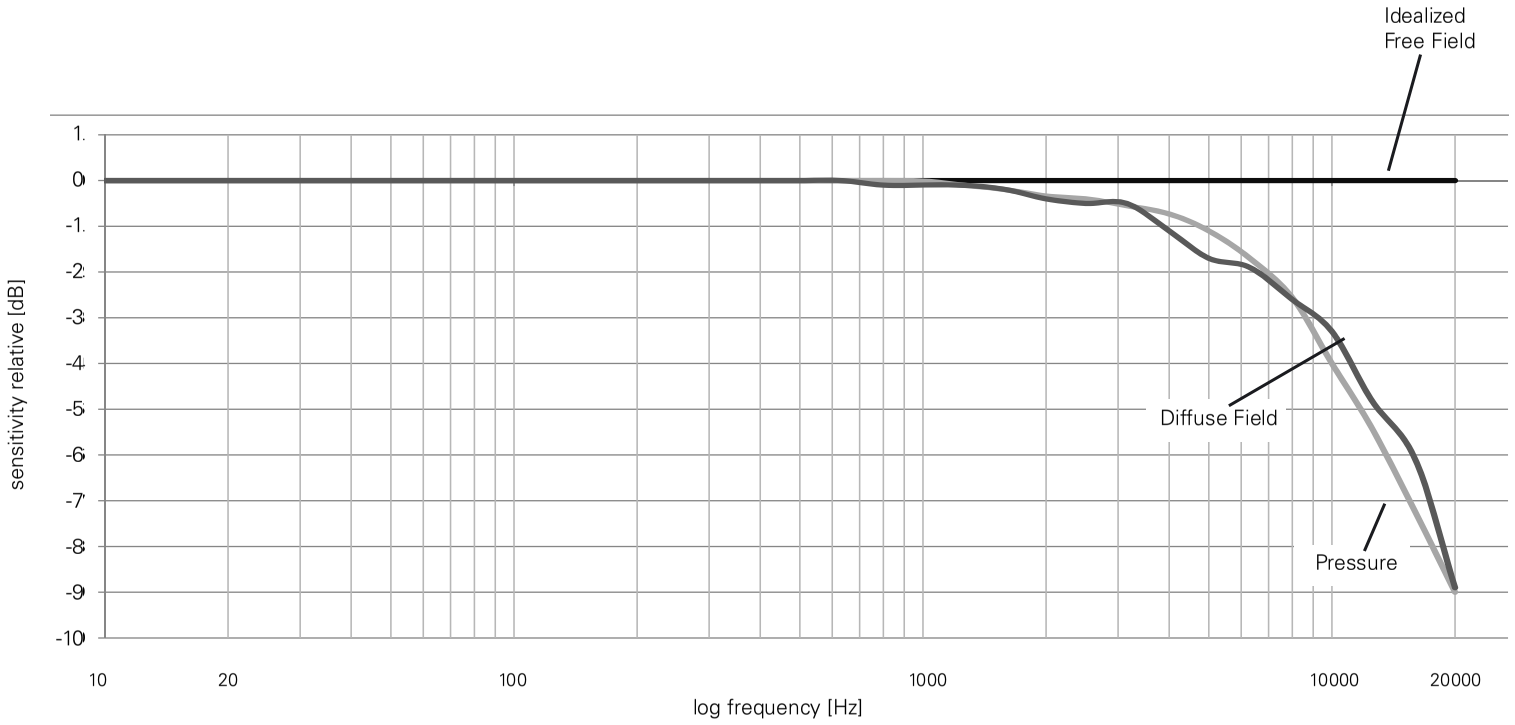

Spectral Correction for horizontal Sound Incidents using the Outdoor Microphone

The outdoor microphone M2230-WP fulfills Class 1 requirements of IEC 61672 and ANSI S1.4 for vertical sound incidence. For compliance with horizontal sound incidence a spectral correction is employed in the associated XL2 Sound Level Meter.

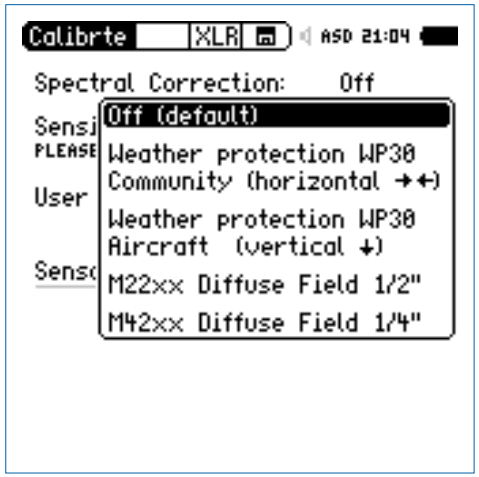

Nominal Frequency [Hz]	Spectral Correction for horizontal Sound Incidents with Firmware V4.20 or higher [dB]	
	1/3 Octave	1/1 Octave
<800	0.0	0.0
800 1000 1250	0.0 0.0 0.1	0.0
1600 2000 2500	0.1 0.3 0.7	0.4
3150 4000 5000	1.3 2.0 2.6	2.1
6300 8000 10000	2.7 3.2 3.7	3.3
12500 16000 20000	4.3 6.1 6.4	5.9

Technical Data PreAmplifier

	MA220 PreAmplifier
Microphone PreAmplifier	Compatible with 1/2" microphone capsules type WS2F in accordance with IEC61094-4
Frequency Range	4 Hz - 100 kHz
Residual Noise Floor typical	1.6 µV(A) at C_in 18pF ≙ 12 dBA @ 20 mV/Pa
Frequency Response Flatness	±0.2 dB
Phase Linearity	< 1° @ 20 Hz - 20 kHz
Maximum Output Voltage	21 Vpp ≙ 7.4 Vrms ≙ 145 dBSPL @ 20 mV/Pa, THD 3%, 1 kHz
Electronic Data Sheet	• Containing user calibration data • Default factory sensitivity = 4.9 V/Pa • Read/write by XL2 Audio and Acoustic Analyzer • NTi Audio ASD in accordance with IEEE P1451.4 V1.0, Class 2, Template 27
Impedance	Input: 20 GOhm // 0.26 pF, Output: 100 Ohm balanced
Power Supply	48 VDC phantom power, 2.3 mA typical
Attenuation	< 0.17 dB (Rphantom 2x 6.8 kOhm)
Connector	Balanced 3-pole XLR
Thread for Capsule	60 UNS2
Weight	90 g, 3.17 oz
Dimensions	Length 142.5 mm (5.6"), diameter 20.5 mm (0.8")
Temperature Range	-10°C to +50°C (14°F to 122°F)
Humidity	5% to 90% RH, non-condensing
NTi Audio #	600 040 040

The product specifications may vary based on the mounted microphone capsule type.

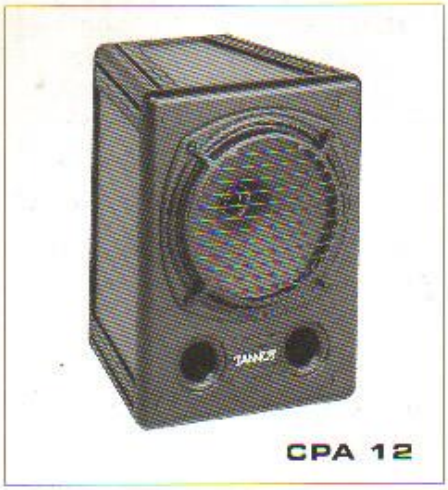

CPA 12

CPA 15

TANNOY CONTRACTOR SERIES CPA 12/15

DESCRIPTION

The Tannoy CPA 12 and CPA 15 have been designed to be versatile compact full range flying loudspeaker systems, developed for music playback and vocal reinforcement in theatre, audio-visual, houses of worship and night club applications.

Tannoy's Engineers have developed two new Dual Concentric drive units for the Contractor Series. Both drive units have lower distortion levels and higher audio fidelity than that expected from studio monitors, let alone PA systems.

The CPA 12 is a two-way passively crossed system, comprising of one 12" PCD (Phase Coherent D) Dual Concentric driver. The CPA 15 uses a 15" version of the Dual Concentric for applications that require extended bass. Ferrofluid is used to cool the HF compression drivers on both models. By using an acoustically time aligned point source, phase coherent Dual Concentric driver the effects of feedback are severely limited. More importantly, as the system is a point source, large clusters/arrays have well balanced tonality. All this is achieved without the use of any electronic signal processing.

The 20° trapezoidal wood frame enclosure utilises a DMT energy braced matrix. This matrix ensures driver rigidity without causing audible resonances. Diffraction and reflection effects are virtually eliminated by using smooth corners and edges on the front baffle. This greatly improves intelligibility.

FEATURES

Point source Dual Concentric transducers
3 Dimensional phase coherent drive unit
DMT enclosure construction
Trapezoidal enclosure for ease of arraying
Well behaved tonality when arrayed
Simple rigging capability
Identical horizontal and vertical off axis performance

APPLICATIONS

Nightclubs and Cabaret
Theatre and cinema reinforcement
Houses of worship
Audio-Visual
Useful building block for small to mid sized arrays

TANNOY
HEAR BELIEVE

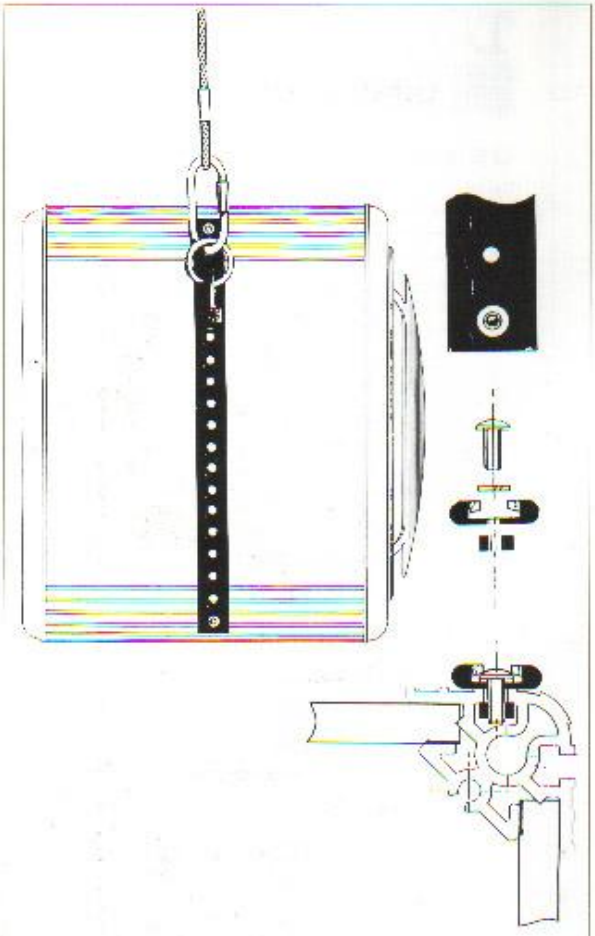

RIGGING

The CPA 12 and 15 enclosures are equipped with an integral aluminium extrusion. This extrusion will readily facilitate the fitting of optional track, including Aeroquip on both side faces, or any similar rigging hardware which can be terminated with M8 nuts and fitted between the top and bottom extrusions.

A CPA rigging kit is available as an optional extra, this comprises -

- 2 x 6 ft lengths of Aeroquip style extrusion
- 16 High tensile M8 bolts
- 16 Washers.
- 16 M8 Nuts.

This allows the rigging to be cut and tailored to the individual application.

STAND MOUNTING

Each enclosure is fitted with two internal M8 nuts on the base of the enclosure which will marry up with an industry standard stand mount for portable applications.

CROSS-OVER

Tannoy uses what can be described as a minimalist cross-over network. This approach results in a more natural reproduction of sound than large complex networks. The air cored inductors and film capacitors are hard wired on to the terminal panel. All components are easily serviceable by removing the terminal panel, even in a fixed installation. The terminal connections are made via 4 pole Speakon connectors. The Speakon has been chosen for its ease of field serviceability.

AMPLIFICATION

Your CPA 12/15 can safely be driven, for music reproduction, with any low impedance amplifier from 100 Watts to 300/400 Watts. However, care should be taken to avoid running the amplifier into clipping. Generally a high power amplifier running free of distortion will do less damage to your CPA 12/15 than a low power amplifier continually clipping. It is also worth remembering that a high power amplifier running at less than 80% of output power generally sounds a lot better than a lower power amplifier running at 100%.

ARCHITECTURAL AND ENGINEERING SPECIFICATIONS

CPA 12

The loudspeaker system shall be of the two-way Dual Concentric type consisting of one reflex loaded 12" low frequency transducer and high frequency compression driver coaxially mounted and coincidentally time aligned within the same frame.

Low and high frequency elements shall be combined by an internal 12dB/octave passive cross-over network operating at 1.5kHz.

Performance of the loudspeaker, without any electronic control shall meet or exceed the following criteria:

Frequency response measured 1 metre on axis with swept sine wave shall be 50Hz-25kHz +3/-6dB. High frequency dispersion at -6dB shall be 60° H x 60° V. The power handling shall be 150 Watts RMS. Rated impedance shall be 8 Ohms. Maximum continuous SPL 1 metre on axis shall be 120dB.

Dimensions shall be 49.2 cm H x 37.2 cm W x 36.0 cm D (19.4" H x 14.6" W x 14.2" D)

The loudspeaker system shall be the Tannoy CPA 12

CPA 15

The loudspeaker system shall be of the two-way Dual Concentric type consisting of one reflex loaded 15" low frequency transducer and high frequency compression driver coaxially mounted and coincidentally time aligned within the same frame.

Low and high frequency elements shall be combined by an internal 12dB/octave passive cross-over network operating at 1.5kHz.

Performance of the loudspeaker without any electronic control shall meet or exceed the following criteria:

Frequency response measured 1 metre on axis with swept sine wave shall be 45Hz-25kHz +3/-6dB. High frequency dispersion at -6dB shall be 60° H x 60° V. The power handling shall be 200 Watts RMS. Rated impedance shall be 8 Ohms. Maximum continuous SPL 1 metre on axis shall be 122dB.

Dimensions shall be 72.0 cm H x 49.2 cm W x 36.0 cm D (28.3" H x 19.4" W x 14.2" D)

The loudspeaker system shall be the Tannoy CPA 15

DIMENSIONS

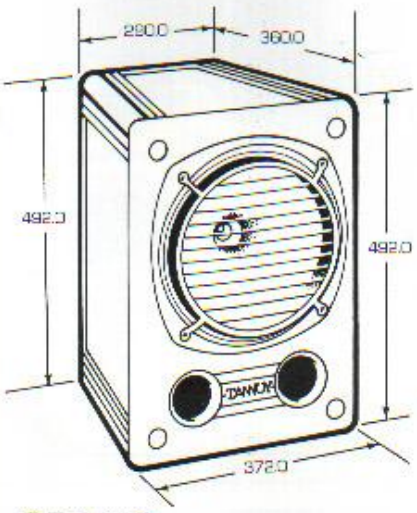

CPA 12

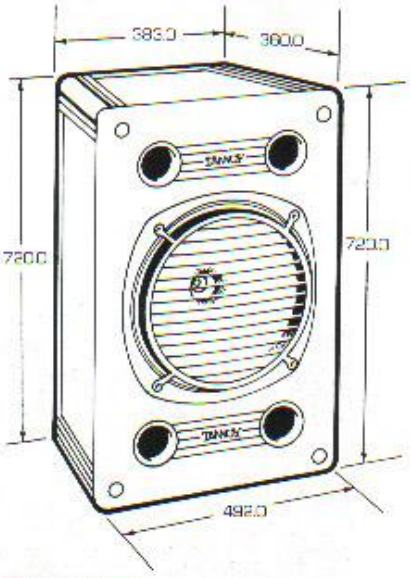

CPA 15

ALL MEASUREMENTS IN MILLIMETRES
DEPTH EXCLUDING GRILLE

CPA 12 VERTICAL

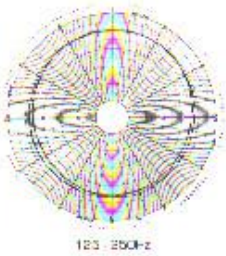

CPA 12 HORIZONTAL

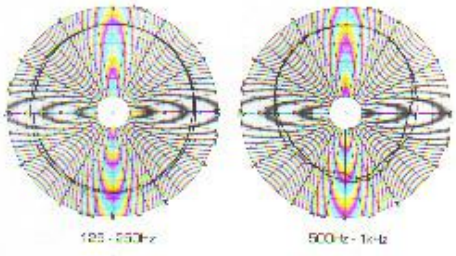

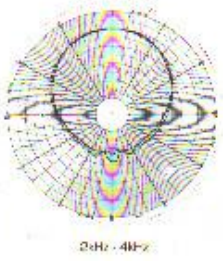

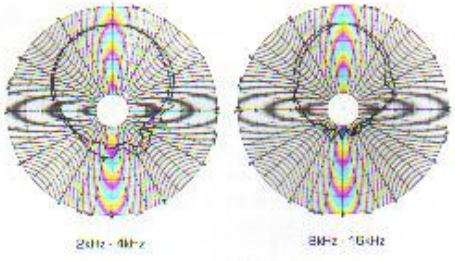

CPA 12 FREQUENCY RESPONSE

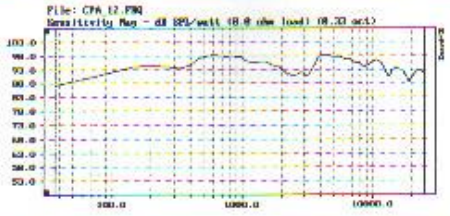

CPA 12 DISTORTION

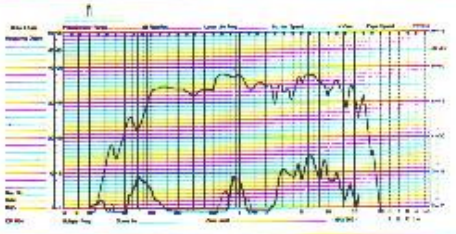

CPA 12 IMPEDANCE CURVE

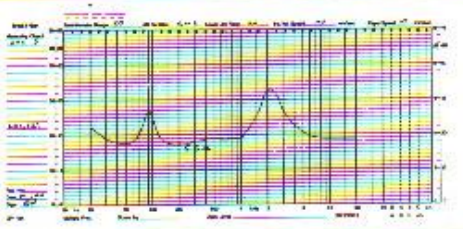

SPECIFICATIONS CPA 12

Frequency Response -3/-6dB	50Hz-25kHz
Recommended Amplifier Power (2)	300 Watts 8 Ohm
Peak Power Handling (3)	450 Watts
Sensitivity (1)	98 dB 1w 1m
Maximum SPL (1)	124 dB
Nominal Impedance	8 Ohms
HF Dispersion -6dB	60° x 60° -10-25 20kHz
DI Averaged (4)	9.0, 400Hz-12kHz
@ 1kHz (ISO)	7.6
@ 2kHz (ISO)	9.1
@ 8kHz (ISO)	12.2
Q Averaged (4)	8.9, 400Hz-12kHz
@ 1kHz (ISO)	5.8
@ 2kHz (ISO)	8.1
@ 8kHz (ISO)	16.8

Distortion (2)

0.1 Full Power	2nd	3rd Harmonic
100Hz	1.3%	0.3%
1000Hz	1.2%	0.3%
10000Hz	2.5%	0.1%
0.01 Full Power	2nd	3rd Harmonic
100Hz	0.5 %	<0.1%
1000Hz	0.4%	0.2%
10000Hz	0.3%	<0.1%

Cross-over point	1.5kHz
Driver Complement	1 x 12" Full range point source Dual Concentric
Enclosure	35L vented utilising DMT energy braced matrix
Connectors	Speakon NL4FC
Weight	20kg (44 lbs)
Flying Hardware	Aeroquip compatible track
Dimensions	49.2 cm H x 37.2 cm W 36.0 cm D
Excluding grille	(19.4" H x 14.6" W x 14.2" D)

SPECIFICATIONS CPA 15

Frequency Response -3/-6dB	45Hz-25kHz
Recommended Amplifier Power (2)	400 Watts 8 Ohm
Peak Power Handling (3)	600 Watts
Sensitivity (1)	100 dB 1w 1m
Maximum SPL (1)	127 dB
Nominal Impedance	8 Ohms
HF Dispersion -6dB	60° x 60° -10-25 20kHz
DI Averaged (4)	10.7, 400Hz-12kHz
@ 1kHz (ISO)	9.3
@ 2kHz (ISO)	11.3
@ 8kHz (ISO)	13.5
Q Averaged (4)	12.8, 400Hz-12kHz
@ 1kHz (ISO)	8.5
@ 2kHz (ISO)	13.5
@ 8kHz (ISO)	22.4

Distortion (2)

0.1 Full Power	2nd	3rd Harmonic
100Hz	0.5%	0.3%
1000Hz	0.9%	0.3%
10000Hz	2.5%	<0.1%
0.01 Full Power	2nd	3rd Harmonic
100 Hz	0.1%	<0.1%
1000Hz	0.1%	0.2%
10000Hz	0.3%	<0.1%

Cross-over point	1.5kHz
Driver Complement	1 x 15" Full range point source Dual Concentric
Enclosure	95L vented utilising DMT energy braced matrix
Connectors	Speakon NL4FC
Weight	31kg (68.2 lbs)
Flying Hardware	Aeroquip compatible track
Dimensions	72.0 cm H x 49.2 cm W x 36.0 cm D
Excluding grille	(28.3" H x 19.4" W x 14.2" D)

NOTES REGARDING SPECIFICATIONS

1) Averaged over quoted bandwidth for half space.

2) 150W/250W RMS based on the test described in the EIA standard RS-426A. However to simulate real life applications more closely the signal is applied for a 6 minute duty cycle over a 6 hour time period.

3) Short term transient assuming no amplification clipping.

4) Unlike other loudspeakers, these systems are Point source Dual Concentric and therefore the figures are true for any axis angle within 360° vertical or horizontal.

WARRANTY

As with all Tannoy professional products the Contractor Series range is covered with a 5 year warranty from the date of manufacture subject to the absence of misuse, overload or accidental damage. No claims will be considered if the serial number has been altered or removed.

Warranty work should only be carried out by an authorised Tannoy Contractor Series dealer or service agent.

This warranty in no way affects your statutory rights.

Our policy commits us to incorporating improvements to our products through continuous research and development. Please confirm current specifications for critical applications with your supplier.

DIFFERENTIAL MATERIAL TECHNOLOGY (DMT)

The study of different materials and their relative behaviours when in intimate contact.

Rounded corners and edges greatly inhibit sound reflections and diffractions from the cabinet boundaries, which are major sources of irregularities in reproduced sound, particularly in terms of the perceived placement of instruments, within the sound stage. For the HF unit to make an effective job of launching all the detail that it can generate into the listening space it must be held rigidly in the cabinet, over the frequencies through which it operates.

This last phrase is the key to the Tannoy cabinets. If a "rigid" cabinet is used, the redundant energy from the rear of the bass unit and frame causes endless resonance problems within the cabinet. Differential Materials Technology provides the answers by using a variety of different adhesives between the rear of the drive unit and brace, and between the cabinet walls and the brace. These lossy couplings effectively transmit and absorb energy in a frequency selective way. Put more simply, at high frequencies the drive unit sees the cabinet as a rigid structure, and at lower frequencies as a resonance absorbing/damping structure, the study of DMT providing an idealistic cabinet solution for the complete frequency range.

DMT AND THE NEW LF UNITS

The 12" and 15" units use new pressure diecast chassis forming the framework for the Dual Concentric, utilising innovative new thinking for LF drive units. The new castings have a very open construction with a vented rear suspension to improve thermal cooling, prevent major reflections and eliminate potential resonant trapped air cavities. Axial rigidity has been optimised to complement the new cabinet design philosophy. While the front surface profile, along with the purpose designed diffraction ring blends the LF and HF wavefront with the front of the cabinet. Our research has shown that, assuming the HF unit is well designed in the first place, this is the single biggest factor in providing smooth HF radiation in Dual Concentrics.

The study of DMT has played a large part in the suspension/termination of the different cones. The characteristic cone termination impedance is matched by the surround material independently of the required suspension compliance. The unit system compliance is provided by the rear suspension where the best degree of mechanical control can be provided. The heart of the LF unit is the motor system which consists of the magnet and voice coil. Computer optimisation of the low frequency magnet gives linear flux linking to the voice coil using low carbon steel pole pieces and an anisotropic barium ferrite magnet. A specially designed pure copper stabilising ring fits over the outer pole of the 12" and 15" units where it reduces eddy current losses, lowers midrange distortion and increases thermal cooling by a massive 50%. In this way, both power compression and reliability are considerably enhanced.

DMT AND THE NEW HF UNITS

A completely new HF unit has been designed for the 12" and 15" using a separate magnet assembly with easy field replacement for the HF diaphragm.
A new design of waveguide has been arrived at by making extensive use of CAD (computer aided design). We call it a waveguide because there is a direct analogy with electromagnetic radiation in that characteristic impedances must be carefully matched without introducing standing waves. The Tannoy HF waveguide matches the acoustic source impedance at the HF diaphragm into the listening environment. The waveguide shapes the wavefront as it travels down from the diaphragm ensuring that path lengths are equal, the wavefront is perpendicular to the fixed surfaces and that the wavefront is spherical. In this way, transverse modes are minimised.

The wavefront shaping begins at the diaphragm surface and because the compression ratio can be kept relatively low with this design, the distortions due to air non linearities are minimised. A hyperbolic flare has been chosen for optimum low frequency performance at the crossover point. The waveguide requires total piston movement over the operating range since any breakup modes within the diaphragm will result in phase shifted components at the start of the waveguide propagation. A rigid piston diaphragm operating to above 25kHz is made from aluminium and magnesium alloy. A special machine has been designed and built to form and extrude the diaphragm and ensures reliable handling for production and field service. The duralumin diaphragm is put through a special alkaline etching process followed immediately by the build process to ensure reliability. The diaphragm assembly is suspended by a precision moulded inert nitrile elastomer surround. This has been designed and tooled using high precision numerically controlled machining techniques with a very narrow roll to eliminate resonances below 25kHz and provide a very stable and consistent mounting.

The roll form ensures high excursions can take place if necessary and provides a fatigue indestructible assembly. High temperature polyamide insulated copper clad aluminium rectangular ribbon conductor is chemically bonded onto a glass fibre former fitting onto the outside of the HF diaphragm skirt. This gives a high temperature (polyamide), very low mass (aluminium wire, glass fibre), high rigidity (rectangular wire, former to outside of diaphragm skirt) high reliability (nitrile suspension, copper clad aluminium) assembly. Linecout materials are crucial for HF units and our new design incorporates beryllium copper flat strip to eliminate fatigue breakages and prevent fusing on unsupported areas under overload conditions. The HF diaphragm assembly is factory mounted onto the waveguide by a newly designed high precision production process to ensure that the spacing between diaphragm and waveguide is consistent and the whole assembly self centres under all conditions when placed on the magnet assembly. Field replacement is therefore extremely simple and no soldering or centering techniques are required.

THE SUM OF THE PARTS

The design considerations have been dealt with here, in isolation, but of course in practice the whole is considerably more than the sum of the parts and the design considerations for each aspect of the performance are strongly interdependent. The role of Tannoy's study of DMT as an overall philosophy in the design of the Contractor Series cannot be overstated. The minimum it can be said to have achieved is a complete understanding of the effect on the sound/energy characteristics of every "nut and bolt" of the Contractor Series.

Appendix E

Additional Results from Chapter 3

These are the equivalent plots to those presented in Section 3.4.1, but corresponding to perturbations in the position of the scattering object rather than perturbations in the size of the scattering object. They provide minimal further insight compared to the results presented in Section 3.4.1 hence they have not been included in the chapter, however the additional plots are included here for completeness.

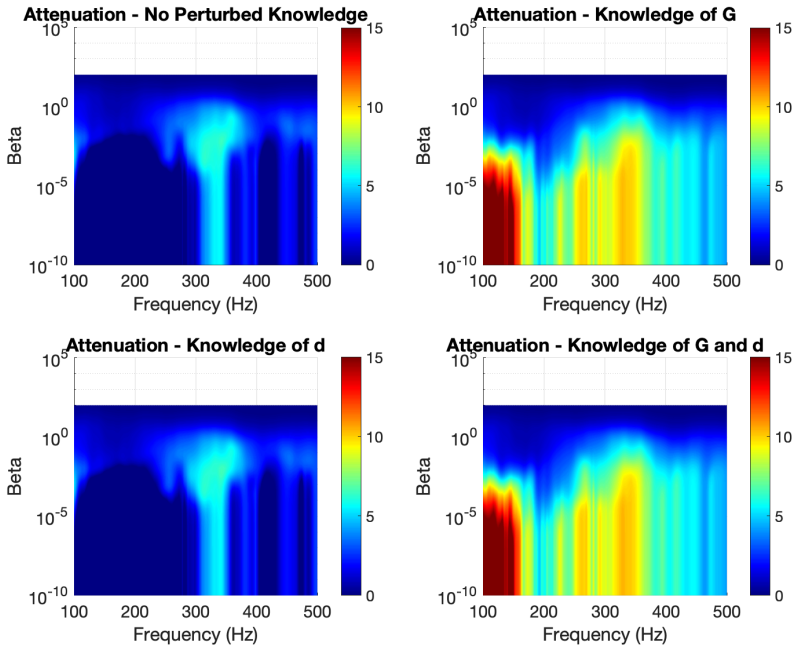

Figure E.1: Contour plots showing the attenuation that the control system is able to achieve in the scattered sound power over frequency and a range of values of β, when the position of the scattering sphere is perturbed by 20 cm and the controller has different levels of knowledge of the perturbations.

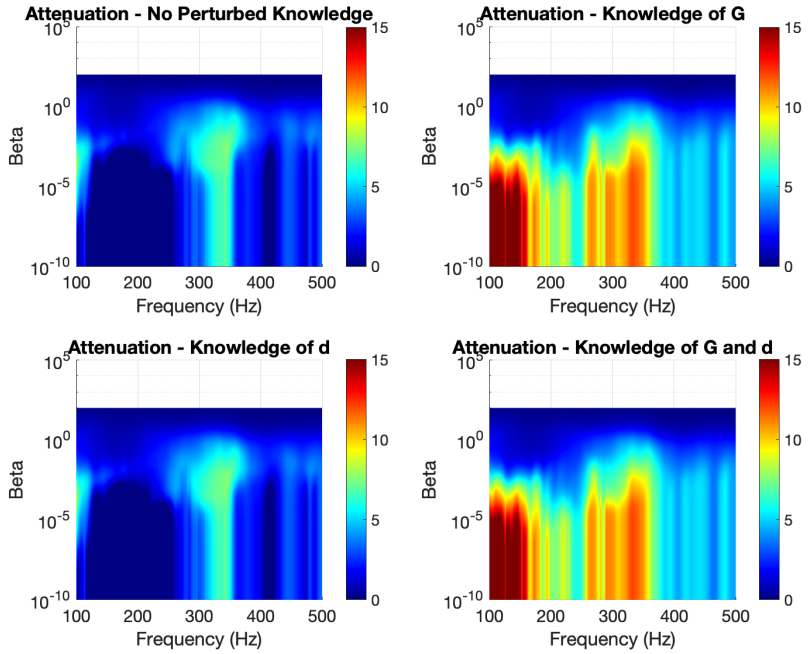

Figure E.2: Contour plots showing the attenuation that the control system is able to achieve in the scattered sound power over frequency and a range of values of β, when the position of the scattering sphere is perturbed by 10 cm and the controller has different levels of knowledge of the perturbations.

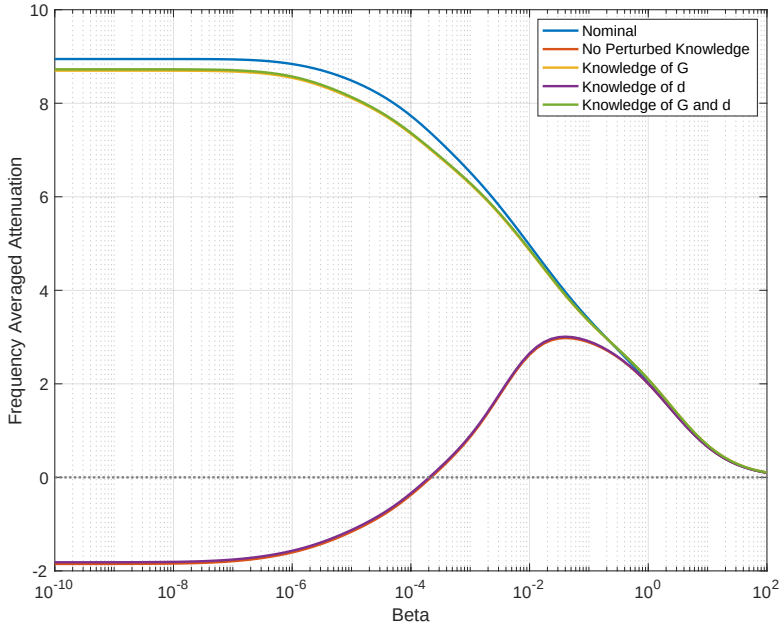

Figure E.3: A plot showing the frequency averaged attenuation in the scattered sound power that the control system is able to achieve with increasing values of regularisation for the nominal case, and when the sphere is perturbed by 20 cm, and the controller has different levels of knowledge of the perturbations.

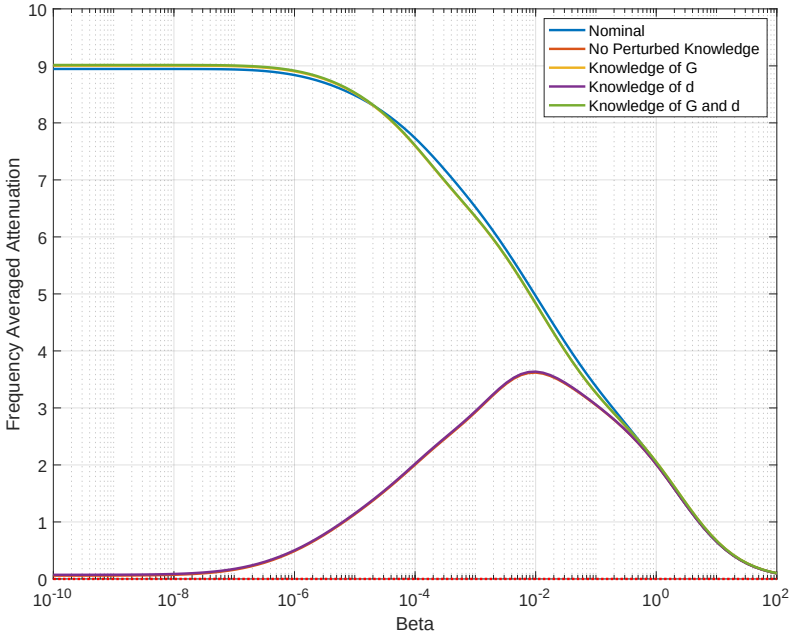

Figure E.4: A plot showing the frequency averaged attenuation in the scattered sound power that the control system is able to achieve with increasing values of regularisation for the nominal case, and when the sphere is perturbed by 10 cm, and the controller has different levels of knowledge of the perturbations.

Appendix F

Convergence Study of Cylindrical Shell FEM/BEM Modelling

Chapter 6 discusses the implementation of a BEM/FEM model to investigate the structural response and acoustic scattering properties of a hollow cylindrical shell when excited by an incident acoustic plane wave. Active Vibration Control was then implemented, and the effect that this has on the scattered field was investigated. It is known that the quality of the data from a numerical model such as this is heavily reliant on the suitability of the mesh [79, 110, 111] and, therefore, a convergence study has been carried out.

To solve the model in COMSOL Multiphysics, a free tetrahedral mesh has been created. In Chapter 6 it is stated that this mesh was scaled such that it had a minimum of 6 elements per wavelength. This is standard practice [75, 81, 112], as it is generally assumed that a finer mesh than this is not necessary. To confirm that this is the case, a convergence study has been implemented by solving the model with increasing mesh resolution from 0.1 elements per wavelength to 10 elements per wavelength. As the maximum frequency investigated in Chapter 6 is 1 kHz, the convergence study has been implemented at this frequency.

The model was excited by a radial structural force applied midway along its length. The total sound power radiated by the cylinder was then calculated using Equation 6.4, and plotted against mesh resolution, as shown in Figure F.1. It can clearly be seen that the results from the model are inconsistent at low mesh resolutions, where the model is prone to high levels of numerical error. However, when it reaches ≈ 4 elements per wavelength, the data converges on a consistent value and is independent of mesh resolution. It can therefore be assumed that the mesh used throughout the numerical model in Chapter 6 is of a sufficiently high density to resolve the necessary detail within the required frequency range without adding unnecessary computational cost.

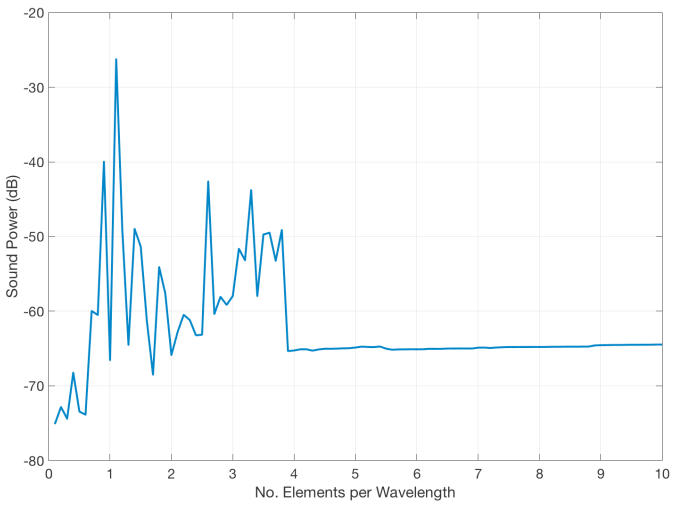

Figure F.1: Convergence study showing the total acoustic power of the cylindrical shell when excited by a 1kHz unit structural force and meshed with varying element sizes.

Appendix G

Manufacturing Drawings for the Aluminium Cylinder

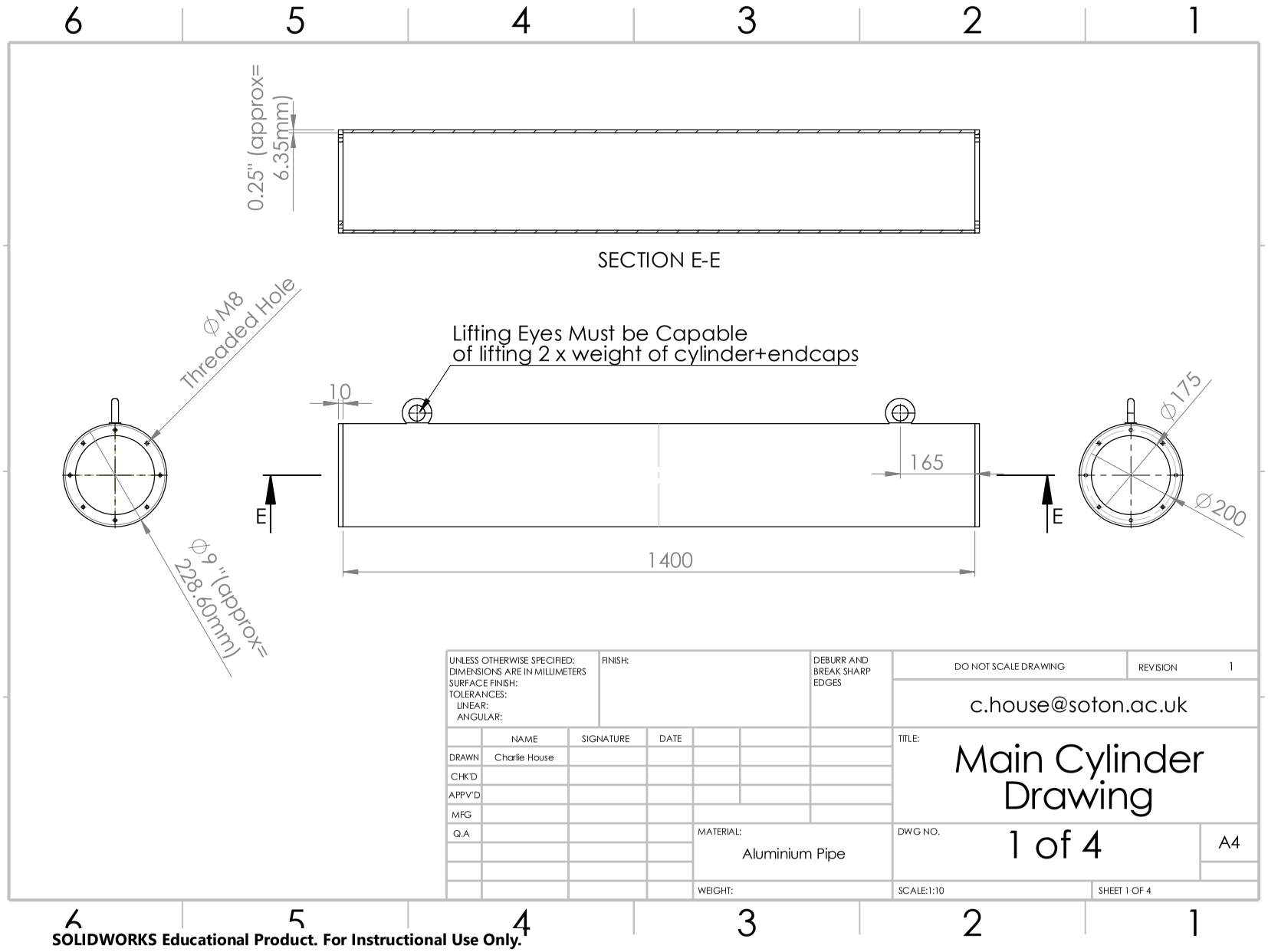

UNLESS OTHERWISE SPECIFIED: DIMENSIONS ARE IN MILLIMETERS SURFACE FINISH: TOLERANCES: LINEAR: ANGULAR:		FINISH:		DEBURR AND BREAK SHARP EDGES	DO NOT SCALE DRAWING	REVISION 1	
					c.house@soton.ac.uk		
	NAME	SIGNATURE	DATE		TITLE: Main Cylinder Drawing		
DRAWN	Charlie House						
CHK'D							
APPV'D							
MFG							
Q.A				MATERIAL: Aluminium Pipe	DWG NO. 1 of 4	A4	
				WEIGHT:	SCALE:1:10	SHEET 1 OF 4	

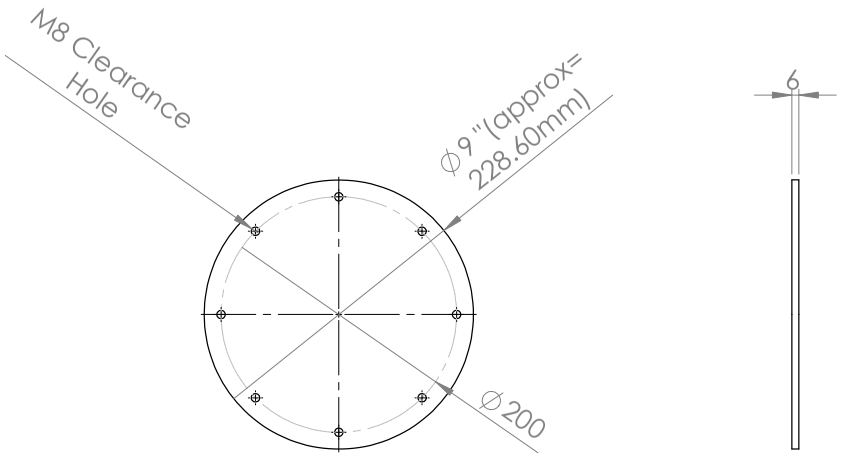

UNLESS OTHERWISE SPECIFIED: DIMENSIONS ARE IN MILLIMETERS SURFACE FINISH: TOLERANCES: LINEAR: ANGULAR:		FINISH:			DEBURR AND BREAK SHARP EDGES	DO NOT SCALE DRAWING	REVISION 1
						c.house@soton.ac.uk	
	NAME	SIGNATURE	DATE			TITLE: End Plate Drawing	
DRAWN	Charlie House						
CHK'D							
APPV'D							
MFG							
Q.A				MATERIAL: 6mm Sheet Aluminium		DWG NO. 2 of 4	A4
				WEIGHT:		SCALE:1:10	SHEET 2 OF 4

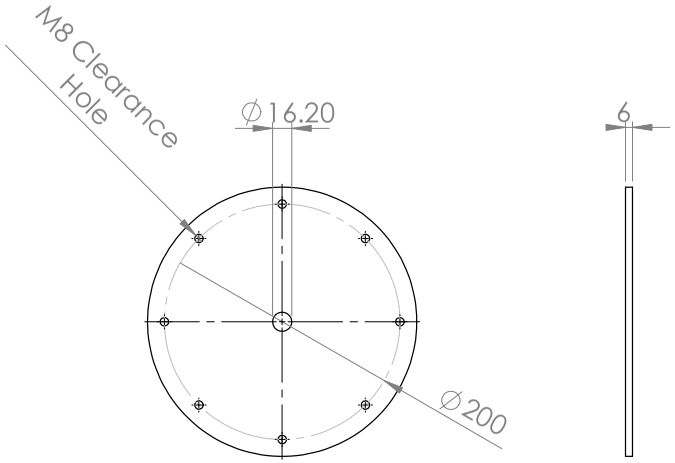

UNLESS OTHERWISE SPECIFIED: DIMENSIONS ARE IN MILLIMETERS SURFACE FINISH: TOLERANCES: LINEAR: ANGULAR:		FINISH:			DEBURR AND BREAK SHARP EDGES	DO NOT SCALE DRAWING	REVISION 1
						c.house@soton.ac.uk	
	NAME	SIGNATURE	DATE			TITLE: Penetrated End Drawing	
DRAWN	Charlie House						
CHK'D							
APPV'D							
MFG							
Q.A				MATERIAL: 6mm Sheet Aluminium		DWG NO. 3 of 4	A4
				WEIGHT:		SCALE:1:5	SHEET 3 OF 4

PART:	NO OFF:
Cylinder Body	1
End Plate	1
Penetrated End Plate	1
M8 Bolt	16

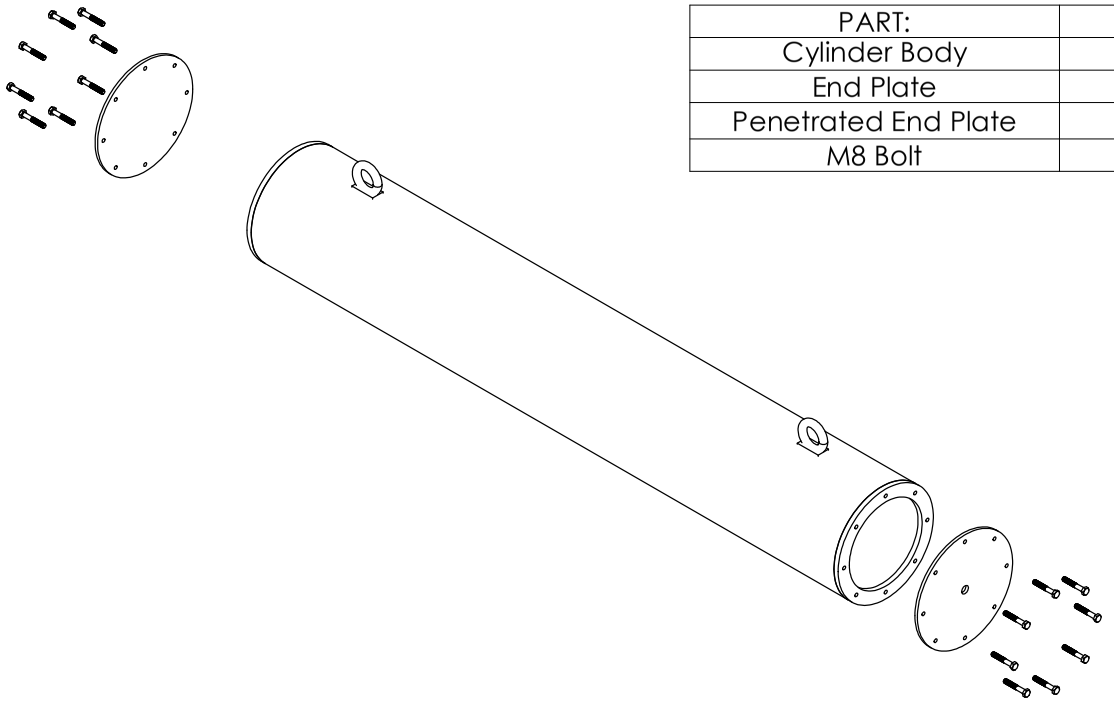

UNLESS OTHERWISE SPECIFIED: DIMENSIONS ARE IN MILLIMETERS SURFACE FINISH: TOLERANCES: LINEAR: ANGULAR:		FINISH:				DEBURR AND BREAK SHARP EDGES	DO NOT SCALE DRAWING	REVISION 1
							c.house@soton.ac.uk	
	NAME	SIGNATURE	DATE				TITLE: Assembly Drawing	
DRAWN	Charlie House							
CHK'D								
APPV'D								
MFG								
Q.A				MATERIAL: NA			DWG NO. 4 of 4	A4
				WEIGHT:			SCALE:1:10	SHEET 4 OF 4

Appendix H

Serial Numbers for Equipment for the Aluminium Cylinder Measurements

- Signal Conditioner - PCB Sensor Signal Conditioner Model Series 481
- Low Pass Filters - 2 x Benchmaster 21M Kemo
- Power Amplifiers - 2 x Monacor STA1508 (Loudspeaker ran over 2 channels in bridge mode, control shakers ran on single channels)
- Acquisition System - dSPACE AutoBox RTI1005, DS2103 DAC, DS2002 ADC
- 20 x Fylde 256AC Mic Preamplifiers
- Control Actuators - 10 x TEAX32C30-4/B
- Accelerometers - 12 x PCB A352 / C67:
    1. SN 26906
    2. SN 63554
    3. SN 26885
    4. SN 63552
    5. SN 59258
    6. SN 26895
    7. SN 26886
    8. SN 63556
    9. SN 26894
    10. SN 26890
    11. SN 26893
    12. SN 26879
- Measurement Microphones - 20 x PCB 130F20 ICP Measurement Microphones

1. SN 50331
2. SN 50329
3. SN 50330
4. SN 50327
5. SN 50350
6. SN 50351
7. SN 50348
8. SN 50332
9. SN 50334
10. SN 50335
11. SN 50336
12. SN 50328
13. SN 50349
14. SN 50354
15. SN 50325
16. SN 50352
17. SN 50326
18. SN 50337
19. SN 50353
20. SN 50333

- Loudspeaker - Tannoy CPA12 Loudspeaker
- Calibrator - Larson Davis CAL250-0122

Appendix I

A Discussion into Possible Differences Between the Simulation Study and Experimental Study in Chapter 6

It is clear from the results presented in Chapter 6 that there are significant differences between the scattering results in the simulation study, which exhibit resonant scattering behaviour, and the scattering results in the experimental study, which do not. Whilst the structural response of the cylinder is similar in both simulated and measured datasets, the scattered sound power is not and, therefore, the effect of AVC on the scattered sound power in the experimental study is inconsistent with the numerical study. It is understood from the simulations that an AVC system would only be able to reduce resonant scattering and, as this is not present in the experimental dataset, it is not surprising that AVC has little effect. An investigation will now be made into a few potential differences between the simulation study and the experimental study, and the effects of these inconsistencies on the scattered sound field will be quantified. A number of differences will be discussed, however in the interests of succinctness updated scattered power plots will only be presented when they differ significantly from the results presented in Figure 6.14.

I.1 Differences in Incident Field

Whilst care was taken to ensure that the measurement setup matched the simulated environment as much as possible, there are inevitably some differences which cannot be avoided. The incident acoustic field in the simulated dataset was generated by a uniform plane wave, whereas in the measurements it was generated by a loudspeaker, close enough to the cylinder to not be considered far-field. It is possible that this difference in the characteristics of the incident field could result in a significantly different scattering response. To investigate this, the computational model was re-run with the background field being generated by a spherical wave emanating from the same position that the loudspeaker was located in the measurements as, at low frequencies, a spherical wave model is more consistent with the acoustic propagation from a loudspeaker than a plane wave model is [113]. After re-running the computational model with this change to the incident field, the scattered pressure directivity plots

and the total scattered power plot were almost identical to those presented in Chapter 6; leading to the conclusion that this minor difference is unlikely to be a significant contributor to the discrepancy between the measured and simulated results presented in Chapter 6.

I.2 Planar Power Evaluation

A potential reason for the measurements and modelling to show inconsistent results is due to the fact that the evaluation of the scattered power in the model was an integration over a sphere surrounding the cylinder, whereas in the measurements the power was evaluated by summing the pressure at 20 discrete locations in a ring around the cylinder. This discretisation of the sound field is unlikely to cause significant problems over the bandwidth being investigated, however evaluating the summation over a plane rather than a sphere may introduce greater errors.

To investigate this, the scattered power from the computational model was re-calculated using Equation 6.7. The scattered pressures were evaluated from distinct points in the model, arranged in a circle around the cylinder with consistent locations to the microphones in the experimental setup. The scattered sound power was then calculated using Equation 6.8, consistent with the measurement results. The scattered acoustic power when calculated using both methods (spherical surface integral vs a planar discrete summation) is plotted in Figure I.1. Whilst there is an overall broadband level shift between the two calculation methods, the magnitude of the resonant peaks in the scattered power are consistent. This implies that the acoustic power evaluation method is not a significant contributor to the differences observed in Chapter 6 between simulation and experimental datasets.

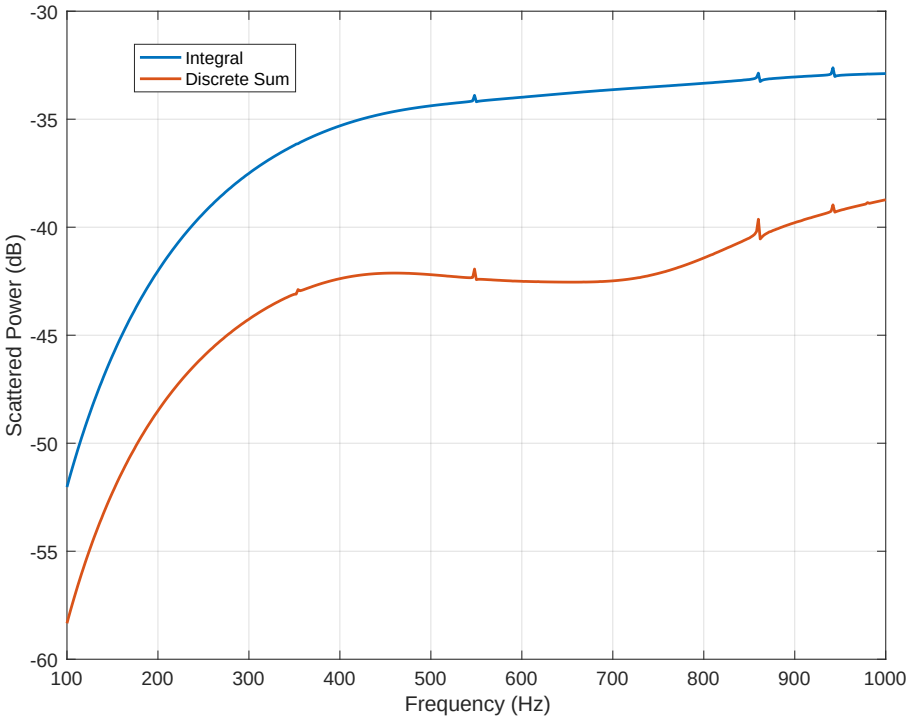

Figure I.1: Modelled scattered power from the cylinder when calculated using an integration, and using a sum over a discrete number of points.

I.3 Effect of Annuli

As was described in Chapter 6, the computational model is based on the scattering object being a perfect cylindrical shell, whereas the real-life scatterer has additional geometry to allow for the removal of the end caps. Whilst any added geometry was minimised as much as possible in the manufacturing and design stages, the thickness of the annulus structure welded to the end of the cylinder cannot be neglected, and will have a significant effect on the structural dynamics of the object. The geometry of the real cylinder can be seen in the schematic presented in Figure 6.15, and in the manufacturing drawings shown in Appendix G.

To investigate this effect, the computational model has been adapted to include a flexible annulus structure on each end. These annuli have been rigidly coupled to the cylinder body (the effects of the welds have been neglected, although these could also be modelled if needed [114]). The end caps have then been rigidly coupled to the annulus structure as it can be assumed that, within the bandwidth of interest, the bolt connections between the end caps and the annulus behave rigidly. This coupling sequence allows the cylindrical shell, the solid annuli, and the end caps to bend and distort freely on the condition they stay fixed to one another.

As in the previous studies, the computational model has been run over a range of frequencies, and the structural response to an acoustic excitation has been calculated. The acoustic scattered power has also been calculated, according to Equation 6.4. This has been performed with both a perfect cylinder, and with the annulus structure on the ends. The structural and acoustic responses are presented in Figures I.2a and I.2b respectively.

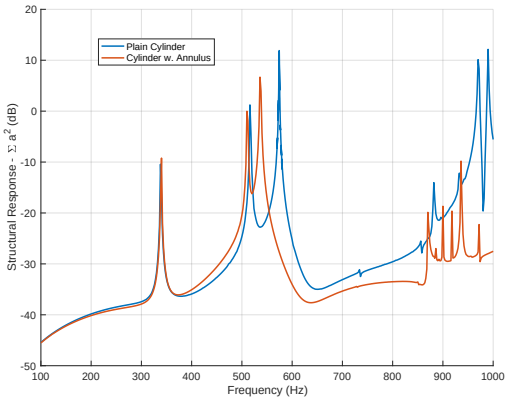

(a) Modelled structural response to an acoustic excitation with and without the annulus structure present.

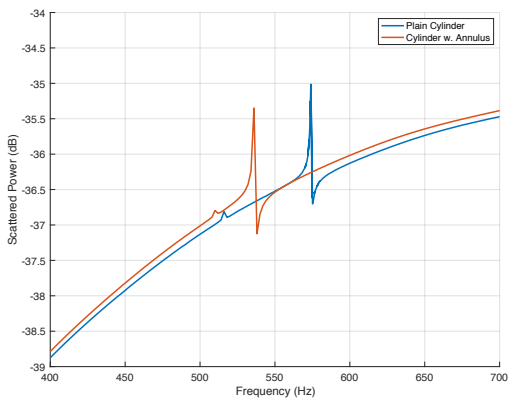

(b) Modelled scattered sound power with and without the annulus structure present. The plot has been scaled to only show the 400Hz - 700Hz region, as this is where the main resonant scattering behaviour occurs.

Figure I.2: Investigating the effects of the annulus structure

Figure I.2a shows how the annuli make minimal difference to the structural response at low frequencies, with the first breathing mode not changing in frequency, however the bending mode has lowered in frequency by 38Hz and is approximately 6 db lower in magnitude. The

higher order modes are also significantly reduced in both magnitude and frequency. Figure I.2b shows that the presence of the annulus lowers the frequency of the resonance in the scattered field, consistent with the frequency of the bending mode reducing, however the relative magnitude of the resonance is unchanged and, therefore, this is unlikely to contribute to the discrepancies between the simulation and experimental results presented in Chapter 6.

I.4 Effect of Shakers

Whilst the shakers chosen to implement AVC on the structure are fairly small relative to the size of the cylinder, the effect that they have on the dynamics of the structure cannot be neglected. When not being driven, a shaker behaves like a Single Degree of Freedom (SDOF) mass spring damper system [115–117] and, therefore, the 10 shakers mounted onto the cylinder for this set of anechoic measurements will likely have a significant effect on the structural response of the cylinder; especially when excited at the resonant frequency of the shakers. To investigate this behaviour, a lumped parameter model of a mass spring damper system was implemented within the numerical model. Ten independent mass-spring-damper systems were simulated within the model as lumped mechanical systems, each of which was excited by a point-evaluation of the radial acceleration of the cylinder and each of which imparts a radial point force onto the cylinder. The properties of these mass-spring-damper systems were obtained by characterising the dynamics of the shakers used in the experimental procedure with a Thiele-Small analysis. This analysis is detailed in Appendix J, and the dynamic properties of the shakers are presented in Table I.1.

Property	Value
Proof Mass	$0.119\mathrm{kg}$
Stiffness	$45191\mathrm{Nm}^{-1}$
Damping	$35.1\mathrm{Nsm}^{-1}$
Resonant Frequency	$98.1\mathrm{Hz}$

Table I.1: Dynamic Properties of Tectonic Elements TEAX 32C30 Shakers

These parameters were used to tune the 10 lumped parameter systems within the computational model. The transfer function between the input of the mass-spring-damper system and the acceleration of the mass on the free end has been plotted, to ensure that the system is behaving as expected, and is presented in Figure I.3.

For reference, a second model was also created with the shakers modelled as simple point masses rather than lumped mechanical systems, to investigate the difference between modelling the shakers as dynamic systems compared to modelling them as a mass loading on the cylinder. Both models were solved over a range of frequencies between 100Hz and 1kHz, with the structural response and acoustic scattered power results presented in Figures I.4a and I.4b respectively.

As expected, Figure I.4b shows that applying a distribution of simple masses over the surface of the cylinder has the effect of lowering the frequency of the resonances. The magnitude of the breathing mode is significantly amplified, whilst the other modes have little change in

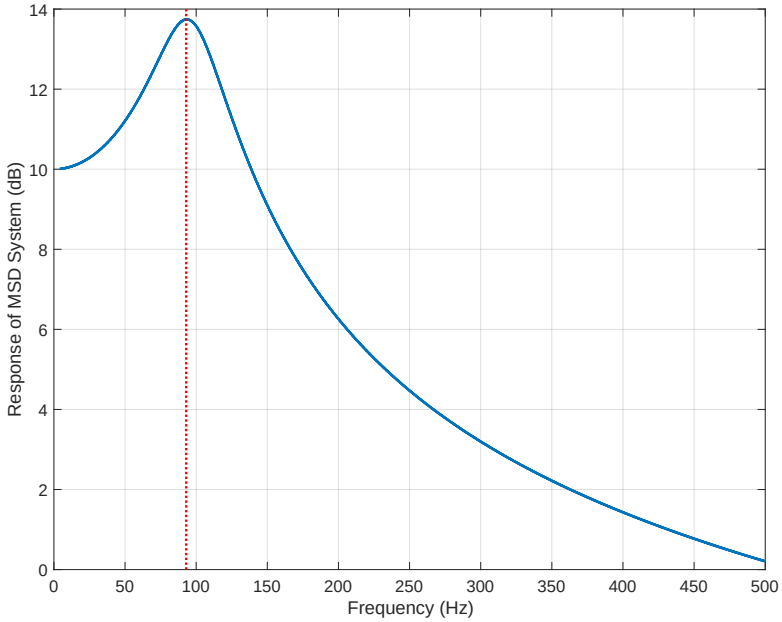

Figure I.3: Simulated transfer function of the mass-spring-damper system, used to model the dynamics of the shakers.

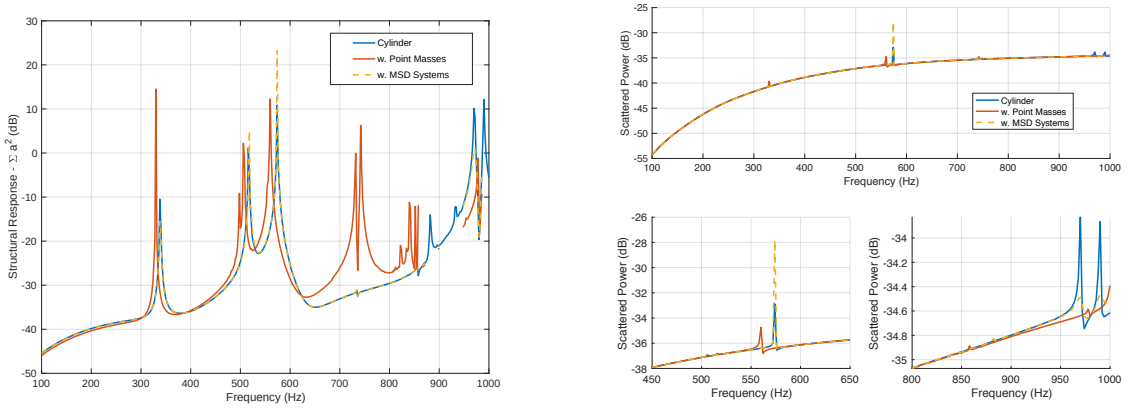

(a) Modelled structural response to an acoustic excitation with the presence of point masses, mass spring damper systems, and with neither.

(b) Modelled scattered power with the presence of point masses, mass spring damper systems, and with neither. The lower plots are zoomed in on the two regions of interest.

Figure I.4: Investigating the effects of the annulus structure

their magnitude. Including mass-spring-damper systems has little effect on the frequency of the resonances, but does increase the magnitude of the bending mode by over 10dB. Figure I.4a shows that the inclusion of multiple mass-spring-damper systems increases the size of the $\sim 550\text{Hz}$ resonant peak in the scattered power by approximately 5dB, but almost completely eliminates the higher frequency resonant peaks. This implies that the impact of the shakers on the cylinder in the measurements discussed above is not the cause of the lack of resonant scattering - in fact it should be increasing the resonant scattering.

To investigate the effects of the the presence of the shakers on the structure experimentally, the structural characterisation of the cylinder discussed in Chapter 6 was repeated with the shakers removed from the structure. Clearly in this configuration AVC cannot be implemented, however it does allow for the effects of the shakers to be quantified. The structural response to an acoustic excitation is presented in Figure I.5, which shows that the presence of the shakers have a significant effect at the first breathing mode, where the structural response is reduced by over 30dB. The magnitudes of the second breathing mode and the first bending mode are reduced by approximately 10dB in each case. This is likely to be a significant contributor to the lack of resonant scattering, as reducing the magnitude of the relevant structural resonance by 10dB will have a significant impact on the resonant scattering behaviour.

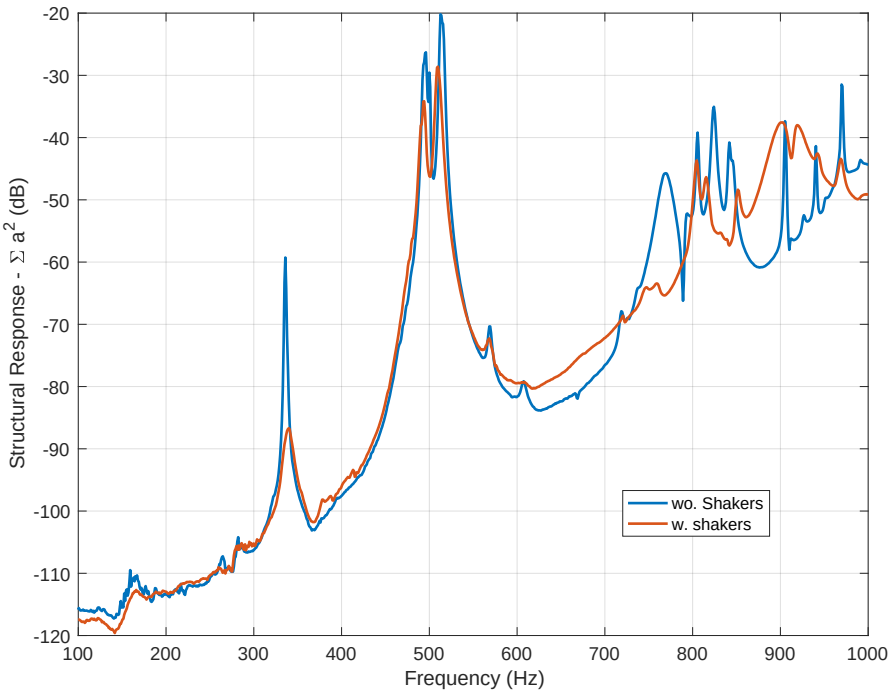

Figure I.5: Measured structural response of the cylinder to an acoustic excitation without the presence of the control shakers on the scattering object.

I.5 Effects of Modelling Boundary Conditions

The computational model discussed in Chapter 6 has free boundary conditions on all sides - that is to say the cylinder in the model is floating in space without any forces imposed upon it except those from the incident acoustic wave. In the real-life experiments, the cylinder is

suspended from the lifting eyes welded onto either end, as shown in Figure 6.22. This will have the effect of resisting translational motion in the horizontal plane, and preventing it in the vertical plane. It will also resist rotational motion in both planes. Considering that the simulations predict the first bending mode to be the one at which resonant scattering occurs, the effect of the boundary conditions restricting the displacement at the ends of the cylinder will likely have a considerable impact on the structural response at this frequency.

To investigate the effect that the boundary conditions will have on the structural and acoustic responses of the cylinder, the simulations have been re-computed with the structure both pinned, and fixed, at the locations of the hanging eyes. COMSOL defines these boundary conditions as [83]:

Pinned: *"The Pinned node adds a point condition that fixes the translations in all directions, that is, all displacements are zero. The rotations are not constrained."*

Fixed: *"The Fixed Constraint node adds a condition that makes the geometric entity fixed; that is, the displacements are zero in all directions. If there are rotational degrees of freedom, they will also be zero."*

As with the previous models the structural response to the acoustic excitation and the scattered sound power have been calculated at each frequency. These results are presented in Figures I.6a and I.6b respectively.

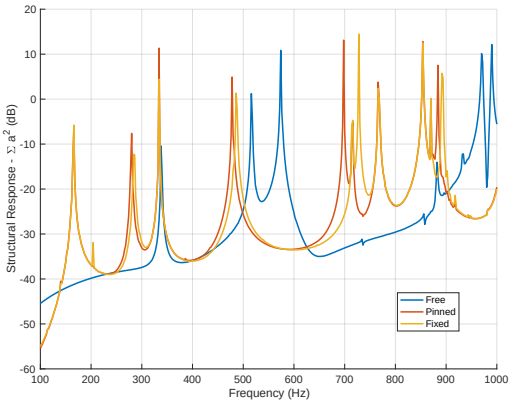

(a) Simulated structural response to an acoustic excitation with various boundary conditions.

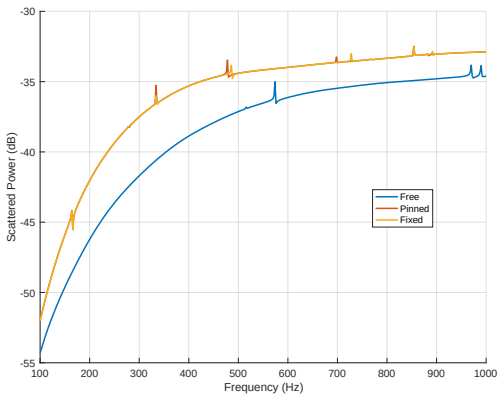

(b) Simulated scattered sound power with various boundary conditions.

Figure I.6: Investigating the effects of boundary conditions on the structural response and acoustic scattered power.

Figure I.6a shows how the inclusion of both the pinned and fixed boundary conditions significantly increases the magnitude of the first breathing mode (approx 334Hz), whilst having little effect on its frequency. The first bending mode is shifted down to 478Hz with the pinned condition, or 486Hz with the fixed condition, and is reduced by 5dB and 9dB respectively. The second breathing mode is pushed up in frequency, and now coincides with a number of the higher frequency modes above 700Hz. Two lower frequency modes are introduced, at 166Hz and 280Hz, corresponding to rigid body modes which have been warped by the

boundary conditions, as shown by the mode shape plots presented in Figure I.7. These resonances appear to correspond to the vertical and horizontal rigid body modes, however the pinning of the two mounting points has caused a sagging action in each case.

Figure I.6b shows the predicted scattered power for the three boundary condition cases. Whereas the free cylinder has one single peak at the bending mode, the cylinders with either pinned or fixed boundary conditions have a number of smaller resonances, corresponding to various mode shapes. Each of these resonances is approximately 1dB or less, which could explain why no resonances were found in the measured scattered fields - identifying a 1dB peak in a real-world measurement is incredibly challenging.

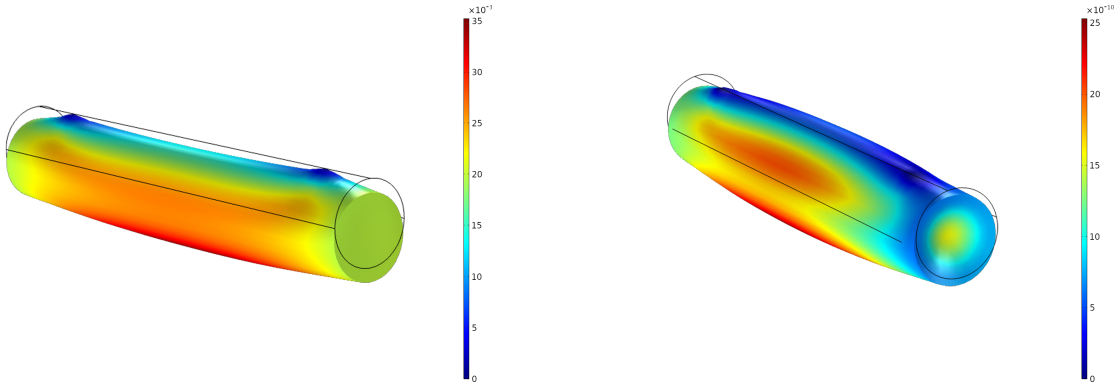

(a) 166 Hz *(b) 280 Hz*

Figure I.7: Surface acceleration magnitude of the cylindrical shell when excited at the two low frequency resonances with either fixed or pinned boundary conditions.

I.6 Conclusions

Chapter 6 presents an investigation into the effects of Active Vibration Control on the soundfield scattered by a flexible structure, using computational and experimental data. Whilst the simulation results show resonant scattering behaviour, which is reduced by the introduction of AVC, the experimental results do not show the presence of resonant scattering. This appendix has discussed a number of potential sources of error between the simulation and experimental datasets, and attempted to quantify what effect these discrepancies would have on the acoustic response. In reality, the discrepancy is likely to be a combination of all of the factors discussed above, however the latter sets of results implies that the presence of shakers on the scattering body, and the boundary conditions at the hanging points, are the most significant contribution to this error. It is not trivial to reduce the effects of these phenomena in an experimental setup without significant changes to the way the measurements are carried out and, therefore, further investigation into this line of research has not been continued under this project.

Appendix J

Control Shaker Characterisation

Appendix I presents a discussion into potential sources of error in the computational modelling discussed in Chapter 6. As part of this investigation, the electroacoustic shakers used in the experiments are simulated as mass-spring-damper systems within the numerical model. For these systems to be accurately tuned to match the dynamics of the real-life shakers, the dynamics of the shakers must first be characterised. A Thiele-Small analysis is a method for characterising the dynamics of an inertial actuator without prior knowledge of its electrical or mechanical properties [113, 118]. After conducting a full Thiele-Small analysis, all of the properties needed to fully describe the performance of an electroacoustic transducer can be calculated. This appendix will present a Thiele-Small analysis on the Tectonic Elements TEAX 32C30 actuators used throughout this project, which in turn will allow these to be simulated within the numerical model presented in Chapter 6 and Appendix I.

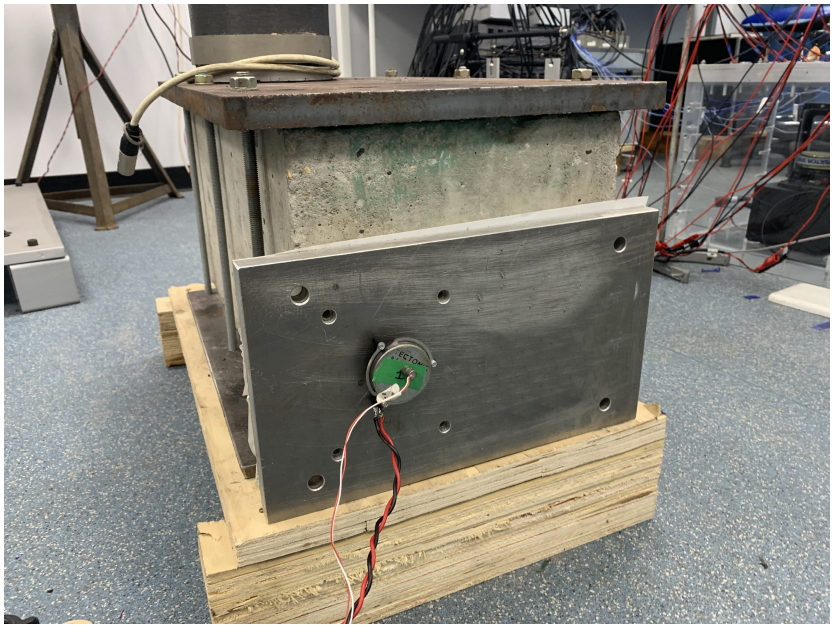

Figure J.1: A photograph showing the actuator being tested, mounted to a rigid block.

These measurements were performed using a dSpace Autobox RTI1005, connected to a DS2103 DAC card and a DS2003 ADC card, set to a sampling frequency of 2.5 kHz. A pair of Benchmaster 21M Kemo low-pass filters (cutoff at 1 kHz) were used as anti-aliasing and

reconstruction filters, and a Lab-Works PA119 power amplifier was used to drive the shaker. The structural response was measured by a PCB A352/C67 accelerometer, which was powered by a PCB481 signal conditioner.

One of the Tectonic Elements TEAX 32C30 actuators actuators was mounted to a rigid block, as shown in Figure J.1, with an accelerometer mounted to the back of it. Only one of the 10 shaker will be characterised in this appendix, and it assumed that the dynamic properties of the other shakers are comparable. The shaker was driven with 30s of bandlimited white noise, and the response was measured at the accelerometer position. A small mass was then placed onto the back of the shaker (Blu-Tac in this case), and the measurement was repeated. This process was carried out for two different sized masses of Blu-Tac, as shown in Figure J.2. The first mass had a weight of 11g, the second of 20g.

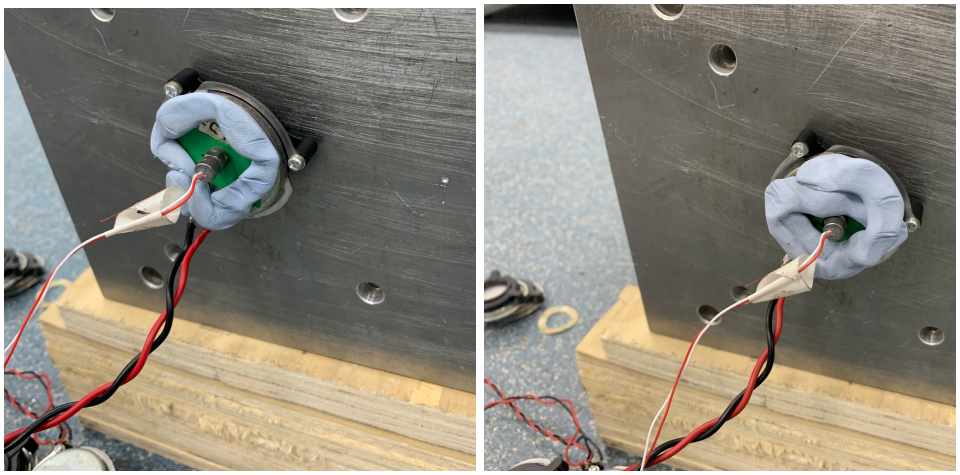

Figure J.2: A photograph showing two different sized masses of Blu-Tac attached to the actuator

The transfer function between the actuator drive signal and the measured accelerometer signal was then calculated for each case using the H1 estimatior, and these responses are plotted in Figure J.3a. Figure J.3a shows how the addition of the mass lowers the resonance in the actuator, but also has the effect of damping the resonance . The resonance of a SDOF system ω_r is given as

$$\omega_r = \sqrt{\frac{k}{m}}, \tag{J.1}$$

where k is the stiffness of the shaker mounts, and m is the moving mass of the shaker. Therefore, by identifying the frequencies of the three resonances shown in Figure J.3a and knowing the amount of mass added each time, the moving mass m of the shaker can be found. As the measurement was repeated with two different sized added masses, two different values for the moving-mass of the shaker can be calculated. These were found to be within 0.5% of one another, and therefore they were simply averaged to give an estimate of the true moving mass of the shaker. This value of m can then be combined with Equation J.1 to give a value for the stiffness of the shaker mounts.

The final mechanical property needed to describe the mechanical properties of the shaker is the damping coefficient. This can be calculated using the half-power bandwidth of the measured resonance [119]. The half power bandwidth $\Delta\omega$ was calculated for the measured transfer function, as shown in Figure J.3b. The Damping Factor Q can then be calculated

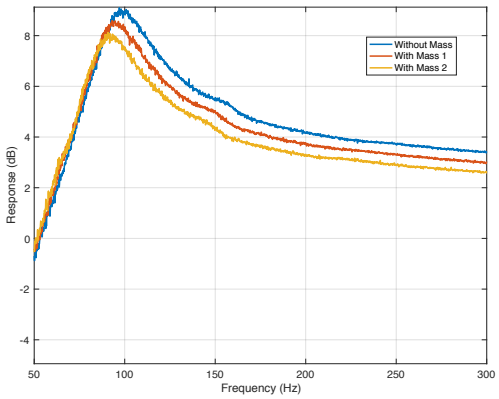

(a) A plot showing the measured resonance in the actuator without any extra, and with two sizes of added mass.

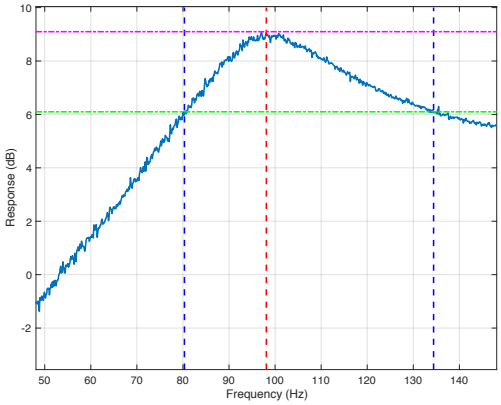

(b) A plot showing the half power bandwidth of the measured resonance of the shaker.

as

$$Q = \frac{\omega_r}{\Delta\omega}, \tag{J.2}$$

from which the damping ratio ζ can be calculated as

$$\zeta = \frac{1}{2Q}. \tag{J.3}$$

The critical damping value C_{crit} for a SDOF system is given as

$$C_{\text{crit}} = 2\sqrt{km}, \tag{J.4}$$

and the damping coefficient C for the given shakers can be calculated as

$$C = \zeta C_{\text{crit}} \tag{J.5}$$

These calculations give values for the mass, stiffness and damping ratio of the Tectonic Elements TEAX 32C30 as:

Property	Value
Moving Mass	0.119kg
Stiffness	45191Nm^{-1}
Damping	35.1Nsm^{-1}
Resonant Frequency	98.1Hz

Table J.1: Dynamic Properties of Tectonic Elements TEAX 32C30 Shakers

A previous study into the dynamics of these shakers has been carried out using the methodology presented in [120], and gives comparable dynamic properties to those presented in Table J.1.

Bibliography

[1] Richard Harrison, Chun Yang, Ching-Fan Lin, Tasso Politopoulos, and Eric Chang. Classification of Underwater Targets with Active Sonar. *Aerospace Control Systems*, pages 534–538, 1993. doi: 10.1109/AEROCS.1993.720991.

[2] T. G. Leighton. *Fundamentals of underwater acoustics*. 1998.

[3] F. E. Toole. In-Head Localization of Acoustic Images. *The Journal of the Acoustical Society of America*, 48(4B):943–949, 1970. ISSN 0001-4966. doi: 10.1121/1.1912233.

[4] Theodor S. Becker, Dirk Jan Van Manen, Carly M. Donahue, Christoph Bärlocher, Nele Börsing, Filippo Broggini, Thomas Haag, Johan O.A. Robertsson, Darren R. Schmidt, Stewart A. Greenhalgh, and Thomas E. Blum. Immersive Wave Propagation Experimentation: Physical Implementation and One-Dimensional Acoustic Results. *Physical Review X*, 8(3):31011, 2018. ISSN 21603308. doi: 10.1103/PhysRevX.8.031011. URL `https://doi.org/10.1103/PhysRevX.8.031011`.

[5] Nele Börsing, Theodor S. Becker, Andrew Curtis, Dirk Jan Van Manen, Thomas Haag, and Johan O.A. Robertsson. Cloaking and Holography Experiments Using Immersive Boundary Conditions. *Physical Review Applied*, 12(2):1, 2019. ISSN 23317019. doi: 10.1103/PhysRevApplied.12.024011. URL `https://doi.org/10.1103/PhysRevApplied.12.024011`.

[6] C. Pinhède, D. Habault, E. Friot, and Ph Herzog. Active control of the field scattered by the rigid wall of a semi-anechoic room—Simulations and full-scale off-line experiment. *Journal of Sound and Vibration*, 506, 2021. ISSN 10958568. doi: 10.1016/j.jsv.2021.116134.

[7] Jacob Hollebon, Filippo Maria Fazi, and Marcos Simon-Galvez. A Multiple Listener Crosstalk Cancellation System Using Loudspeaker-Dependent Regularization. *J. Audio Eng. Soc.*, 69(3):191–203, 2021. doi: https://doi.org/10.17743/jaes.2020.0067.

[8] Investigation of the Disturbance Produced by a Spherical Obstacle on the Waves of Sound. In *Proceedings of the London Mathematical Society*, 1873.

[9] J. Van Bladel. Low-Frequency Scattering by Hard and Soft Bodies. *The Journal of the Acoustical Society of America*, 44(4):1069–1073, 1968. ISSN 0001-4966. doi: 10.1121/1.1911197.

[10] Oleg A. Godin. Scattering of a spherical wave by a small sphere: An elementary solution. *The Journal of the Acoustical Society of America*, 130(4):EL135–EL141, 2011. ISSN 0001-4966. doi: 10.1121/1.3629140.

[11] Earl G. Williams. *Fourier Acoustics - Sound Radiation and Nearfield Acoustical Holography*. Elsevier, 1999. ISBN 978-0-12-753960-7.

[12] C. Athanasiadis, P. A. Martin, and I. G. Stratis. On spherical-wave scattering by a spherical scatterer and related near-field inverse problems. *IMA Journal of Applied Mathematics (Institute of Mathematics and Its Applications)*, 66(6):539–549, 2001. ISSN 02724960. doi: 10.1093/imamat/66.6.539.

[13] Oleg A. Godin. Rayleigh scattering of a spherical sound wave. *The Journal of the Acoustical Society of America*, 133(2):709–720, 2013. ISSN 0001-4966. doi: 10.1121/1.4774277.

[14] James J. Faran. Sound Scattering by Solid Cylinders and Spheres. *The Journal of the Acoustical Society of America*, 23(4):405–418, 1951. ISSN 0001-4966. doi: 10.1121/1.1906780. URL `http://asa.scitation.org/doi/10.1121/1.1906780`.

[15] R D Doolittle and Herbert Überall. Sound Scattering by Elastic Cylindrical Shells. *Journal of the Acoustical Society of America*, 272(39), 1966.

[16] L Flax, L R Dragonette, and Uberall H. Theory of elastic resonance excitation by sound scattering. *Journal of the Acoustical Society of America*, 63(723), 1978.

[17] J Diarmuid Murphy, Edward D Breitenbach, and Herbert Überall. Resonance scattering of acoustic waves from cylindrical shells. *Acoustical Society of America*, 677, 1978.

[18] J. Diarmuid Murphy, Jacob George, and Herbert Überall. Isolation of the resonant component in acoustic scattering from fluid-loaded cylindrical shells. *Wave Motion*, 1(2):141–147, 1979. ISSN 01652125. doi: 10.1016/0165-2125(79)90016-7.

[19] Yu. I. Bobrovnitskiĭ. Impedance theory of sound absorption: The best absorber and the black body. *Acoustical Physics*, 52(6):638–647, dec 2006. ISSN 1063-7710. doi: 10.1134/S1063771006060030. URL http://link.springer.com/10.1134/S1063771006060030.

[20] Yu. I. Bobrovnitskii. A new impedance-based approach to analysis and control of sound scattering. *Journal of Sound and Vibration*, 297(3-5):743–760, 2006. ISSN 10958568. doi: 10.1016/j.jsv.2006.04.030.

[21] Yifeng Fu, Imrana I. Kabir, Guan Heng Yeoh, and Zhongxiao Peng. A review on polymer-based materials for underwater sound absorption. *Polymer Testing*, 96:107115, 2021. ISSN 01429418. doi: 10.1016/j.polymertesting.2021.107115. URL https://doi.org/10.1016/j.polymertesting.2021.107115.

[22] Tao Meng. Simplified model for predicting acoustic performance of an underwater sound absorption coating. *JVC/Journal of Vibration and Control*, 20(3):339–354, 2014. ISSN 10775463. doi: 10.1177/1077546312461027.

[23] G. Ma and P. Sheng. Acoustic metamaterials: From local resonances to broad horizons. *Science Advances*, 2(2):e1501595–e1501595, 2016. ISSN 2375-2548. doi: 10.1126/sciadv.1501595. URL http://advances.sciencemag.org/cgi/doi/10.1126/sciadv.1501595.

[24] Ying Cheng, Fan Yang, Jian Yi Xu, and Xiao Jun Liu. A multilayer structured acoustic cloak with homogeneous isotropic materials. *Applied Physics Letters*, 92(15), 2008. ISSN 00036951. doi: 10.1063/1.2903500.

[25] J. B. Pendry and Jensen Li. An acoustic metafluid: Realizing a broadband acoustic cloak. *New Journal of Physics*, 10:0–9, 2008. ISSN 13672630. doi: 10.1088/1367-2630/10/11/115032.

[26] Lucian Zigoneanu, Bogdan Ioan Popa, and Steven A. Cummer. Three-dimensional broadband omnidirectional acoustic ground cloak. *Nature Materials*, 13(4):352–355, 2014. ISSN 14764660. doi: 10.1038/nmat3901.

[27] Yafeng Bi, Han Jia, Wenjia Lu, Peifeng Ji, and Jun Yang. Design and demonstration of an underwater acoustic carpet cloak. *Scientific Reports*, 7(1):1–10, 2017. ISSN 20452322. doi: 10.1038/s41598-017-00779-4. URL http://dx.doi.org/10.1038/s41598-017-00779-4.

[28] Peter A Kerrian, Amanda D Hanford, Dean E Capone, Benjamin S Beck, Peter A Kerrian, Amanda D Hanford, Dean E Capone, and Benjamin S Beck. Development of a perforated plate underwater acoustic ground cloak. *Journal of the Acoustical Society of America*, 2303, 2019. doi: 10.1121/1.5127844.

[29] K. T. Tan, H. H. Huang, and C. T. Sun. Optimizing the band gap of effective mass negativity in acoustic metamaterials. *Applied Physics Letters*, 101(24), 2012. ISSN 00036951. doi: 10.1063/1.4770370.

[30] Paul Leug. Process of Silencing Sound Oscillations, 1936.

[31] Harry F. Olson and Everett G. May. Electronic Sound Absorber. *The Journal of the Acoustical Society of America*, 25(6):1130–1136, 1953. ISSN 0001-4966. doi: 10.1121/1.1907249. URL http://asa.scitation.org/doi/10.1121/1.1907249.

[32] J. Garcia-Bonito, S. J. Elliott, and M. Bonilha. Active cancellation of pressure at a point in a pure tone diffracted diffuse sound field. *Journal of Sound and Vibration*, 201(1):43–65, 1997. ISSN 0022460X. doi: 10.1006/jsvi.1996.0742.

[33] P.A. Nelson and S.J. Elliott. *Active Control of Sound*. Academic Press, London, 1991. ISBN 978-0125154253.

[34] Boaz Rafaely. Zones of quiet in a broadband diffuse sound field. *The Journal of the Acoustical Society of America*, 110(1):296–302, 2002. ISSN 0001-4966. doi: 10.1121/1.1377632.

[35] Stephen J. Elliott, PA Nelson, Ian Stothers, and CC. Boucher. In-Flight experiments on the Active Control of Propeller-Induced Cabin Noise. *Journal of Sound and Vibration*, 140(2):191–217, 1990. ISSN 10958568. doi: 10.1016/0022-460X(90)90524-4.

[36] S. Daley, F. A. Johnson, J. B. Pearson, and R. Dixon. Active vibration control for marine applications. *Control Engineering Practice*, 12(4):465–474, 2004. ISSN 09670661. doi: 10.1016/S0967-0661(03)00135-7.

[37] Stephen J. Elliott. *Signal Processing for Active Control*. Academic Press, 2001. ISBN 0-12-237085-6.

[38] Jordan Cheer. Active control of scattered acoustic fields: Cancellation, reproduction and cloaking. *The Journal of the Acoustical Society of America*, 140(3):1502–1512, 2016. ISSN 0001-4966. doi: 10.1121/1.4962284. URL http://dx.doi.org/10.1121/1.4962284.

[39] Daniel Eggler, Hyuck Chung, Fabien Montiel, Jie Pan, and Nicole Kessissoglou. Active cloaking of rigid and elastic cylindrical scatterers. *Acoustics 2017*, (1):2–7, 2017.

[40] Emmanuel Friot and C. Bordier. Real-time active suppression of scattered acoustic radiation. *Journal of Sound and Vibration*, 278(3):563–580, 2004. ISSN 0022460X. doi: 10.1016/j.jsv.2003.10.064.

[41] Emmanuel Friot, Régine Guillermin, and Muriel Winninger. Active control of scattered acoustic radiation: A real-time implementation for a three-dimensional object. *Acta Acustica united with Acustica*, 92(2): 278–288, 2006. ISSN 16101928.

[42] Ning Han, Xiaojun Qiu, and Shengzhen Feng. Active control of three-dimension impulsive scattered radiation based on a prediction method. *Mechanical Systems and Signal Processing*, 30:267–273, 2012. ISSN 08883270. doi: 10.1016/j.ymssp.2012.01.023. URL http://dx.doi.org/10.1016/j.ymssp.2012.01.023.

[43] Fernando Guevara Vasquez, Graeme W. Milton, and Daniel Onofrei. Exterior cloaking with active sources in two dimensional acoustics. *Wave Motion*, 2011. ISSN 01652125. doi: 10.1016/j.wavemoti.2011.03.005.

[44] Gregory Futhazar, William J. Parnell, and Andrew N. Norris. Active cloaking of flexural waves in thin plates. *Journal of Sound and Vibration*, 356:1–19, 2015. ISSN 10958568. doi: 10.1016/j.jsv.2015.06.023. URL http://dx.doi.org/10.1016/j.jsv.2015.06.023.

[45] Charlie House, Jordan Cheer, and Steve Daley. An investigation into the performance limitations of active acoustic cloaking using an acoustic quiet-zone. In *178th Meeting of the Acoustical Society of America*, volume 39, San Diego, 2019. Acoustical Society of America.

[46] Charlie House, Jordan Cheer, and Steve Daley. An Investigation into the Effect of Uncertainty on Active Acoustic Cloaking. In *Inter Noise 2020*, pages 1–10, 2020.

[47] Harry F. Olson. Gradient Loudspeakers. *The Journal of the Acoustical Society of America*, 53(1): 344–344, 1973. ISSN 0001-4966. doi: 10.1121/1.1982431.

[48] D. Onofrei and E. Platt. On the synthesis of acoustic sources with controllable near fields. *Wave Motion*, 2018. ISSN 01652125. doi: 10.1016/j.wavemoti.2017.10.004.

[49] Mingsian R. Bai, Jeong-Guon Ih, and Jacob Benesty. *Acoustic Array Systems: Theory, Implementation, and Application*. Wiley-IEEE Press, 2014. ISBN 978-0-470-82723-9.

[50] Philip Coleman, Philip J. B. Jackson, Marek Olik, Martin Møller, Martin Olsen, and Jan Abildgaard Pedersen. Acoustic contrast, planarity and robustness of sound zone methods using a circular loudspeaker array. *The Journal of the Acoustical Society of America*, 135(4):1929–1940, 2014. ISSN 0001-4966. doi: 10.1121/1.4866442. URL http://asa.scitation.org/doi/10.1121/1.4866442.

[51] Guy Bart Stan, Jean Jacques Embrechts, and Dominique Archambeau. Comparison of different impulse response measurement techniques. *AES: Journal of the Audio Engineering Society*, 50(4):249–262, 2002. ISSN 00047554.

[52] Angelo Farina. Advancements in impulse response measurements by sine sweeps. *Audio Engineering Society - 122nd Audio Engineering Society Convention 2007*, 3(October):1626–1646, 2007. URL http://www.aes.org/e-lib/browse.cfm?elib=14106.

[53] Gene H Golub, Per Christian Hansen, and Dianne P O'Leary. Tikhonov Regularization and Total Least Squares. *Society for Industrial and Applied Mathematics Journal on Matrix Analysis and Applications*, 1999. doi: 10.1137/S0895479897326432.

[54] Lawrence E Kinsler and Austin R Frey. *Fundamentals of Acoustics*. John Wiley & Sons, 4th edition, 2000. ISBN 978-0471847892.

[55] Martin Møller, Martin Olsen, Finn Agerkvist, Jakob Dyreby, and Gert Munch. Circular loudspeaker array with controllable directivity. *128th Audio Engineering Society Convention 2010*, 3:1640–1651, 2010.

[56] J.J do Rego Silva. *Acoustic and Elastic Wave Scattering using Boundary Elements*. WIT Press, 1994. ISBN 978-1853122934.

[57] E A Skelton and J H James. *Theoretical Acoustics of Underwater Structures*. Imperial College Press, 1997. ISBN 978-1-86094-085-9. doi: https://doi.org/10.1142/p072.

[58] Gene H Golub and Charles F Van Loan. *Matrix Computations*. The John Hopkins University Press, Maryland, 4th edition, 2013. ISBN 9781421407944.

[59] Seyyed M. Hasheminejad and M. Rajabi. Scattering and active acoustic control from a submerged piezoelectric-coupled orthotropic hollow cylinder. *Journal of Sound and Vibration*, 318(1-2):50–73, 2008. ISSN 0022460X. doi: 10.1016/j.jsv.2008.04.005.

[60] M. Rajabi and A. Mojahed. Active acoustic cloaking spherical shells. *Acta Acustica united with Acustica*, 104(1):5–12, 2018. ISSN 18619959. doi: 10.3813/AAA.919140.

[61] Charlie House, Jordan Cheer, and Steve Daley. On the use of Virtual Sensing for the Real-Time Detection and Active Control of a Scattered Acoustic Field. In *International Congress on Sound and Vibration*, number 1, pages 1–8, 2019.

[62] C. Testa and L. Greco. Prediction of submarine scattered noise by the acoustic analogy. *Journal of Sound and Vibration*, 426:186–218, 2018. ISSN 10958568. doi: 10.1016/j.jsv.2018.04.011. URL `https://doi.org/10.1016/j.jsv.2018.04.011`.

[63] Stephen J. Elliott, Jordan Cheer, Jung Woo Choi, and Youngtae Kim. Robustness and regularization of personal audio systems. *IEEE Transactions on Audio, Speech and Language Processing*, 20(7): 2123–2133, 2012. ISSN 15587916. doi: 10.1109/TASL.2012.2197613.

[64] S.J. Elliott, Woomin Jung, and Jordan Cheer. Causality and Robustness in the Remote Sensing of Acoustic Pressure, with Application to Local Active Sound Control. In *ICASSP*, 2019.

[65] Stephen J. Elliott, Jin Zhang, Chung Kwan Lai, and Jordan Cheer. Superposition of the uncertainties in acoustic responses and the robust design of active control systems. *The Journal of the Acoustical Society of America*, 148(3):1415–1424, 2020. ISSN 0001-4966. doi: 10.1121/10.0001965.

[66] K. H. Baek and S. J. Elliott. Effects of plant and disturbance uncertainties in active control systems on the placement of transducers. *Journal of Sound and Vibration*, 230(2):261–289, 2000. ISSN 0022460X. doi: 10.1006/jsvi.1999.2615.

[67] Guo yong Jin, Tie jun Yang, You hong Xiao, and Zhi gang Liu. A simultaneous equation method-based online secondary path modeling algorithm for active noise control. *Journal of Sound and Vibration*, 303 (3-5):455–474, 2007. ISSN 10958568. doi: 10.1016/j.jsv.2006.11.039.

[68] Jarosław Figwer. Secondary path model identification in active noise control. *2010 15th International Conference on Methods and Models in Automation and Robotics, MMAR 2010*, pages 110–113, 2010. doi: 10.1109/MMAR.2010.5587253.

[69] PA Nelson and SH Yoon. Estimation of Acoustic Source Strength By Inverse Methods: Part I, Conditioning of the Inverse Problem. *Journal of Sound and Vibration*, 233(4):639–664, 2000. ISSN 0022460X. doi: 10.1006/jsvi.1999.2837.

[70] Jordan Cheer, Vinal Patel, and Simone Fontana. The application of a multi-reference control strategy to noise cancelling headphones. *The Journal of the Acoustical Society of America*, 145(5):3095–3103, 2019. ISSN 0001-4966. doi: 10.1121/1.5109394.

[71] Yu. I. Bobrovnitskii. A new solution to the problem of an acoustically transparent body. *Acoustical Physics*, 50(6):647–650, 2004. ISSN 1063-7710. doi: 10.1134/1.1825093.

[72] Roure Alain and Albarrazin Anne. The Remote Microphone Technique for Active Noise Control. *Active 99*, 29:1233–1244, 1999.

[73] Woomin Jung. *Mid-frequency Local Active Control of Road Noise*. PhD thesis, University of Southampton, 2018. URL `http://eprints.soton.ac.uk/id/eprint/427150`.

[74] Charlie House, Jordan Cheer, and Steve Daley. The Effect of Active Vibration Control on the Sound Field Scattered from a Flexible Structure. In *ISMA - International Conference on Noise and Vibration Engineering*, Leuven, 2018.

[75] COMSOL Multiphysics. Acoustic-Structure Interaction. Technical report.

[76] Qing-Huo Liu and Jianping Tao. The perfectly matched layer for acoustic waves in absorptive media. *The Journal of the Acoustical Society of America*, 102(4):2072–2082, 2002. ISSN 0001-4966. doi: 10.1121/1.419657.

[77] Stephen Kirkup. The BEM in Acoustics. page 161. Integrated Sound Software, 1998. ISBN 0 953 4031 06.

[78] R J Astley. Wave envelope and infinite element schemes for acoustical radiation. *International Journal for Numerical Methods in Fluids*, 3(December 1982):507–526, 1983.

[79] Y. M. Tang, A. F. Zhou, and K. C. Hui. Comparison of FEM and BEM for interactive object simulation. *CAD Computer Aided Design*, 38(8):874–886, 2006. ISSN 00104485. doi: 10.1016/j.cad.2006.04.014.

[80] COMSOL Multiphysics. How to Use the Boundary Element Method in Acoustics Modeling, 2018. URL `https://uk.comsol.com/blogs/how-to-use-the-boundary-element-method-in-acoustics-modeling/`.

[81] Denny Fritze, Steffen Marburg, and Hans Jürgen Hardtke. FEM-BEM-coupling and structural-acoustic sensitivity analysis for shell geometries. *Computers and Structures*, 83(2-3):143–154, 2005. ISSN 00457949. doi: 10.1016/j.compstruc.2004.05.019.

[82] Dominique Chapelle and Klaus-Jurgen Bathe. *The Finite Element Analysis of Shells - Fundamentals*. Springer-Verlag Berlin Heidelberg, 2nd edition, 2011. ISBN 978-3-642-16407-1. doi: 10.1007/978-3-642-16408-8.

[83] COMSOL Multiphysics. Structural Mechanics Module. *Manual*, page 454, 2008. ISSN 00401951. doi: 10.1007/978-1-4939-2760-9_14. URL `www.comsol.de`.

[84] Aldo Rona. The acoustic resonance of rectangular and cylindrical cavities. *Proceedings of the 13th CEAS/AIAA Aeroacoustics Conference*, 1(3):1–12, 2007. ISSN 1748-3018. doi: 10.1260/174830107782424110. URL `http://hdl.handle.net/2381/1986`.

[85] G. C. Gaunaurd, E. Tanglis, H. Überall, and D. Brill. Interior and exterior resonances in acoustic scattering - I. Spherical targets. *Il Nuovo Cimento B Series 11*, 76(2):153–175, 1983. ISSN 03693554. doi: 10.1007/BF02721550.

[86] Wen H. Lin and A C Raptis. Acoustic scattering by elastic solid cylinders and spheres in viscous fluids. *The Journal of the Acoustical Society of America*, 73(3):736, 1983. ISSN 00014966. doi: 10.1121/1.389039. URL `http://scitation.aip.org/content/asa/journal/jasa/73/3/10.1121/1.389039`.

[87] Chung Y. Tsui, Glenn N. Reid, and Guillermo C. Gaunaurd. Resonance scattering by elastic cylinders and their experimental verification. *Journal of the Acoustical Society of America*, 80(2):382–390, 1986. ISSN NA. doi: 10.1121/1.394089.

[88] Lawrence Flax, Guillermo C. Gaunaurd, and Herbert ÜBERALL. *Theory of Resonance Scattering*, volume 15. 1981. ISBN 0124779158. doi: 10.1016/B978-0-12-477915-0.50008-7.

[89] The Gorilla Glue Company. Data Sheet - Gorilla Glue Epoxy Resin, 2016. URL `https://www.gorillatough.com/wp-content/uploads/Clear-Gorilla-Glue.pdf`.

[90] British Standards Institution. BS EN ISO 3745 : 2012. 2012.

[91] Earl G. Williams, Jeffery D. Tippmann, Sandrine T. Rakotonarivo, Zachary J. Waters, Philippe Roux, and W. A. Kuperman. Experimental estimation of in vacuo structural admittance using random sources in a

non-anechoic room. *The Journal of the Acoustical Society of America*, 142(1):103–109, 2017. ISSN 0001-4966. doi: 10.1121/1.4990953. URL http://asa.scitation.org/doi/10.1121/1.4990953.

[92] Daniel Eggler, Hyuck Chung, Fabien Montiel, Jie Pan, and Nicole Kessissoglou. Active noise cloaking of 2D cylindrical shells. *Wave Motion*, 87:106–122, 2019. ISSN 01652125. doi: 10.1016/j.wavemoti.2018.08.006. URL https://doi.org/10.1016/j.wavemoti.2018.08.006.

[93] Y I Bobrovnitskii. Impedance acoustic cloaking. *New Journal of Physics*, 12:0–20, 2010. ISSN 13672630. doi: 10.1088/1367-2630/12/4/043049.

[94] Charlie House, Jordan Cheer, and Steve Daley. An Experimental Investigation into Active Structural Acoustic Cloaking of a Flexible Cylinder. *Applied Acoustics*, 2020.

[95] Colin Hansen and Scott Snyder. *Active Control of Noise and Vibration*. CRC Press, 1st edition, 1996. ISBN 978-0419193906.

[96] Manfred Morai and Evanghelos Zafiriou. *Robust Process Control*. Prentice Hall, 1988. ISBN 978-0137821532. doi: https://doi.org/10.1002/aic.690371216.

[97] Naoto Abe. Practical stability and disturbance rejection of internal model control for time-delay systems. *Proceedings of the IEEE Conference on Decision and Control*, 2(December):1621–1622, 1996. ISSN 01912216. doi: 10.1109/cdc.1996.572764.

[98] Lennart Harnefors and Hans Peter Nee. Model-based current control of ac machines using the internal model control method. *IEEE Transactions on Industry Applications*, 34(1):133–141, 1998. ISSN 00939994. doi: 10.1109/28.658735.

[99] Mikio Tohyama. *Sound and Signals*. Springer-Verlag Berlin, Berlin, 2011. ISBN 978-3-642-20122-6. doi: 10.1007/978-3-642-20122-6.

[100] C. R Fuller, Colin H. Hansen, and Scott Snyder. Active control of sound radiation from a vibrating rectangular panel by sound sources and vibration inputs: An experimental comparison. *Journal of Sound and Vibration*, 145(2), 1991. doi: https://doi.org/10.1016/0022-460X(91)90587-A.

[101] Robert L Clark and Chris R Fuller. Active Control of Structurally Radiated Sound from an Enclosed Finite Cylinder. *Journal of Intelligent Material Systems and Structures*, 5(3):379–391, 1994. doi: https://doi.org/10.1177/1045389X9400500311.

[102] Paolo Gardonio and Stephen J. Elliott. Smart panels for active structural acoustic control. *Smart Materials and Structures*, 13(6):1314–1336, 2004. ISSN 09641726. doi: 10.1088/0964-1726/13/6/005.

[103] Jordan Cheer and Steve Daley. Active structural acoustic control using the remote sensor method. *Journal of Physics: Conference Series*, 744(1), 2016. ISSN 17426596. doi: 10.1088/1742-6596/744/1/012184.

[104] Joseph Milton, Jordan Cheer, and Steve Daley. Experimental identification of the radiation resistance matrix. *The Journal of the Acoustical Society of America*, 145(5):2885–2894, 2019. ISSN 0001-4966. doi: 10.1121/1.5102167.

[105] Darren B Ward, Zhi Ding, and Rodney A Kennedy. Broadband DOA Estimation Using Frequency Invariant Beamforming. *IEEE Transactions on Signal Processing*, 46(5):1463–1469, 1998.

[106] Kainam Thomas Wong and Michael D Zoltowski. Root-MUSIC-Based Azimuth-Elevation Angle-of-Arrival Estimation with Uniformly Spaced but... *IEEE Transactions on Signal Processing*, 47(12):3250, 1999. ISSN 1053587X. URL http://search.ebscohost.com/login.aspx?direct=true{&}db=a9h{&}AN=2593648{&}site=ehost-live{&}scope=site.

[107] N Y Wang and P Agathoklis. A new high-resolution-and-capacity DOA estimation technique based on subarray beamforming. *Signals, Systems and Computers, 2004. Conference Record of the Thirty-Eighth Asilomar Conference on*, 2(9):2345–2349 Vol.2, 2004. ISSN 10586393.

[108] Dumidu S. Talagala, Wen Zhang, and Thushara D. Abhayapala. Broadband DOA estimation using sensor arrays on complex-shaped rigid bodies. *IEEE Transactions on Audio, Speech and Language Processing*, 21(8):1573–1585, 2013. ISSN 15587916. doi: 10.1109/TASL.2013.2255282.

[109] Stephen Elliott, Mihai Orita, and Jordan Cheer. A Modal Approach to Acoustic Scattering and its Active Control. In *International Congress on Sound and Vibration*, pages 1–8. International Institute of Acoustics & Vibration, 2021.

[110] Greg Wilson, D. A. Aruliah, C. Titus Brown, Neil P. Chue Hong, Matt Davis, Richard T. Guy, Steven H.D. Haddock, Kathryn D. Huff, Ian M. Mitchell, Mark D. Plumbley, Ben Waugh, Ethan P. White, and Paul Wilson. Best Practices for Scientific Computing. *PLoS Biology*, 12(1), 2014. ISSN 15449173. doi: 10.1371/journal.pbio.1001745.

[111] Greg Wilson, Jennifer Bryan, Karen Cranston, Justin Kitzes, Lex Nederbragt, and Tracy K. Teal. Good Enough Practices in Scientific Computing. *arXiv*, pages 1–21, 2016. URL http://arxiv.org/abs/1609.00037.

[112] COMSOL Multiphysics. Acoustic Scattering off an Ellipsoid. Technical report, 2012.

[113] Phillip Newell and Keith Holland. *Loudspeakers: For music recording and reproduction*. Focal Press, 2006. ISBN 978-0240520148.

[114] Z. Barsoum and A. Lundbäck. Simplified FE welding simulation of fillet welds - 3D effects on the formation residual stresses. *Engineering Failure Analysis*, 16(7):2281–2289, 2009. ISSN 13506307. doi: 10.1016/j.engfailanal.2009.03.018. URL http://dx.doi.org/10.1016/j.engfailanal.2009.03.018.

[115] Wm Leach and William Marshall Leach Jr. Loudspeaker voice-coil inductance losses: Circuit models, parameter estimation, and effect on frequency response. *Journal of the Audio Engineering Society*, 50 (6):442–450, 2002. ISSN 0004-7554. URL http://80.apps.webofknowledge.com.dialog.cvut.cz/full{_}record.do?product=WOS{&}search{_}mode=GeneralSearch{&}qid=1{&}SID=N1qjTWMf6Fh29SzSR5R{&}page=1{&}doc=1.

[116] Frederick V Hunt. Electroacoustics;: The analysis of transduction, and its historical background (Harvard monographs in applied science). (5):260, 1954. URL http://www.amazon.com/Electroacoustics-transduction-historical-background-monographs/dp/B0007ILDYM.

[117] Stephen Crandall. *Dynamics of Mechanical and Electromechanical Systems*. Krieger Publishing, 1982. ISBN 978-0898745290.

[118] Neville Thiele. Loudspeakers in Vented Boxes-1. *AES: Journal of the Audio Engineering Society*, 19(5): 382–392, 1971. ISSN 00047554. URL http://www.scopus.com/inward/record.url?eid=2-s2.0-0015055662{&}partnerID=tZOtx3y1.

[119] Tom Irvine. The Half Power Bandwidth Method for Damping Calculation. (2):1–8, 2005.

[120] Mattia Dal Borgo, Maryam Ghandchi Tehrani, and Stephen John Elliott. Identification and analysis of nonlinear dynamics of inertial actuators. *Mechanical Systems and Signal Processing*, 115:338–360, 2019. ISSN 10961216. doi: 10.1016/j.ymssp.2018.05.044. URL https://doi.org/10.1016/j.ymssp.2018.05.044.